



<https://theses.gla.ac.uk/>

Theses Digitisation:

<https://www.gla.ac.uk/myglasgow/research/enlighten/theses/digitisation/>

This is a digitised version of the original print thesis.

Copyright and moral rights for this work are retained by the author

A copy can be downloaded for personal non-commercial research or study, without prior permission or charge

This work cannot be reproduced or quoted extensively from without first obtaining permission in writing from the author

The content must not be changed in any way or sold commercially in any format or medium without the formal permission of the author

When referring to this work, full bibliographic details including the author, title, awarding institution and date of the thesis must be given

Enlighten: Theses

<https://theses.gla.ac.uk/>
research-enlighten@glasgow.ac.uk

**INVESTIGATIONS OF THE PHYSICAL AND MAGNETIC
MICROSTRUCTURE OF CoCr THIN FILM
PERPENDICULAR MAGNETIC RECORDING MEDIA**

by David John Rogers

submitted for the degree of Doctor of Philosophy at the Department of
Physics and Astronomy, University of Glasgow.

March 1990

© 1990 David J. Rogers.

ProQuest Number: 11003371

All rights reserved

INFORMATION TO ALL USERS

The quality of this reproduction is dependent upon the quality of the copy submitted.

In the unlikely event that the author did not send a complete manuscript and there are missing pages, these will be noted. Also, if material had to be removed, a note will indicate the deletion.



ProQuest 11003371

Published by ProQuest LLC (2018). Copyright of the Dissertation is held by the Author.

All rights reserved.

This work is protected against unauthorized copying under Title 17, United States Code
Microform Edition © ProQuest LLC.

ProQuest LLC.
789 East Eisenhower Parkway
P.O. Box 1346
Ann Arbor, MI 48106 – 1346

"I can't believe that," said Alice.

"Can't you?" the Queen said, in a pitying tone. "Try again: draw a long breath, and shut your eyes."

Alice laughed. "There's no use trying," she said:

"One can't believe impossible things."

"I daresay you haven't had much practice," said the Queen. "When I was your age, I always did it for half-an-hour a day. Why, sometimes I've believed as many as six impossible things before breakfast."

L. Carroll (1871). *Through the looking glass*.

CONTENTS

ACKNOWLEDGEMENTS

DECLARATION

SUMMARY

CHAPTER 1: FERROMAGNETISM AND MAGNETIC RECORDING

1.1	Introduction	1
1.2	Basic Ferromagnetism	2
1.3	Energy Considerations for Ferromagnetic Thin Films	3
1.4	Principles of Magnetic Recording	7
1.5	Formats for High Density Magnetic Recording	10
1.6	Perpendicular Recording Media	13

CHAPTER 2: TECHNIQUES AND INSTRUMENTATION

2.1	Introduction	19
2.2	Basic Electron Beam / Specimen Interaction	20
2.3	Magnetic Imaging Techniques	22
2.4	The Conventional Transmission Electron Microscope	24
2.5	The Scanning Transmission Electron Microscope	30
2.6	The Vacuum Generators HB5 STEM	37
2.7	The JEOL 2000FX	42
2.8	The AN10000 System	43

CHAPTER 3: SAMPLE PREPARATION AND BASIC MICROSTRUCTURAL CHARACTERISATION

3.1	Introduction	44
3.2	Specimen Preparation	44
3.3	Experimental Methods	48
3.4	Results and Analysis	49
3.5	Discussion	52

CHAPTER 4: MICROCOMPOSITIONAL ANALYSIS

4.1	Introduction	53
4.2	Considerations For EDX Microanalysis of CoCr Thin Films	53
4.3	Investigation of the Effect of Substrate Temperatures for CoCr Layers Deposited Directly onto PET	58
4.4	Investigation of the Effect of a Ge Underlayer on Local Composition	67
4.5	Chrysanthemum Pattern (CP) Cr Segregation	74
4.6	Overall Conclusions	81

CHAPTER 5: SIMULTANEOUS IMAGING OF PHYSICAL AND MAGNETIC MICROSTRUCTURE

5.1	Introduction	84
5.2	Experimental Technique	85
5.3	Study of CoCr Deposited onto PET at 30C	89

5.4	Study of CoCr Deposited onto PET at 90C	95
5.5	Stray Field Simulation	98
5.6	General Discussion and Conclusions	100

CHAPTER 6: LORENTZ MICROSCOPY OF TRACKS IN PERPENDICULAR CoCr

6.1	Introduction	102
6.2	Recording on Films Thin Enough for TEM Investigations	103
6.3	Specimen Preparation	103
6.4	Experiment	104
6.5	Results and Discussion	109
6.6	Conclusions	110

CHAPTER 7: CONCLUSIONS AND FUTURE WORK

7.1	Conclusions	112
7.2	Future Work	118

APPENDIX 1:	Macroscopic Characterisation Techniques	122
--------------------	---	-----

APPENDIX 2:	Analysis Program for EDX Spectra	124
--------------------	----------------------------------	-----

REFERENCES

ACKNOWLEDGEMENTS

Much of the credit for the successful completion of this thesis must go to the many people who helped me during the course of the study. First of all I would like to thank my supervisor, Professor J. N. Chapman, for excellent guidance throughout. Special mention is also due to Drs J.P.C. Bernards for the success of the collaboration with Philips Research Laboratories and to Dr S. McVitie for many useful discussions and much practical assistance. I am also much indebted to Professor R. P. Ferrier for his support and for the provision of the electron microscope facilities in the Solid State Group at the University Of Glasgow.

Although too numerous to mention individually I would like to express my gratitude to all the members of the Solid State group at Glasgow and all in the Magnetics group at Philips for their help and advice. For maintaining the microscopes and specimen preparation facilities at Glasgow I would like to thank the following: Dr W. A. P. Nicholson, Mr A. Howie, Mr J. Simms and Miss M. Low. For much practical assistance during the course of the project I would like to thank Mr A. D. Young and D. McDonald and for producing a not inconsiderable number of photographic prints I would like to thank Mr I. McVicar. For use of their word-processing facilities I would like to thank the Gravitational Waves group and for plotting several of the graphs shown in chapter 4 I would like to thank Mr D. Donnet. For providing financial assistance and equipment I would like to thank both the SERC and Philips and for providing the CP films in chapter 4 I would like to thank Dr Y. Maeda. Finally, I would like to thank my family for all their support and encouragement.

DECLARATION

This thesis is a record of the work carried out by me in the Department of Physics and Astronomy at the University of Glasgow. The work described herein is my own, apart from the manufacture of the films and the preparation of some of the electron microscope samples. All films were provided by Philips Research Laboratories in the Netherlands apart from the "chrysanthemum pattern" samples described in chapter 4 which were provided by Dr. Y. Maeda of NTT Laboratories in Japan. Some of the work contained in the thesis has been published in the papers:

"Analysis of Magnetic Domain Structures in CoCr Sputtered Films Using Differential Phase Contrast Electron Microscopy", J.N. Chapman, D.J. Rogers, J.P.C. Bernard*, Journal de Physique, supplement 12, (1988)

"Determination of Local Composition in CoCr Films Deposited at Different Substrate Temperatures", D.J. Rogers, J.N. Chapman, J.P.C. Bernard*, S.B. Luitjens*, IEEE Trans. Magn. 25 (1989).

A number of the results in Chapter 4 were reported at the International Colloquium on Magnetic Films and Surfaces, ICMFS-12, a satellite meeting of the International Conference on Magnetism 1988.

This thesis has not previously been submitted for a higher degree.

* Philips Research Laboratories, P.O. Box 80000, 5600JA Eindhoven, The Netherlands.

SUMMARY

The work presented in this thesis is concerned with improving the understanding of the relationship between the physical and magnetic microstructure in CoCr thin film perpendicular magnetic recording media. This was investigated using a combination of transmission electron microscope (TEM) techniques to study a series of CoCr films with systematically adjusted growth conditions.

The first chapter begins with an outline of basic ferromagnetism and the energy considerations governing the domain configuration in ferromagnetic thin films. General principles of magnetic recording are then discussed, with a more detailed treatment of media, high density recording formats and the properties of CoCr for perpendicular recording.

Chapter 2 introduces basic TEM imaging theory and describes the conventional transmission electron microscopes (CTEM's) and the dedicated scanning transmission electron microscope (STEM) used in this project. The chapter then discusses techniques for imaging magnetic structures and the use of high resolution energy dispersive x-ray (EDX) microanalysis in the STEM for microcompositional investigations.

The first sections in chapter 3 discuss the planar and cross-sectional specimen preparation techniques adopted for all the work in this thesis. The remainder of the chapter describes the study of a series of CoCr layers grown to various thicknesses and with different compositions. Bulk physical and magnetic characterisation are combined with microstructural investigations in the CTEM. The work demonstrates that bulk measurements alone are insufficient to predict the physical, and therefore the magnetic microstructure, of CoCr thin films. It also

illustrates the usefulness of such a study as part of any investigation of the microscopic properties of CoCr recording media.

The next three chapters contain the experimental results which form the core of the thesis. Chapter 4 describes the experiments conducted on CoCr films using EDX microanalysis. Planar sections were investigated to allow correct positioning of the probe on a particular region of specimen and thus reveal, directly, the local elemental composition associated with features of the microstructure. Study was made of films deposited at different substrate temperatures both with and without a Ge underlayer. The results obtained using this technique provided detailed quantitative data on the extent and pattern of Cr segregation in each film.

Chapter 5 describes the improvements in the differential phase contrast (DPC) mode of Lorentz microscopy in the STEM which facilitated simultaneous imaging of the physical and magnetic microstructure of thinned cross-sections of CoCr films. The results from the application of this technique to the study of the effect on the microstructure of substrate temperature during deposition are then interpreted in conjunction with the compositional information from chapter 4.

The importance of direct microscopic study of recorded tracks in CoCr perpendicular recording media forms the introduction for chapter 6. The chapter then explains the development and results of a successful method for direct observation of the tracks with the Fresnel mode of Lorentz microscopy in the JEOL 2000FX TEM.

The final chapter draws conclusions on the results of the project and presents proposals for possible future investigations of CoCr perpendicular magnetic recording media.

CHAPTER 1 - FERROMAGNETISM AND MAGNETIC RECORDING

1.1 INTRODUCTION

The magnetic properties of ferromagnetic thin films are often seen to depend on the corresponding physical microstructure. To understand the nature of this relationship it is therefore desirable to have as full a description as possible of both. It has been shown (Morrison 1981, McFadyen 1986) that under favourable conditions a comprehensive description of both of these can be obtained using the electron microscopes and related equipment available in Glasgow University.

A class of magnetic materials currently under extensive investigation is that suitable for high density data recording. Information storage densities reported for such media are already of the order of 1 bit per square micron (Hecht 1990, Luitjens et al. 1988). The relation between the magnetic and physical microstructure in these media is on such a small scale that little is known directly about the microscopic processes involved. As a result of this it becomes increasingly difficult to optimise the materials for recording purposes.

A natural application of the techniques developed by Morrison and McFadyen is therefore the study of thin film magnetic recording media. A project was proposed employing a range of electron microscopy techniques to investigate a series of CoCr thin films. The aim of this study was an improved understanding of the fundamental mechanisms determining the recording potential. CoCr films with flexible substrates (base materials) were chosen for the study because they represent one of

the most promising of the new generation of magnetic recording media (Iwasaki & Takemura 1975, Iwasaki & Nakamura 1977, Ouchi & Iwasaki 1987¹).

By way of introduction to the thesis this chapter discusses basic ferromagnetism, magnetic recording and the use of CoCr as a perpendicular magnetic recording medium.

1.2 BASIC FERROMAGNETISM

A ferromagnet is a material which has a nonvanishing net magnetic moment (ie spontaneous magnetisation) in the absence of an applied magnetic field. This phenomenon occurs at finite temperatures below a critical value called the Curie temperature (T_C). Ferromagnets can be metals, alloys or oxides.

In a ferromagnetic material each individual atom has an intrinsic magnetic moment due to the orbital motion and/or spin of unpaired electrons. The resulting bulk magnetic moment indicates that the individual magnetic vectors have a preferred parallel orientation. This implies that there exists a coupling between the independent moments stronger than the randomising effect of thermal agitation. At temperatures exceeding T_C there is no longer any net magnetic moment in the absence of a field since thermal disordering effects are sufficient to disrupt the magnetic alignment. T_C is a function of the material and therefore characterises a ferromagnet.

Weiss (1907) proposed that ferromagnetism could be understood in terms of an internal molecular field \underline{H}_m directly proportional to the sample magnetisation, \underline{M} . For a typical ferromagnet at room

temperature H_m is $\sim 3 \times 10^9 \text{ A.m}^{-1}$. Heisenberg (1928) showed that the origin of the molecular field lay in quantum mechanical exchange coupling of electron spin moments promoting the parallel alignment of all the magnetic dipoles.

1.3 ENERGY CONSIDERATIONS FOR FERROMAGNETIC THIN FILMS

In practice ferromagnets generally do not have all internal magnetic moments aligned in the same direction. This is because there are interactions other than exchange coupling which influence their orientation. A stable magnetisation distribution, for a given ferromagnet, is a state in which the sum of the various energy contributions is minimised. This produces a sample divided into one or more regions in which all magnetic vectors are aligned preferentially in a single direction. Each of these regions is called a magnetic domain.

The theoretical calculation of the domain configuration for a bulk ferromagnetic sample is an almost intractable problem. This study is, however, concerned only with investigations into the domain configurations in ferromagnetic thin films. In this case the problem is considerably simplified since one spatial dimension is significantly reduced. The following discussion outlines the main energy contributions which must be taken into account.

1.3.1 Exchange Energy, E_e

By the Pauli exclusion principle two electrons with the same spin

cannot have the same spatial wavefunction whilst two electrons with oppositely directed spins can. The electrostatic energy of a system of atomic spin moments will therefore depend on the relative orientation of the spins. For a ferromagnetic sample the overall exchange energy can be taken as the sum over the whole system of the exchange energy for all pairs of neighbouring spins. The exchange energy between two neighbouring spin moments, U , can be represented:

$$U = - 2J_{ij} \underline{S}_i \cdot \underline{S}_j \quad 1.1$$

where J_{ij} is the exchange coupling constant (which is related to the overlap of electron orbitals and is positive for a ferromagnet) and $\underline{S}_i, \underline{S}_j$ are the atomic electron spin moments. Therefore U is at a minimum for \underline{S}_i and \underline{S}_j parallel, in other words, for the moments magnetically aligned.

1.3.2 Magnetostatic Energy, E_m

The magnetostatic energy is due to the Coulomb interaction between magnetic "free poles". Volume and surface magnetic charge lead to an external stray field distribution and an internal field, \underline{H}_d . This internal field opposes the generating magnetisation and is therefore termed a demagnetising field. For particle of volume V and surface area S , \underline{H}_d is given by:

$$\underline{H}_d(\underline{r}) = \frac{1}{4\pi} \int_V \frac{-\nabla \cdot \underline{M}}{r^2} dV + \frac{1}{4\pi} \int_S \frac{(\underline{M} \cdot \underline{n})}{r^2} dS \quad 1.2$$

where \underline{r} is the position vector for the field points, \underline{n} is the unit vector normal to the surface, the divergence of \underline{M} represents the magnetic volume charge and $\underline{M} \cdot \underline{n}$ represents the surface magnetic charge. This leads to a magnetostatic energy expression:

$$E_m = -\frac{1}{2}\mu_0 \int_V \underline{M} \cdot \underline{H}_d dV \quad 1.3$$

The extent of this demagnetising effect is therefore dependent on both the sample geometry and the internal magnetisation.

1.3.3 Anisotropy Energy, E_a

In crystalline samples the spin-orbit coupling of the electrons in the lattice produces energetically preferred orientations for the magnetic vector along specific crystal axes (magnetic easy axes). CoCr films grown for perpendicular recording have a hexagonal close packed (hcp) structure with uniaxial anisotropy directed along the normal to the film plane. For this crystal structure the magnetocrystalline anisotropy energy density, E_k (kJ.m^{-3}) is a function of the angle between the magnetisation vector, ϕ , and the c-axis and is given, to first order, by:

$$E_k = K_u \sin^2 \phi \quad 1.4$$

where K_u is the uniaxial anisotropy constant (kJ.m^{-3}) which can be obtained from torque magnetometer measurements (appendix 1).

The magnetisation in a sample can also interact with the elastic properties of a material and cause an increase in the strain energy of the

sample. This can create easy axes of magnetisation and introduce a strain anisotropy energy term into the magnetisation distribution considerations. This magnetostriction energy is important for continuous thin film recording media because of the considerable stress at the head/film interface.

1.3.4 Domain Wall Energy, E_w

Separating the domains within a ferromagnetic sample are transition layers called domain walls. These are regions in which the magnetisation vector rotates between the directions of magnetisation of adjacent domains. They can be important for magnetic recording if their width, shape or orientation limits the maximum information storage density (figure 1.1). For a ferromagnetic thin film there are three common types of domain wall and they are classified according to the manner in which the magnetisation rotates (figure 1.2). The direction of magnetisation can either rotate about an axis in the plane of the wall (the Bloch wall), about an axis perpendicular to the plane of the wall (the Neel wall) or through a combination of both of these (the cross-tie wall).

The rotation of the magnetic moments in a domain wall produces an exchange energy per unit area and, depending on the type of wall, sometimes a magnetostatic energy per unit area. Magnetic anisotropy can also influence the domain walls, adding another contribution to the domain wall energy. Domain wall energy, whilst being a result of energy terms already considered, can be looked upon as an independent energy term.

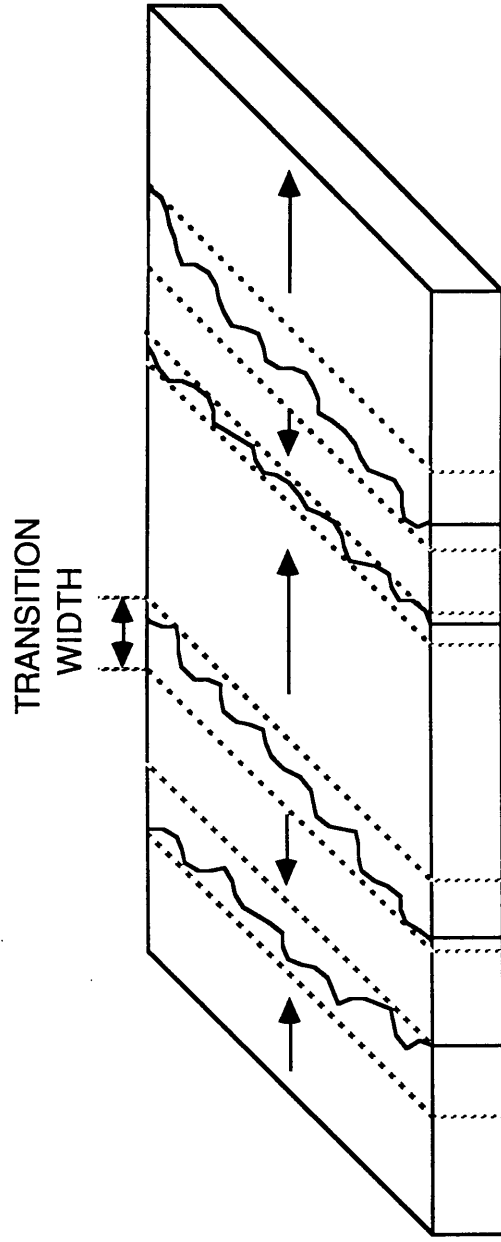
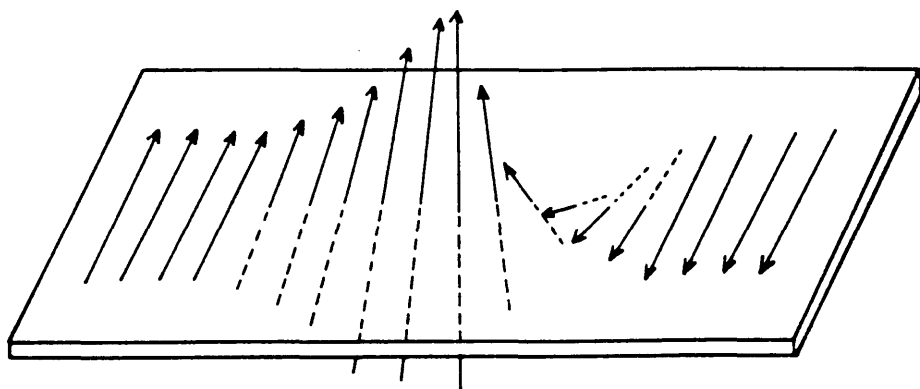


Figure 1.1 Domains and transition widths in a longitudinal thin film recording medium.

a



b

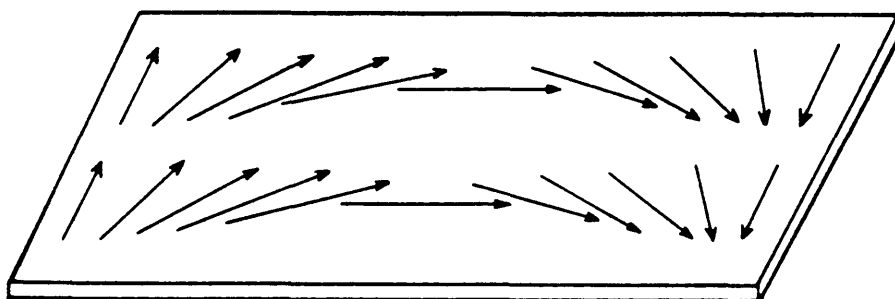


Figure 1.2 Rotation of direction of magnetisation in a) a Bloch wall and b) a Neel wall.

1.3.5 Discussion

From the above, the total magnetic energy, E_t , for a ferromagnetic thin film can be written:

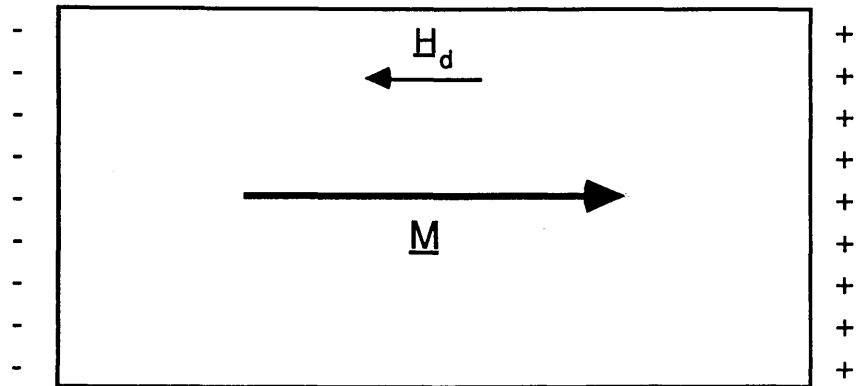
$$E_t = E_e + E_m + E_a + E_w \quad 1.4$$

In general, the size of domains will be controlled by the magnetostatic and wall energies whilst a high anisotropy term will dictate the geometry and direction of magnetisation. A simple illustration of this is the case of a ferromagnetic particle with uniaxial anisotropy directed along the major axis (figure 1.3a). For this system reduction of the magnetostatic energy can be achieved by increasing the number of domains (figure 1.3b). This leads, however, to an increase in exchange and wall energies.

1.4 PRINCIPLES OF MAGNETIC RECORDING

A schematic of the conventional magnetic recording process is shown in figure 1.4. In such a system an input signal generates a current in a transducer known as the recording (or write) head. This causes a field to be applied to a magnetic recording medium moving at constant velocity past the head. This medium is effectively a permanent magnet on which the applied field writes a series of magnetic domains. The domains are retained by the medium, when the write field is removed, as a pattern of remanent magnetisation in a track along the direction of motion. When this domain pattern passes by the playback (or read) head transducer the external field distribution induces a current in the head.

a)



b)

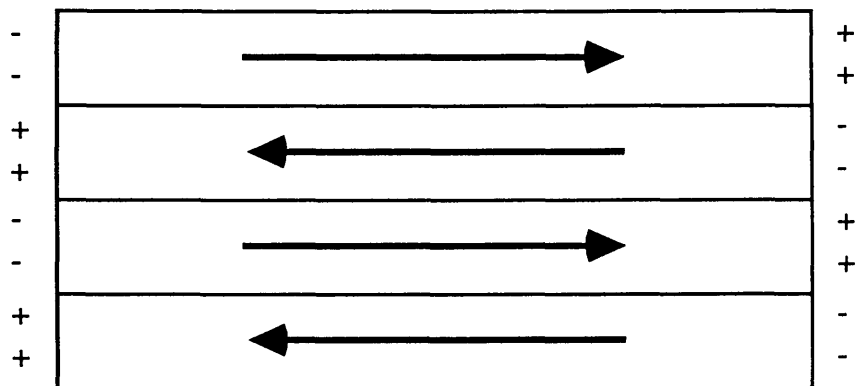


Figure 1.3

- a) Uniformly magnetised ferromagnetic sample with uniaxial anisotropy;
b) Magnetostatic energy reduction through increased number of domains.

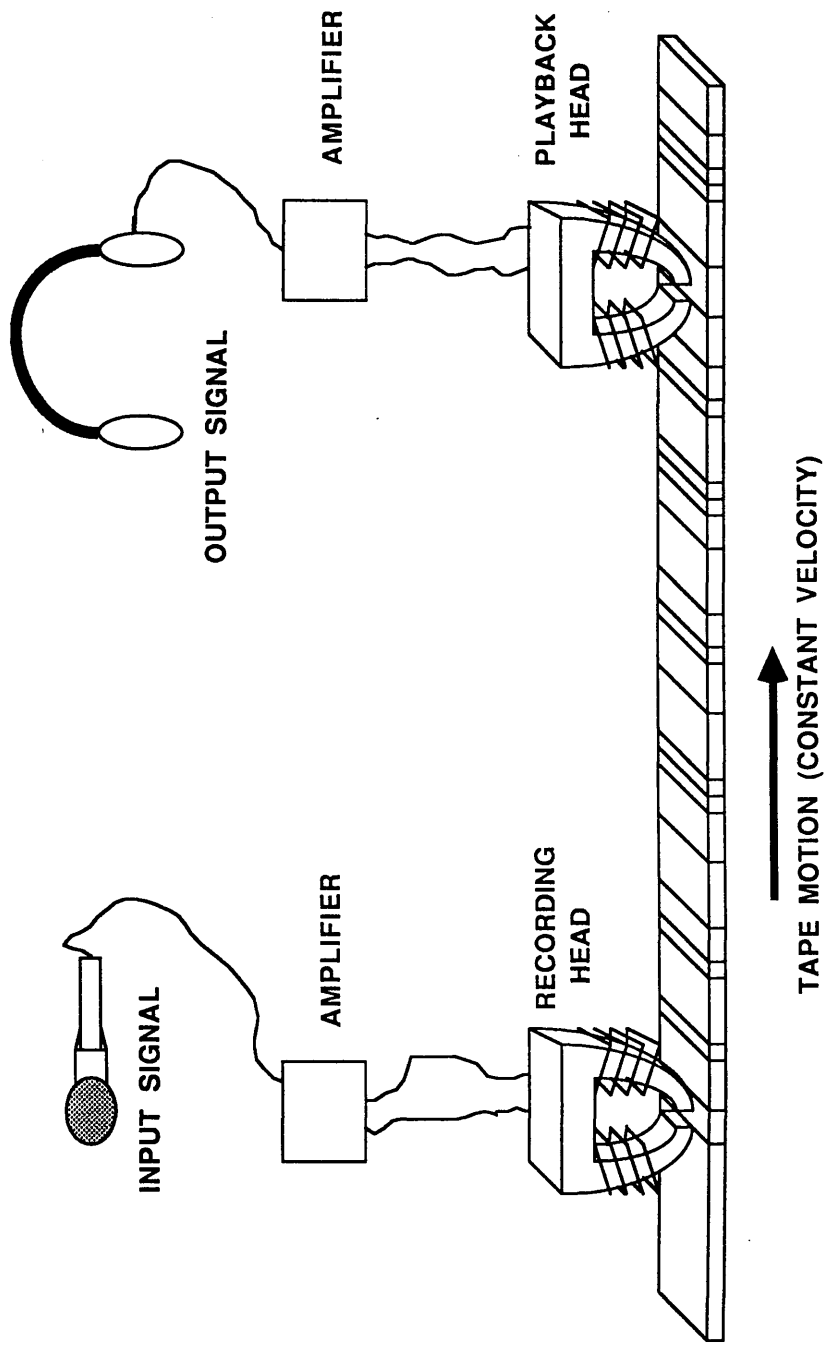


Figure 1.4 Simplified illustration of the basic magnetic recording process.

This can be converted to give an output proportional to the original input signal (for a more detailed description see Jorgensen (1980), White (1985) or Mee & Daniel (1987)).

The important goals of a practical version of such a system are :

- 1) to have a playback which is a faithful reproduction of the input signal to the recorder and
- 2) to create the highest possible data packing density on the medium which results in the minimum storage volume.

There are a number of aspects to a recording system, each of which can be considered as a separate research field. This project is principally concerned with properties of the recording media and so the rest of this section gives a general explanation of the main considerations in the design of a recording medium.

1.4.1 Magnetic Recording Media

In addition to fulfilling the above requirements an ideal recording medium should be capable of an infinite number of cycles of erasure and recording. Furthermore, long term storage and multiple reading should not cause significant deterioration of the magnetic pattern on the medium provided that it is not subject to an applied magnetic field of strength comparable to that of a recording head write field.

The three main types of magnetic recording media currently available are flexible disks, hard disks and tapes. All of these usually comprise a thin hard-magnetic (registration) layer supported by a non-magnetic substrate. The magnetic layer can be either particulate or continuous in nature. Magnetically the medium should have a high hysteresis loop squareness and a high saturation magnetisation, M_s

(figure 1.5). The medium will then have a high remanent magnetisation, M_r (magnetisation of medium once saturating field is removed) and a high coercivity, H_c (the reverse field required to demagnetise the medium). The high M_r is necessary to give sufficient field strength above the surface of the medium to induce a detectable signal in the read head, and the high H_c prevents unwanted erasure of data by any weak fields to which the medium may be subjected during storage.

Another important consideration in the design of a recording medium is the durability of the medium, since prolonged life of media, and therefore the recording system, depend on protection of the film and head surfaces. Improved medium strength, flexibility and smoothness can all help to prevent excessive wear. The best protection, however, is achieved through either non-contact recording in which the fixed head "flies" on a cushion of air just above the moving medium, or by application of a thin coating of lubricant tailored to the particular head/medium pairing. In both these solutions though the read field strength at the head is reduced, thus lowering the detectable signal.

1.4.2 Recording Densities

Information storage densities are usually quoted as bits per unit area of medium (areal densities), but areal density can be divided into linear density (bits of information per unit length of track) and track density (the number of tracks per unit width of film). Total storage volume is also dependent on the thickness of the medium. For a conventional recording medium these three aspects of recording density should not be considered as separate, since adequate signal level depends on all of them. This can be illustrated by the example of increasing the linear

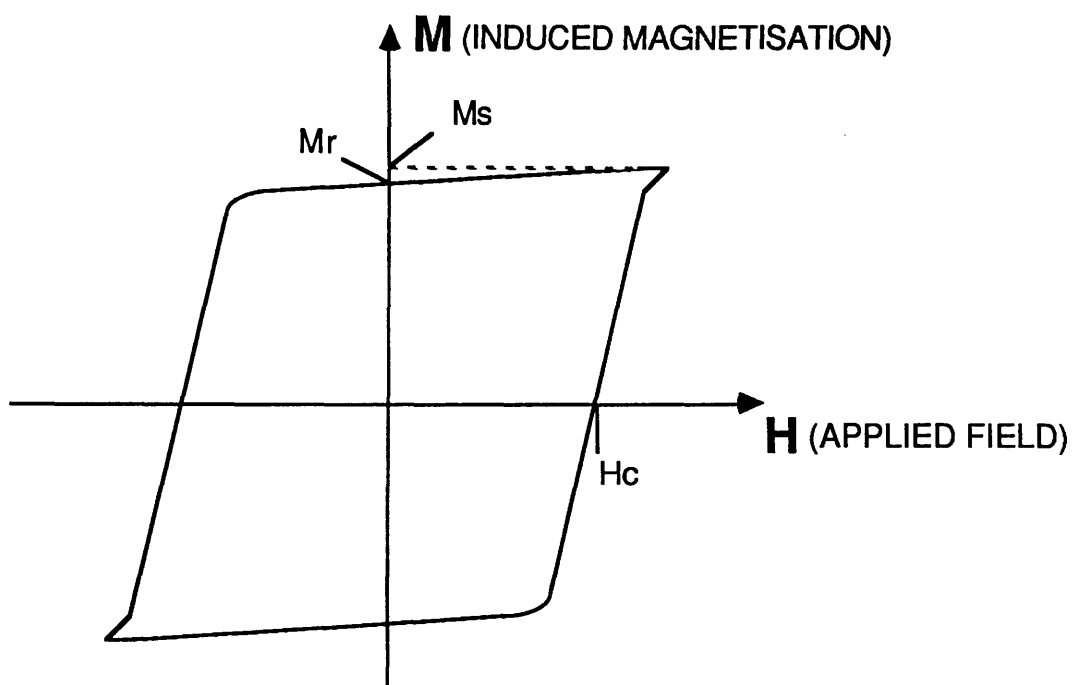


Figure 1.5 Model hysteresis loop for magnetic recording medium.

density for a given medium thickness. In this case either track width must be increased (track density decreased) or M_r must be increased, to compensate for the loss in signal. Areal recording densities incorporate this concept of interdependence of linear density, track density and medium properties and are often quoted as a measure of the recording capability. In practice, improvements in areal storage densities are often realised through a combination of lower system noise and decreased head-to-medium spacing which reduces the minimum signal required.

1.5 FORMATS FOR HIGH DENSITY MAGNETIC RECORDING

In order to improve recording densities whilst maintaining fidelity it has been found necessary not only to improve existing heads and media but also to explore alternative recording formats. This section discusses longitudinal, perpendicular and magneto-optical recording which are three of the modes currently being investigated for high density magnetic recording.

1.5.1 Longitudinal Magnetic Recording

Longitudinal recording is the most widely used mode of magnetic recording. In conventional longitudinal recording the magnetisation in the domains lies in the plane of the film. The crucial limiting factor for recording densities in these films is the transition region between neighbouring domains. Magnetostatic energy considerations create demagnetising effects (figure 1.6a) which cause a broadening of this region and thereby limit the obtainable storage densities. There are two

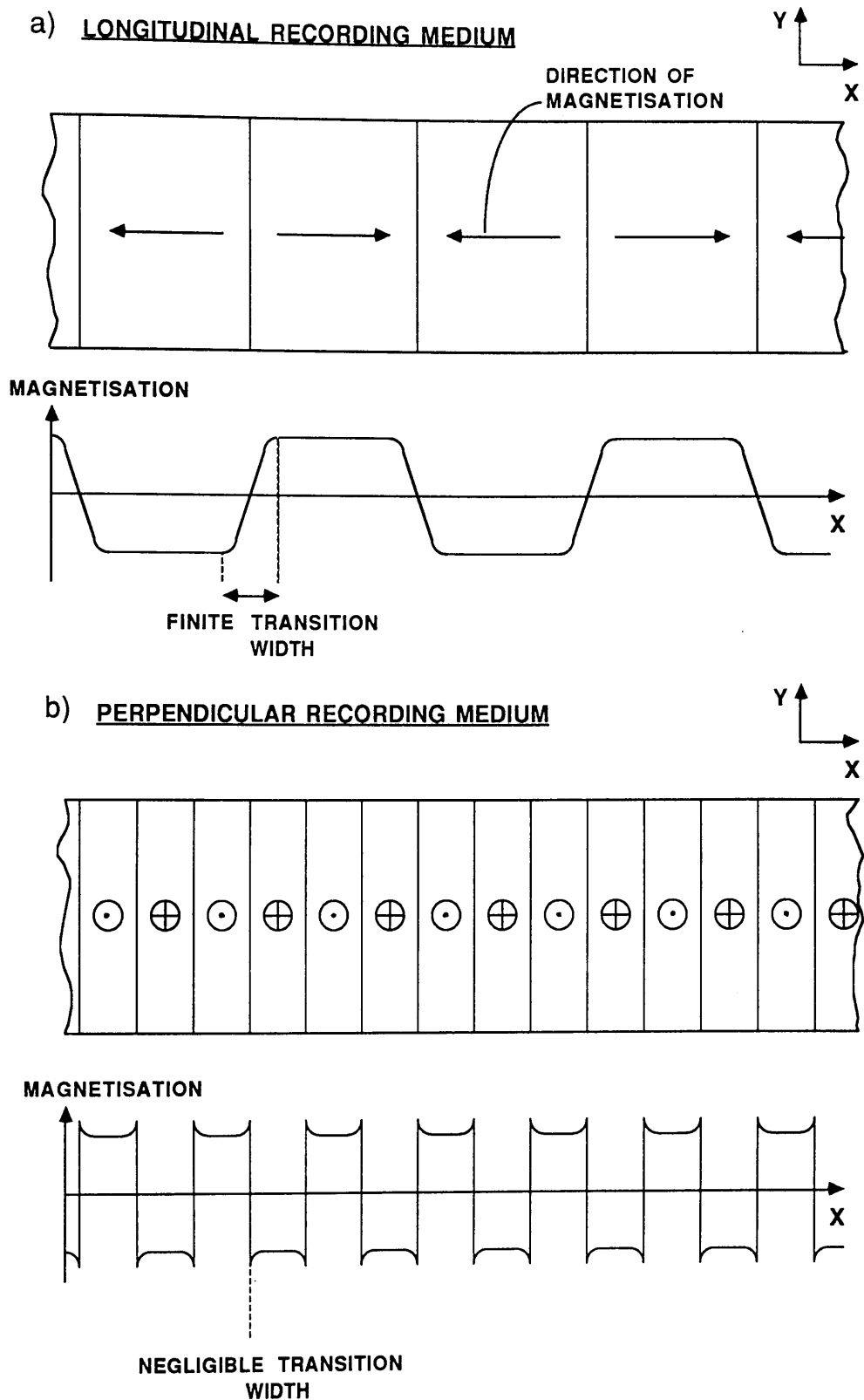


Figure 1.6

a) The effect of the demagnetising field on the magnetisation transition in a longitudinal medium, and b) the elimination of the demagnetising effect in a perpendicular medium.

main groups of longitudinal recording media; particulate and continuous thin film.

In particulate media individual magnetic particles (eg. acicular Fe_2O_3 or CrO_2) are embedded in a binder matrix with their magnetic easy axes preferentially oriented along the film. As well as the demagnetising effect recording densities can also be limited by the particle size and ordering. The minimum bit size, however, is a function of $M_r D/H_c$ (Suzuki 1984) where D is the thickness of the magnetic layer. This imposes thickness constraints on the particles. Difficulties with production of very thin particles make particulate media less promising for future high density recording.

In continuous longitudinal recording media the magnetic layer is a metallic film less than 100nm thick with an easy axis of magnetisation usually in the plane of the film (eg. CoP or CoNiP) (metal evaporated CoNi films, although classed as "longitudinal" have a component of magnetisation lying out of the plane of the film). In this case the minimum transition width is generally controlled by a zig-zag (or saw-tooth) domain wall configuration which forms to reduce the magnetostatic energy. The transition width is again a function of $M_r D/H_c$ (Dressler & Judy 1974).

The reported current maximum for areal recording density in particulate CrO_2 films is $0.4 \text{ bits} \cdot \mu\text{m}^{-2}$. Higher areal recording densities of $1 \text{ bit} \cdot \mu\text{m}^{-2}$, are however reported for metal evaporated CoNi films (Luitjens et al. 1988).

1.5.2 Perpendicular Magnetic Recording

Perpendicular recording, although sometimes referred to as a new

mode, was the first way considered (Poulsen 1898) for storing information magnetically. Interest concentrated subsequently, however, on other recording formats until the mid 1970's when Iwasaki and Nakamura (1977) generated renewed interest in the mode by pointing out the potential for the retention of a high density of magnetic flux reversals. In perpendicular recording, anti-parallel magnetic transitions are formed normal to the medium surface. The demagnetising effect which acts to increase transition widths between adjacent domains in longitudinal media is therefore eliminated (figure 1.6b). The resulting sharp transition between domains enables the retention of a very high density of magnetic flux reversals in which M_r becomes larger and more stable as recording density increases (Ouchi & Iwasaki, 1984). Current reports indicate maximum estimated recording densities of $\sim 1 \text{ bit} \cdot \mu\text{m}^{-2}$ (Luitjens et al. 1988).

1.5.3 Magneto-Optical Recording

Early "optical" recording involved "write once, read many time" (WORM) technology which, as such, is not a direct competitor to conventional recording. In more recent magneto-optical recording, domains are written thermo-magnetically in a ferrimagnetic thin film of a rare-earth transition metal alloy (eg GdTbFe or TbFeCo) and read back magneto-optically via the optical polar Kerr effect (Greidanus & Klahn 1989). This technique enables multiple cycles of erasure and recording.

A magnetic field is applied to the film. Tracks are written by heating the medium locally above the compensation temperature T_{comp} or Curie temperature using a focused high power laser. On readback the

direction of magnetisation within the recorded domains determines the plane of polarisation of a reflected low power laser probe which can be used to generate an output signal. By applying a varying magnetic write-field a magnetic pattern can therefore be written with minimum bit size shorter than the wavelength of light. The optical resolution of the current read process, however, severely limits the realisable linear density.

Linear recording densities of the order of hundreds of nanometres (wavelength of laser used to read information) have already been exceeded by more conventional media. With magneto-optical media, however, it is the very high track density (1000 tracks per inch as opposed to 100 per inch on a Winchester disk) which gives it a high areal storage density $\sim 1 \text{ bit} \cdot \mu\text{m}^{-2}$. Although this experimental capacity is comparable with the recording densities achievable with other high density recording media at the moment, the problem of the optical resolution limit is felt to be a considerable drawback as regards the future potential.

1.6 PERPENDICULAR RECORDING MEDIA

To be suitable for high density perpendicular magnetic recording a medium should have a high perpendicular coercivity, H_c , typically in the range of $20\text{-}100 \text{ kA} \cdot \text{m}^{-1}$, a high M_s of approximately $400 \text{ kA} \cdot \text{m}^{-1}$ and a large positive effective perpendicular magnetic anisotropy K_{eff} , (typically $20\text{-}25 \text{ kJ} \cdot \text{m}^{-3}$) to give an easy axis of magnetisation perpendicular to the film plane. Additionally, the medium should ideally have a rotational mechanism for magnetisation reversal (Suzuki 1984, Ouchi & Iwasaki 1987²) to maximise the potential recording density

(see section 1.6.2).

Several materials other than CoCr have been proposed as candidates for perpendicular recording (Ouchi & Iwasaki 1987¹), the drawbacks with the most promising of which are outlined below:

MnBi has been shown to have a magnetisation reversal mechanism based on domain wall movement and hence it will not support high recording densities. Ba ferrite films have poor noise characteristics because the particle size cannot be reduced significantly without prohibitive reduction in the signal level. Rigid disks made with either Fe or Co particles plated in fine pits in anodic-oxidised aluminite have so far been too difficult to manufacture in the required double layer form. Finally several Co-metal alloys, which fulfil most of the necessary criteria, do not have a K_{eff} which is either as high or as reproducible as that for CoCr.

1.6.1 CoCr As A Perpendicular Recording Medium

Most experimental CoCr thin films are now produced by radio frequency (rf) sputter deposition from a bulk CoCr target onto a flexible substrate (usually polyester or polyimide). With a target Cr concentration in the region of 20 atomic % this process reliably produces a hexagonal close packed (hcp) columnar structure with crystallographic c-axis perpendicular to the film plane. The advantages of this method of manufacture are that the film properties are reproducible and that the CoCr layer has good adhesion with the substrate or underlayer.

In this deposition process nucleation of CoCr crystallites must occur before any columnar growth develops. Film growth subsequent to

nucleation occurs along the hcp c-axis perpendicular to the surface of the substrate. This produces a layer with mean column diameter between a tenth and a twentieth of the thickness of CoCr irrespective of the perpendicular H_C or M_S (Iwasaki et al. 1980). The nucleation process, however, generally leaves a disordered layer with in-plane easy axis of magnetisation at the base of the columns. Introduction of an amorphous Ge layer beneath the CoCr in the deposition process is found to reduce the extent of this disordered layer and thereby increase the magnetocrystalline anisotropy (Futamoto et al. 1985). The mechanism through which this occurs is not completely understood.

The most important growth parameters in determining the magnetic properties of the resultant film are background vacuum pressure, sputtering Ar gas pressure, target composition and substrate temperature during deposition, T_s (Lodder & Wielinga 1984). The dispersion angle of the hcp c-axis, $\Delta\theta_{50}$, obtained from rocking-curve measurements (appendix 1), gives a measure of how closely the column c-axis is aligned with the normal to the film plane. The background and Ar pressures are adjudged to be optimal when this is minimised ($\approx 10^{-7}$ and $\approx 10^{-5}$ torr respectively). The perpendicular H_C , the M_S , and K_{eff} all show a dependence on T_s . The K_{eff} is seen to depend strongly on the level of Cr in the target (Andra & Danan 1987). This suggests that the perpendicular anisotropy of these films is mainly due to magnetocrystalline anisotropy. Increasing the target Cr concentration causes a decrease in the saturation magnetisation, M_S . A balance must therefore be reached for which the films have both a high perpendicular anisotropy and a high M_S . A Cr concentration of approximately 21 atomic % is now widely accepted as the optimum (see chapter 3).

The properties which make CoCr a good perpendicular recording

medium can be summarised as follows:

- 1) CoCr is a solid solution in which M_s can be easily controlled by the level of non-magnetic Cr.
- 2) The M-H loop shows a large hysteresis loss in the perpendicular direction and the in-plane direction is a hard axis of magnetisation.
- 3) The perpendicular H_c is high and can be controlled during fabrication by varying the substrate temperature.
- 4) The material has a high perpendicular anisotropy which is independent of the perpendicular H_c and M_s .
- 5) The film is mechanically strong, chemically stable and the surface is extremely smooth.

1.6.2 Domain Structure in CoCr Thin Films

There are two main theoretical models for the nature of the domain pattern in CoCr thin films with perpendicular anisotropy (Koster & Arnoldussen 1987, Hoffmann 1986, Ohkoshi & Kusuda 1983, Zhu & Bertram 1989). The first is a particulate model in which individual columns, or small groups of columns act as isolated magnetic units, ideally with a rotational mechanism for magnetisation reversal (see below). The second is of a film with stripe domains and strong exchange coupling at column boundaries, in which magnetisation reversal occurs through domain wall movement. In the first model the coercivity of the film is determined by the magnetocrystalline anisotropy in the grains, the grain shape, grain coupling and the stress state of the grains. In the second model coercivity is controlled by the wall energy which in turn is affected by magnetocrystalline anisotropy, magnetostatic energy at the wall, stress variations, film roughness and compositional irregularities. In practice both these domain models may be operative in CoCr films

(Bernards et al. 1989). The extent to which each model holds, however, is seen to be strongly dependent on the growth conditions and is believed to be linked to the segregation of Cr to column boundaries (Hoffmann 1986, Chapman et al. 1986, Sugita et al. 1981, Smits et al. 1983, Parker et al. 1989).

The question of preferred magnetisation reversal mode in the particulate model (mentioned in the introduction to section 1.6) can be understood with reference to improved recording density. For linear recording density it is uncertain whether it makes a difference if a perpendicular anisotropy film undergoes magnetisation reversal by either particle-like switching or reverse domain nucleation and domain wall motion. The micromagnetic structure of the recorded pattern, and therefore the media noise are, however, found to depend on the mode of reversal (Koster & Arnoldussen 1987, Ouchi & Iwasaki 1987², de Bie et al. 1987). This is important because, as mentioned in section 1.4.2, reductions in the system noise are often the means by which areal recording densities can be improved. Experimental evidence supporting both models suggests that the mode of magnetisation reversal depends on the detailed deposition conditions (Lodder et al. 1987).

1.6.3 Recording With CoCr

Heads are designed in conjunction with the mode of recording. In perpendicular mode the aim is to produce a strong well defined field with a direction of induction perpendicular to the film plane and a precisely controlled lateral position. In the read process the aim is to have a very high sensitivity to the perpendicular component of the external stray field distribution produced by the information recorded

in the film. There are currently three main head/medium formats which have been developed for use with perpendicular recording media. The first two generally record on a single-layer medium in which the only magnetic layer is the registration layer. These modes employ either a ring head or a single pole type (SPT) head with an additional "auxiliary" pole piece below the medium. A head/medium format which is considered highly promising for perpendicular magnetic recording (Zieren 1988, Nakamura & Iwasaki 1984) is the SPT head combined with a double-layer medium (figure 1.7). In this set-up the head induces a well defined perpendicular field in the registration layer and the soft magnetic underlayer acts as a flux path in much the same way as a "keeper" on a permanent magnet.

1.6.4 Summary

In sections 1.6.1 and 1.6.2 we have seen that the magnetic properties of rf deposited CoCr films depend on the physical properties of the films, which are in turn controlled by the large number of growth parameters influencing the microstructure. Reduction of the bit size can be achieved through a better understanding of the effect on the resultant domain structure of each of the important growth parameters.

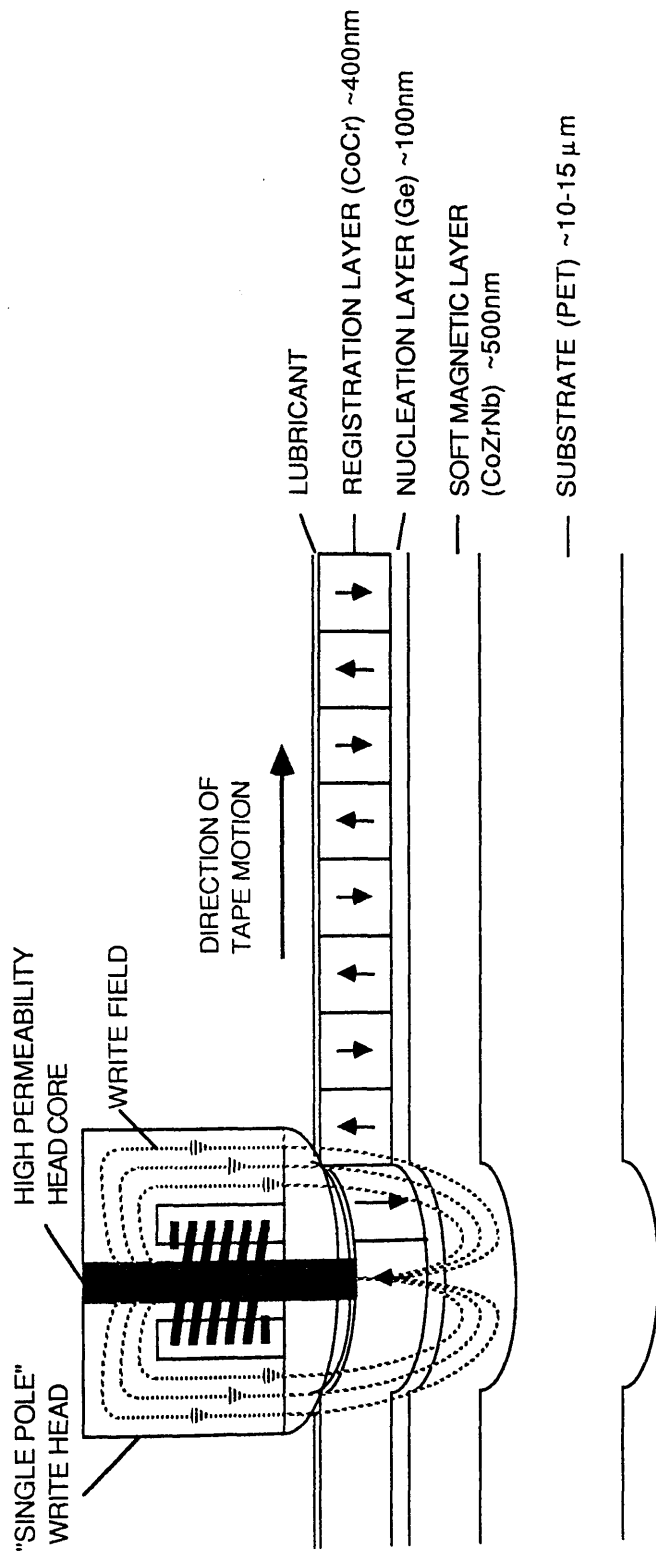


Figure 1.7 Perpendicular recording in the double-layer/single pole head configuration.

CHAPTER 2 - TECHNIQUES AND INSTRUMENTATION

2.1 INTRODUCTION

In an optical microscope a beam of visible light is used to investigate the structure of specimens to a resolution limited ultimately by the wavelength of the light (optimum resolution $\sim 0.2\mu\text{m}$). Ruska and Knoll (1931) found that, using magnetic lenses and a vacuum environment, a beam of electrons with a smaller wavelength than light could be used in a similar manner to create a microscope with a much higher resolution. The beam of fast electrons employed in a modern version of such an electron microscope can be used to extract not only high resolution quantitative microstructural data but also micromagnetic and microcompositional information from a thin film specimen (McFadyen 1986).

This chapter begins with an outline of the theories behind electron-beam/specimen interactions with particular emphasis on those of interest for magnetic imaging and x-ray microanalysis. A brief consideration of the merits and drawbacks of various magnetic imaging techniques is then followed by a discussion of the conventional transmission electron microscope (CTEM) and scanning transmission electron microscope (STEM) techniques and equipment which were employed in this work. The final section gives a breakdown of the image and spectrum collection and processing facilities available with the Link Analytical AN10000 computer system.

2.2 BASIC ELECTRON-BEAM / SPECIMEN INTERACTION

When a fast electron is incident on a thin film specimen in the electron microscope it can either pass straight through unscattered or undergo one, or a combination, of several scattering processes. These processes can be conveniently divided into two categories. The first category is elastic scattering in which interaction directly with the atomic potential results in a deflection in the path of the electron but no significant resultant change in its energy. The second category is inelastic scattering in which, for example, there is an interaction with the atomic electrons causing the loss of some of the incident electron beam energy. The energy imparted to the atom in inelastic scattering stimulates electron excitation in the atom. This may result in the generation of x-ray photons, Auger electrons, optical photons or plasmons (conduction electron oscillations). Alternatively de-excitation may produce phonons (lattice vibrations) within the specimen. It can be seen therefore that the inelastic scattering process forms the basis for many analytical techniques. It should be noted, however, that inelastic scattering is not favourable for high resolution work because it is less localised in the specimen than elastic scattering.

Any theoretical treatment of the beam/specimen interaction is likely to involve certain assumptions about the nature of the scattering process (Reimer 1982). Theory and experiment agree, however, that the intensity distribution in the transmitted beam is, to varying degrees, a function of specimen thickness, composition, density, magnetisation and crystal structure. For the purposes of this project a detailed consideration

of all of these is not essential. The following discussion is therefore restricted to the two cases of principal interest which are the interaction of the incident electron beam with a magnetic specimen and the stimulation of characteristic x-ray photons.

The interaction with a magnetic thin film specimen can be understood with reference to the Aharonov and Bohm effect (1959). This shows that the phase difference between two electrons travelling along different paths but with the same start and end points is directly proportional to the magnetic flux enclosed by the two paths. In figure 2.1 the phase difference $\Delta\phi$ between the electrons travelling along L_1 and L_2 is given by :

$$\phi_2 - \phi_1 = \Delta\phi = 2\pi\left[\frac{L_2 - L_1}{\lambda} - \frac{e\Phi}{h}\right] \quad 2.1$$

where L_1 and L_2 are the lengths of the electron paths (m), λ is the wavelength of the electron beam (3.7×10^{-12} m for 100 keV electrons), h is Plank's constant (6.63×10^{-34} J.s), e is the charge on an electron (1.619×10^{-19} C) and Φ is the magnetic flux enclosed (Wb).

It follows from this for a magnetic thin film specimen (figure 2.2) of thickness t (m) and with in plane magnetic induction that is only a function of x (assuming $L_1 \simeq L_2$) that :

$$\Delta\phi = \frac{-2\pi e}{h} t \int_{x_1}^{x_2} B_y(x) dx \quad 2.2$$

where $B_y(x)$ is the value of $B_y(x,z)$ averaged over z and is defined by :

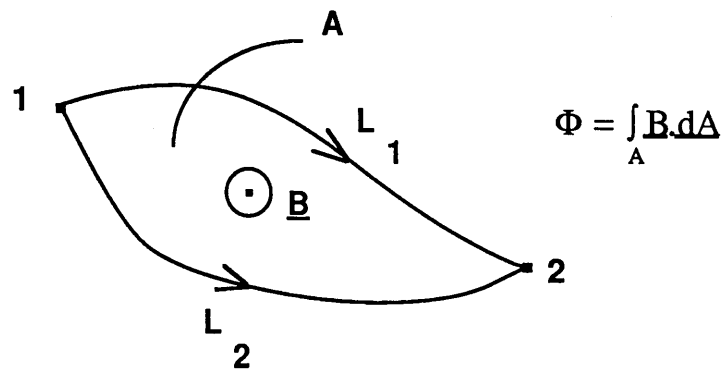


Figure 2.1 Idealised set up illustrating the Aharonov and Bohm effect.

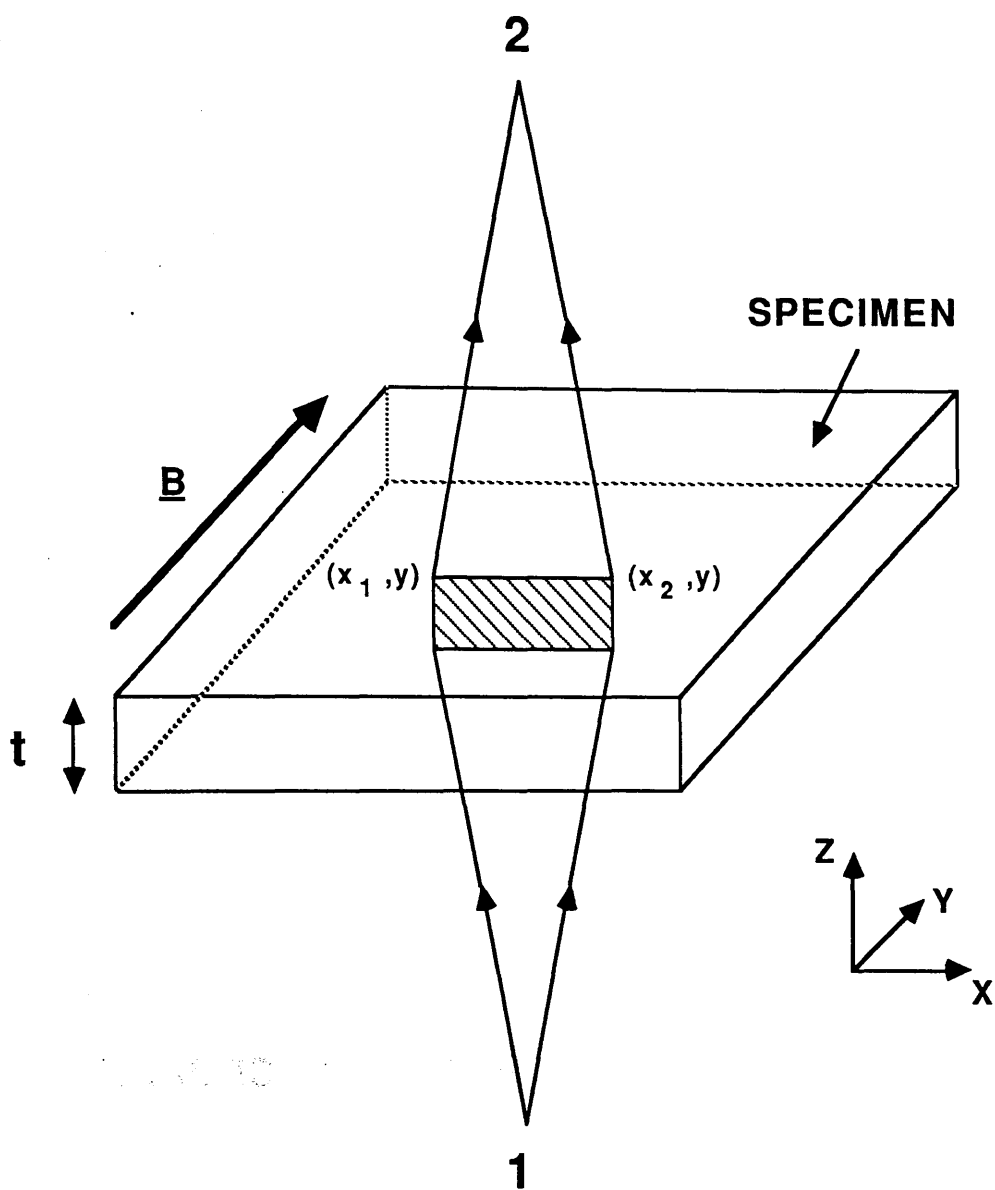


Figure 2.2

An illustration of the Aharanov and Bohm effect with a magnetic thin film.

$$B_y(x) = \frac{1}{t} \int_{-\infty}^{\infty} B_y(x, z) dz \quad 2.3$$

Equation 2.2 shows that if there is only a magnetic interaction, then the specimen may be regarded as a pure phase object.

X-ray photon generation occurs by one of two independent mechanisms. The first of these is bremsstrahlung production in which x-rays are generated by the acceleration of electrons in the field of the nuclei of the specimen. These x-rays have a continuous energy distribution up to the incident electron energy and cannot be used to yield compositional data. The second process involves the ionisation of inner shell levels in the atoms of the specimen and re-occupation of the vacant energy levels, through radiative transitions, by outer shell electrons. The emitted x-rays in this case have energies characteristic of the particular transition and therefore of the element.

2.3 MAGNETIC IMAGING TECHNIQUES

There are many magnetic imaging techniques not employed in this work. A consideration of some of the most notable of these serves as a comparison for the transmission electron microscope (TEM) magnetic imaging modes described in sections 2.4 and 2.5.

Bitter Patterns: This was the first technique for direct magnetic imaging (1931). It involves the preferential accumulation of small magnetic particles in fluid suspension at regions of high magnetic field gradient. Using this technique it is possible to obtain surface information

with which the size and shape of domains in many magnetic materials can be determined. It is limited, however, in that it has optical resolution and it does not indicate directions of magnetisation.

Kerr and Faraday effects: These depend on the rotation of the plane of polarisation of light when it is reflected (Kerr) or transmitted (Faraday) from a magnetic specimen. An illustration of the use of the Kerr effect is given by Rave et al. (1987) and of the Faraday effect by Dillon (1958). Both these techniques have the advantage that they can be used for dynamical studies and that they leave the specimen undamaged. Restrictions are that the Kerr effect only provides surface information and the Faraday effect requires transparent specimens. Both techniques have only optical resolution.

Electron holography: This involves the recovery of phase information from the object through the interference of a deflected and a reference beam brought together using a biprism (Tonomura 1987). With this technique it is possible to construct contour maps equivalent to lines of magnetic force. Among the advantages are that it is possible to obtain quantitative information on the average flux density and that it is possible to separate out a focused image of the physical microstructure, an electrostatic component of phase shift and a magnetic component of phase shift. Drawbacks with the technique include the exacting instrumental stability, specimen thickness and beam coherence requirements. In general, therefore, only domain structures near the edge of a thin magnetic specimen may be studied. Hence applicability of technique is restricted.

Magnetic force microscopy (MFM): When the surface of a magnetic sample is moved past a ferromagnetic stylus (or tip) the flexible cantilever, on which the tip is mounted, is deflected by magnetic forces. This deflection can be measured using a scanning tunneling microscope

(STM) or interferometry techniques to yield an image of the magnetic fields (Grutter et al. 1988). Although this technique is again limited to surface studies it does have the potential for resolutions of the order of 30nm.

2.4 THE CONVENTIONAL TRANSMISSION ELECTRON MICROSCOPE (CTEM)

The CTEMs employed in this study were a Philips 400T, a JEOL 100C, a JEOL 1200 EX and a JEOL 2000 FX (CTEM/STEM). This section deals with the principles and techniques common to all the microscopes rather than each individually. A more detailed explanation of the advantages available with the JEOL 2000 FX, however, is given in section 2.7.

The standard imaging mode in a TEM can be thought of as the electron-optical analogue of imaging in an optical microscope. Hence much of the theory of image formation used for light optics can be employed when considering the electron microscope. For the most part electron-optics can be treated geometrically using a classical model, in which imaging is considered in terms of a beam, or ray, of particles. To understand phase contrast, however, a second, wave-optical, approach must be invoked. This model treats imaging in terms of the phase and amplitude of an electron-wave propagating through the microscope. In the following discussions, the wave-optical approach has been adopted where it aids understanding, or where the explanation requires reference to the phase of a scattered wave.

2.4.1 Illumination System

In a typical CTEM (figure 2.3) we have an electron gun comprising, for instance, a heated tungsten or lanthanum hexaboride source emitting electrons at one end of a vacuum column. This source or "tip" is held at a fixed negative potential (of say 100 kV) with respect to an anode from which a fine diverging beam of fast electrons propagates down the microscope column. This illumination is projected onto the specimen by means of two condenser lenses which permit variation of the area of specimen irradiated. Ideally this gives an electron beam with uniform current density, which may be considered as a plane electron-wave, incident on the specimen.

2.4.2 Bright Field Imaging

The objective lens focuses the transmitted intensity distribution to produce a diffraction pattern of the illuminated area of specimen in the back focal plane (BFP). In wave-optical terms this diffraction pattern is the fourier transform of the wave transmitted by the specimen. To form a bright field (BF) image the intensity distribution is projected onto an electron-fluorescent viewing screen or photographic plate inside the vacuum chamber.

Contrast in BF images can result from two mechanisms; amplitude contrast and phase contrast. BF amplitude contrast arises from the removal of part of the scattered intensity distribution by the objective aperture. Improvements in image contrast obtained through use of smaller apertures, however, are at the expense of resolution since the scattered electrons carry the detailed information about the specimen.

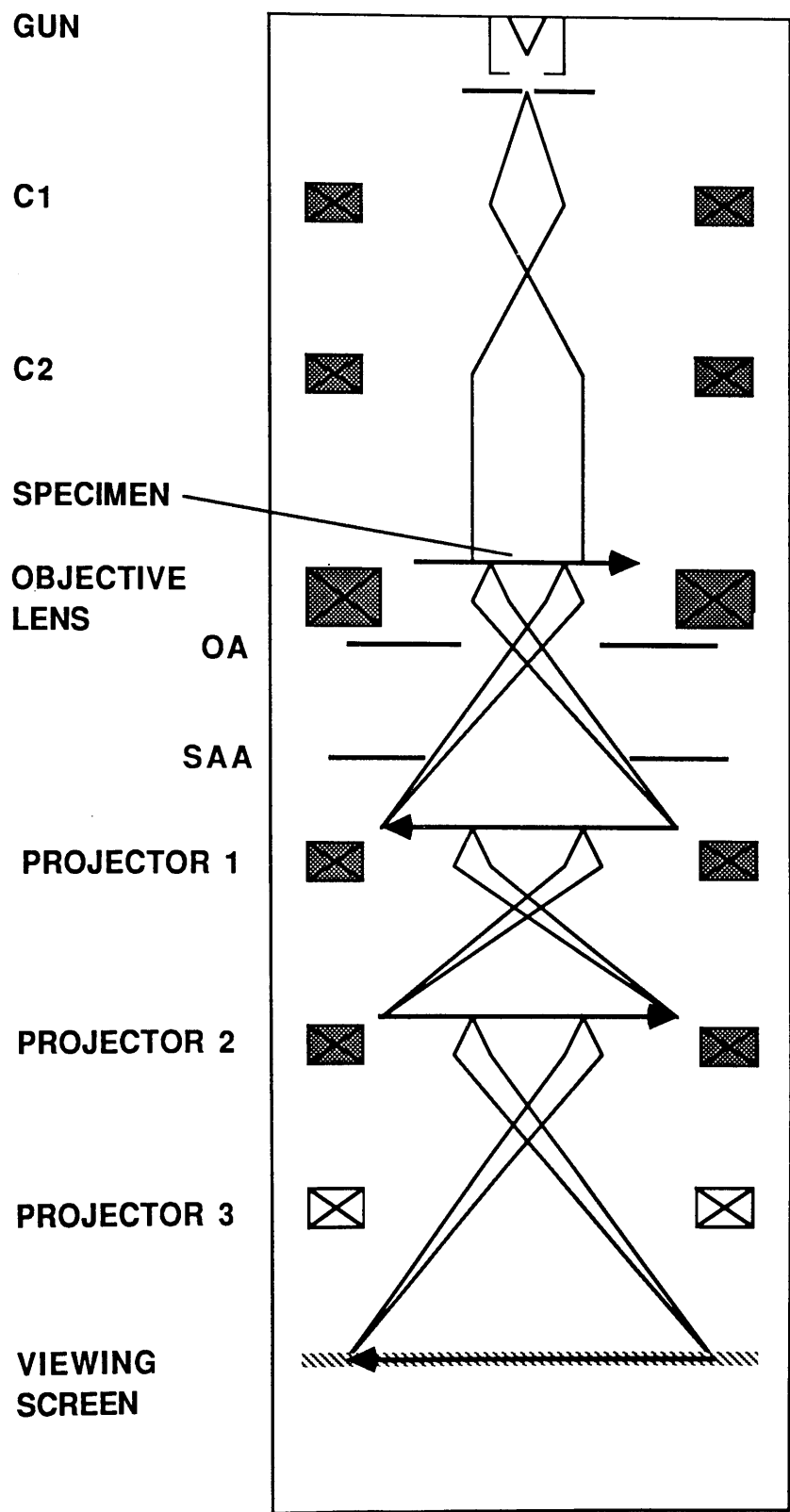


Figure 2.3

A simplified schematic of a typical CTEM.

The smallest objective aperture consistent with the required resolution should therefore be used. BF phase contrast is produced by interference between the incident and scattered wave at the image point. Lens aberrations, which are much more important in a TEM than in an optical microscope, modify this phase and produce an aberrated wave. The effect of lens aberrations combined with the energy spread of the electron gun (typically 1-2eV) is to limit the transfer of high spatial frequency phase information.

2.4.3 Dark Field Imaging & Selected Area Diffraction Patterns

The uniform bright background in a BF image is produced by the direct beam. Since this background contains no information and reduces the image contrast, a useful technique is to image the specimen with the undiffracted beam removed. This is called dark field (DF) imaging and can be accomplished in a CTEM through either displacement of the objective aperture or tilting of the illuminating beam.

In the investigation of crystalline specimens the periodicity of atom positions can produce Bragg reflections in the transmitted beam. Since all electrons scattered through the same angle at the specimen intersect the BFP at the same radial position these generate a set of regularly spaced spots in the diffraction pattern. By adjusting the projector and objective lens excitations, it is possible to make the viewing screen conjugate, not to the specimen plane, but to the focal plane of the objective lens. This allows observation of the diffraction pattern. With knowledge of the lens settings such patterns can be used to determine the crystal structure and lattice parameters.

2.4.4 Resolution

In a CTEM the resolution of the objective lens usually determines the resolution of the microscope. This is because the other lenses merely serve to project and magnify the image which the objective lens produces. Chromatic aberration is small provided there is an essentially monochromatic source, lens voltages and currents are very stable and specimens are thin enough to prevent a high proportion of electrons being inelastically scattered. Assuming astigmatism is correctable, spherical aberration of the objective lens is the most important limiting factor for resolution.

2.4.5 Lorentz Microscopy in a CTEM

This deals with the interaction of the beam with the specimen via the Lorentz force. Lorentz microscopy requires an illumination aperture smaller than the magnetic deflection angle β so that the coherence of the beam is high enough for the deflection to be detectable. Additionally the specimen must be situated in magnetic field free space. The former criterion can be realised by strongly exciting the first condenser lens. In most CTEMs, because the specimen is usually situated in the field of the objective lens (sufficient to eliminate any magnetic structure of interest), the latter criterion can only be met by switching the lens off. The magnification and resolution for Lorentz microscopy are therefore often restricted (magnification restricted typically to $<1000\times$).

In low angle electron diffraction a diffraction pattern is imaged with an α_i of the order of 10^{-2}mrad and a long camera length (effective distance from the specimen to the image plane) of the order of tens of

metres. In the case of a ferromagnetic thin film with uniaxial anisotropy ideally we have domains with antiparallel directions of magnetisation separated by 180° domain walls. The primary beam in the diffraction pattern is therefore split into 2 spots with angular separation 2β . This is equal to the spot separation divided by the camera length. The magnitude of the Lorentz deflection angle, β (rad), for a thin film of thickness, t , and uniform magnetic induction, B_0 (T), is given by:

$$\beta = eB_0\lambda t/h \quad 2.4$$

This technique can be used to detect small magnetic deflections in the transmitted beam.

It is possible to perform magnetic imaging in a CTEM, using the Fresnel and Foucault modes of Lorentz microscopy (Chapman 1984). In Fresnel microscopy the image is defocused in order to observe the Fresnel diffraction pattern. From the geometrical model shown in figure 2.4 it can be seen that changes in the direction of magnetisation produce regions of high and low intensity in the image plane.

The principal advantages of the Fresnel mode are the operational simplicity, the generally high contrast levels, the lack of directional dependence of contrast and the possibility of quantitative deductions (although this is difficult). There are, however, serious drawbacks to offset these advantages. The technique is only sensitive to changes in magnetisation direction, and so the scattered intensity is not proportional to the magnetisation in the specimen. Deduction of the direction of magnetisation in the domains and the angle through which the magnetisation rotates across domain walls is not possible. In addition to

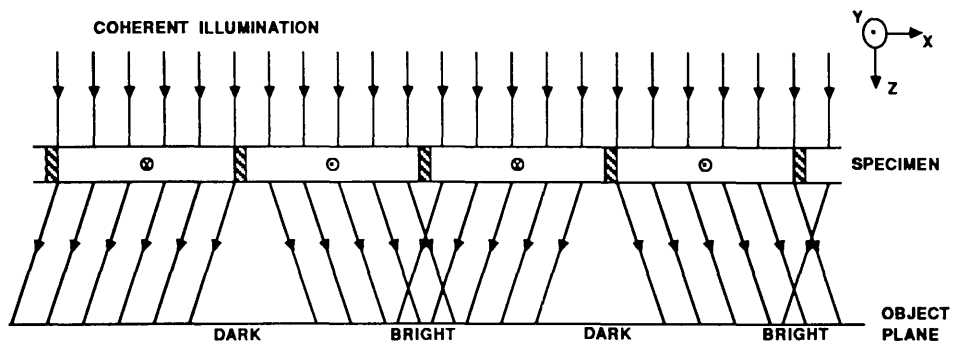


Figure 2.4 Ray diagram illustrating the generation of Fresnel contrast from a magnetic specimen.

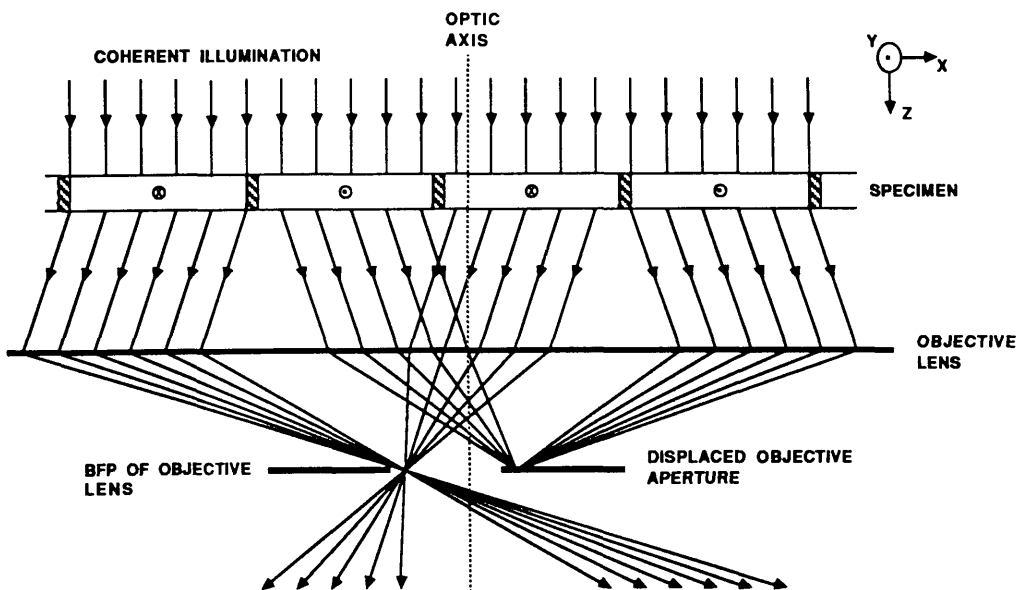


Figure 2.5 Ray diagram illustrating Foucault contrast generation through displacement of the objective aperture.

this, the image is out of focus so that non-magnetic features appear blurred.

Contrast generation in Foucault microscopy can be understood geometrically from the ray diagram in figure 2.5. In this figure the contribution to the final in-focus image of domains magnetised in one direction is removed by displacing the objective aperture until it cuts off that part of the beam. These domains are then dark in the final image. Domain walls in this case appear in the image as boundaries between dark and bright areas.

Unfortunately, however, there are also some serious drawbacks associated with this mode. First of all the objective aperture should ideally be in the same plane as the diffraction pattern since any displacement reduces the area of specimen in which Foucault contrast can be observed. This is difficult to achieve in most CTEMs because, as mentioned above, the objective lens is switched off. Other problems with Foucault imaging are that there is a highly non-linear relationship between specimen magnetisation and image intensity, and that the image intensity distribution is very sensitive to the exact position of the aperture. Thus if a quantitative description of the magnetic microstructure is required other TEM techniques are more suitable (see section 2.5.4).

Foucault imaging is good, however, in that it yields some information on the direction of magnetisation and that it is an in-focus method. Thus it compliments the Fresnel mode and a study combining both modes provides a simple qualitative method for investigating magnetic thin films.

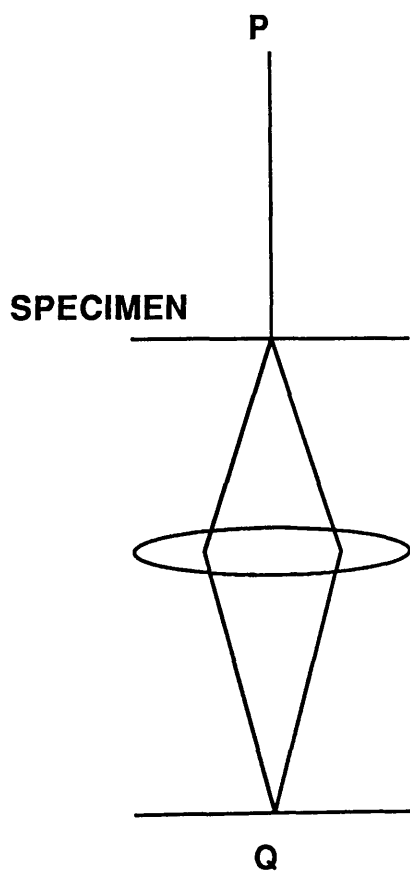
2.5 THE SCANNING TRANSMISSION ELECTRON MICROSCOPE (STEM)

The theorem of reciprocity was first discussed by Helmholtz (1860) with regard to light optics. In wave-optics it implies that the excitation of a wave at a point Q by a wave from source P is the same as that detected at Q' with the source at P' (figure 2.6). In a STEM a small electron probe is formed in the specimen plane and scanned across an area of specimen in a sequential raster fashion. It can be seen from figure 2.6 that the ray diagram for a STEM is therefore the reciprocal of that for a CTEM.

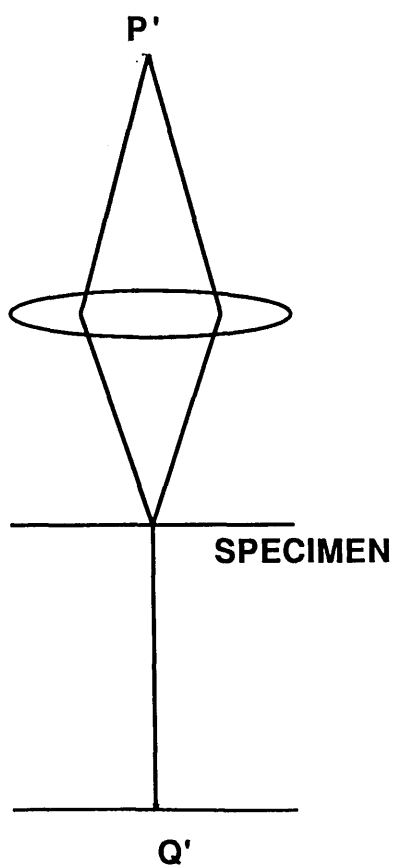
Cowley (1969) has shown using a reciprocity theorem that images equivalent to CTEM images can be obtained in a correctly configured STEM. Other approaches (Humphreys 1981) and studies employing the STEM have confirmed this work (Chapman et al.1979). This section gives a general description of the STEM followed by discussions of magnetic imaging and x-ray microanalysis in a STEM.

2.5.1 Illumination System

Figure 2.7 shows a schematic of a typical STEM. The probe in a field emission gun (FEG) STEM is an image of a high brightness electron source in the specimen plane. In such a microscope energy spread in the emitted electrons is typically between 0.2 and 0.5eV. The diameter of the virtual source is generally of the order of 2 to 7nm. One or more condenser lenses with short focal length can demagnify this source down to between 0.2 and 0.5nm. The probe is then scanned across the specimen by means of coils arranged in front of the objective lens,



a) CTEM



b) STEM

Figure 2.6 Reciprocity between normal CTEM and STEM imaging modes.

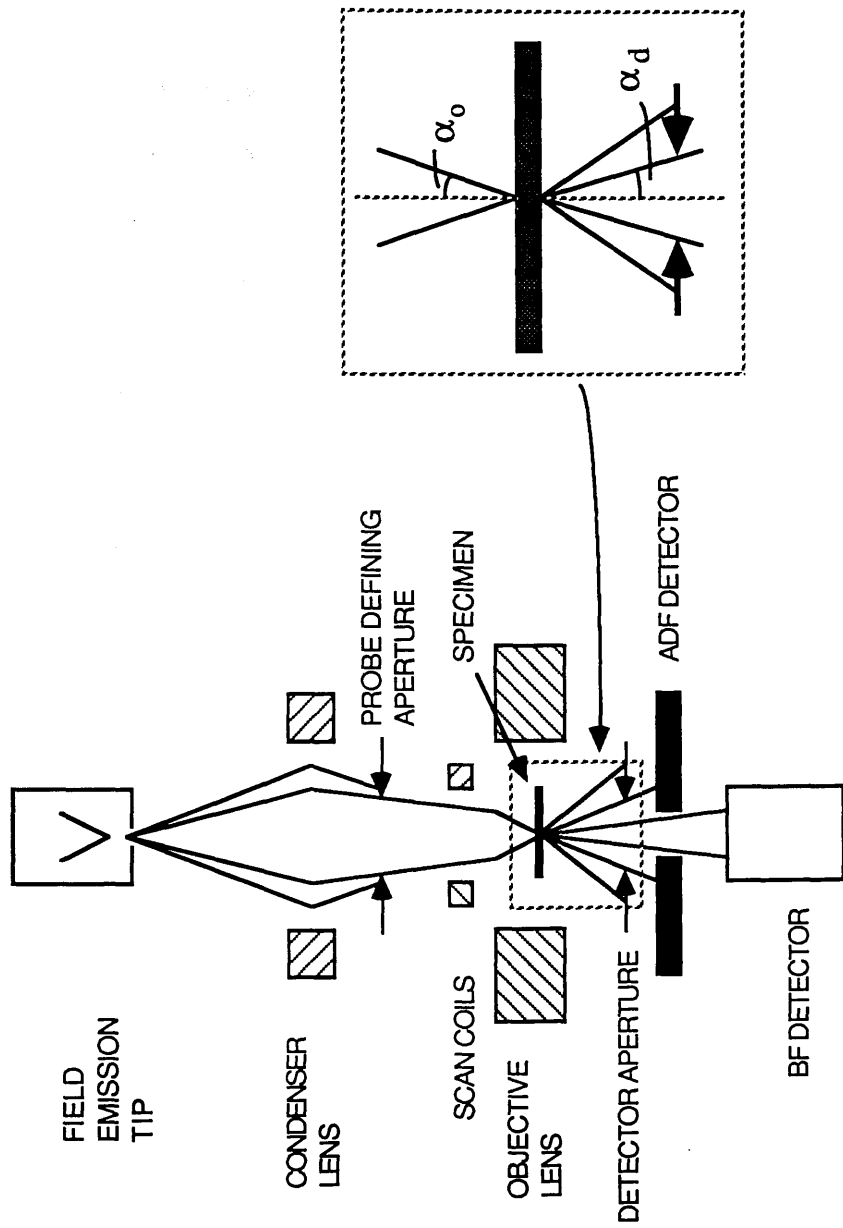


Figure 2.7 A simplified schematic of a typical STEM.

the prefield of which can be used as an additional condenser. Probe current at the specimen is typically of the order of 1nA.

2.5.2 Detection

In a STEM the electrons transmitted by the specimen are collected with an electron detector rather than being imaged on a viewing screen or a photographic plate. Different imaging modes can be selected by varying the size and geometry of the detector and the image contrast is controlled by the size and position of a detector aperture.

For thin specimens the STEM is essentially free from chromatic aberration arising from energy losses in the specimen. Additionally each pixel of the image is acquired sequentially (unlike in the CTEM where the whole image is acquired simultaneously) and several images can be collected in parallel in either analogue or digital form. The possibilities are therefore good for contrast enhancement, noise filtering and signal combination. If an electron spectrometer is installed the STEM can also be used for either electron energy loss spectroscopy (EELS) of a selected area or for energy selecting microscopy.

2.5.3 Resolution

Resolution of the image depends on the size of the electron source, the objective lens aberration, the defocus of the objective lens and the wavelength of the electron beam. A proper treatment of this requires reference to the amplitude and phase contrast transfer functions (ACTF and PCTF) for the particular imaging mode.

It is incorrect to characterise resolution by a single number. For a

given imaging condition, though, it is possible to estimate the diameters of the coherent and incoherent probe contributions. For most TEMs the optimum condition for high resolution bright field imaging occurs at the Scherzer defocus (defocus of the objective lens is introduced to partly compensate for unwanted phase shifts in the scattered wave). This is given by:

$$\Delta z = (C_s \lambda)^{1/2} \quad 2.5$$

where Δz is the defocus and C_s is the third order spherical aberration coefficient for the lens (typically 0.5 to 4mm). At this defocus a broad band of spatial frequencies is imaged with positive phase contrast.

The coherent probe diameter, d_c , is determined by spherical aberration in the probe forming lenses and diffraction at the probe forming aperture. An estimate of this can be made if the spherical aberration, the illumination aperture and the defocus of the objective lens are known:

$$d_c^2 = \left(\frac{1}{2} C_s \alpha_o^3 \right)^2 + \left(\frac{1.22 \lambda}{\alpha_o} \right)^2 \quad 2.6$$

From this the optimum α_o can be calculated by differentiating with respect to α_o and setting the derivative equal to zero. This leads to an expression for α_o :

$$\alpha_o = (1.4 \lambda / C_s)^{1/4} \quad 2.7$$

Substituting this condition back into equation 2.6 gives:

$$d_c = 1.3(C_s \lambda^3)^{1/4}$$

2.8

The incoherent probe diameter, d_i , is determined geometrically from the demagnification of the probe forming lenses. The total probe diameter, d_t , and thus a measure of the resolution, is calculated by adding d_c and d_i either linearly or in quadrature. For the VG HB5 STEM d_t can be less than 1nm.

2.5.4 STEM Magnetic Imaging

By the reciprocity theorem Fresnel and Foucault imaging can be conducted in the STEM. In a STEM it is also possible, however, to perform the differential phase contrast (DPC) mode of Lorentz microscopy, first suggested by Dekkers and De Lang in 1974. In the DPC imaging mode the gradient of the phase shift in the transmitted beam is detected by means of a large axial brightfield electron detector split into either two semi-circles or four quadrants.

This can be illustrated classically from the simplified schematic in figure 2.8. With no deflection in the path of the beam the intensity incident on each of the individual quadrants in the detector is equal. When a magnetic specimen is introduced, whilst the sum of the signals from all four quadrants will still form a bright field image, the Lorentz deflection, β_L , in the beam causes an imbalance in the signal detected by opposite quadrants. It can be seen from figure 2.8 that the signal from the left hand side of the detector (quadrants A+D) is proportional to $\pi\alpha_o^2/2 - 2\beta_L\alpha_o$ whilst that from the right (quadrants B+C) is proportional to $\pi\alpha_o^2/2 + 2\beta_L\alpha_o$. The "difference signal" ($[B+C]-[A+D]$) is therefore proportional to $4\beta_L\alpha_o$. From equation 2.4 it can be seen, for

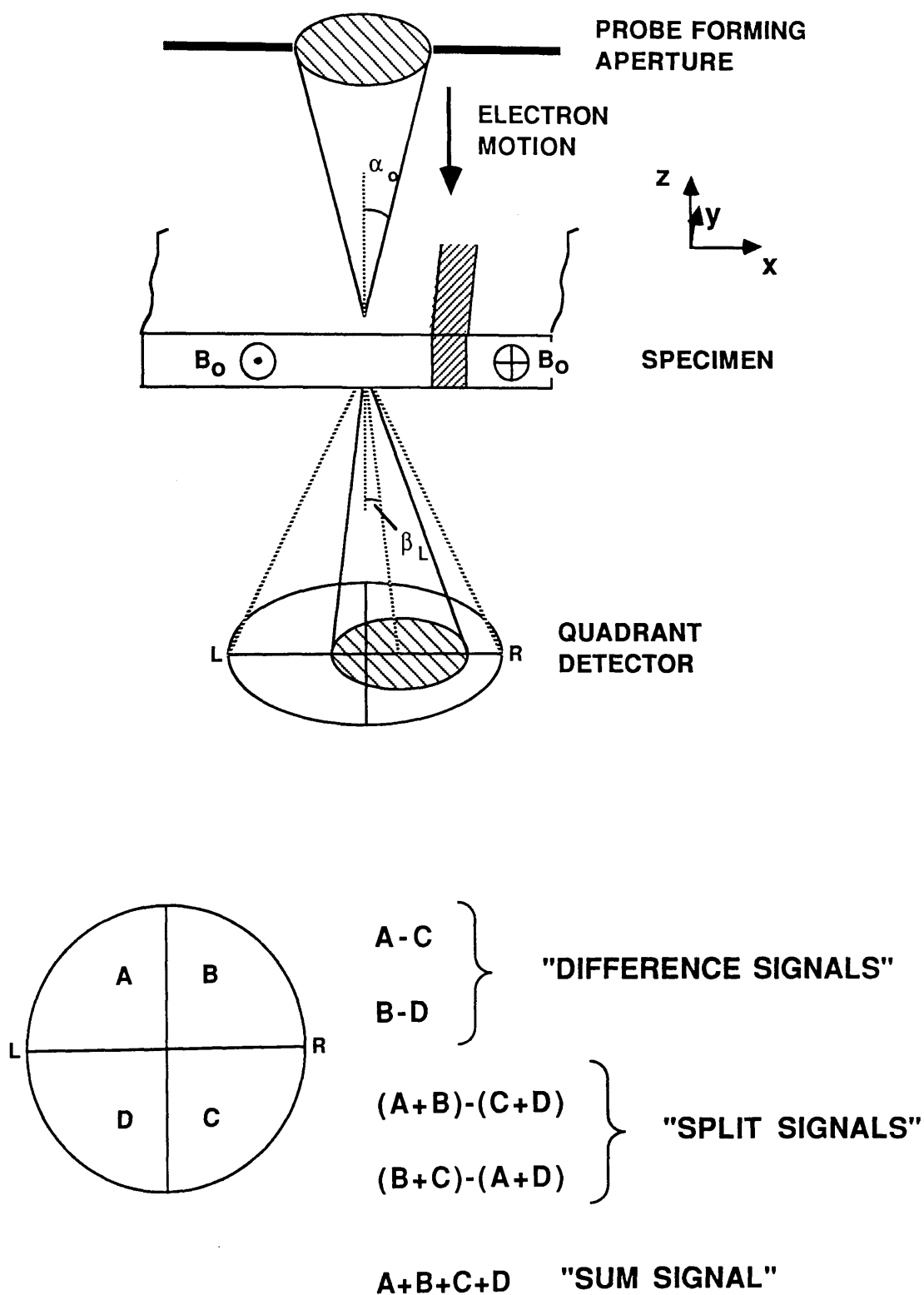


Figure 2.8 Schematic of DPC imaging in a STEM.

a specimen with y-component of magnetisation $B_y(x,z)$, that β_L is given by:

$$\beta_L = \frac{e\lambda}{h} \int_{-\infty}^{\infty} B_y(x, z) \cdot dz = \frac{e\lambda}{h} B_y(x)t \quad 2.9$$

Hence the difference signal is proportional to the average in-plane component of magnetic induction multiplied by the specimen thickness.

A more thorough wave-optical approach to DPC imaging has been adopted by Cowley (1976). The following discussion outlines the main details and is illustrated in figure 2.9. For a point (ie fully coherent) source, the wavefunction incident on the STEM specimen $\Psi_o(\underline{r})$ can be represented by the fourier transform of the wavefunction at the probe forming aperture:

$$\Psi_o(\underline{r}) = \text{FT}[A(\underline{u})\exp\{i\chi(\underline{u})\}] \quad 2.10$$

where \underline{r} is the position vector in the specimen plane, \underline{u} is the position vector in reciprocal space, $A(\underline{u})$ is the aperture function, which has value 1 inside the aperture and 0 outside it, and $\chi(\underline{u})$ is the phase factor, which includes the effects of defocus and spherical aberration for the probe forming lens.

Assuming that there is only elastic scattering, the effect of a thin magnetic specimen on $\Psi_o(\underline{r})$ can be represented by a transmission function $q(\underline{r}-\underline{R})$, which from equation 2.2 can be written:

$$q(\underline{r}-\underline{R})=\exp\{-i\Delta\phi(\underline{r}-\underline{R})\} \quad 2.11$$

where \underline{R} is the position vector for the point about which the electron

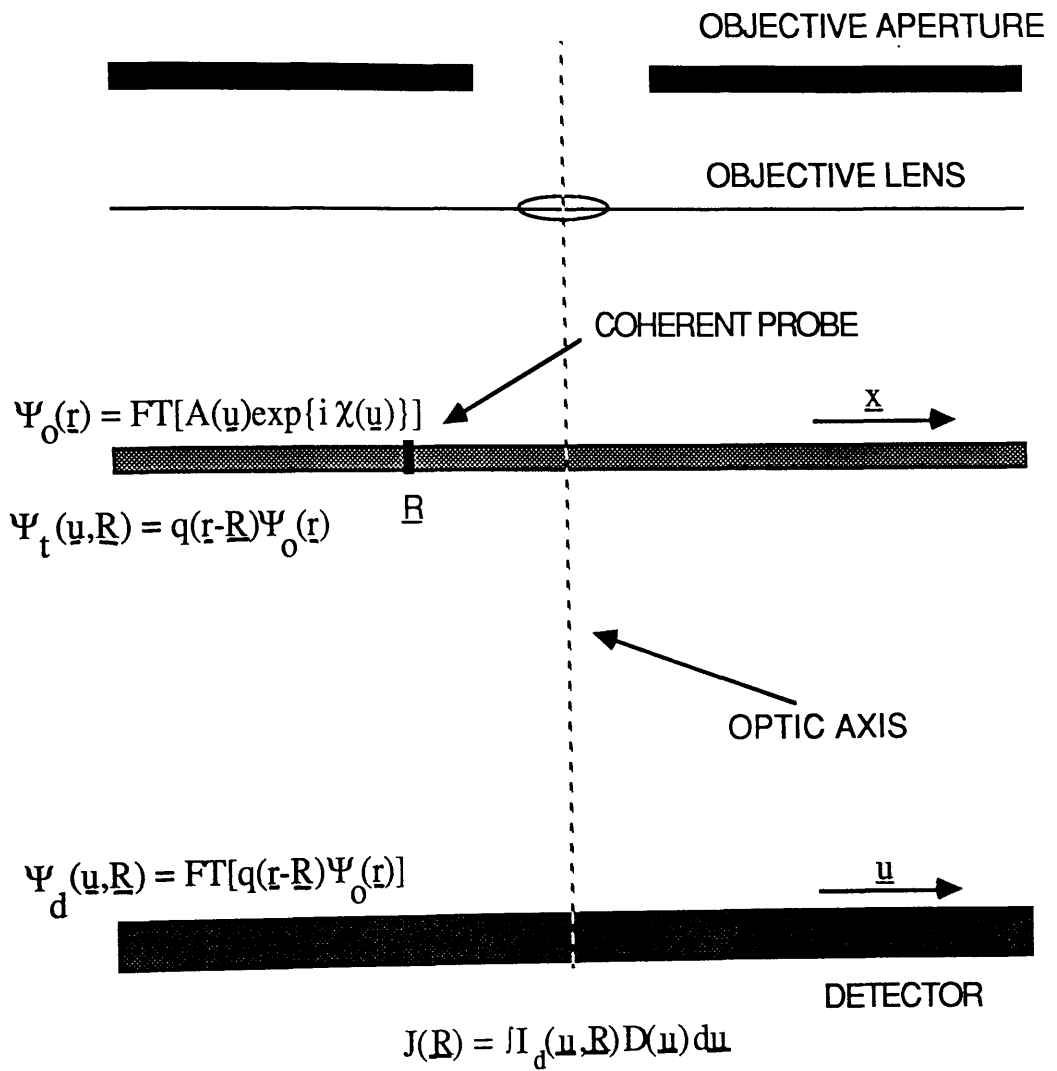


Figure 2.9 The propagation of an electron wavefunction through a STEM in DPC imaging mode.

probe is centred. The wave amplitude on the detector plane is the fourier transform of the wavefunction at the specimen exit plane:

$$\Psi_d(\underline{u}, \underline{R}) = \text{FT}[q(\underline{r}-\underline{R})\Psi_o(\underline{r})] \quad 2.12$$

The intensity of the detected beam $I_d(\underline{u})$ is then easily calculable from:

$$I_d(\underline{u}, \underline{R}) = |\Psi_d(\underline{u}, \underline{R})|^2 \quad 2.13$$

giving a signal at the detector $J(\underline{R})$:

$$J(\underline{R}) = \int I_d(\underline{u}, \underline{R}) D(\underline{u}) d\underline{u} \quad 2.14$$

where $D(\underline{u})$ is the detector response function.

For a split detector, $D(\underline{u})$ has value 1 for all $\underline{u} > 0$ and -1 for all $\underline{u} < 0$, (ie it is antisymmetric about the instrument axis for which $\underline{u} = 0$). This is an example of an antisymmetric detector response function.

Any antisymmetric response function $D_o(\underline{u})$ can be represented as the product of a symmetric (even) and an antisymmetric (odd) function. For the case of a split detector the odd response function, $D(\underline{u})$, illustrated above is related to the conventional even detector response function, $D_e(\underline{u})$, by:

$$D(\underline{u}) = D_e(\underline{u}).G(\underline{u}) \quad 2.15$$

where $G(\underline{u}) = 1$ if u is > 0 and -1 if u is < 0 (u is the co-ordinate of \underline{u} parallel to the real-space x -axis). Taking the fourier transform of this expression gives:

$$\text{id}(\underline{R}) = d_e(\underline{R}) * (\pi i x)^{-1} \quad 2.16$$

Since convolution with the function $1/x$ gives much the same effect as differentiation with respect to x , the phase function appears in the image in differentiated form. In other words the detector responds linearly to phase gradients. This can be expressed:

$$J(\underline{R}) \propto \nabla \phi(\underline{R}) \quad 2.17$$

From equation 2.2 it follows for a ferromagnetic specimen that:

$\frac{\partial \phi}{\partial x} = -\frac{etB_y}{h}$ and $\frac{\partial \phi}{\partial y} = -\frac{etB_x}{h}$. A DPC signal which yields a map of one component of the phase gradient can be used directly to give the average component of the in-plane magnetic induction orthogonal to the direction of differentiation.

Thus both a wave-optical and a classical approach show that by taking suitable combinations of quadrant signals it is possible to recover, simultaneously, an incoherent BF image and images sensitive to orthogonal components of in-plane magnetic induction.

2.5.5 Energy Dispersive X-Ray (EDX) Microanalysis & High Angle Annular Dark Field (ADF) Imaging

High resolution energy dispersive x-ray (EDX) microanalysis is a technique which can be employed in a STEM to determine the local elemental composition of a thin specimen (Hall and Gupta 1979, Lorimer 1983). The method relies on the production of characteristic x-rays from a volume of specimen excited by a focused electron probe held stationary

with respect to the specimen. These x-ray photons enter a semiconductor detector in the microscope and produce photoelectrons which ionise the detector atoms. The ions in turn de-excite and generate electron-hole pairs. The number of pairs produced is directly proportional to the energy of the original photo-electron. A bias voltage applied across the detector separates the electrons and holes and a current proportional to the incident photon energy is generated. The current pulse is measured and the channel of a multi-channel analyser corresponding to this photon energy is incremented accordingly. This produces an x-ray spectrum from which it is possible to quantify the local concentrations of the elements in the specimen (see chapter 4 for a more detailed explanation of considerations for x-ray microanalysis of CoCr thin films).

When conducting EDX microanalysis in a STEM it is important to select a suitable imaging mode with which to locate the electron probe during spectrum collection. Signals collected from electrons scattered through high angles have intensities which are predominantly attributable to elastic scattering. These signals show a strong dependence on atomic number, Z (McGibbon 1989) and a low susceptibility to crystallographic contrast. It is possible to form an image at such scattering angles using an annular dark field (ADF) detector in a STEM (see section 2.6.4). This kind of image can be very useful when conducting x-ray microanalysis on CoCr thin films (see chapter 4).

2.6 THE VACUUM GENERATORS HB5 STEM

The VG HB5 at Glasgow has been extended and modified to allow many different analysis techniques. This section gives an outline of the essential mechanical and theoretical considerations biased towards the

techniques used in this project.

2.6.1 The Field Emission Gun

In the extended VG HB5 (figure 2.10) we have a very high brightness field emission electron gun (Crewe 1971) with a single crystal tungsten cathode tip approximately 100 nanometres in diameter. This tip requires an operating vacuum of $<10^{-10}$ torr to prevent production of ions near the cathode which could damage the tip. A pressure difference between the column, where the pressure is 10^{-9} torr, and the gun chamber is maintained by means of the differential pumping aperture.

The full electron velocity is generated in two stages, firstly through a 3 kV extraction voltage and then through a second accelerating anode to take the beam up to 100kV. This assembly forms an essentially monochromatic virtual source approximately 6.5 nanometres in diameter (Morrison 1981).

A high brightness source is required to give the high probe current and small probe size necessary to maximise the resolution whilst minimising acquisition time. During normal operation of the microscope a small current ("flash") must be passed periodically through the tip to remove contaminants which build up on the cathode surface and reduce the emitted intensity of electrons.

2.6.2 Pre-specimen Optics

The VG HB5 has three independent lenses before the specimen; two condenser lenses, C1 and C2, and the pre-specimen field of the objective lens. These allow a number of different operating conditions.

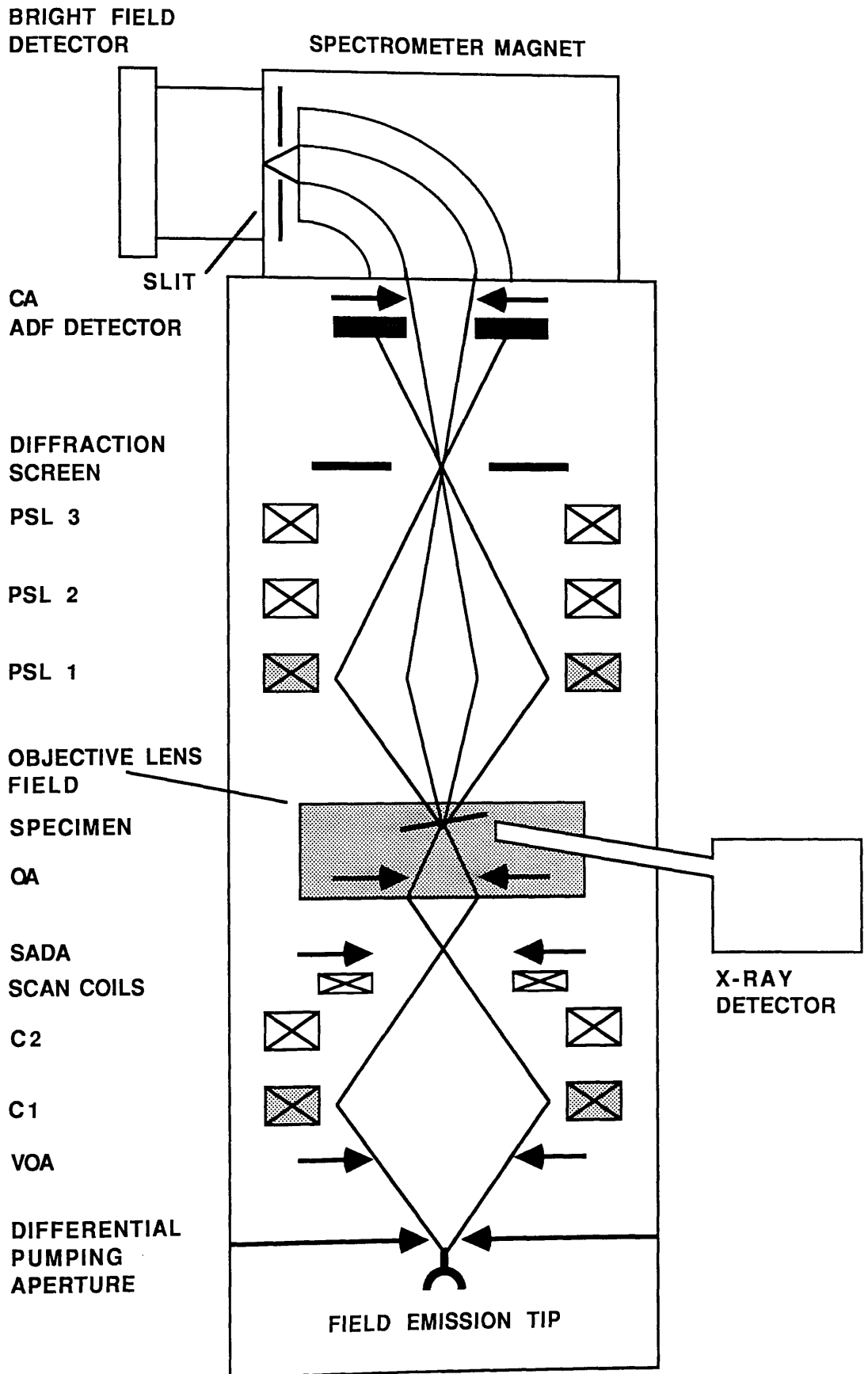


Figure 2.10 Schematic of the modified VG HB5 STEM.

In normal operation the specimen in the STEM is located in an objective lens field of the order of 0.8T. Magnetic imaging is not possible in this configuration since this field is sufficient to destroy the domain structure in a magnetic specimen. There are two ways to overcome this in the VG HB5, the first of which is operation with the objective lens switched off. When imaging with this limitation a single condenser lens operating mode is the most straightforward to align and use. In this mode however there is very little control over the probe size and resolution is severely limited (see below). To obtain sufficiently small incoherent probe sizes for higher resolution studies a second mode is therefore necessary in which both the condenser and the objective lenses are excited. This is possible using a special specimen cartridge to permit positioning of the specimen anywhere from 20 to 40mm above the normal seating position. The specimen is thus situated out of the field of the weakly excited objective lens.

Morrison (1981) investigated the PCTF and ACTF for DPC imaging with both a split and a quadrant detector. The Scherzer defocus condition was found to give the most favourable operating conditions. In this project initial DPC studies (see chapter 5) were conducted with C2 as the probe forming lens. C2 was chosen rather than C1 because it has a smaller magnification (0.94 as opposed to 1.99) and therefore gives a smaller probe (although with C2 the probe current is lower). A 100 μ m selected area aperture (SAA) was used as the probe defining aperture. The d_c , d_i , α_o and I_p for these operating conditions were calculated by Morrison (1981) and are given in table 2.1. Subsequent DPC studies were performed with C1 on and the objective lens weakly excited (see above). The d_c , d_i , α_o and I_p for operation in this mode with a 100 μ m real objective aperture (OA) defining the probe were discussed by

LENSES	MODE	PROBE DEFINING APERTURE	α_o	d_i	d_c	I_p
C1+OBJ	EDX	100 μm VOA	11 mrad	0.3nm	2.4nm	0.2nA
C2	DPC	100 μm SAA	0.5mrad	6.2nm	10nm	0.2nA
C1+OBJ ^(WEAKLY EXCITED)	DPC	100 μm OA	2.0mrad	4.5nm	3.0nm	1.0nA

Table 2.1 Operating modes for the VG HB5 STEM employed in this project.

Chapman et al. (1978). These are also given in table 2.1.

The EDX microanalysis described in chapter 4 was conducted with both C1 and the objective lens highly excited. This mode permits the small probe size and high probe current necessary to stimulate sufficient characteristic x-rays from a small area of specimen in only a short period of time. To reduce the possibility of backscattered electrons contributing to the spectra, the 100 μ m virtual objective aperture (VOA) was selected in preference to a real OA as the probe defining aperture. The d_c , d_i , α_o and I_p for this mode were discussed by Crozier (1985) and McFadyen (1986) and are given in table 2.1 (see chapter 4 for further instrumental considerations).

2.6.3 Post-specimen Lenses

There are three post-specimen lenses which allow the selection of a wide range of camera lengths. The function of these lenses is to match the angular distribution of the scattered electrons to the geometry of the various detectors. Correct adjustment of this can be achieved through insertion of a diffraction screen in front of the detector plane. This enables observation of the enlarged far-field diffraction pattern produced in the detector plane. For normal imaging only PSL 3 is used, for DPC imaging PSL's 2 and 3 are used and for high angle ADF imaging (to compress the angular distribution of the signal) PSL 1 only is used.

2.6.4 The Detectors

The bright field detector is a small on-axis photoelectric detector which comprises a scintillator coupled using a light pipe to a photomultiplier tube. It detects only that part of the electron beam which

has been unscattered or scattered through a small angle and therefore passes through the centre of the ADF detector. In normal imaging mode it gives an image equivalent to a CTEM bright field image.

The ADF detector is an annular scintillator also coupled to a photomultiplier tube. With inner and outer diameters of 3.3 and 25mm, respectively, it normally detects only electrons which have been scattered through large angles at the specimen. In the modified HB5 the range of acceptance angles for the scattered intensity distribution is determined by the post-specimen lens settings (typical high inner and outer acceptance angles are 85 and 200mrad respectively).

The quadrant detector is a windowless Centronic semiconductor photodiode detector. It is 11mm in diameter and has four symmetrical sections separated by 200 μ m thick strips of SiO₂ (see figure 2.8). It is operated without a bias and is impedance matched to the pre-amplifiers. These amplifiers convert the signals to voltages which are then fed into a mixer unit. A signal is then selected and sent to a CRT for display.

The x-ray detector used in this project is a Link Analytical lithium drifted silicon (Si(Li)) detector. The detector subtends a solid angle of 0.04sr at the specimen and its axis is oriented at an angle of 10.5° to the horizontal in the specimen plane. The crystal itself is held between two gold electrodes with a potential difference of 500V. Between the crystal and the microscope column there is a protective beryllium window ~8 μ m thick which reduces the detector efficiency to less than unity for incident x-ray energies below 3keV.

2.7 THE JEOL 2000FX

The main disadvantage with a TEM that usually operates with accelerating voltages $\leq 100\text{kV}$ is that specimen thickness is generally restricted to $\leq 200\text{nm}$ (Morrison 1981). The JEOL 2000 FX TEM has a maximum accelerating voltage of 200kV which gives it more flexibility as regards specimen thickness.

In CTEM mode the 2000 FX is well suited to investigations of magnetic specimens. As mentioned in section 2.4.5, one of the main drawbacks normally associated with magnetic imaging is the requirement that the objective lens be switched off. This severely limits the magnification (in the 120kV JEOL 1200EX it was possible to image the specimen up to a magnification of $5300\times$ in field free space). To overcome this problem the objective pole piece of the JEOL 2000FX has been designed to allow excitation of the objective lens with the specimen in field free space. Observations of magnetic specimens can then be conducted at higher magnifications without affecting the magnetic microstructure. As well as this advantage, having the objective excited means that the diffraction pattern can be in the objective aperture plane. This allows more accurate positioning of the aperture when performing the Foucault mode of Lorentz microscopy (see section 2.4.5).

In the STEM mode the main differences from a FEG STEM are that there is no field emission tip, the microscope does not operate under VHV conditions and (for DPC imaging) there are no descans coils. Descan is performed by varying the ratio of the currents in the scan coils and the PSL configuration so that the rocking point of the beam is conjugate to the detector plane. The principal disadvantages of the 2000FX, compared with the HB5, are attributable to the increased source

size. These are lower probe current ($<0.1\text{nA}$) and poorer resolution ($\sim 50\text{nm}$). Advantages over the HB5 are that thicker specimens can be examined and specimens can be inserted and removed more easily.

2.8 THE AN 10000 SYSTEM

The Link Analytical AN 10000 system is a dedicated computer capable of digital acquisition, processing and storage of images and spectra. Individual images can be acquired at the operators choice of resolution (up to 512×512 pixels), precision (up to 16 bits/pixel), dwell-time/pixel and number of integrations. Images are recorded directly onto an internal hard disk and can be backed up onto quarter inch tapes or three and a half inch floppy disks. Back-up loading and down-loading times can be reduced by grouping of related images into a "study" memory unit. The software package also has a range of display and image processing capabilities.

The spectrum acquisition system and the related software package also provide a wide range of operator variable parameters including energy calibration, spectrum energy range and resolution (20.48 keV and 20eV per channel respectively in these investigations), window designation and labelling and also peak identification and labelling. Other useful features include the count rate display, several background correction programs and, as for the images, a time saving memory grouping or "rootfile" of related spectra.

CHAPTER 3 - SAMPLE PREPARATION & BASIC MICROSTRUCTURAL CHARACTERISATION

3.1 INTRODUCTION

This chapter is concerned with standard CTEM microstructural characterisation, together with sample preparation and analysis. These are illustrated through a report of an investigation conducted on a selected group of nine CoCr thin films. The sample preparation techniques employed for CTEM work are also applicable for the STEM studies described in the following chapters and so these will be considered in some detail.

3.2 SPECIMEN PREPARATION

All the CoCr films studied in this project were produced using the radio frequency (rf) sputter deposition process (figure 3.1). In this process we have a vacuum chamber (typically 10^{-7} torr) in which there are one or more targets of known composition and a flexible substrate onto which the layers are deposited. The substrate is mounted on a water cooled holder to prevent heat damage. Ar gas is fed into the chamber and an rf alternating voltage is applied to the target, partially ionising the gas. The Ar ions are accelerated by the voltage and sputter off surface layers from the target material. The released atoms are then deposited on the earthed substrate. The thickness of layer deposited can be controlled through the gas pressure and the deposition time. The

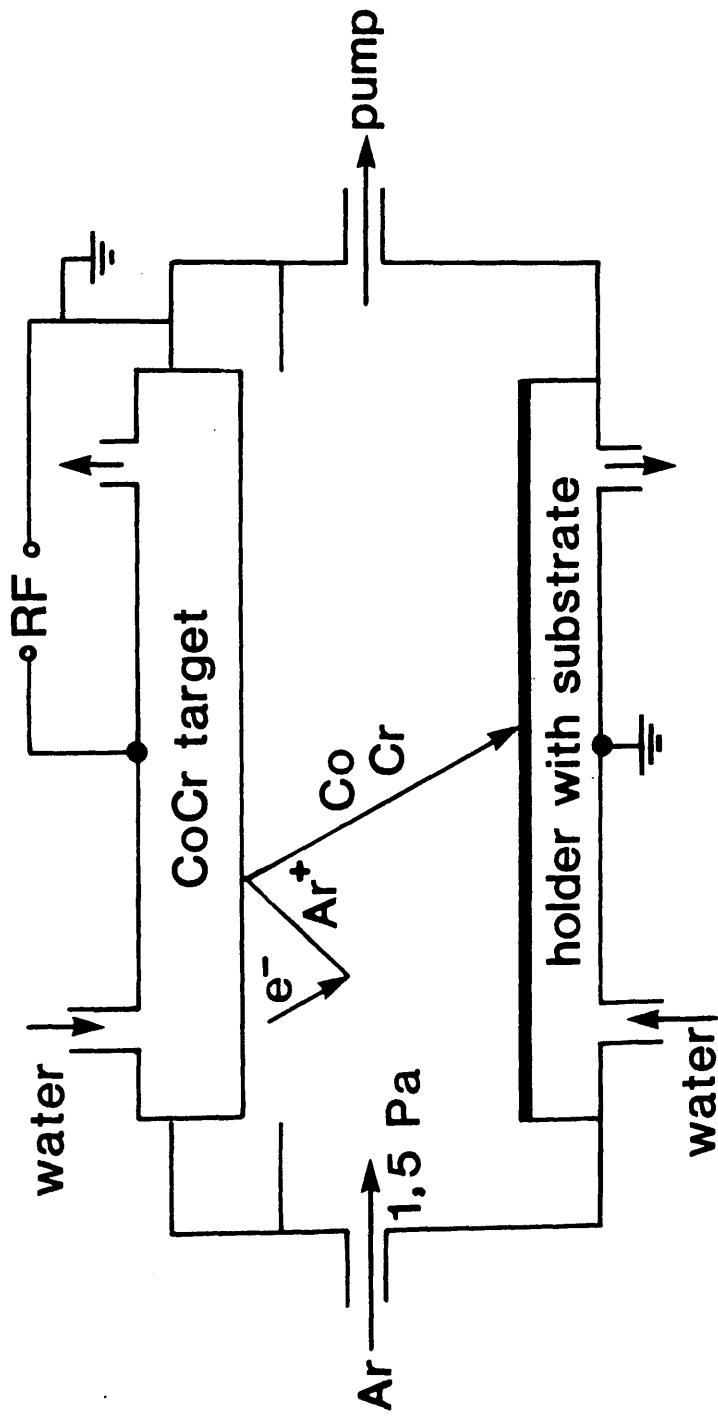


Figure 3.1

An illustration of the rf sputter deposition process.

substrate temperature during deposition can be regulated by a flow of water through the holder.

For the series of films considered in this chapter a polyester (PET - polyethylene terephthalate) substrate was used and an amorphous Ge underlayer 400nm thick was deposited prior to the CoCr. CoCr layers were grown to 100, 400 and 800nm in thickness with targets of 15, 21 and 25 atomic % Cr. These thicknesses and compositions were selected because they are respectively below, on and above the recognised specifications for a practical recording layer (Bernards et al. 1987, Luitjens et al. 1988, Grundy & Ali 1983).

The macroscopic physical and magnetic constants for the film were determined using bulk characterisation techniques (appendix 1). The as-deposited films were too thick for direct examination in the electron microscope and so thinned cross-sections and planar sections of all the films had to be prepared (figure 3.2). Requirements governing the preparation were that the samples had to have as large an area as possible of near uniform thickness which was transparent to 100kV electrons and that the section had to be robust enough for repeated insertion and removal from the microscope. The section dimensions also had to be such that it would fit in the specimen cartridge. The techniques adopted for the preparation are described below.

3.2.1 Preparation Of Cross-sections

Transverse sections have several advantages over planar sections. In transverse sectioning the thickness of the CoCr layer is not reduced and the initial growth layer remains intact. The interfaces between underlayers are also unchanged. The film thickness along the easy axis

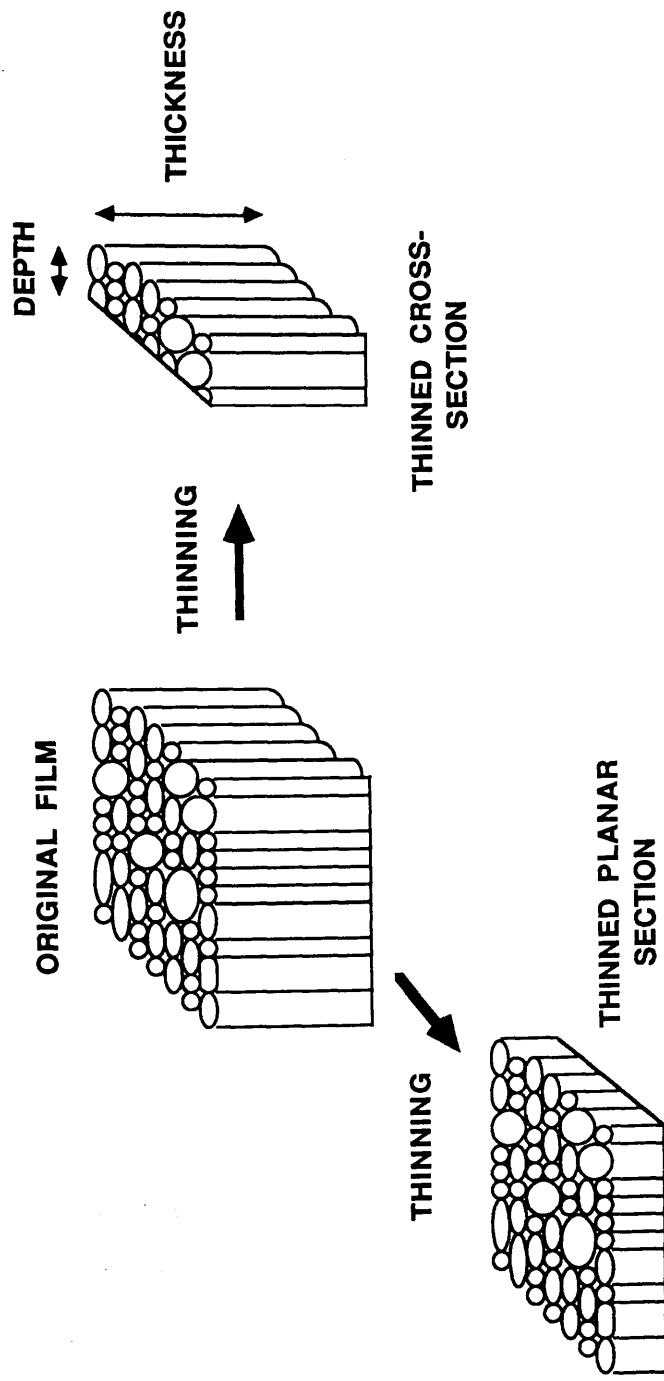


Figure 3.2 Planar and cross-sections of CoCr.

of magnetisation is therefore as-deposited. Hence the magnetic structure in cross-sections is expected to more closely resemble that of the original film. Cross-sectional samples of perpendicular media are also more useful for magnetic studies because the magnetic induction is perpendicular to the beam and therefore causes the maximum deflection to the beam.

The two commonly accepted methods for the preparation of cross-sections for the transmission electron microscope are microtoming and Ar ion beam milling. Microtoming involves the slicing of films embedded in resin with a diamond blade. The films are cut perpendicular to the film plane and sections can, with difficulty, be made less than 100nm thick. This technique, whilst less complicated than ion milling, does cause plastic deformation in the specimen which results in poorer column definition (figure 3.3). Ion beam milling is therefore the preferred technique (Futamoto 1986). In Ar ion beam milling the specimen is held on a rotating stage inside a vacuum chamber (figure 3.4). Ionised Ar atoms are accelerated through a potential in an ion gun and focused on the centre of the specimen. The accelerated beam sputter-etches layers from the top and/or bottom of the specimen until the required thickness is reached. The whole specimen stage is cooled by a flow of liquid nitrogen to prevent thermal damage to the specimen. Ar etching is, however, a slow process and so cross-sectional samples must to some extent be thinned prior to milling. The process used in this project is similar to that developed for thinning of semi-conductor samples (Chew & Cullis 1987) and is detailed below.

Small sections ~15mm x 1.5mm were cut from the sputtered disc of film and were glued between two strips of Si wafer ~15mm x 2.5mm x 1mm (figure 3.5). Care was taken to ensure that the CoCr layer, rather than the substrate, was near the centre of the "sandwich". This was

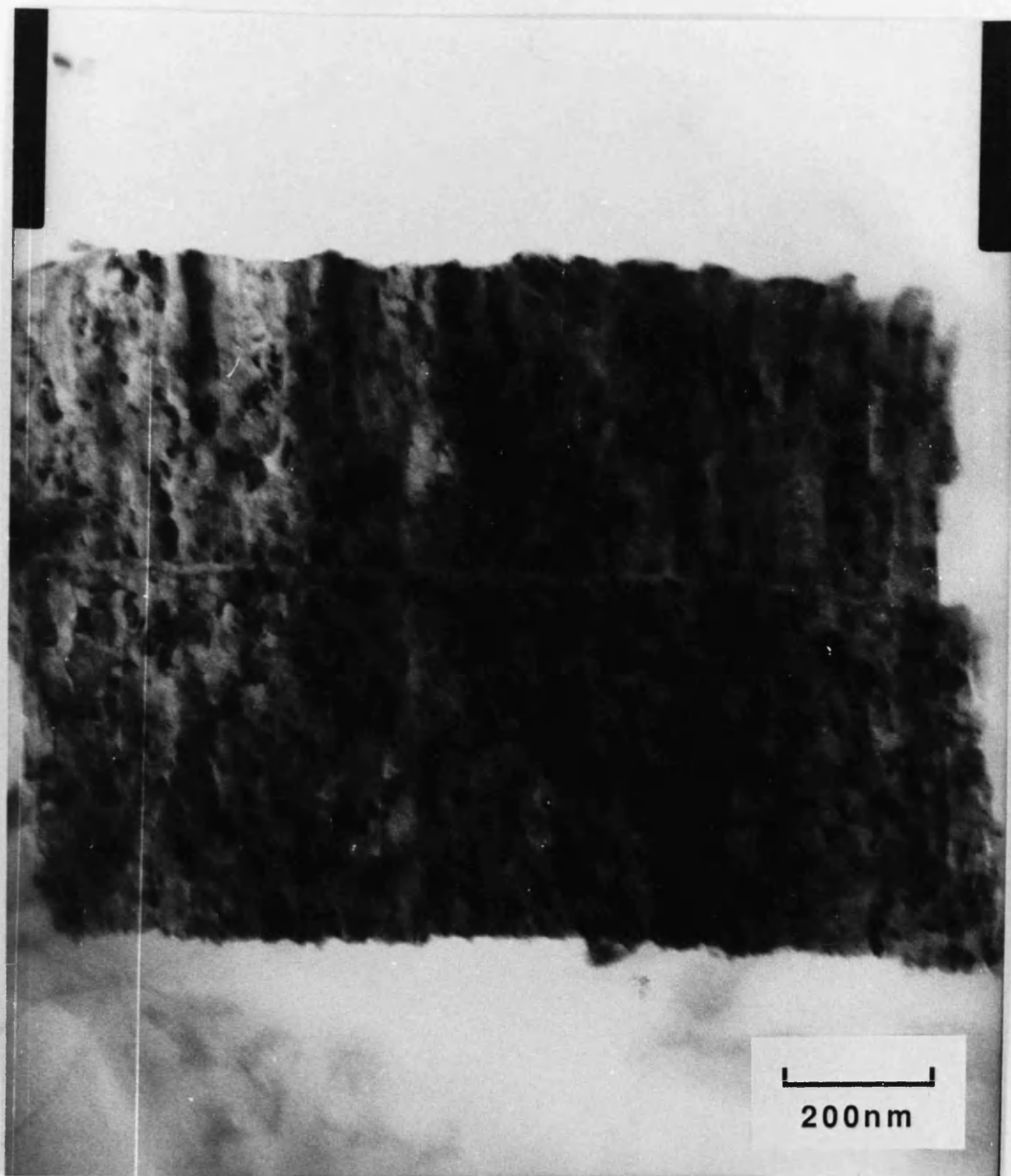


Figure 3.3

A CTEM bright field image of a microtomed cross-section of a film with a 400nm thick CoCr upper layer and a 450nm thick NiFe lower layer separated by a 15nm thick Ti layer.

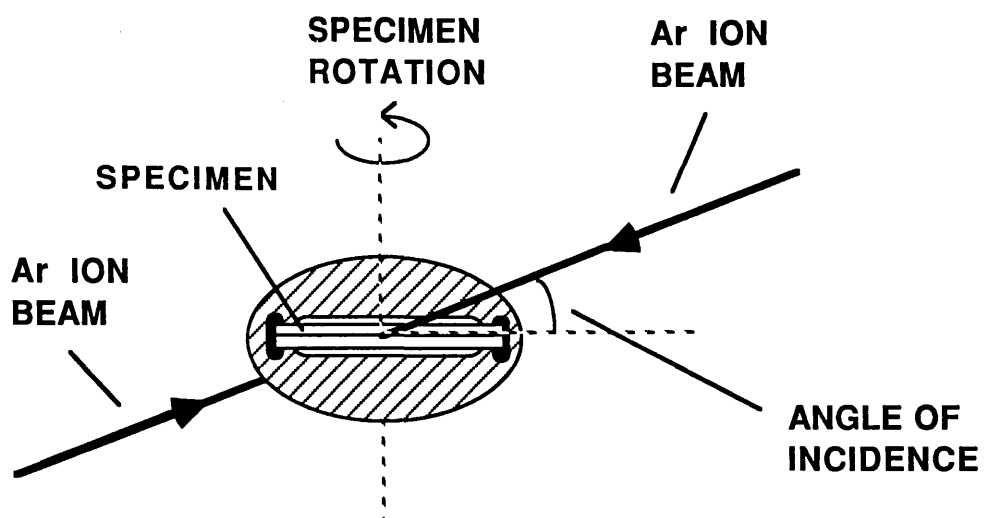


Figure 3.4 Ar ion-beam milling of a CoCr cross-section.

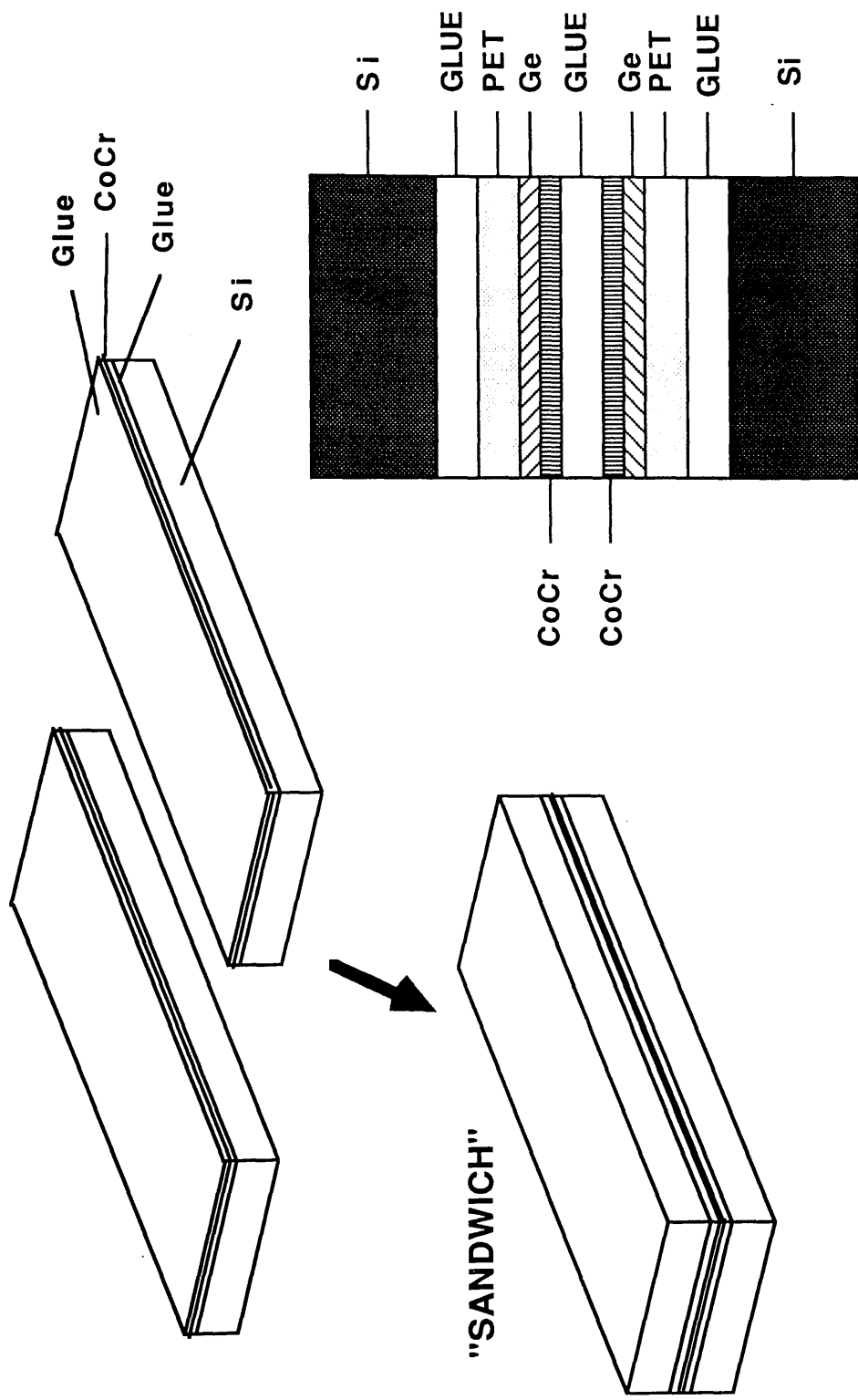


Figure 3.5 Making a Si "sandwich" of sections of CoCr film.

straightforward since the films showed a tendency to curl away from the CoCr side. All bonding was performed using an epoxy resin, the thickness of which was minimised by compression of the "sandwich". Before glueing, surface contaminants were removed ultrasonically in acetone to prevent the likelihood of specimen fracture. The sandwich was then mounted vertically inside an open-topped gelatine capsule or mould using a piece of plasticine. A quick-setting two-component polymer resin (Technovit) was mixed and poured in. Once the resin had set the gelatine capsule was removed leaving the sandwich in a column of polymer resin. This gave the sample enough rigidity and strength for cutting.

Transverse sections, $\sim 200\mu\text{m}$ thick, of the resin in which the sample was now held were cut using a diamond blade saw (figure 3.6). These sections were mounted on a metal block using beeswax and further thinned to between 30 and $50\mu\text{m}$ by polishing using progressively finer grades of diamond powder with a water lubricant. When the thickness was judged to be less than $50\mu\text{m}$, from micrometer measurements, the polishing was stopped, the samples were removed from the block and the Technovit was dissolved away using a warm tri-chloro ethylene solution. The remaining section was then carefully glued onto a Cu electron microscope specimen grid (figure 3.7). Finally the sample was thinned from both sides in the ion mill using an accelerating potential of $\sim 6\text{kV}$ and a beam current of $\sim 20\mu\text{A}$ with the guns inclined at $8-10^\circ$ to the specimen plane. This was continued until, under optical microscope observation, a small hole appeared at the centre of the section in which slivers of the film appeared to be free of glue (figure 3.8). The duration of this process varied between 12 and 24 hours depending on the thickness of the section after polishing.

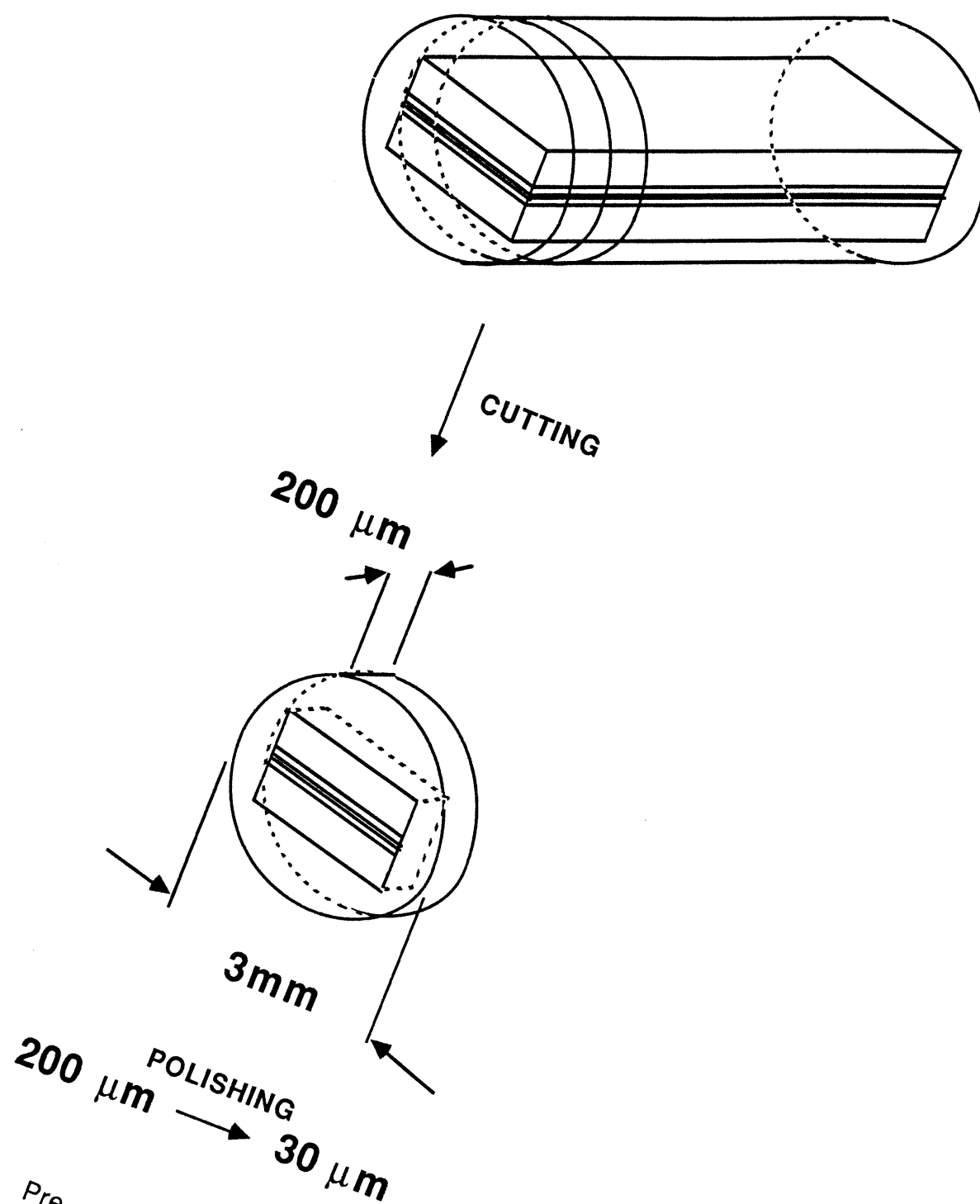


Figure 3.6

Pre-milling thinning of the CoCr cross-section.

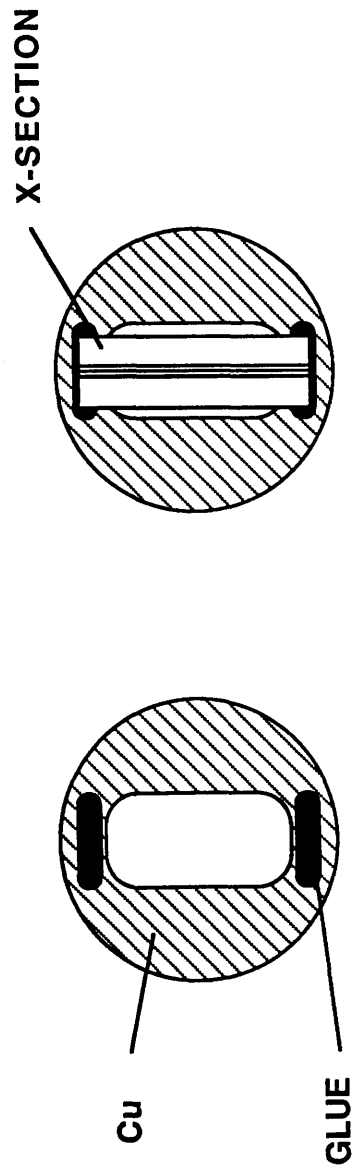


Figure 3.7 Glueing the cross-section to a Cu electron microscope specimen holder.

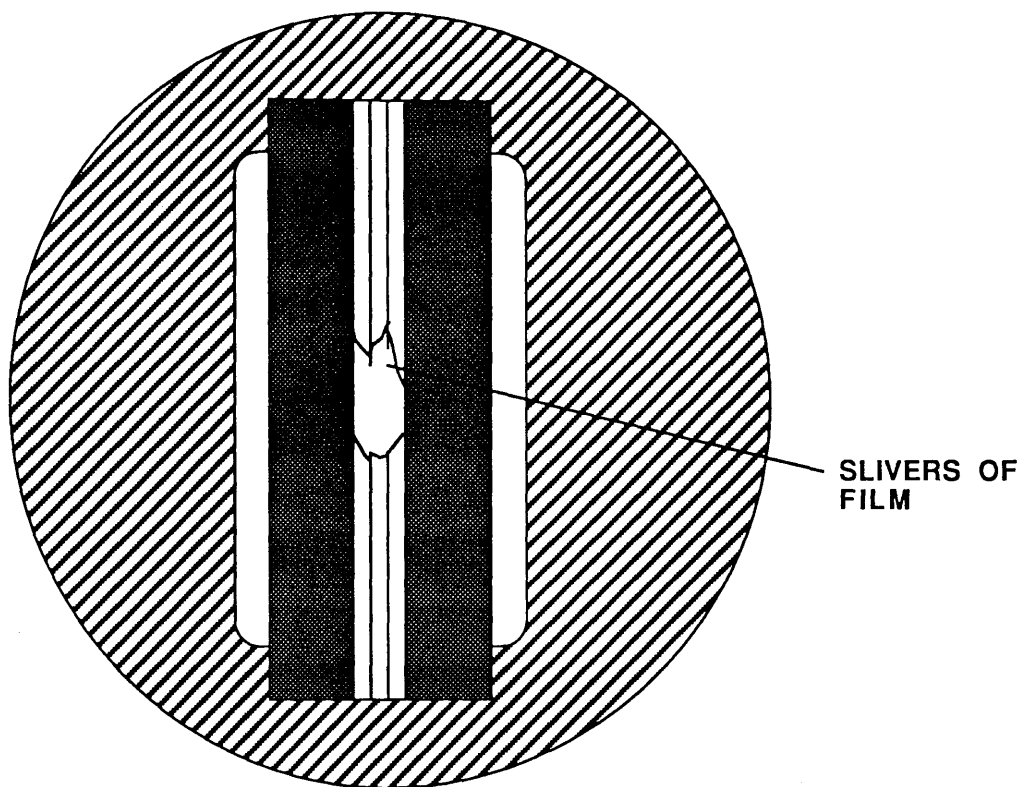


Figure 3.8

The appearance of a thinned cross-section of CoCr.

3.2.2 Preparation Of Planar Sections

Planar sections of CoCr thin films are much easier to make than cross-sections. There is a much higher success rate in their preparation and they are better suited for spot EDX microanalysis in the STEM (see chapter 4). To make planar sections conventional folding Cu specimen grids were modified by cutting away the mesh from one side and inserting a suitably sized section of film with the substrate facing the open side. The substrate was removed by immersion in a 1:3 preparation of fluoro-acetic acid and di-chloro methane. The sample was then Ar ion beam milled from the substrate side to remove the initial layer of CoCr but leave the more developed columnar structure. The accelerating potential, beam current and angle of incidence were as for the cross-section and thinning was continued until the central area had been completely milled away (figure 3.9). The region around the hole in the film was then thin enough for analysis. In general this took between 1 and 3 hours depending on the initial film thickness.

3.3 EXPERIMENTAL METHODS

CTEM studies on the group of samples involved bright field, dark field and crystal diffraction pattern studies. Mean column diameter, variation in column diameter, the Ge layer, the extent depthwise of columnar growth, column definition and the interfaces between underlayers were examined. The macroscopic properties of the films were then interpreted in terms of the findings. Examples of typical images and a description of the results are given in the next section.

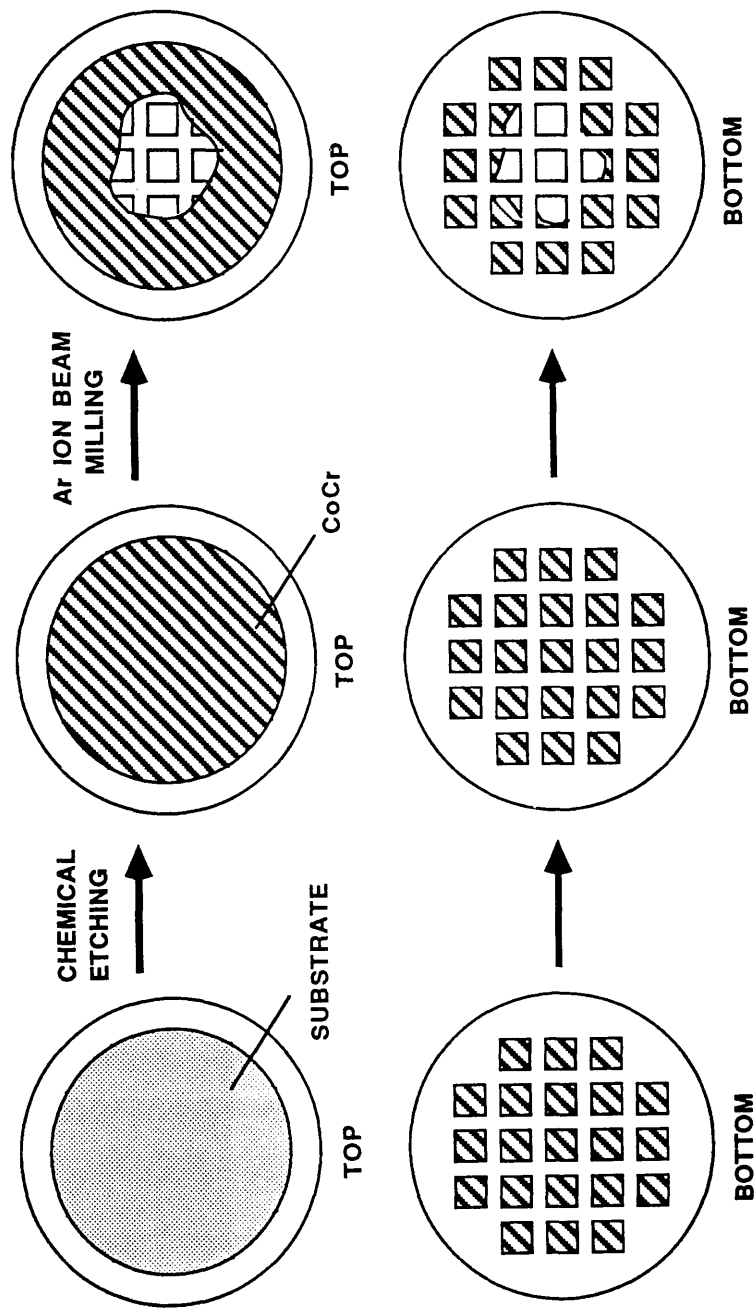


Figure 3.9 The thinning of a planar section of CoCr.

3.4 RESULTS AND ANALYSIS

The expected (see section 1.6.1) columnar structure with c-axis perpendicular to the film plane was revealed in cross-sectional BF images (figure 3.10). In this image the CoCr/Ge interface has fractured giving a bright dividing line between the two layers. This is not typical behaviour and is probably the result of a stress experienced at the interface. Moire fringes observed in some of the grains are indicative of an area of specimen more than one column in depth.

From such cross-sections individual columns were seen to extend throughout almost the entire thickness of all the CoCr layers with a thin disordered layer (~10-30nm) visible at the base of the columns (figure 3.11). Typical selected area diffraction patterns from regions, of the order of 15-20nm in diameter, in a cross-section of CoCr film are shown in figure 3.12. The patterns correspond to a) the columns in the CoCr layer, b) the disordered layer at the base of the columns and c) the Ge layer. The spot diffraction pattern in a) is for the beam directed along a hcp basal plane. This confirms that the columns had a hcp structure with c-axis along the film normal. The hcp a and c lattice repeats were calculated to be $0.26 \pm 0.04\text{nm}$ and $0.42 \pm 0.04\text{nm}$ respectively. This is in accordance with results reported for bulk CoCr (Parker et al. 1989), the similar atomic radii of Co and Cr (0.125nm for both) and the a and c lattice parameters of 0.25nm and 0.41nm (Kittel 1953) for hcp Co. For diffraction pattern b) the presence of rings at the same radial spacings as the spots in diffraction pattern a) and the appearance of rings at different radial spacings are indicative of a region with a hcp CoCr structure of varying c-axis orientation. The rings in diffraction pattern c) reveal a diamond structure in the Ge layer with a mean lattice repeat of $0.61 \pm 0.04\text{nm}$ as compared with a value of

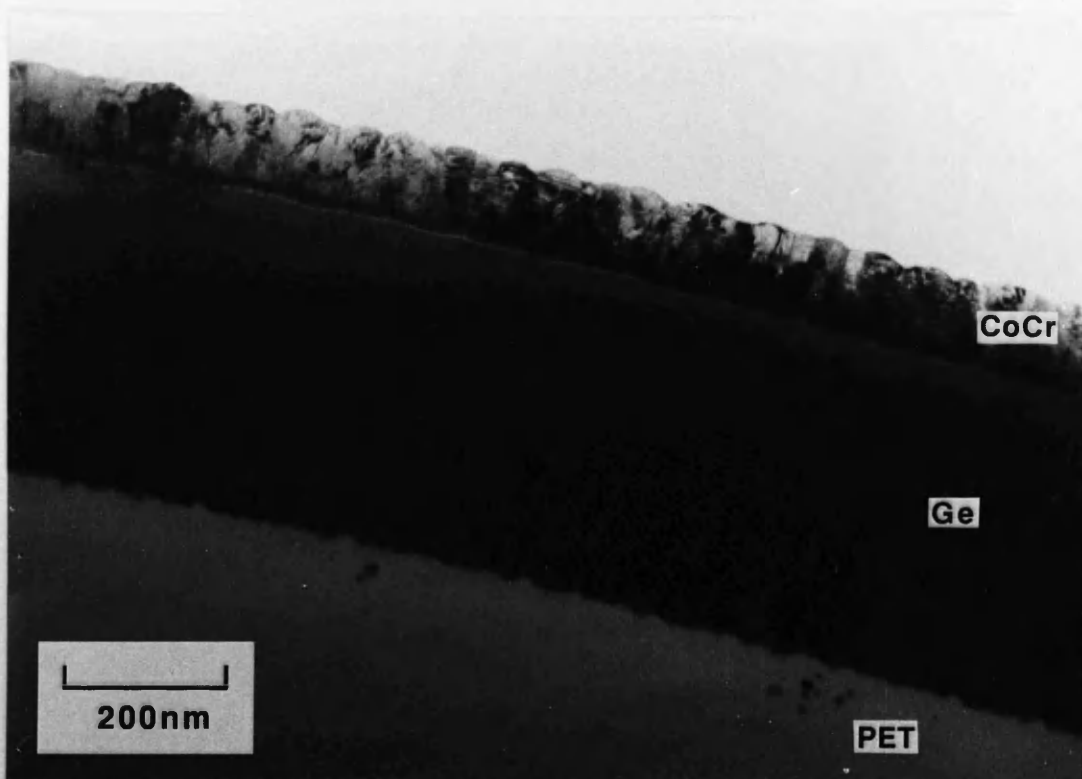


Figure 3.10 CTEM BF image of a CoCr cross-section with a 100nm thick CoCr layer and a 400nm thick Ge layer.

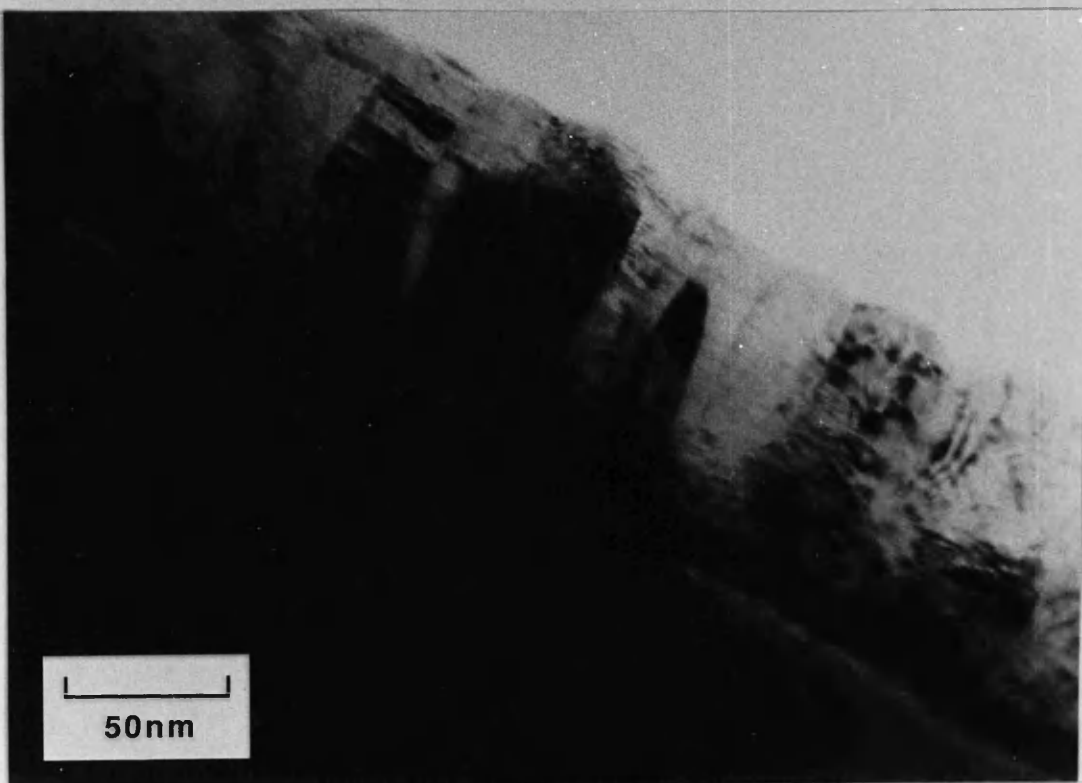


Figure 3.11 CTEM BF image of a CoCr cross-section showing the disordered layer at the base of the CoCr columnar structure.

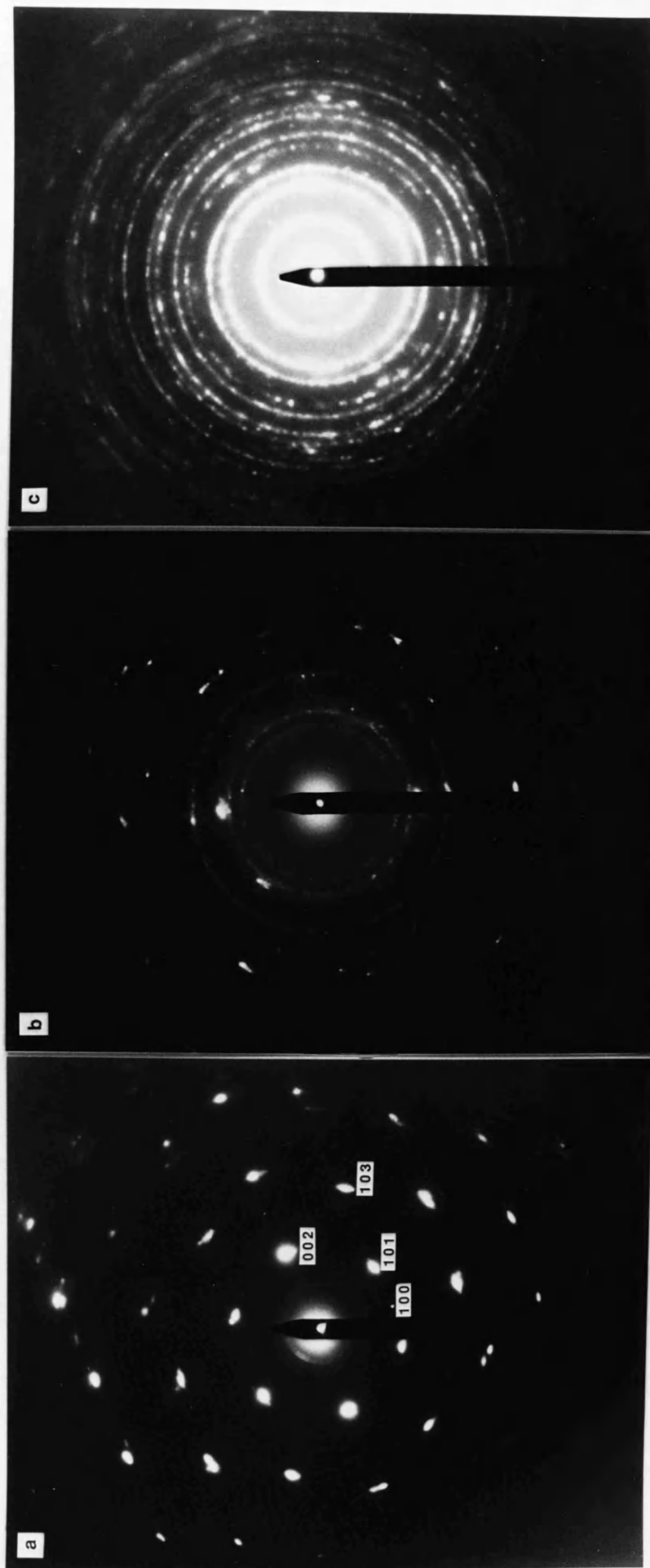


Figure 3.12

Selected area diffraction patterns from a CoCr cross-section corresponding to

a) the CoCr columns, b) the CoCr disordered layer and c) the Ge layer.

0.57nm given by Kittel (1953). BF (figure 3.10) and DF images (figure 3.13) of cross-sections, however, suggest that the Ge layer appears to be at least partly amorphous. Futamoto (1985) has proposed that the Ge may have a crystal structure at the surface favouring hcp CoCr nucleation (the atomic radius of Ge is 0.122nm which is similar to that of Co and Cr). Schrauwen et al. (1988) have also reported a dual nature for the Ge layer with the bottom of the layer sealing the substrate whilst the top serves as a nucleation layer.

Figure 3.14 shows an image of a typical planar section in which the top of the columns can clearly be seen. Whilst all the columns do not have a perfect hexagonal shape the boundaries, in general, form polygons with between 4 and 6, approximately straight, sides. The grains were found to vary in size in each film with measurements in cross and planar sections being internally consistent. Column diameter was taken to be the distance between the centres of opposite sides or the centre of one side and the opposite corner. The mean diameter, estimated over a large number of columns, was dependent on both film thickness and Cr concentration. Column width tended to increase in thicker films with the largest of all being found in the 25 atomic % Cr film (table 3.1). Measurement of column diameter was difficult for all films because of the variability in column shape and size (normally diameters between 10 and 100nm), but in films with poor column definition it was almost impossible. Column definition, or the ease with which individual columns could be distinguished, was found to be dependent on Cr concentration and independent of layer thickness. The column definition was found to be best in the 21 and 15 atomic % Cr films with much poorer definition in the 25 atomic % Cr films (figures 3.14 and 3.15). The estimate of mean column diameter is therefore



Figure 3.13 CTEM DF image of a CoCr cross-section with a 100nm thick CoCr layer and a 400nm thick Ge layer.

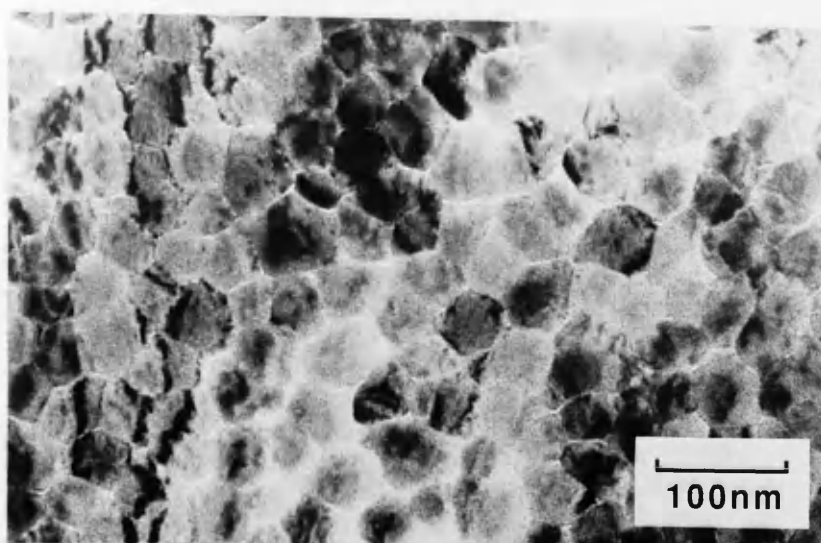


Figure 3.14 CTEM BF image of a planar section of a 21 atomic % Cr film of CoCr.

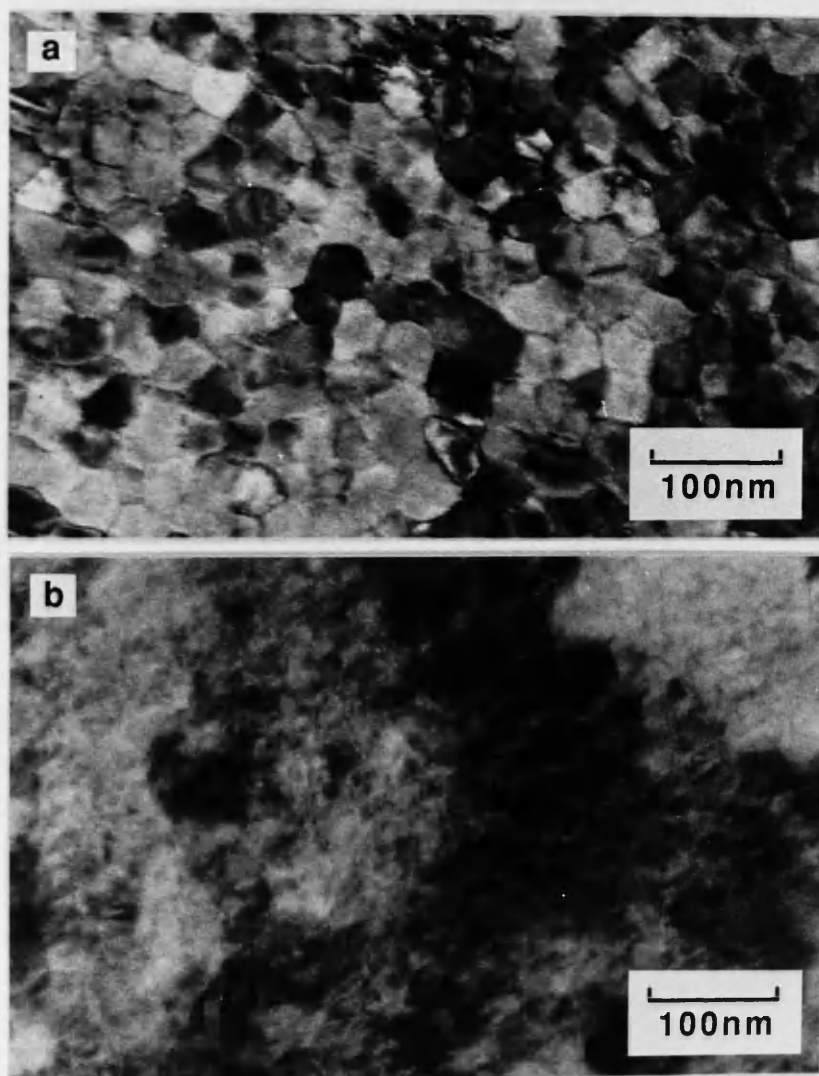


Figure 3.15 CTEM BF images of planar sections of a) 15 atomic % Cr and b) 25 atomic % Cr films of CoCr.

SAMPLE	D (nm)	COL. DIAM. (nm)	$\Delta\theta_{50}$ (DEG.)	ATOMIC % Cr
1	100	30 + 10	10.8	21
2	400	30 + 10	6.8	
3	800	50 + 10	6.0	
4	100	20 + 10	3.7	15
5	400	20 + 10	2.3	
6	800	30 + 10	1.6	
7	100	40 + 30	5.0	25
8	400	70 + 30	3.9	
9	800	70 + 30	4.1	

Table 3.1

Physical properties of films studied in chapter 3.

more accurate for the 21 and 15 atomic % Cr films.

A typical selected area diffraction pattern corresponding to a region, of the order of $0.5\mu\text{m}$ in diameter, in a planar section of CoCr is shown in figure 3.16. In this diffraction pattern only some of the rings observed in the diffraction pattern for the disordered layer in the cross-section (figure 3.12b) are visible. This is consistent with the beam being directed along the hcp c-axis.

In dark field images, planar sections showed groupings of columns giving the same crystal plane reflections. This effect showed no dependence on deposited film thickness and the clearest examples were in the films with 21 atomic % Cr (figure 3.17).

The magnetic properties of the films are given in table 3.2. From this it can be seen that the films produced with a target of 15 atomic % Cr all have low M_r and large negative values for K_1 , the first order component of perpendicular anisotropy (kJ.m^{-3}). These films will not have an easy axis of magnetisation perpendicular to the film plane and will retain only low magnetisation when the write signal is removed. Apart from the 800nm thick film the films produced with a target of 25 atomic % Cr have a small M_r and a small perpendicular H_c . These films will also not retain a high magnetisation when the write field is removed and will be easily demagnetised. Thus the 800nm thick film produced with the 25 atomic % Cr target and the films produced with the 21 atomic % Cr target will have better magnetic properties for perpendicular recording (see chapter 1, section 1.6.1). Of these, the 400nm thick 21 atomic % Cr film is best for recording purposes because the 100nm film is too thin to retain a strong signal and the 800nm thick film decreases the volume recording density.

An apparent conflict between the magnetic and the physical

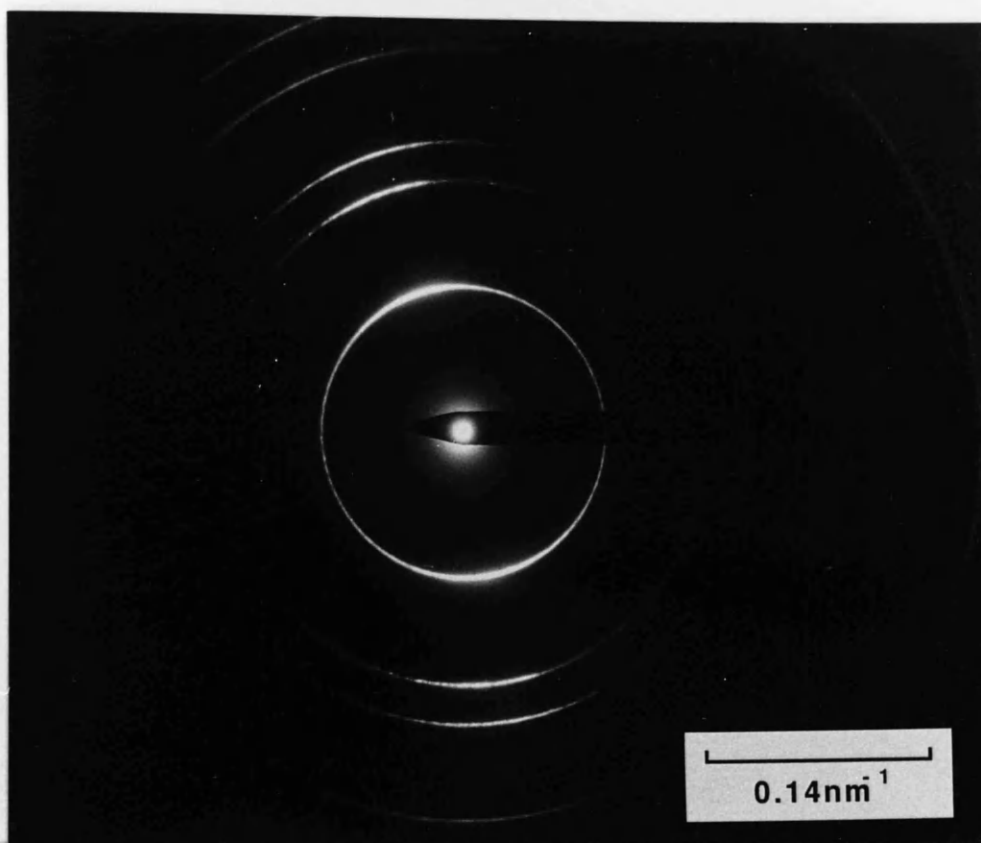


Figure 3.16 Selected area diffraction pattern from a typical CoCr planar section

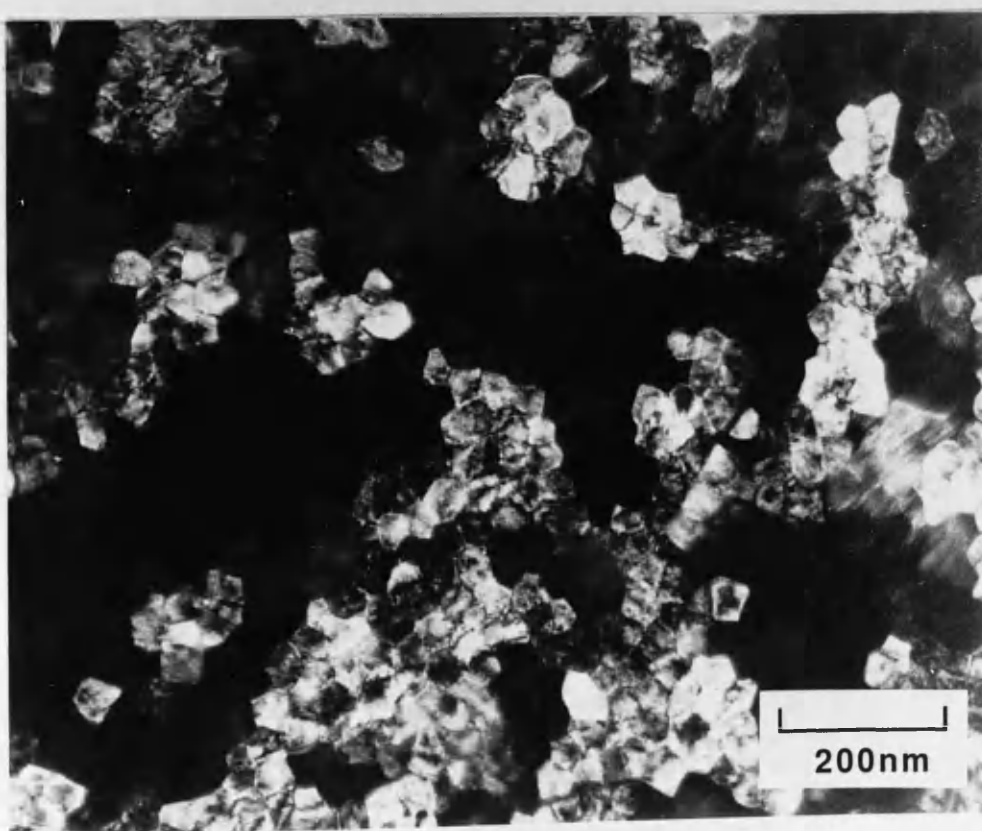


Figure 3.17 CTEM DF image of planar section of CoCr.

SAMPLE	M_s (kA.m ⁻¹)	M_r (kA.m ⁻¹)	PERP. H_c (kA.m ⁻¹)	K_1 (kJ.m ⁻³)
1	430	38.7	24.1	23.4
2	430	38.7	29.5	23.0
3	450	36.0	30.0	29.9
4	550	16.5	16.1	-85.9
5	640	6.4	16.4	-78.8
6	610	6.1	6.9	-80.9
7	300	12.0	8.0	21.1
8	320	9.6	6.3	23.3
9	340	30.6	24.8	35.1

Table 3.2 Magnetic properties of films studied in chapter 3.

properties arises in the fact that the $\Delta\theta_{50}$ (see table 3.1) is smallest in the low atomic % Cr films with negative K_1 . As mentioned in chapter 1, section 1.6.1 a small $\Delta\theta_{50}$ would intuitively be expected of a film with a high perpendicular magnetic anisotropy. In this case, however, the concentration of Cr is such that the magnetic moment of Co is not sufficiently diluted.

3.5 DISCUSSION

The results in this chapter show that the physical microstructure is very complex and that the bulk properties are extremely sensitive to changes in the growth conditions. In addition, they show that basic characterisation techniques can provide essential background information on which films to study and information necessary to understand observed magnetic structure. The magnetic microstructure, however, depends in detail on any elemental segregation and various geometrical aspects of the columnar structure. A good understanding of the links between the physical and magnetic microstructure will therefore only be obtained through a study combining microcompositional and micromagnetic characterisation with the above techniques.

CHAPTER 4 - MICROCOMPOSITIONAL ANALYSIS

4.1 INTRODUCTION

In a CoCr thin film the local concentrations of Co and Cr can have an important influence on the micromagnetic properties (see chapter 1). Knowledge of both the absolute level and the pattern of any elemental segregation is therefore essential for an understanding of the detailed magnetic properties of a CoCr layer. This chapter describes the use of high spatial resolution EDX microanalysis in the extended VG HB5 STEM to investigate the dependence of the local Co to Cr ratio on the physical microstructure for a series of CoCr films with systematically adjusted growth conditions.

4.2 CONSIDERATIONS FOR EDX MICROANALYSIS OF CoCr THIN FILMS

As explained in chapter 2, the intensity of characteristic x-ray photons produced when a region of specimen is irradiated with 100keV electrons provides a measure of the local elemental composition. In this study we are concerned primarily with the local concentrations of Co and Cr and therefore need to know the respective numbers of characteristic x-rays emitted. In an x-ray spectrum the channel about which a given peak is centred corresponds to the photon energy, and the total number of counts in the peak is proportional to the number of photons at that energy incident on the detector. In practice, however,

spectra collected from a thin film such as CoCr also include energy contributions from bremsstrahlung radiation and characteristic x-rays emitted by other elements present in the excited volume. It was therefore necessary to calculate the number of counts which actually corresponded to the characteristic x-rays of Co and Cr before the relative concentrations could be deduced.

4.2.1 Background Correction

The first step in this procedure was to remove the bremsstrahlung from the energy region of interest. In the vicinity of the Co and Cr x-ray peaks the energy variation of the bremsstrahlung was approximately linear. Appendix 2 describes the program written for the AN10000 to strip the background counts from each spectrum. The ratio of the numbers of $K\alpha$ to $K\beta$ x-rays emitted from a given element is a constant greater than 1. Comparison of the ratio of Co/Cr $K\alpha$ peak counts from different spectra was therefore the most straightforward way of accurately analysing concentrations of Co and Cr.

Before this could be done, however, the background corrected spectrum had to be checked for elements with characteristic photon peaks which coincided with the Co or Cr $K\alpha$ peaks. For the specimens investigated in this study the only impurity for which such a correction was needed was Fe (see sections 4.3.3 and 4.4.2 for other impurities detected and possible origins). The Fe $K\beta$ peak is centred about an energy within the spread of the Co $K\alpha$ peak. To calculate what contribution it made to the total number of Co $K\alpha$ counts the number of counts in the identifiable Fe $K\alpha$ peak was multiplied by a constant derived from the relevant partition function (the ratio of $K\alpha$ to

[K α +K β] x-ray production), as given by Gray et al. (1983). The number of Fe K β counts was calculated and deducted at the same time as the background fit was carried out (appendix 2).

4.2.2 Generation and Detection Efficiencies for Characteristic X-rays

To turn the total recorded x-ray counts in the corrected K α peaks into absolute atomic compositions of the form Co_{100-x}Cr_x required a knowledge of the relative efficiencies of x-ray generation and detection for the elements of interest. When using a Si(Li) detector Co and Cr K α peaks are detected with similar efficiencies. There is, however, a difference in their generation efficiencies. Following Cliff and Lorimer (1972) this can be expressed as a factor k_{CoCr} which relates the number of atoms of each element in the excited volume (n) to the measured number of characteristic x-rays corresponding to that element (N) thus :

$$\frac{n_{\text{Co}}}{n_{\text{Cr}}} = k_{\text{CoCr}} \frac{N_{\text{Co}}}{N_{\text{Cr}}} \quad 4.1$$

This factor is given by Gray et al. (1983) to be:

$$k_{\text{CoCr}} = \frac{\omega_{\text{Cr}} p_{\text{Cr}} \sigma_{\text{Cr}} \epsilon_{\text{Cr}}}{\omega_{\text{Co}} p_{\text{Co}} \sigma_{\text{Co}} \epsilon_{\text{Co}}} = k_{\text{CrCo}}^{-1} \quad 4.2$$

where p is the partition function, ω is the fluorescence yield (probability of emission of a characteristic x-ray rather than an Auger electron), σ is the ionisation cross-section with 100keV incident electrons (cm²sr⁻¹) and ϵ is the efficiency of the detector (see table 4.1).

Insertion of the given values in equation 4.2 yields a figure of 1.076 for k_{CoCr} .

For specimens of finite thickness, x-ray absorption within the specimen must also to be taken into account. Beer's law relates the transmitted x-ray photon intensity, I_A , to the incident x-ray photon intensity, I_O , for a specimen of element, A, thus:

$$I_A = I_O \exp(-\mu_A \rho x) \quad 4.3$$

where μ_A is the mass absorption coefficient for element A (cm^2g^{-1}), ρ is the density of the element (g.cm^{-3}) and x is the length of the x-ray path through the specimen (cm). For a uniform CoCr specimen this leads to an absorption correction factor for equation 4.1 of:

$$\frac{\mu_{\text{CoCr}}^{\text{Co}} [1 - \exp \{ - \mu_{\text{CoCr}}^{\text{Cr}} \rho_{\text{CoCr}} t \}]}{\mu_{\text{CoCr}}^{\text{Cr}} [1 - \exp \{ - \mu_{\text{CoCr}}^{\text{Co}} \rho_{\text{CoCr}} t \}]} \quad 4.4$$

where $\mu_{\text{AB}}^{\text{A}}$ is the absorption coefficient for x-rays of element A in specimen AB (cm^2g^{-1}), ρ_{CoCr} is the density of the CoCr specimen (g.cm^{-3}) and t is the x-ray path length in the specimen (cm). The respective mass absorption coefficients are very similar (see table 4.1). Thus for the film thicknesses considered in this study (see section 4.3.2) the absorption correction factor was calculated to be approximately equal to 1.

Secondary x-ray fluorescence effects are generally small in thin films, and need only be accounted for if strong x-ray fluorescence occurs in equivalent bulk specimens. They will not be considered in this work.

QUANTITY ELEMENT	P	ω	$\sigma_{100\text{keV}}$ ($\times 10^{-21} \text{ cm}^2 \text{ sr}^{-1}$)	ε	μ_{CoCr} ($\text{cm}^2 \text{ g}^{-1}$)
Co	0.878	0.370	0.317	≈ 1	130
Cr	0.882	0.279	0.451	≈ 1	117

Table 4.1 Factors used to calculate k_{CoCr}

4.2.3 Resolution For EDX Microanalysis

Assuming specimen drift during spectrum acquisition is negligible (see section 4.3.2) the spatial resolution of EDX microanalyses in the HB5 is limited by the probe size and beam spreading in the specimen (due to high angle elastic scattering). These beam broadening effects impose the fundamental limit on how small a volume of specimen can be examined. Reed (Goldstein et al. 1977) proposed a model stating that the diameter of the circle, on the exit surface of the specimen, containing 90% of the electron trajectories, b (cm), is given by:

$$b = 6.25 \times 10^{-5} \frac{Z}{E_0} \left[\frac{\rho}{A} \right]^{1/2} t^{3/2} \quad 4.5$$

where Z is the mean atomic number, A is the mean atomic weight, ρ is the specimen density (g.cm^{-3}), E_0 is the incident electron beam energy (eV) and t is the specimen thickness (cm). The excitation volume predicted by this model for an incident beam of diameter 2.4nm is illustrated in figure 4.1. McFadyen (1986) investigated beam spreading in a CoCr specimen for the operating mode employed in these studies. He demonstrated that the beam profile produced using a Monte Carlo simulation agreed well with the Reed model up to film thicknesses of 130nm. Reed's model was used in the estimation of resolution in the following work.

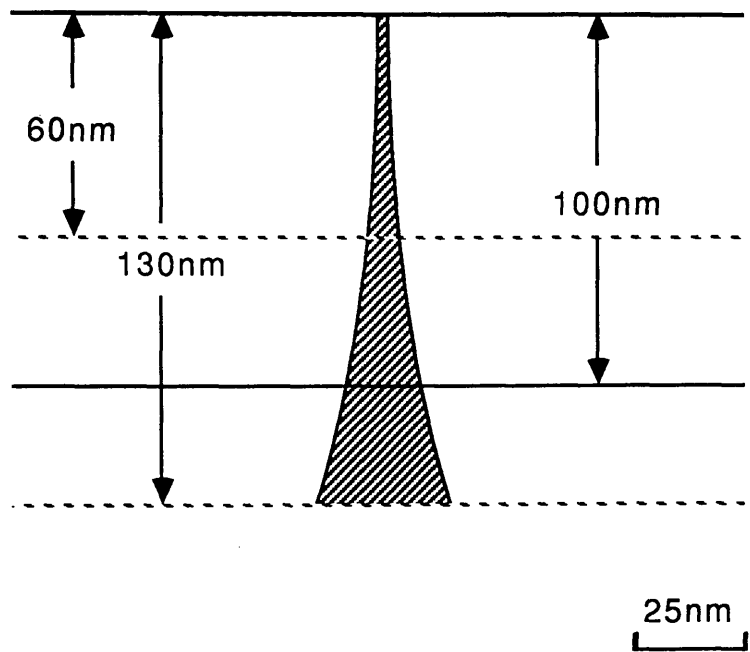


Figure 4.1 Beam spreading for 100keV electrons in CoCr alloy using a formula due to Reed.

4.3 INVESTIGATION OF THE EFFECT OF SUBSTRATE TEMPERATURE FOR CoCr LAYERS DEPOSITED DIRECTLY ONTO PET

4.3.1 Motivation For Investigation

As stated in chapter 1 a particularly important parameter in influencing the magnetic properties of CoCr thin films is the temperature of the substrate (T_s) during deposition (Smits et al. 1983). VSM measurements show a coercivity typically 4 to 6 times lower for a CoCr film deposited directly onto a polyethylene terephthalate (PET) substrate whose initial temperature is 30C (low T_s) than for one whose initial temperature is 90C (high T_s). Furthermore, recording experiments on the same films (de Bie et al. 1987, Bernards et al. 1989) reveal a maximum in the noise spectrum indicative of the presence of stripe domains only in the case of the low T_s films. These magnetic observations suggest that there should be differences evident in the local distribution of the Co and Cr within the crystal structure.

4.3.2 Experimental Method

Films with CoCr layers 400nm thick were produced by rf sputter deposition of a $\text{Co}_{78.5}\text{Cr}_{21.5}$ target directly onto a 12.5 μm thick PET substrate. All growth parameters were identical apart from the substrate temperature. To avoid the problems associated with operation of electronic temperature measuring equipment in the vicinity of the rf voltage a fluoro-optic device was employed to monitor substrate temperature. This consisted of a phosphor tip (or probe) at the end of

†The substrate temperature for both films was observed to rise during film deposition. After an initial sharp rise the temperature increased approximately linearly with time. For the low Ts film the mean temperature during deposition was 80C and the maximum temperature was $\leq 130\text{C}$. For the high Ts film the mean temperature during deposition was 140C and the maximum was $\leq 190\text{C}$.

††With thinned planar sections the lower part of the film microstructure is etched away and thus microanalysis is conducted on an area of CoCr for which the mean temperature during deposition is higher than that for the film as a whole.

an optical fibre with black fluorocarbon cladding. This probe was placed in thermal contact with the substrate through a heat conductive paste. The substrate temperature could then be estimated from the intensity of one of the fluorescent emission lines of phosphor. Initial substrate temperature for one film was 30C (low Ts) and for the other was 90C (high Ts).[†] VSM measurements showed the high Ts film to have a mean volume perpendicular H_C of 74kA.m⁻¹ whilst for the low Ts film a mean value of 14kA.m⁻¹ was recorded.

Specimens 400nm thick cannot be observed directly in a 100kV transmission electron microscope and so some thinning of the as-grown film was required. Thus there was a choice of whether to prepare either planar sections or cross-sections for these studies. Previous compositional investigations (McFadyen 1986) highlighted two major problems encountered when conducting high resolution "spot" microanalyses on thinned cross-sections of CoCr with a focused electron probe. Firstly, it was hard to locate suitably oriented column boundaries and, secondly, it was difficult to be sure that the probe was only exciting a small contribution from anything other than a boundary region. Planar sections were therefore used instead of cross-sections in an attempt to overcome both these problems (figure 4.2).^{††}

Planar samples were prepared by Ar ion-beam milling, as described in chapter 3. Standard CTEM physical microcharacterisation was performed on each specimen prior to EDX microanalysis. All x-ray work was carried out in the extended VG HB5 STEM. Specimens were loaded between 14 and 16 hours in advance of the commencement of each analysis to allow the specimen stage to reach a state of thermal equilibrium, thus lowering the extent of any specimen drift. With the operating conditions described in chapter 2 (objective and C1 lenses excited and a 100µm VOA inserted as the probe forming aperture) α_0

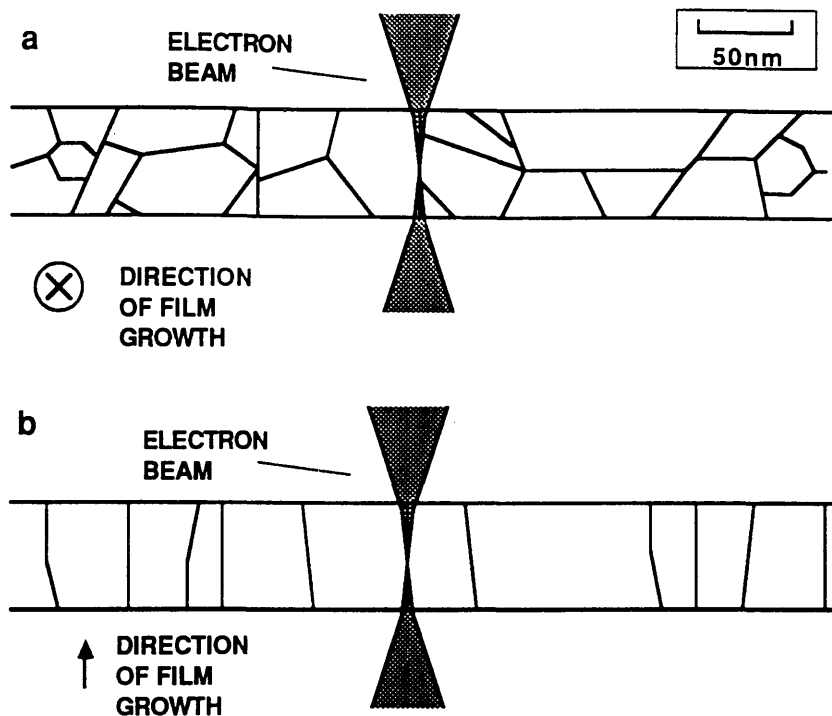


Figure 4.2 Schematic illustrating focused electron probe exciting the boundary phase in a) a cross-section and b) a planar section of CoCr.

was 11mrad, probe diameter was 2.4nm and I_p was 0.2nA. The specimen was tilted towards the detector (x and y tilts of -20° and $+20^\circ$) so that absorption of x-rays from the specimen in the holder and grid was minimised. A 25 μ m SAA was inserted to set the beam cross-over point and to act as a spray aperture (prevent stray electrons from exciting unwanted instrumental contributions from, for example, the Cu grid or the objective lens pole piece).

To achieve the angular compression in the scattered beam required to form a high angle ADF image PSL 1 was excited at a coarse/fine setting of -4/4.8. This gives a camera length of approximately 55mm. McGibbon (1989) measured the inner and outer acceptance angles of the ADF detector for two camera lengths with only PSL 1 excited. From these the setting of -4/4.8 was estimated to correspond to acceptance angles ranging from ≈ 60 mrad to 200mrad.

For each sample, several suitably thin areas of specimen were selected using the ADF image. Such an image was used in preference to the bright field image because it has a lower susceptibility to crystallographic contrast. The effect of this was to give an image in which the column boundaries were more clearly defined whilst confusing detail within the columns was substantially reduced. This was helpful for correct positioning of the probe on column boundaries.

A further problem encountered during the EDX microanalysis of these specimens was that of beam-induced contamination. This phenomenon is related to the polymerisation of trace levels of organic vapours present in the microscope and is particularly severe with small probe sizes and high probe currents. The effect of the polymerisation in this case was that insulating layers were built up on the irradiated area of specimen with the supply of contaminant diffusing from

neighbouring areas of specimen. This was readily observable as a progressive darkening and loss of detail in the bright field image (or alternatively a lightening and loss of detail in the ADF image). In order to avoid the beam-spreading and resultant loss of resolution caused by this effect, a large region around each selected area of specimen was "flooded" with electrons to polymerise, and thus immobilise, the local supply of contaminant. Flooding was performed for a particular area of specimen by reducing the magnification (which increased the scanned area and therefore reduced the time for which the probe was at a given position), removing all apertures between the source and the specimen and irradiating for a period of approximately 5 minutes. After completing this procedure the rate of contamination was low enough for a sufficient period of time to complete the microanalysis.

X-ray spectra were acquired from the area as a whole ($\simeq 1\mu\text{m}^2$) and from positions selected at locations in grain boundaries and within the columns. The spectra were recorded using the Link Analytical AN10000 and the average count-rate, dead time and current recorded on the VOA were noted for each acquisition. Positions from which spectra were acquired were selected using the high angle ADF image. Polaroid prints of the ADF image on the STEM display monitor for the area analysed were used during the experiment to record the exact point of acquisition for each spectrum. ADF and bright field images from each area were saved in digital form using the AN10000. The precision of these images was set at 8 bits per pixel and each pixel was allocated a dwell time of $51\mu\text{s}$.

Figure 4.3 shows a typical EDX spectrum from a CoCr thin film. For the films considered in this section (for count times of 20s) the number of counts in the Cr $K\alpha$ peak varied between $\simeq 600$ and 2000 and

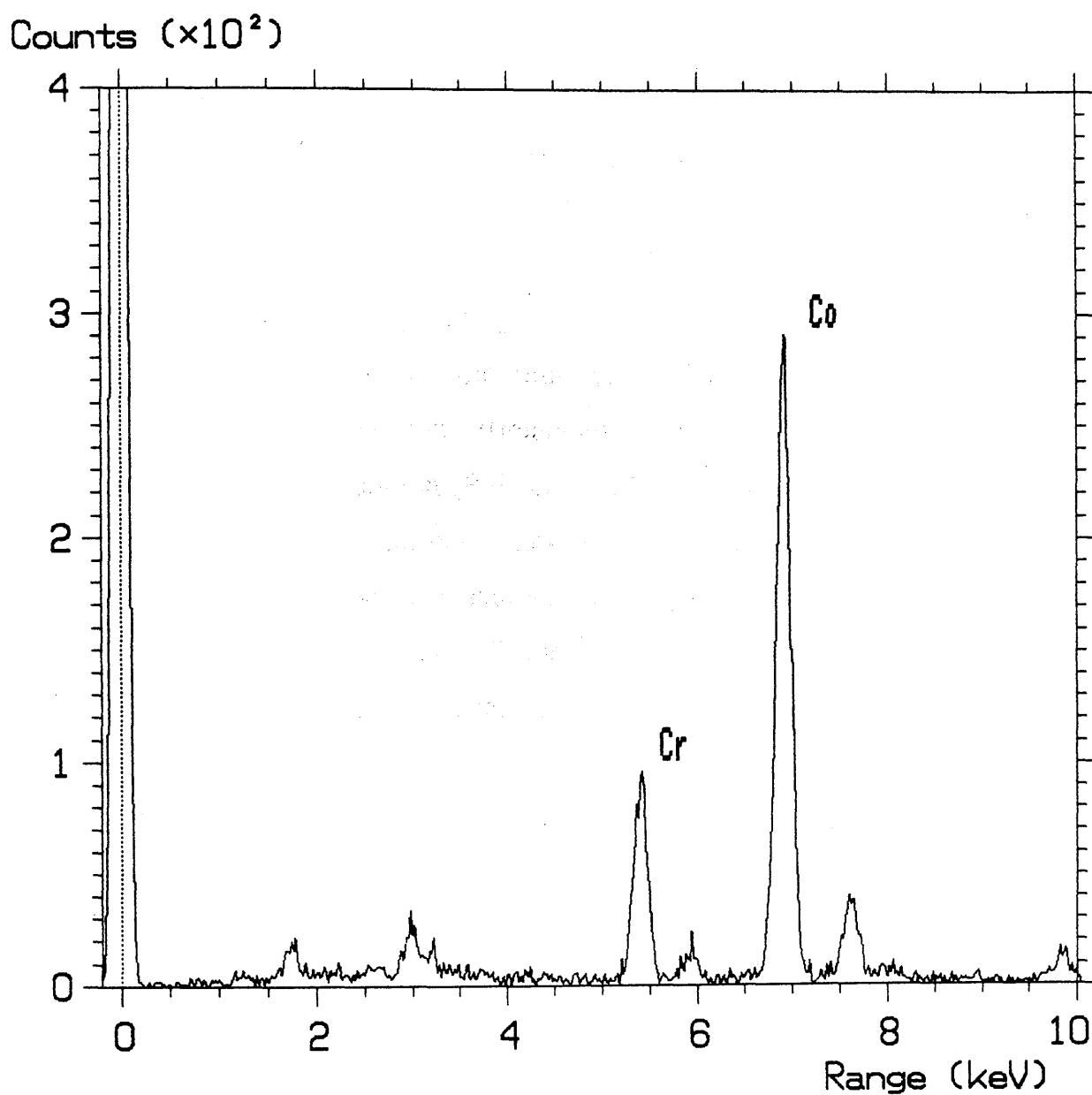


Figure 4.3 Typical EDX spectrum acquired from planar section of CoCr.

the number of counts in the Co $K\alpha$ peak varied between $\simeq 2000$ and 7000. From Poisson statistics this led to an inherent error in the Co/Cr count ratio of between 2.5 and 4.5%. Reduction of the random error could be achieved by counting for a longer time but this increased the risk that the analysis pertained to a larger volume due to specimen drift. Using counting times of 20s no specimen drift was discernable so that the spatial resolution of the analyses was limited by a combination of the probe size and beam spreading.

With knowledge of the number of $K\alpha$ counts and the x-ray generation and detection efficiencies it was possible to estimate the lower limit for resolution (Reimer 1982). Assuming a hcp structure (see chapter 3) the approximate thickness of specimen for the maximum number of counts was calculated to be approximately 120nm. Using the Reed model (see section 4.2.3) this was seen to correspond to a diameter of the circle, on the exit surface of the specimen, containing 90% of the electron trajectories of less than 27nm. From this the spatial resolution for these microcompositional analyses was calculated to be between approximately 2 and 6nm (Chapman et al. 1986, McGibbon 1989).

4.3.3 Results

CTEM bright field images of typical thinned areas in the planar sections of both films are shown in figures 4.4 and 4.5. In these it can be seen that the microstructure of the high Ts film is better defined than that of the low Ts film. From such images the mean column diameter for both the high and low Ts films was estimated to be between 40 and 50nm. Annotated examples of high angle ADF and corresponding BF images of areas used for the EDX microanalysis, in both films, are shown in figures 4.6 and 4.7. From these the boundary phase was

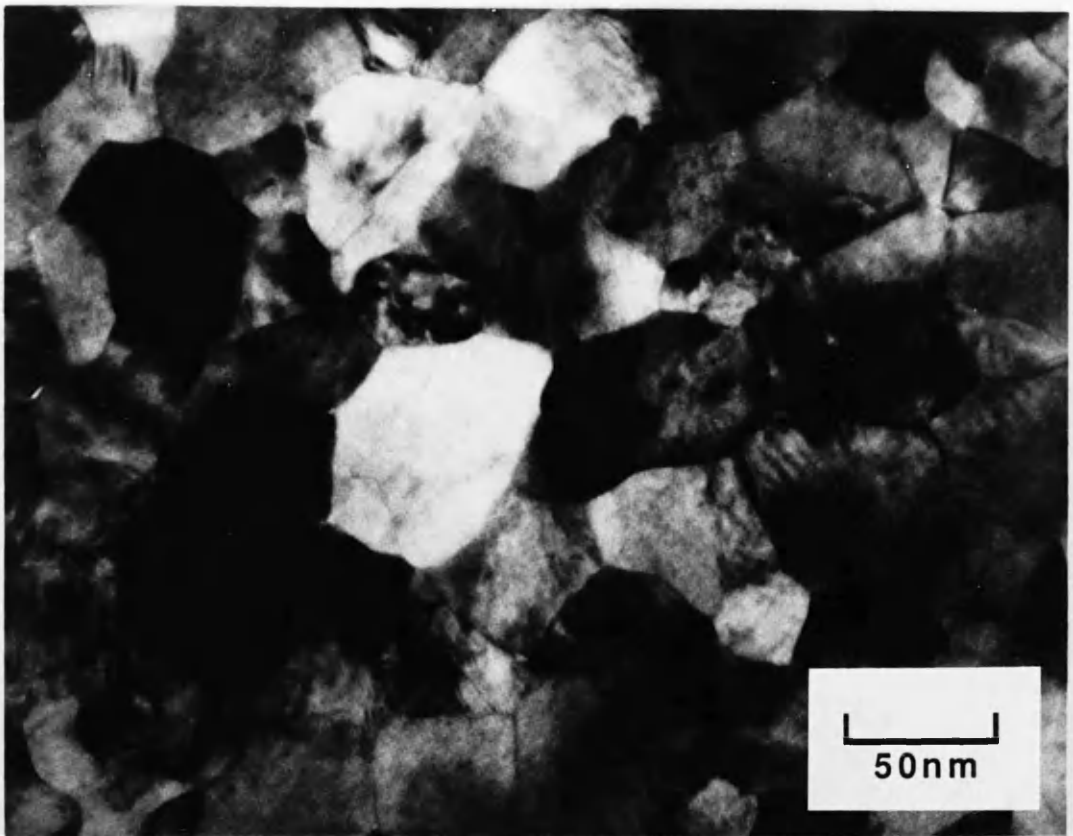


Figure 4.4 CTEM BF image of typical area in the high Ts film deposited directly onto PET.

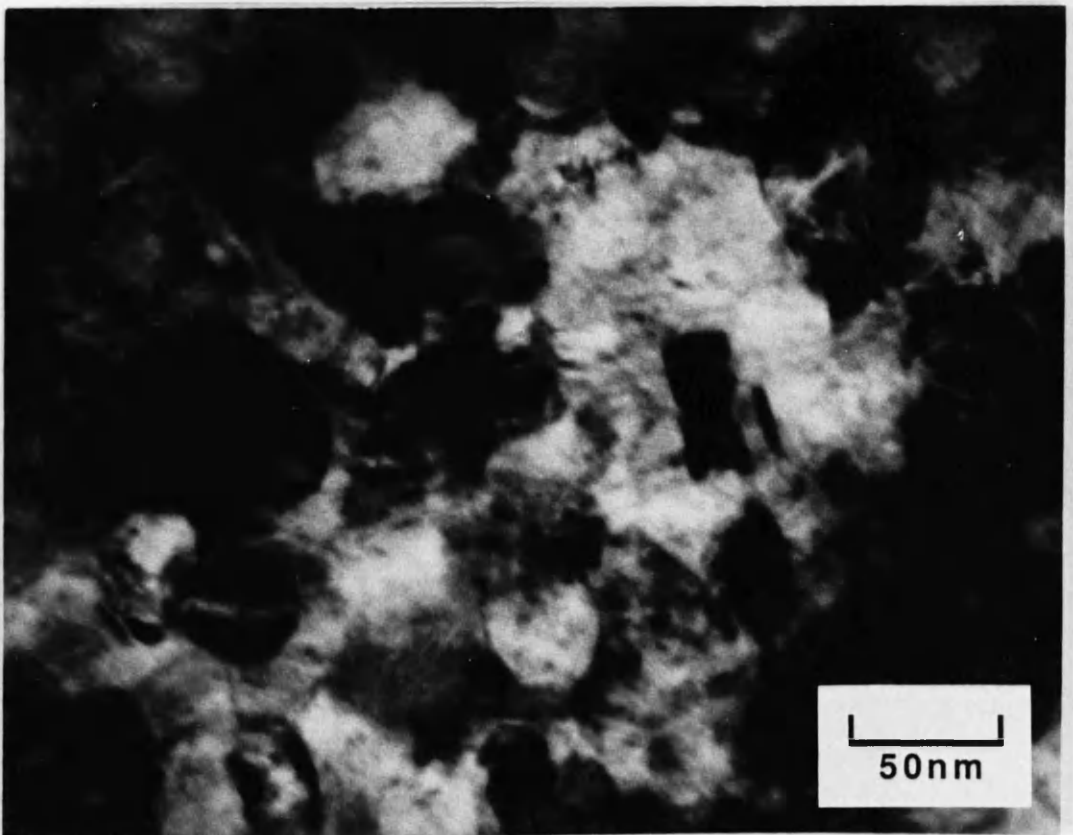


Figure 4.5 CTEM BF image of typical area in the low Ts film deposited directly onto PET.

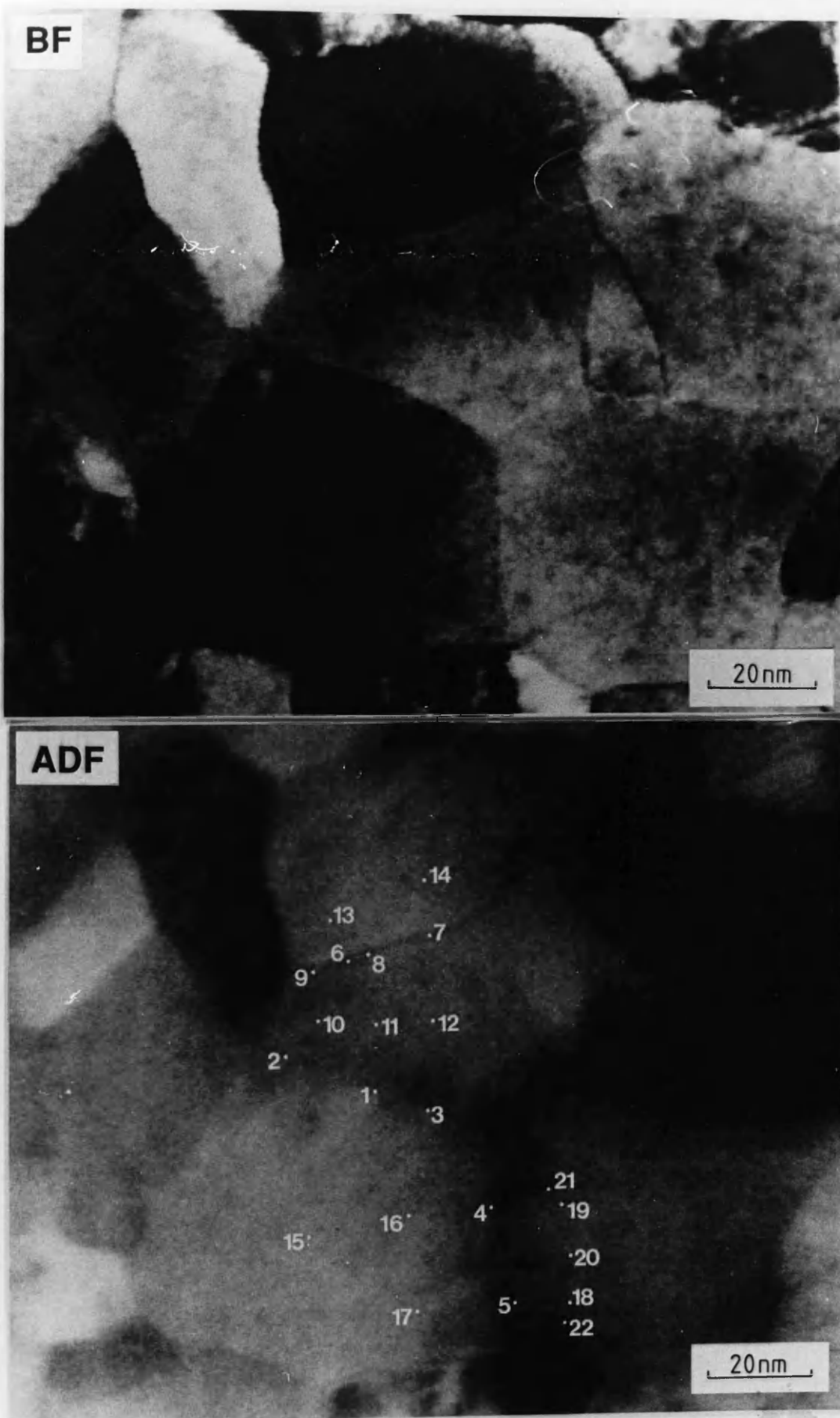


Figure 4.6

STEM BF image and corresponding ADF image of typical area analysed in the high Ts film deposited directly onto PET.

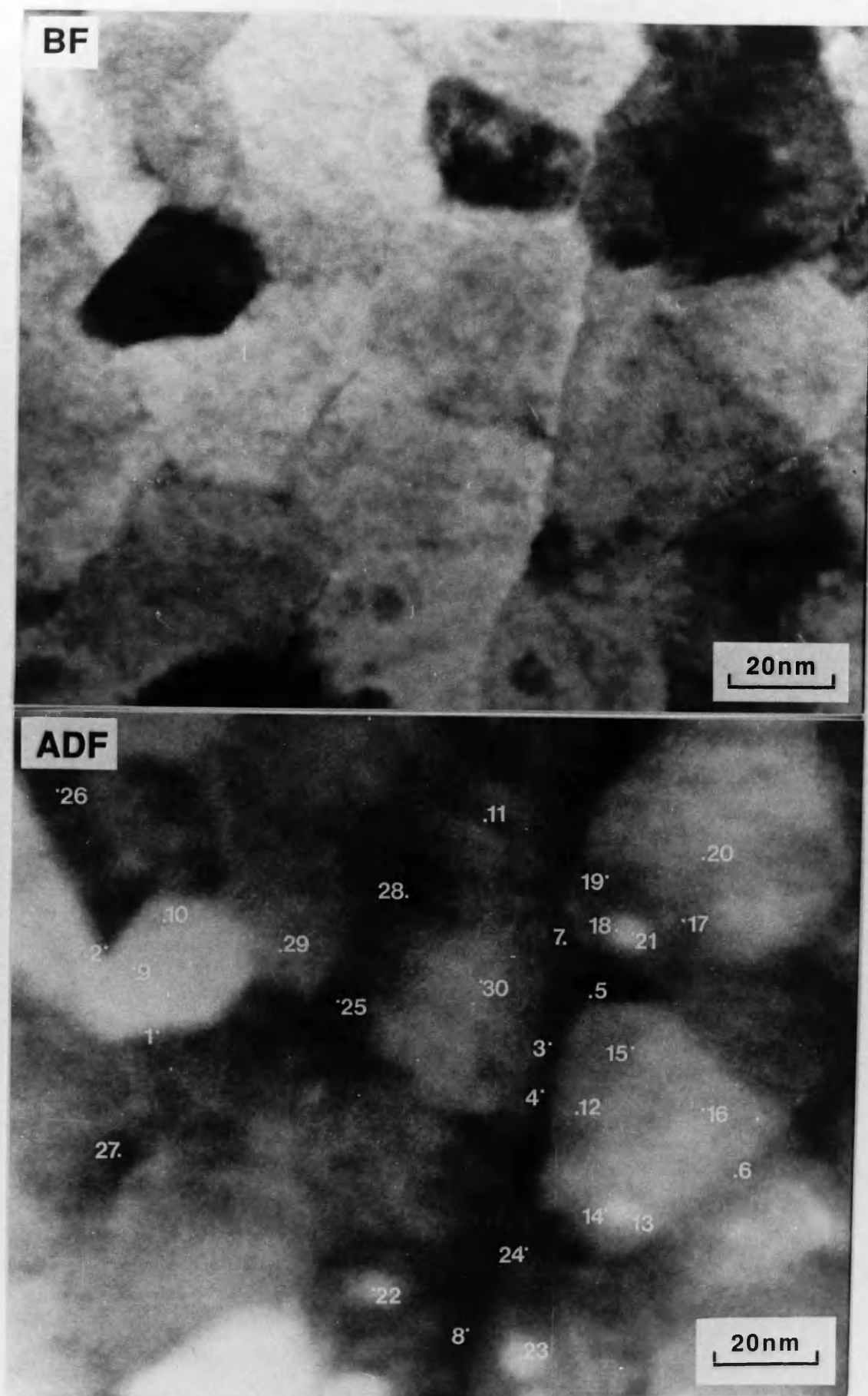


Figure 4.7

STEM BF image and corresponding ADF image of typical area analysed in the low T_s film deposited directly onto PET.

estimated to be between 1 and 6nm wide for both films. This range of values reflects the difficulty in determining the true extent of the boundary region. In total 7 distinct areas were investigated and over 250 spectra were recorded.

In addition to Co and Cr some of these spectra contained Fe, Si and Ar peaks. The origin of each of these can be explained thus: the Fe was probably an impurity present during film deposition, the Si peak was probably due to either Si pump oil present in the ion-mill vacuum or fluorescence of a "dead" layer of Si at the surface of the detector crystal and the Ar could have been an artefact of the ion-milling process.

Figure 4.8 shows histograms of the Co/Cr $K\alpha$ count ratio measured in the low and high T_s films. From these it can be seen that for the low T_s film the distributions with the probe centred on the boundaries and within the columns are very similar, the mean ratios and associated standard errors being 3.33 ± 0.02 and 3.41 ± 0.03 . The corresponding ratio for the overall area was 3.40 ± 0.03 . Thus, no significant segregation of Cr to the boundaries was observed. By contrast, in the high T_s case the mean Co/Cr ratio for the probe centred on the boundary, 2.50 ± 0.06 , differs greatly from that when it is centred on the columns, 3.34 ± 0.08 . The corresponding ratio for the overall area this time was 3.10 ± 0.04 . This suggests a much enhanced level of Cr at the column boundaries. In addition to this, whilst the spread of the boundary distribution for the high T_s film is similar to the spread of the boundary and column distributions for the low T_s film (≤ 1.2), the spread of the column distribution for the high T_s film is much greater (~ 4).

The difference between the average measured Co to Cr ratios for the areas examined in the two films may arise as the result of a systematic

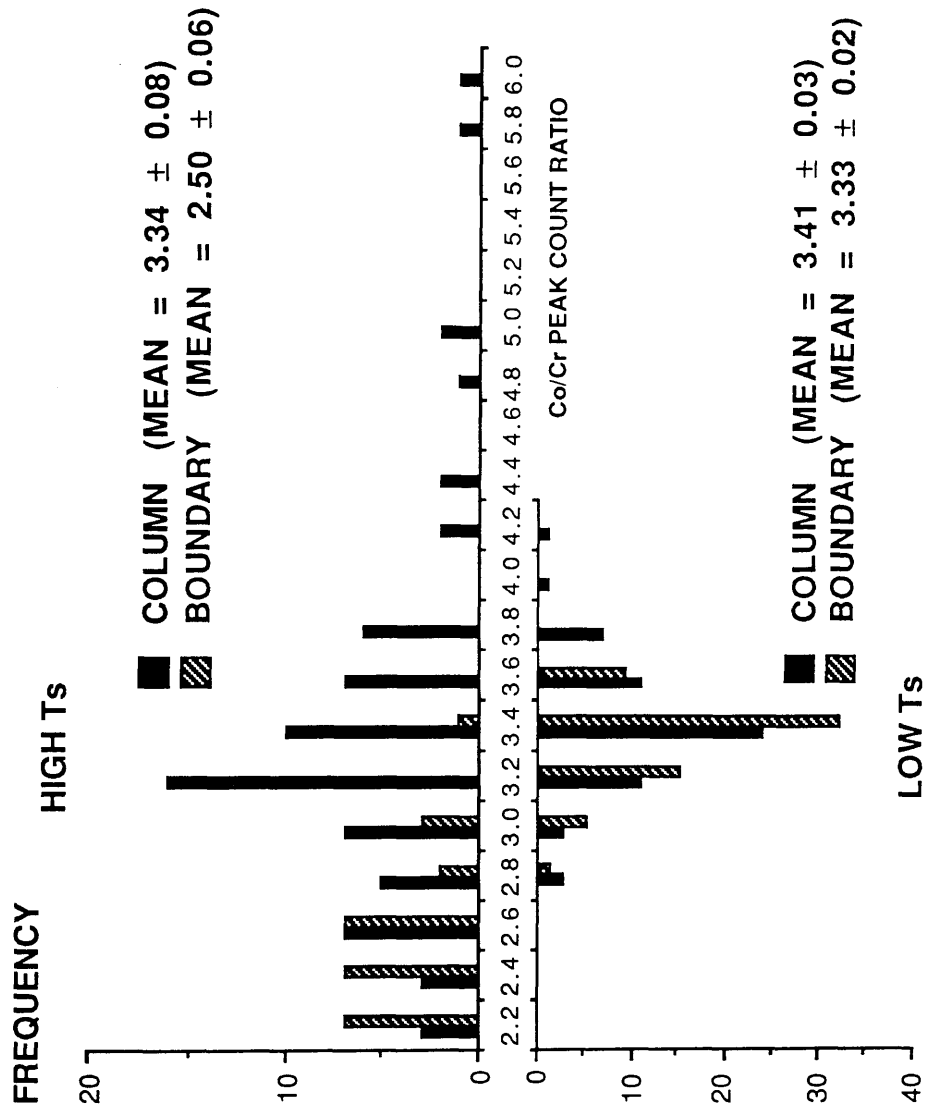


Figure 4.8 Histograms of Co/Cr K α count ratios for boundaries and columns in both the low and high Ts films deposited directly onto PET.

error in the method with which areas were selected for examination. Although the utmost care was taken to analyse areas representative of the film as a whole, local regions of film were selected in which the columns and column boundaries could be easily distinguished. In this ADF imaging mode the sensitivity of the contrast to atomic number, combined with the boundary segregation of Cr, could have meant that in the high T_s film areas were inadvertently chosen for which the average level of Cr was higher than that for the film as a whole. This, however, was not the case in the low T_s film since no significant level of Cr segregation to the column boundaries was evident.

To understand the implications of a given level of Cr segregation for the magnetic properties of the films it was necessary to convert the figures for the Co/Cr $K\alpha$ count ratio to values for the atomic fraction of Cr, X (referring, as before, to the composition expressed as $Co_{100-X}Cr_X$). This was performed using the procedure explained in section 4.2 and mean values of X for the boundaries, columns and overall area of each film are given in table 4.2. It should be noted that any error in the generation factor used to calculate these values affects all the results in the same way and as such it is a systematic error. Thus the percentage differences between results pertaining to boundaries and columns remain unchanged from the values given in figure 4.8. The total systematic error in the resulting value for X was estimated to be $< \pm 1$.

To investigate the possibility of the measured Co/Cr ratio varying with specimen thickness, the total numbers of Co and Cr $K\alpha$ peak counts were divided by the corresponding current detected on the VOA (a fixed fraction of the incident beam current, generally of the order of 100nA). Plots were then made of {Co $K\alpha$ peak counts} / {VOA current} against {Cr $K\alpha$ peak counts} / {VOA current}. Figures 4.9

<div>SAMPLE REGION</div>	HIGH Ts (NO Ge)	LOW Ts (NO Ge)
AREA	23.1 ± 0.3	21.5 ± 0.2
COLUMN	21.8 ± 0.6	21.4 ± 0.2
BOUNDARY	27.1 ± 0.7	21.8 ± 0.1

Table 4.2 Mean atomic fraction of Cr measured
for regions in low and high Ts films
deposited directly onto PET.

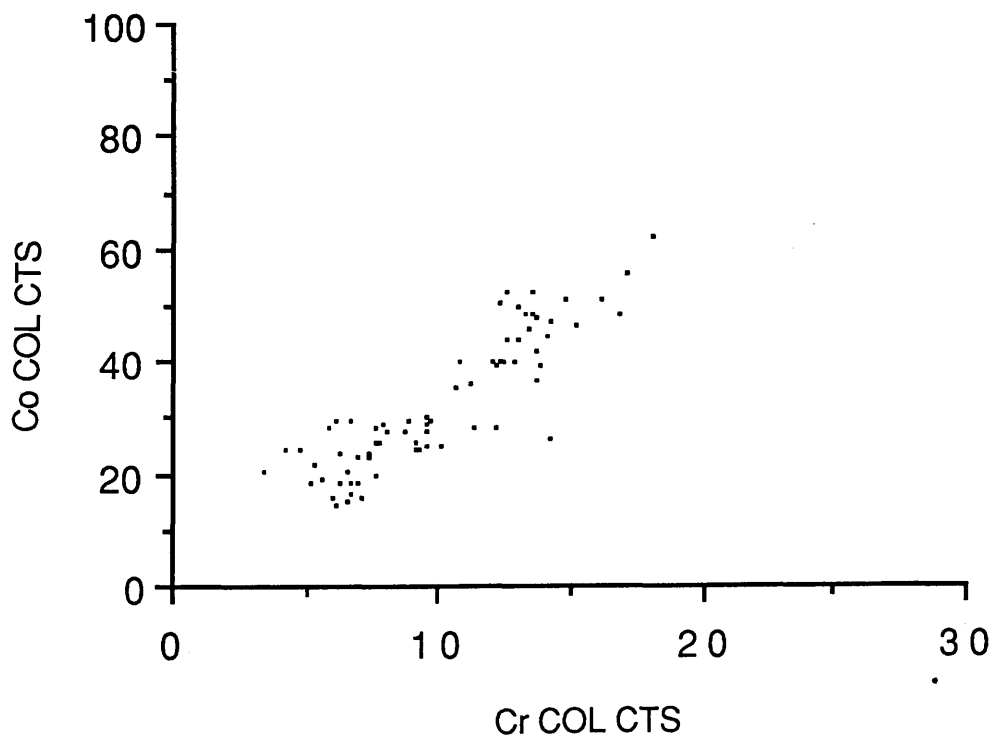
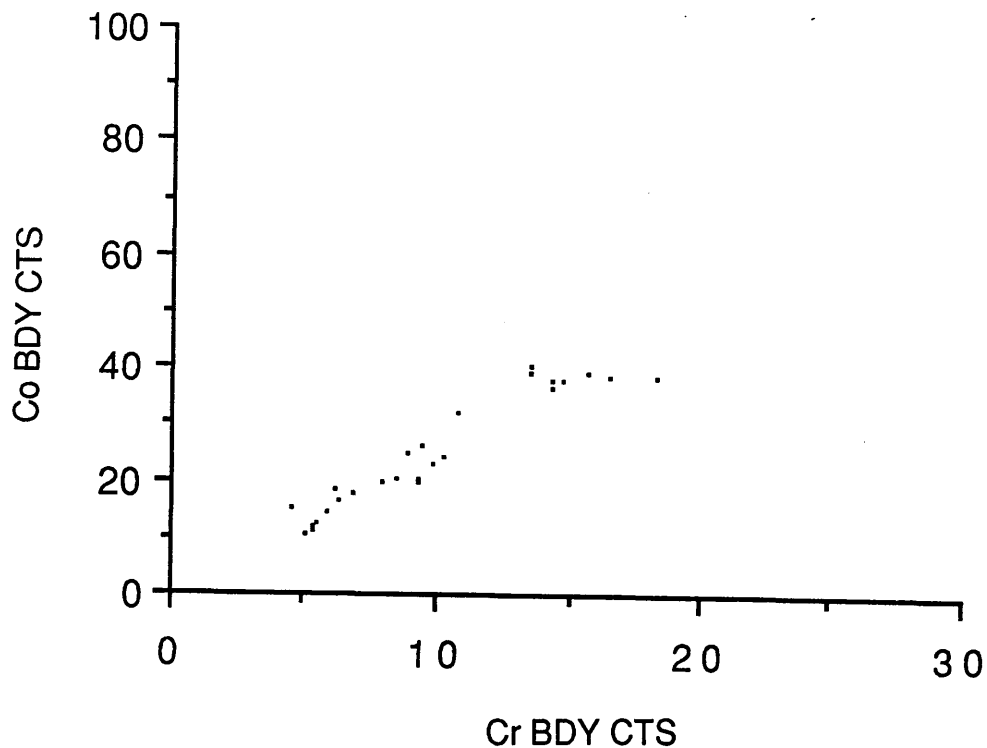


Figure 4.9 $\{\text{Co K}\alpha \text{ counts}\}/\{\text{VOA current}\}$ plotted against $\{\text{Cr K}\alpha \text{ counts}\}/\{\text{VOA current}\}$ for boundaries and columns in the high T_s film deposited directly onto PET.

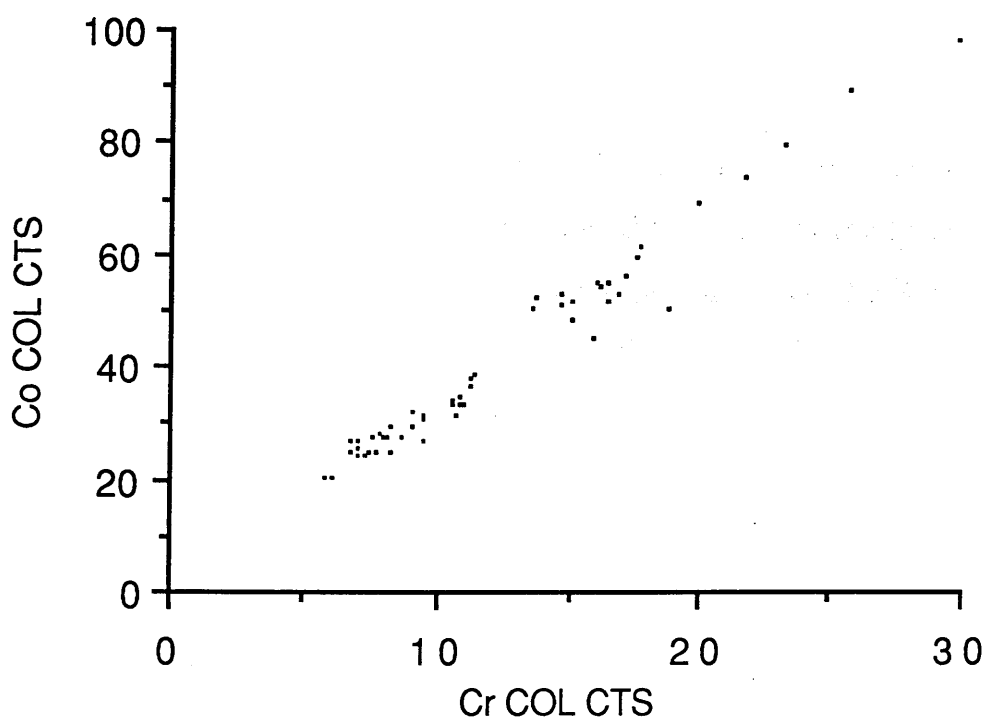
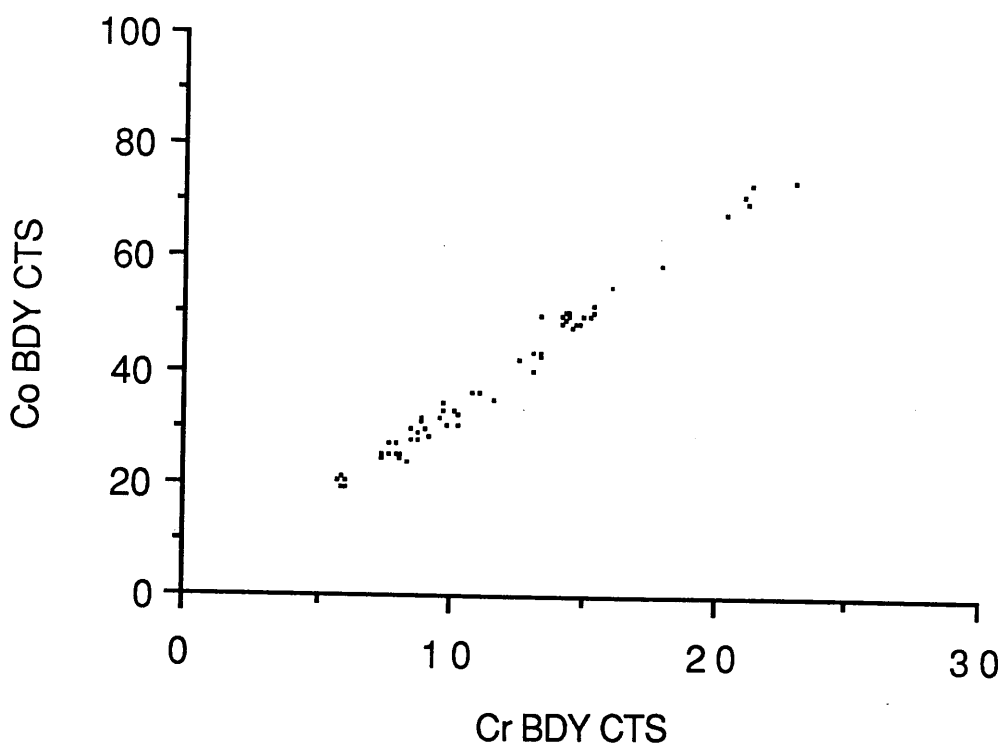


Figure 4.10 $\{\text{Co K}\alpha \text{ counts}\}/\{\text{VOA current}\}$ plotted against $\{\text{Cr K}\alpha \text{ counts}\}/\{\text{VOA current}\}$ for boundaries and columns in the low T_s film deposited directly onto PET.

and 4.10 show these plots for spectra from both the high and low Ts films. From these graphs it can be seen that a linear fit is appropriate over the full range of the distribution. This justifies the averaging of the Co/Cr count ratio over all thicknesses examined. A least squares fit confirmed the validity of this approach with correlation coefficients, R , of 0.99 for both columns and boundaries in the low Ts film and 0.96 and 0.89 respectively for the boundaries and columns in the high Ts film. These figures again emphasise that for the high Ts film there was a generally greater spread of results from the linear fit than in the low Ts film, with a noticeably poorer fit for the high Ts columns.

From figures 4.9 and 4.10 it can also be seen that the spread of the distributions for the thinnest areas of specimen was greater than that for thicker areas. To investigate this, the effect of random fluctuations in the numbers of atoms in the volume excited by the beam on the spread of these distributions was considered. The numbers of atoms in the volume excited by the beam were estimated from the numbers of counts in the $K\alpha$ peaks using the approach employed to calculate the thickness of film in section 4.3.2. For the thinnest regions analysed the $K\alpha$ peak counts corresponded to numbers of Co and Cr atoms of approximately 6.9×10^4 and 2.0×10^3 respectively. Random errors in these numbers led to an uncertainty in the Co/Cr ratio of 0.8%. For the thicker regions of specimen the numbers of Co and Cr atoms in the excited volume were estimated to be 4.8×10^6 and 1.4×10^5 respectively, giving an uncertainty in the ratio of 0.1%. The increase in the spread in the distributions in figures 4.9 and 4.10 due to random fluctuations in the numbers of atoms in the excited volume was therefore much smaller than that attributable to random fluctuations in the number of counts (see section 4.3.2).

From figures 4.9 and 4.10 it is possible to make an estimate of the

range of compositions detected for a given region. This can be done by calculating the gradients of the lines forming an "envelope" enclosing the spread of the points and comparing them with the range of gradients predicted by random errors in the numbers of counts. For both the columns and boundaries in the low Ts film such envelopes gave bounds for the variation in X of ± 0.3 whilst the variation in X, from the range of gradients calculated from the random error in the number of counts, was ± 0.2 . For the high Ts film column and boundary regions the envelopes gave variations in X of ± 1.7 and ± 1.2 respectively whilst random variations in the numbers of counts again predicted bounds of ± 0.2 for both.

4.3.4 Discussion & Conclusions

In the low Ts film the local composition distributions measured at the boundaries and within the columns did not differ significantly. For the areas of film analysed no dependence of the local composition on the thickness of specimen was observed. Compositional variations were similar for both columns and boundaries with variations in atomic fraction only slightly greater than could be accounted for by random errors in the x-ray counts. Thus the film showed a high degree of compositional homogeneity and the results were consistent with there being exchange coupling at column boundaries throughout the film. This in turn is in accord with the low perpendicular coercivity and with stripe domains being supported in a magnetised sample.

For the high Ts film the mean level of Cr measured in the columns did not differ significantly from that for the overall film. The compositions measured at the boundaries, however, revealed a mean

increase in X of 4. For the areas of film analysed no dependence of the local composition on the thickness of specimen was observed. Compositional variations were generally higher than for the low T_s film with variations in atomic fraction for the boundaries and columns approximately 9 and 6 times greater, respectively, than could be accounted for by random errors in the x-ray counts.

By contrast with the low T_s film therefore the high T_s film was found to be markedly inhomogeneous with appreciable composition variations within the columns and significant Cr enrichment at the boundaries. The latter is consistent with magnetic measurements (Sugita et al. 1981, Smits et al. 1983) and magnetisation reversal models (Ouchi et al. 1987). An increase in X of this magnitude would be expected to have a substantial effect on the local magnetic properties and would probably be sufficient (Sugita et al. 1981, Bolzoni et al. 1983, Grundy & Ali 1983, Andra & Danan 1987) to introduce a predominantly non-magnetic layer between columns. In any event the exchange coupling would be substantially reduced so that columns would to a much greater extent be independent magnetic units. This is consistent with the much higher perpendicular coercivity observed in such films and with the lower noise observed in recording experiments for layers deposited at higher T_s (Luitjens et al. 1988).

4.4 INVESTIGATION OF THE EFFECT OF A Ge UNDERLAYER ON LOCAL COMPOSITION

Another very important parameter in influencing the physical and magnetic properties of a CoCr thin film is the use of a Ge underlayer.

As mentioned in chapter 1 such an underlayer is seen to induce columnar growth in the CoCr film earlier in the deposition process, thereby reducing the extent of the disordered region at the base of the grains. Measurements of bulk properties show that films with a Ge underlayer have a higher perpendicular anisotropy and a smaller average $\Delta\theta_{50}$ than those deposited directly onto a substrate. For these films an elevated substrate temperature during deposition was again seen to improve the perpendicular coercivity. A study was therefore proposed to investigate the local elemental segregation in CoCr layers deposited at different substrate temperatures onto a Ge underlayer.

4.4.1 Experiment

A layer of Ge 400nm thick was rf sputter deposited onto a PET substrate. 400nm thick CoCr layers were deposited onto the Ge at initial substrate temperatures of 60C (low Ts) and 200C (high Ts) and with all other conditions identical to those used for the direct deposition onto the substrate described in the previous section.[†] VSM measurements showed the high Ts film to have a mean volume perpendicular H_c of 70kA.m⁻¹ whilst for the low Ts film a mean value of 20kA.m⁻¹ was recorded. All EDX microanalysis was again conducted in the STEM using the same method and operating conditions as in section 4.3. For count times of 20s, in spectra for the column and boundary regions, the number of counts in the Cr K α peak varied between \simeq 400 and 2000 counts and the number of counts in the Co K α peak varied between \simeq 1500 and 7500 counts. This led to an inherent random error in the Co/Cr count ratio of between 2.5 and 5.6%. Additionally, this variation in number of counts corresponded to a similar range of specimen thicknesses, and therefore a similar range of resolutions to that estimated for the specimens

†The marked difference between the microstructure for the high T_s film on Ge and that for both the low T_s film on Ge and the films deposited directly onto PET is probably partly attributable to the higher temperature at which this film was deposited.

analysed in section 4.3.

4.4.2 Results

CTEM studies revealed a physical microstructure in the low Ts films with column definition not quite as distinct as that observed in the high Ts film deposited directly onto the substrate (figure 4.11). The mean column diameter was estimated to be between 40 and 50nm. The film deposited at high Ts showed a microstructure with much poorer column definition and in which there were small regions, or elongated "spots", of bright contrast randomly distributed across the columnar structure (figure 4.12).[†] Mean column diameter for this film was also estimated to be between 40 and 50nm and the spots had dimensions between approximately 3 x 5nm and 5 x 20nm.

Using the same technique as in the previous section compositional analyses were again taken with the probe centred on boundaries and within columns. In addition to the impurities observed in films investigated in section 4.3, Ge was observed in the EDX spectra for these films. This can be attributed to small amounts of Ge from the underlayer remaining in the film after thinning. Typical annotated STEM ADF and corresponding BF images for both films are shown in figures 4.13 and 4.14. From such images the width of the boundary was estimated to be between 1 and 6nm for both films.

Histograms of the Co/Cr K α count ratio for columns and boundaries in the high and low Ts films deposited on Ge are shown in figure 4.15. In all 14 distinct areas (again $\simeq 1\mu\text{m}^2$) were investigated and over 380 spectra were recorded. For the low Ts film the mean ratios and associated standard errors for the probe positioned on boundary regions

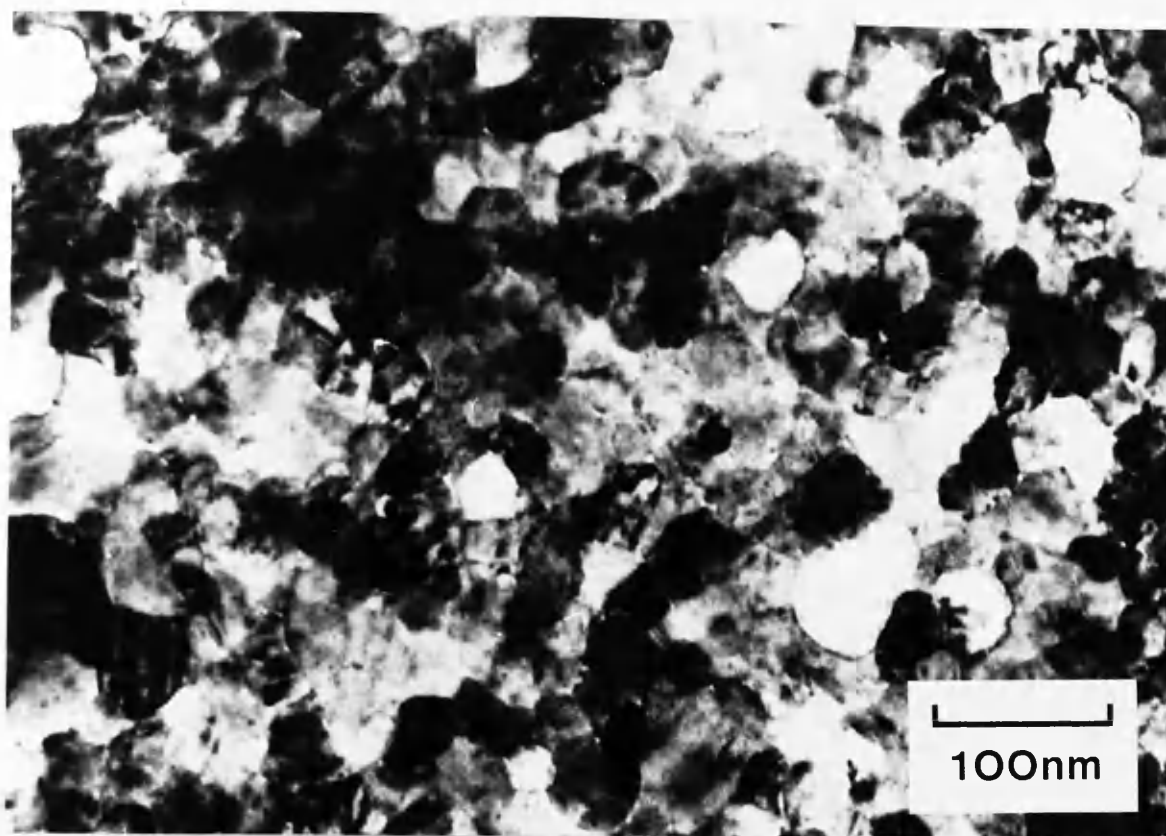


Figure 4.11 CTEM BF image of typical area in the low Ts film deposited onto Ge.

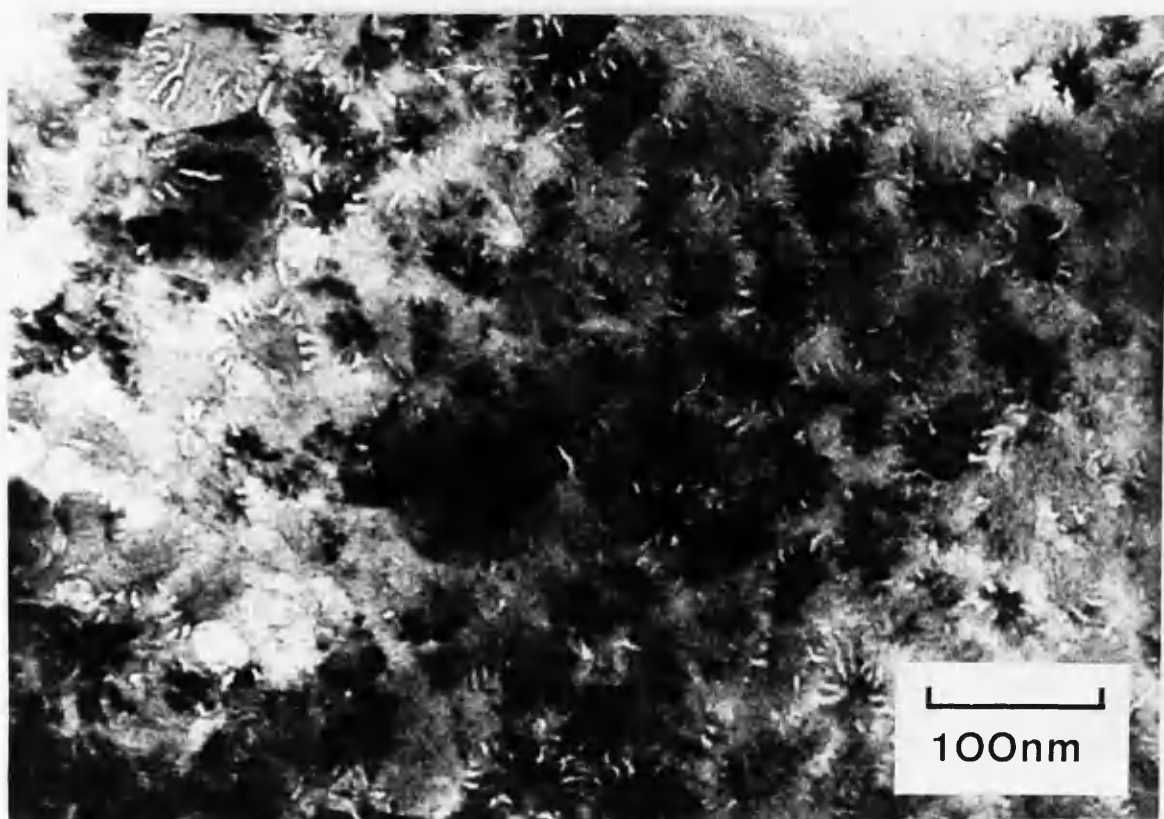


Figure 4.12 CTEM BF image of typical area in the high Ts film deposited onto Ge.

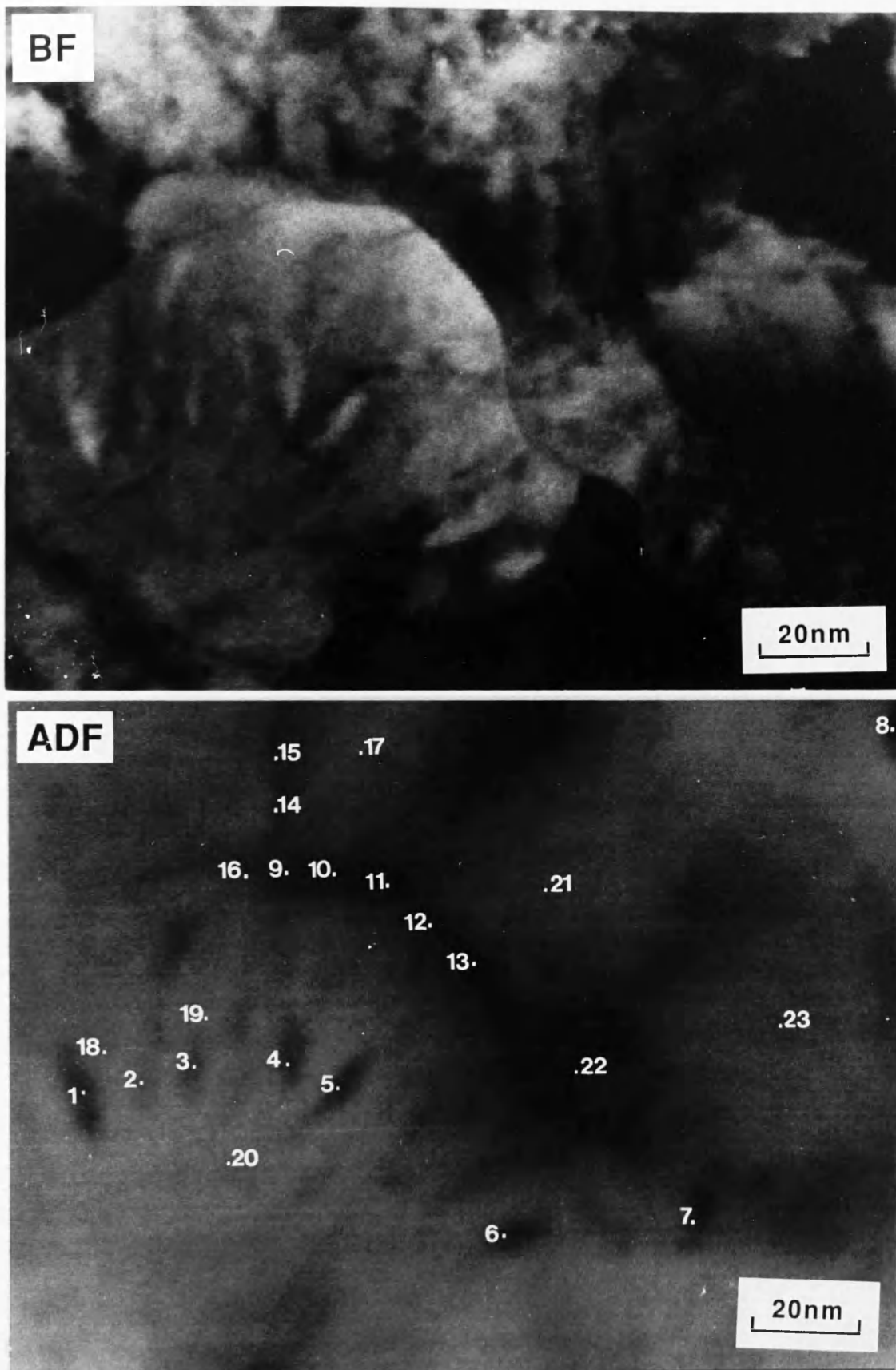


Figure 4.13 STEM BF image and corresponding ADF image of typical area analysed in the high Ts film deposited onto Ge.

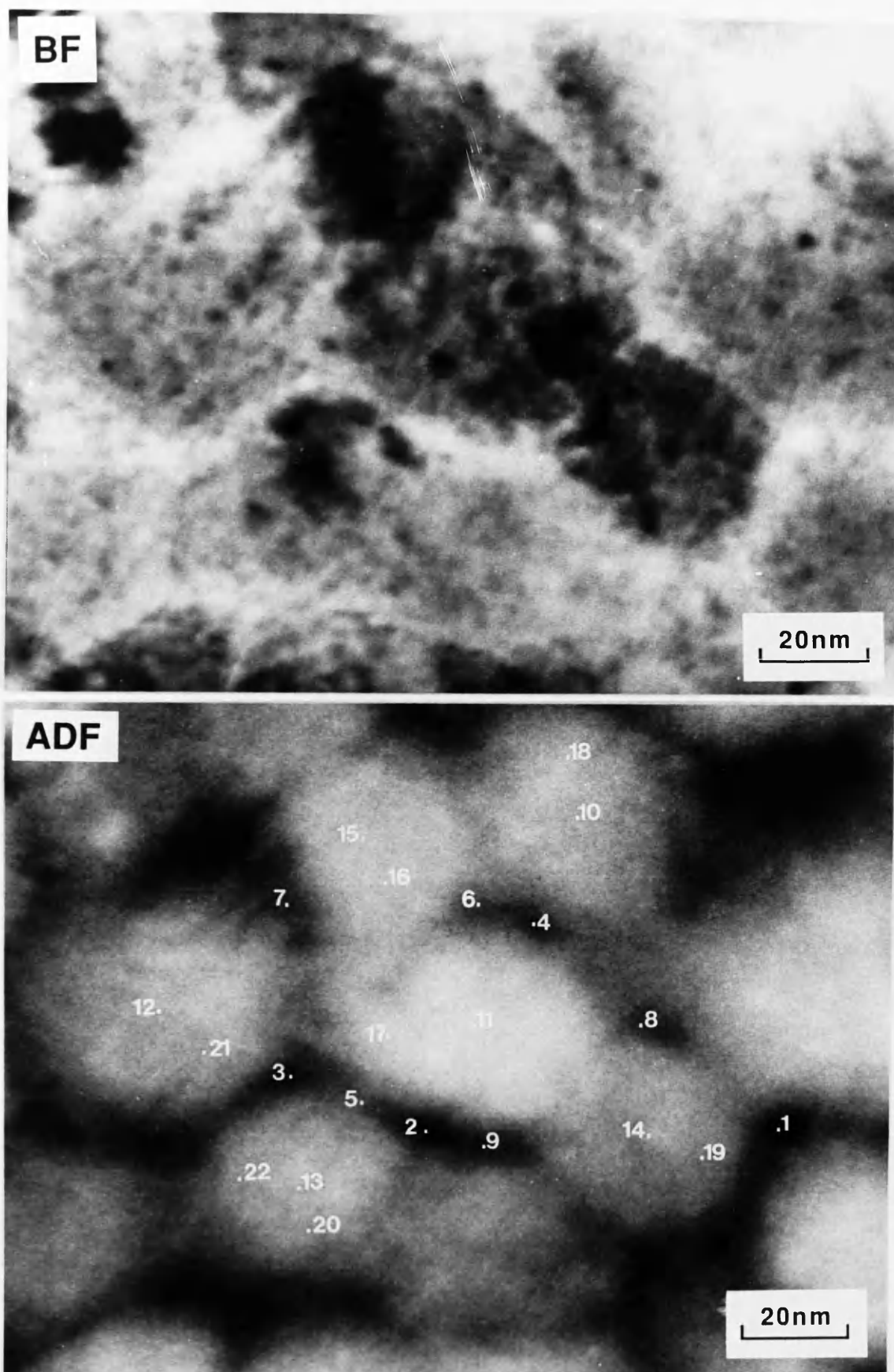


Figure 4.14 STEM BF image and corresponding ADF image of typical area analysed in the low T_s film deposited onto Ge.

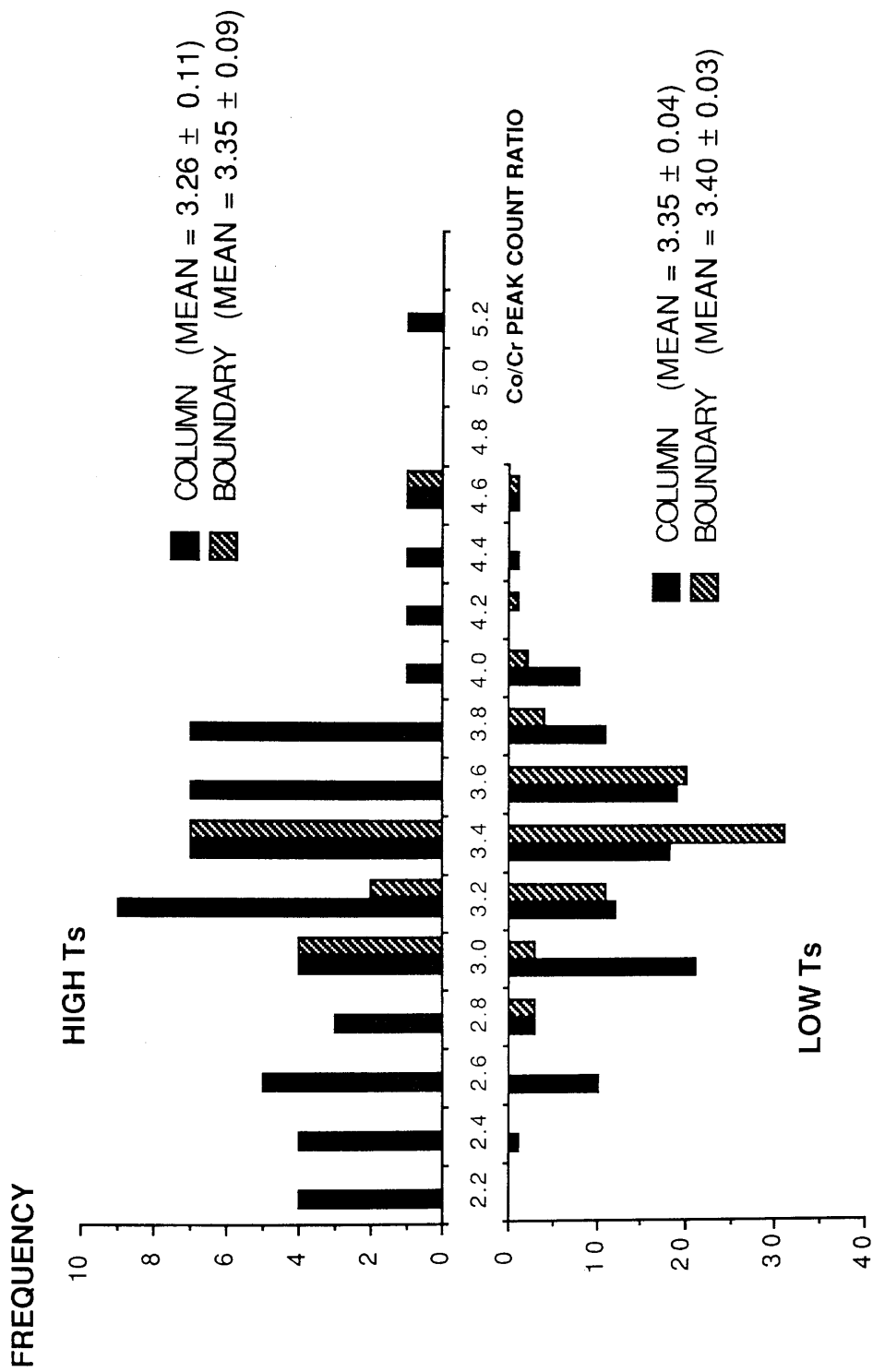


Figure 4.15 Histograms of Co/Cr $K\alpha$ count ratios for boundaries and columns in both the high and low Ts films deposited onto Ge.

and within columns were 3.40 ± 0.03 and 3.35 ± 0.04 respectively with an average for the general areas analysed of 3.49 ± 0.04 . The corresponding mean boundary and column ratios (avoiding bright spots) for the high Ts film were 3.35 ± 0.09 and 3.26 ± 0.11 respectively with an overall area mean of 3.41 ± 0.03 . Thus it can be seen that there was no pronounced boundary segregation of Cr for either film and in the case of the high Ts film the width of the column distribution was larger than that of the low Ts film on Ge (a spread $\simeq 3$ as opposed to a spread $\simeq 2$). The Co/Cr $K\alpha$ count ratio histogram for spectra acquired with the probe positioned on the bright "spots" of the high Ts film is shown in figure 4.16. This graph shows a more variation in the Co/Cr $K\alpha$ count ratio (spread $\simeq 5$), than the high Ts histogram in figure 4.15, with a mean and associated standard error of 3.10 ± 0.17 . The reduced number of counts in the spectra for these regions indicated that they were, in general, thinner than the rest of the specimen with the random error in the Co/Cr $K\alpha$ count ratio varying between 3.0 and 8.0% (spectra for many of the spots had too small a number of counts to be included). The figures for the mean Co/Cr $K\alpha$ count ratios were converted to values for the mean atomic fraction of Cr (see section 4.2.2). These are given in table 4.3 for the boundaries, columns and overall area in both films and the bright spots in the high Ts film.

Any dependence of the ratios on film thickness was investigated by graphing $\{\text{Co } K\alpha \text{ peak counts}\}/\{\text{VOA current}\}$ against $\{\text{Cr } K\alpha \text{ peak counts}\}/\{\text{VOA current}\}$. The plots for the columns and boundaries in both films and for bright spots in the high Ts films are shown in figures 4.17-4.19. For these figures it can be seen that a linear fit is appropriate over the full range of the distribution. This again confirms the validity of taking an average of the Co/Cr count ratio over all thicknesses

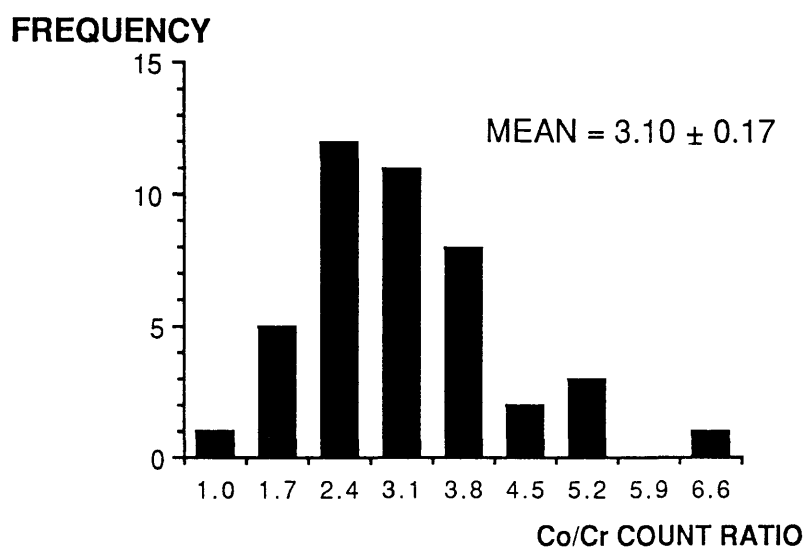


Figure 4.16 Histogram of Co/Cr K α count ratios for bright spots in the high Ts film deposited onto Ge.

SAMPLE REGION	HIGH Ts (ON Ge)	LOW Ts (ON Ge)
AREA	21.4 ± 0.2	21.0 ± 0.2
COLUMN	22.2 ± 0.7	21.7 ± 0.3
BOUNDARY	21.7 ± 0.6	21.5 ± 0.2
COLUMN CENTRE		24.1 ± 0.6
GENERAL COLUMN		20.1 ± 0.5
BRIGHT SPOTS	23.1 ± 1.3	

Table 4.3 Mean atomic fraction of Cr measured for regions in the low and high Ts films deposited onto Ge.

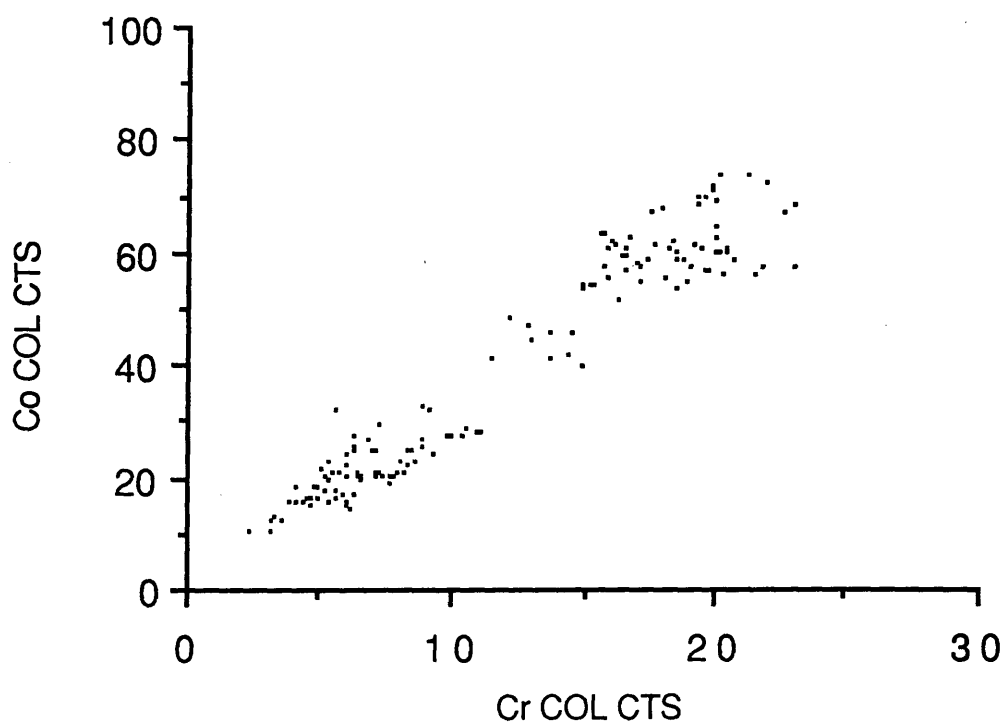
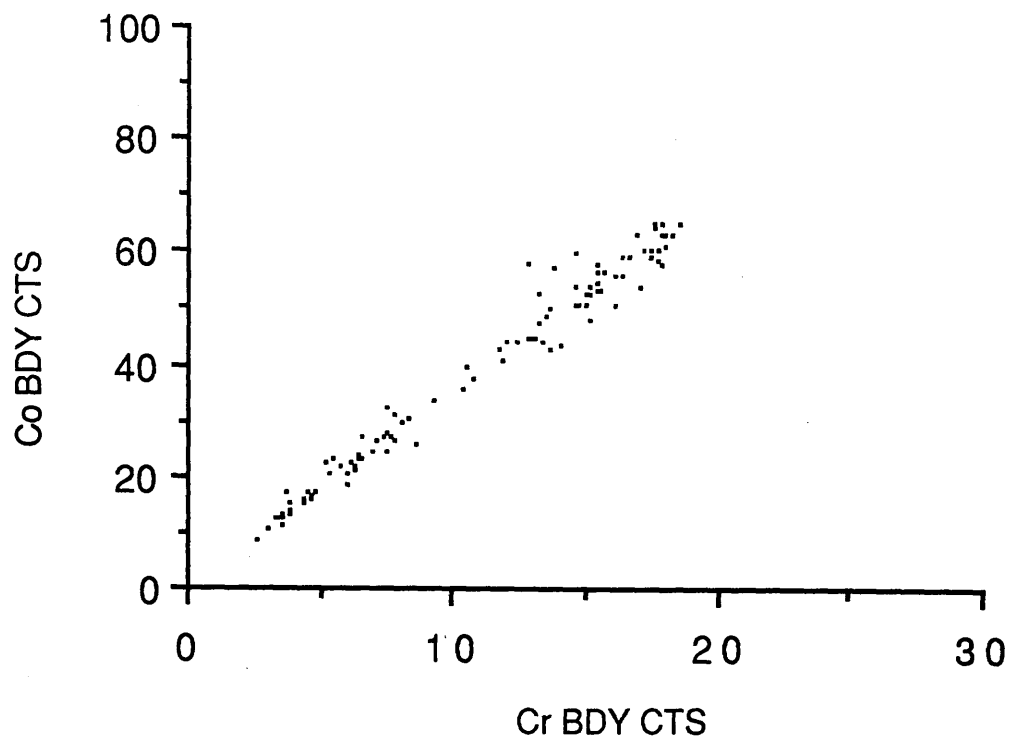


Figure 4.17 $\{\text{Co K}\alpha \text{ counts}\}/\{\text{VOA current}\}$ plotted against $\{\text{Cr K}\alpha \text{ counts}\}/\{\text{VOA current}\}$ for boundaries and columns in the low T_s film deposited onto Ge.

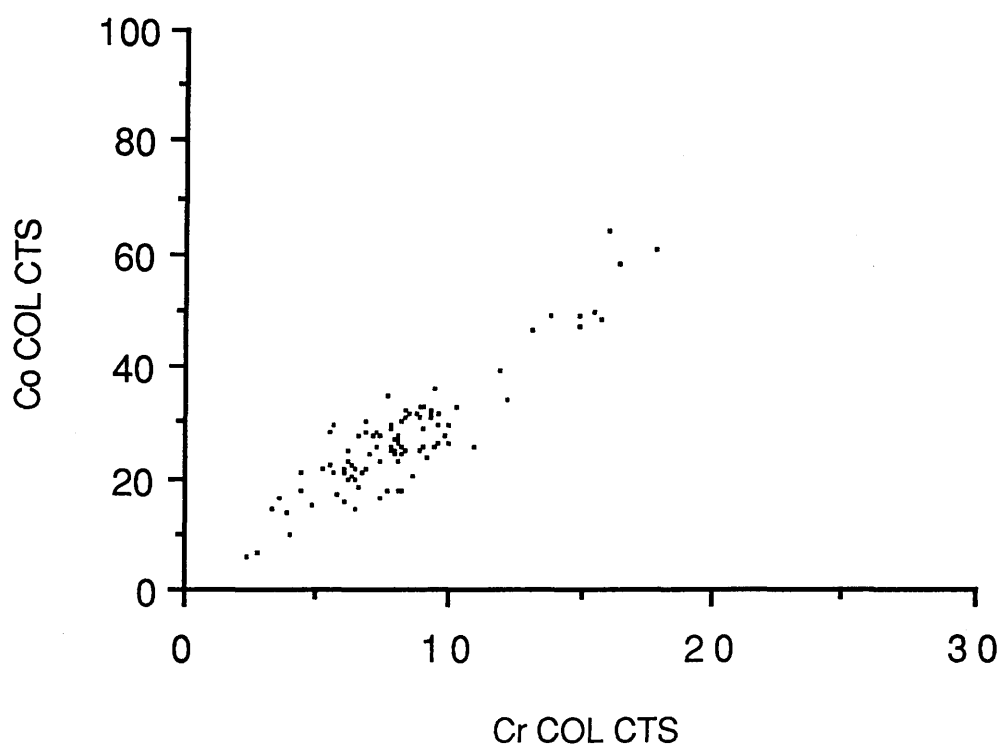
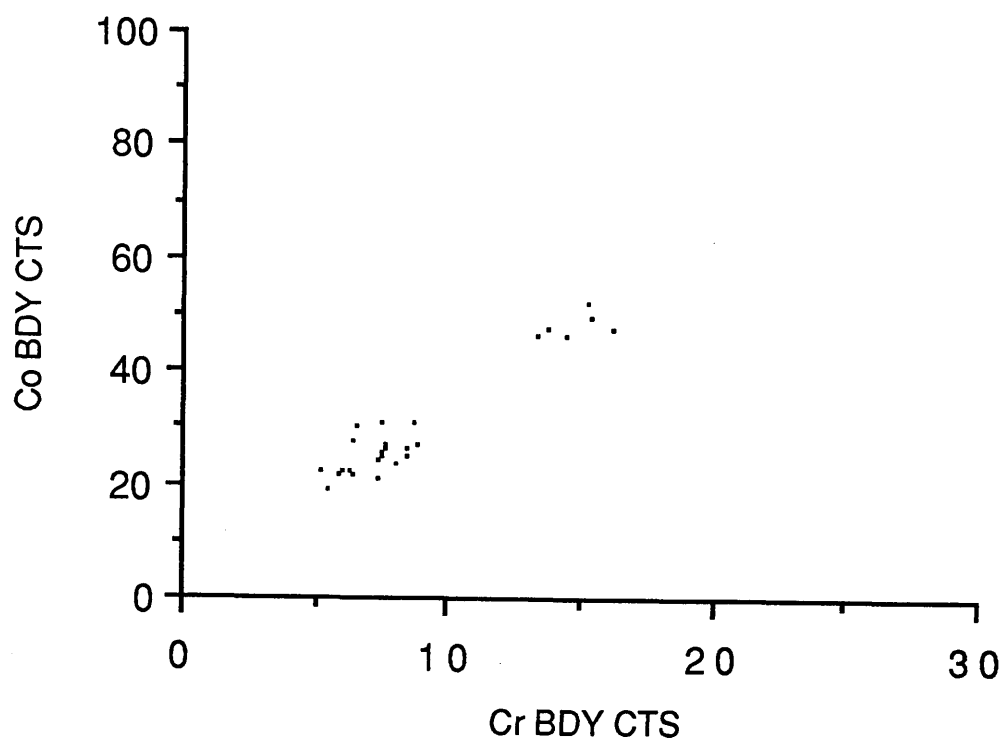


Figure 4.18 $\{Co\ K\alpha\ counts\}/\{VOA\ current\}$ plotted against $\{Cr\ K\alpha\ counts\}/\{VOA\ current\}$ for boundaries and columns in the high T_s film deposited onto Ge.

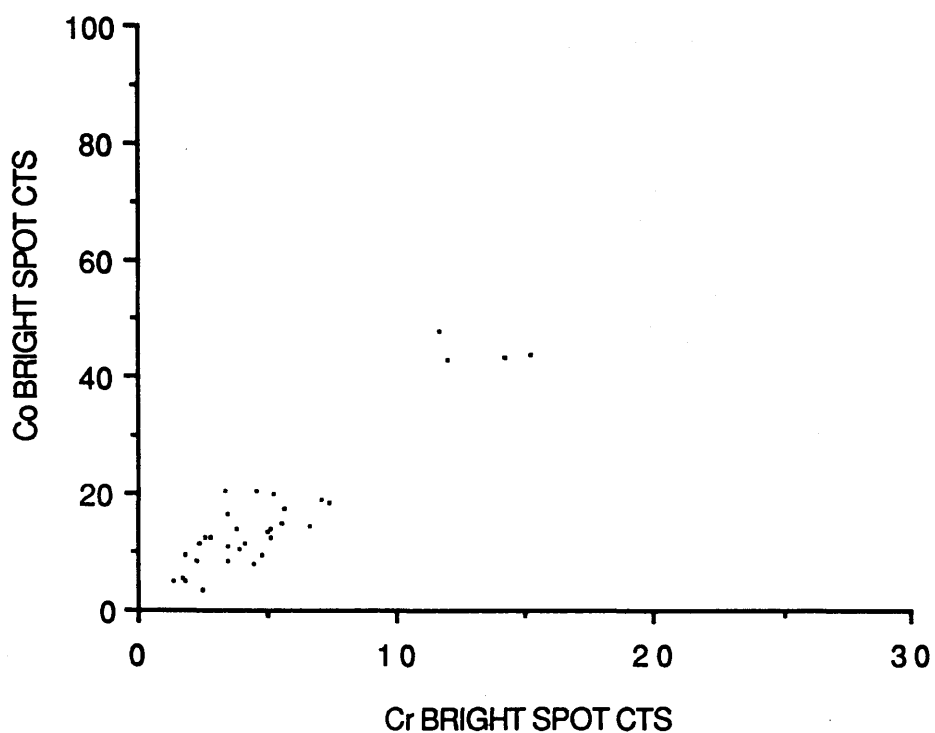


Figure 4.19 $\{\text{Co K}\alpha \text{ counts}\}/\{\text{VOA current}\}$ plotted against $\{\text{Cr K}\alpha \text{ counts}\}/\{\text{VOA current}\}$ for the bright spots in the high Ts film deposited onto Ge.

examined. The correlation coefficients, R values, for the the low Ts columns and boundaries were 0.96 and 0.99 respectively, as compared with column, boundary and bright spot R values of 0.91, 0.96 and 0.92 for the high Ts film. These R values show that the correlation of the data to a linear fit is generally better for the low Ts film (as for direct deposition onto substrate) and that the boundaries have a better fit than the columns.

The extent of compositional inhomogeneity was estimated from the graphs in figures 4.17-4.19 by comparing the range of gradients forming the envelopes for the spread of the distributions with the range predicted by random errors in the number of counts (as in section 4.3.3). For the high Ts film the envelope gave variations in X for the columns and boundaries of ± 0.7 and ± 0.6 respectively, whilst the random variations in the number of counts predicted variations in X of ± 0.2 in both cases. The range of envelope gradients for the columns and boundaries in the low Ts film was ± 0.6 and ± 0.5 respectively whilst the random error predicted a variation in X of ± 0.2 for both. For the bright spots in the high Ts film the envelope was difficult to define because most of the spectra had relatively small numbers of counts resulting in large errors in Co/Cr K α count ratio (see section 4.3.3). Bounds for the variation in X were, however, estimated to give variation in gradient of ± 0.9 with corresponding variation from random error in number of counts of ± 0.3 .

Whilst conducting the microanalysis on the low Ts film it was observed that the minimum Co/Cr K α count ratio corresponded to probe positions close to the column centre. Since this was not investigated explicitly using the above method a further study was made with the probe positioned at what was judged to be the column centres and at other positions within the columns. The histogram presented in

figure 4.20 shows the Co/Cr K α count ratios for column centres and general column positions in the low Ts film. The mean ratios for the probe positioned at centres and at other general positions within the column were 2.93 ± 0.08 and 3.70 ± 0.09 respectively (mean for area = 3.49 ± 0.04). The atomic fractions of Cr corresponding to these values are given in table 4.3. These results indicate a significantly enhanced level of Cr at the column centre relative to the column as a whole in the low Ts film. This would explain the spread of the column distribution being greater than the spread of the boundary distribution in the low Ts histogram shown in figure 4.15.

As presented these results imply that the probe could be correctly positioned at the centre of a given column. The irregularity in the shape of the individual grains, however, meant that in nearly every case designation of a probe position as the column centre was a subjective decision. To overcome this problem spectra were collected with the probe positioned at regular spacings of about 5nm along orthogonal paths across the columns from diametrically opposite points on the boundaries. This technique was used to investigate columns in the low and, for comparison, high Ts films. BF and annotated ADF images of a typical area analysed are shown in figure 4.21. Figure 4.22 shows the corresponding plot of Co/Cr K α count ratios against probe position. Figures 4.23 and 4.24 show similar plots for two other areas examined in the low Ts film. The error bars indicated for the ratios are the random errors calculated from the total number of counts in the peaks. These plots indicate a pattern of segregation in which the column centre has a marked level of Cr enrichment. Moving radially away from the centre, the ratio of Co to Cr ratio increases smoothly out to a band (or ring) in the column between the boundary and centre which is Co rich.

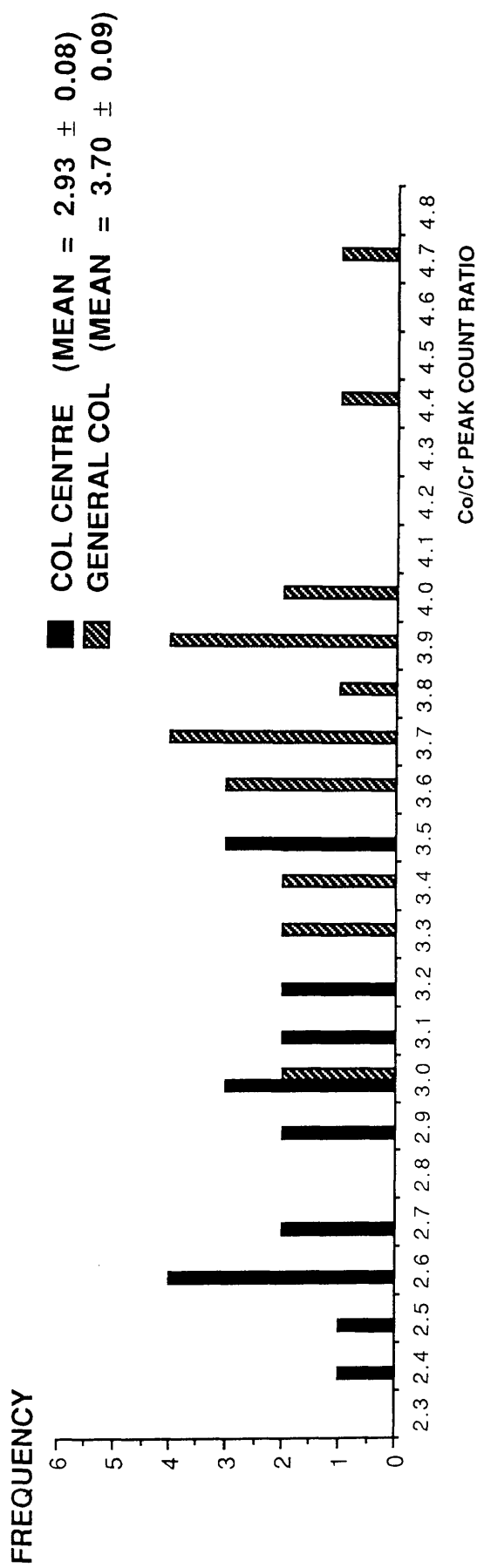


Figure 4.20 Histogram of Co/Cr K α count ratios for column centres and general column positions in the low Ts film deposited onto Ge.

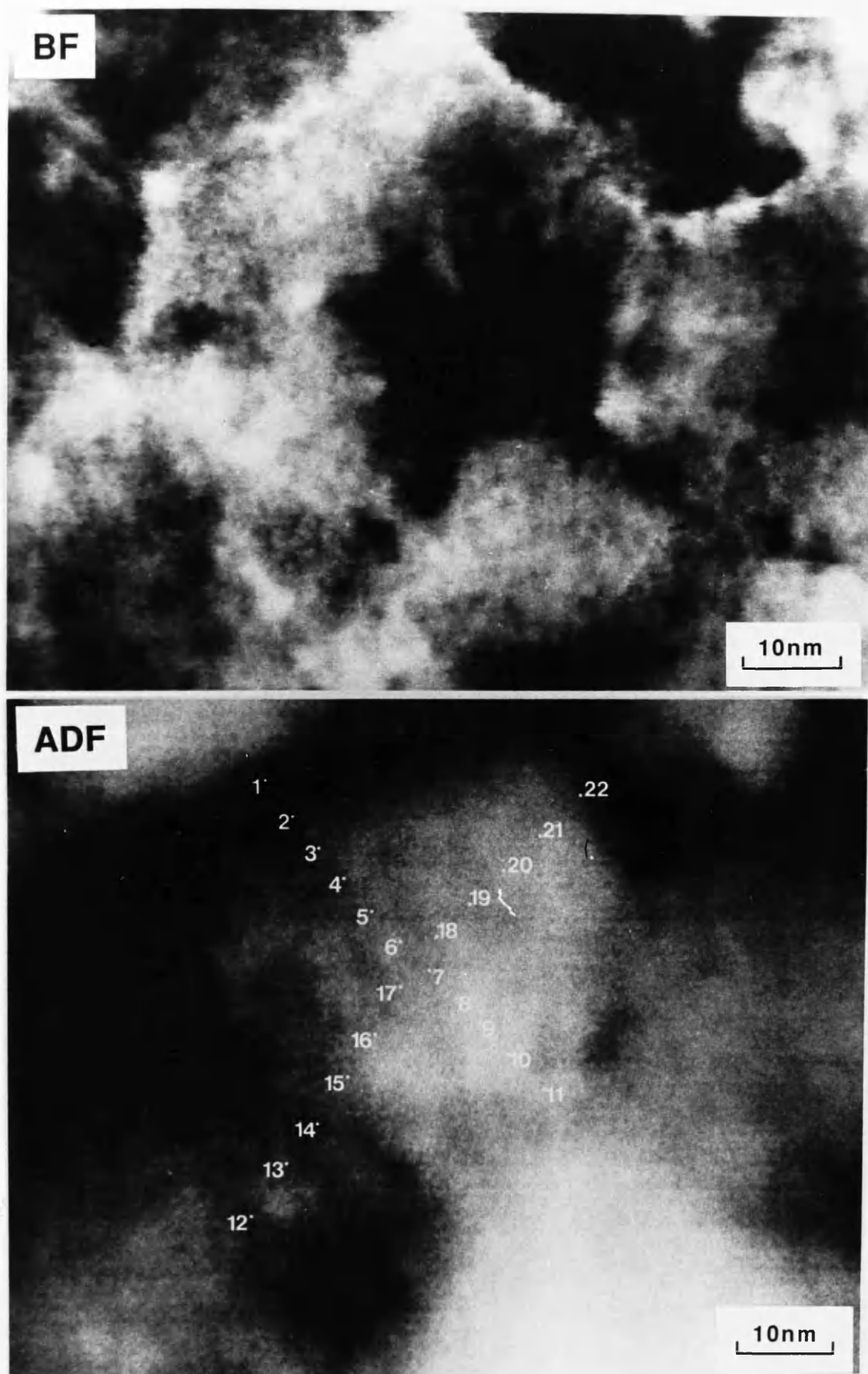


Figure 4.21 STEM BF image and corresponding annotated ADF image of area in low Ts film on Ge showing probe position for orthogonal scans across column.

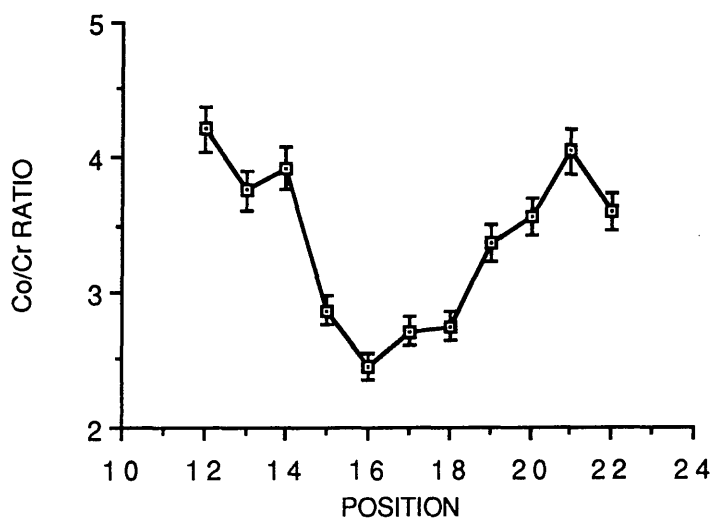
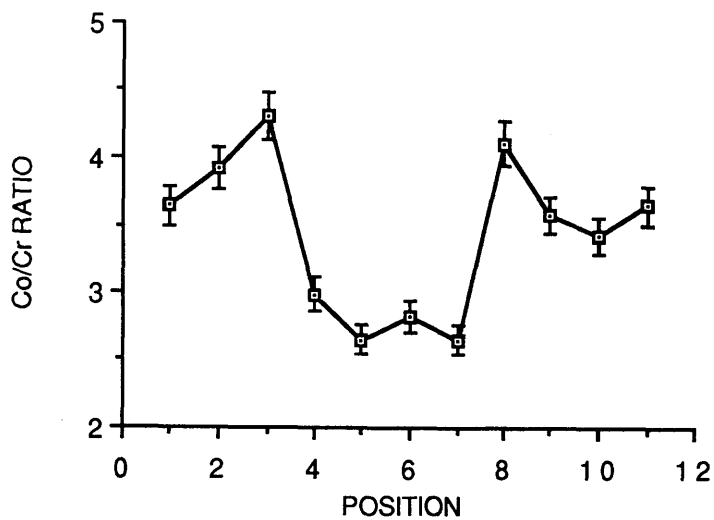


Figure 4.22 Plots of Co/Cr $K\alpha$ count ratios against probe position for orthogonal scans across column in low Ts film on Ge.

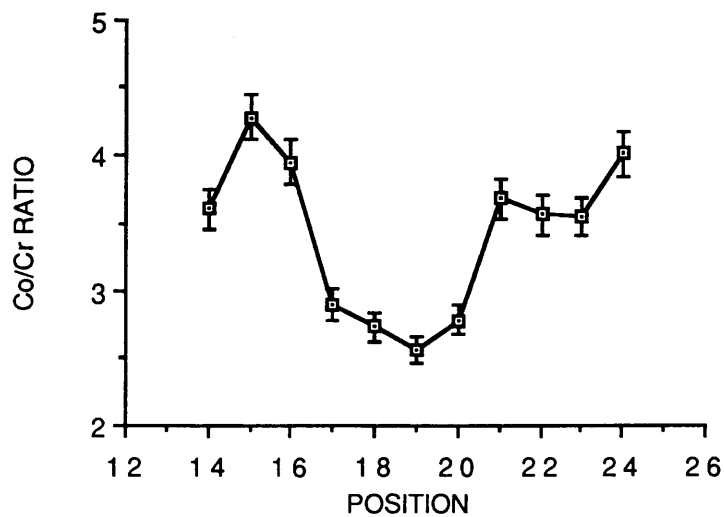
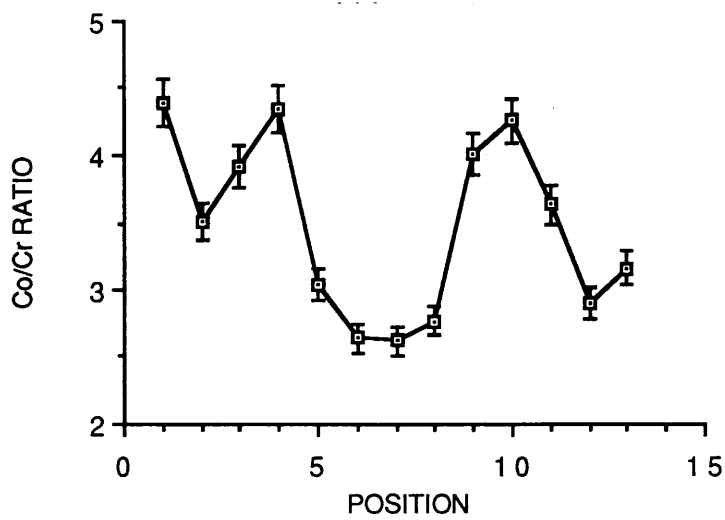


Figure 4.23 Plots of Co/Cr $K\alpha$ count ratios against probe position for orthogonal scans across column in low Ts film on Ge.

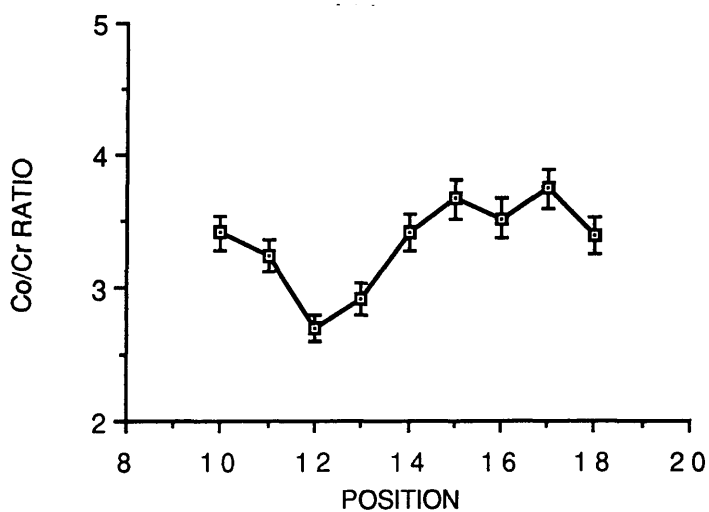
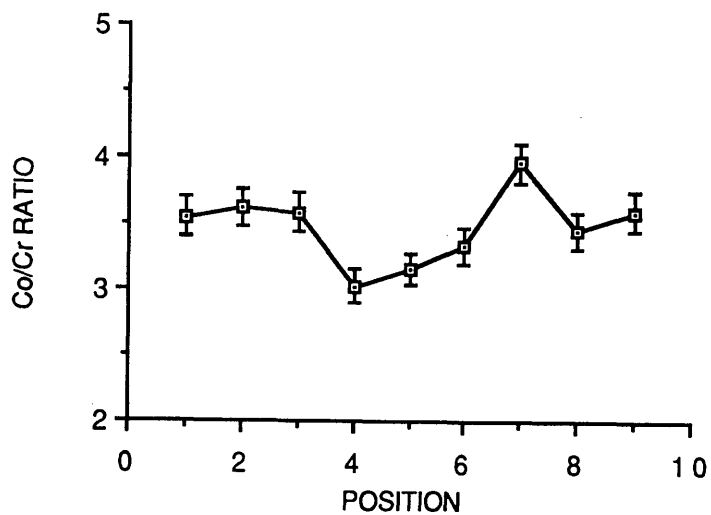


Figure 4.24 Plots of Co/Cr $K\alpha$ count ratios against probe position for orthogonal scans across column in low Ts film on Ge.

Outside this ring there is a smooth decrease in the Co to Cr ratio to the boundary region which has a level of Cr near the average for the general area. In figure 4.24 the effect is seen to be less pronounced. This is probably because this section of specimen, from the total number of counts, was deduced to be thicker, by a factor of 2.5, than the other areas scanned. The affect of this would be an increase in beam spreading which would cause a reduction in resolution. This would reduce the sensitivity to any highly localised compositional variations.

Figure 4.25 shows STEM bright field and annotated ADF images of a typical area analysed in the high Ts film. Figure 4.26 shows the corresponding plot of Co/Cr $K\alpha$ count ratios against probe position. Figures 4.27 and 4.28 show similar plots for two other areas examined in the high Ts film. In these plots no dependence of the ratio on the proximity of the probe to the centre or boundary is apparent. The lack of smooth compositional variation across the column and the relatively large magnitude of the swings in ratio between neighbouring points does, however, suggest a microstructure with small-scale randomly distributed regions or "pockets" of either Co or Cr richness relative to the average level.

4.4.3 Deductions & Conclusions

For the low Ts sample there appears to be a regular pattern of Cr segregation to the column centres. A mean increase in X of 3.1 was recorded for the column centres. This level of Cr is not sufficient to make the column centres predominantly non-ferromagnetic and it is not obvious what affect, if any, it would have on the magnetic microstructure.

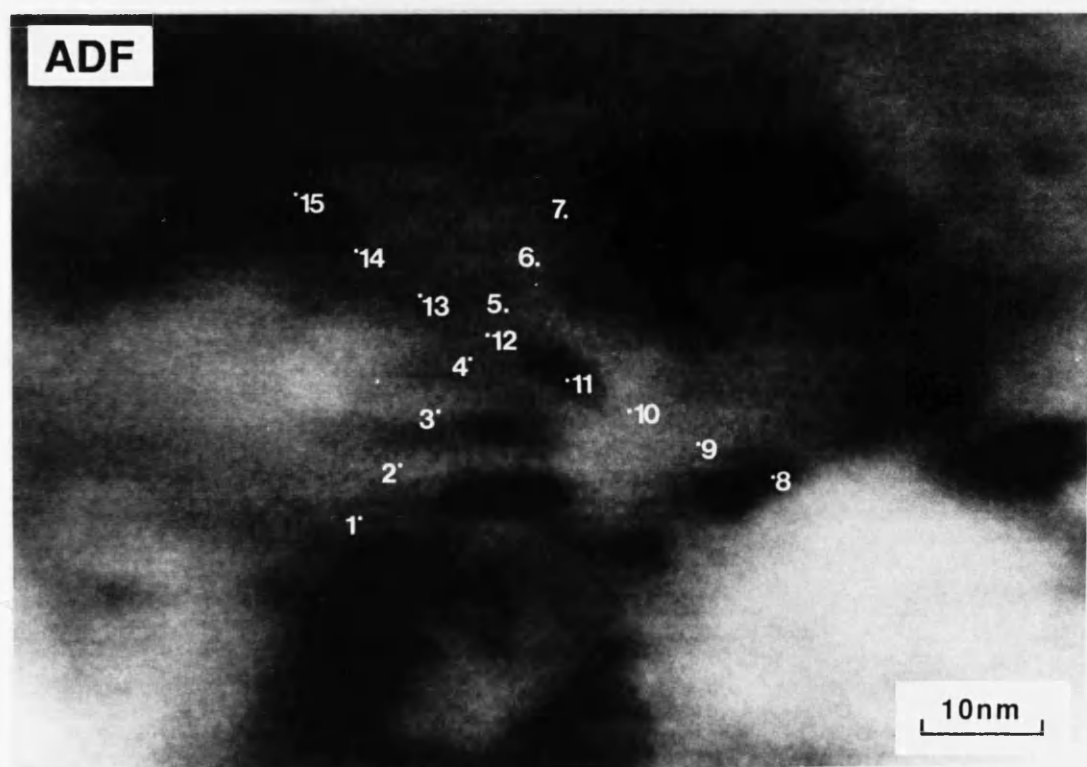
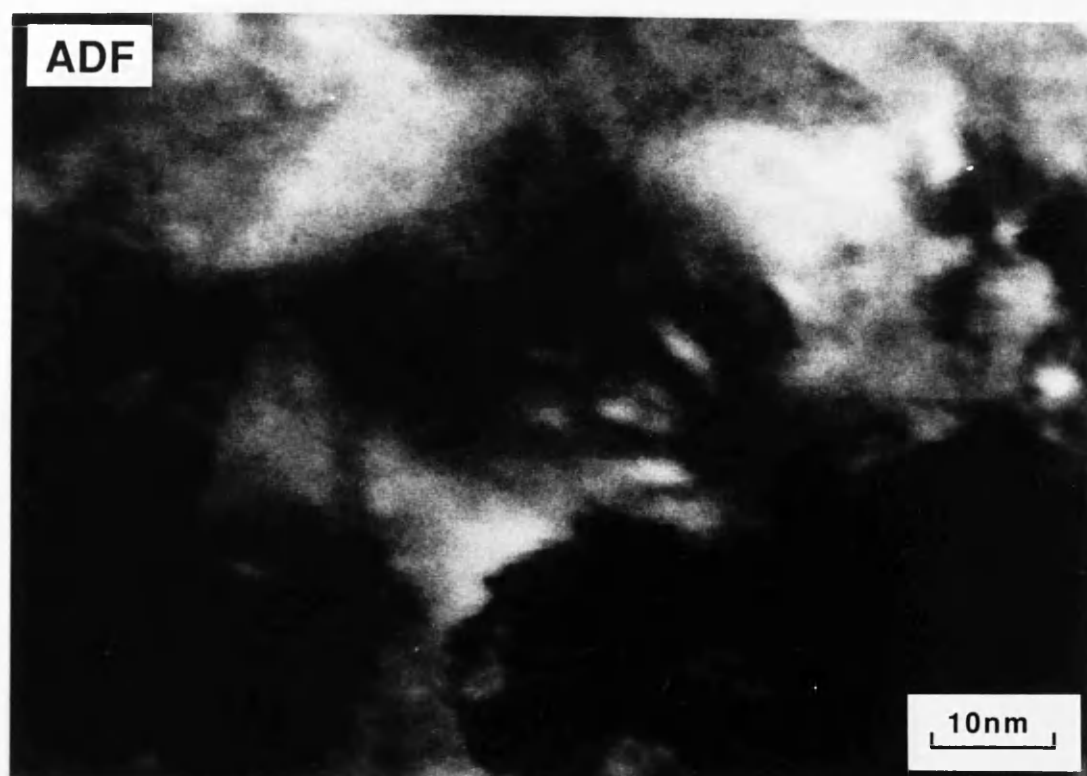


Figure 4.25 STEM BF image and corresponding annotated ADF image of area in high Ts film on Ge showing probe position for orthogonal scans across column.

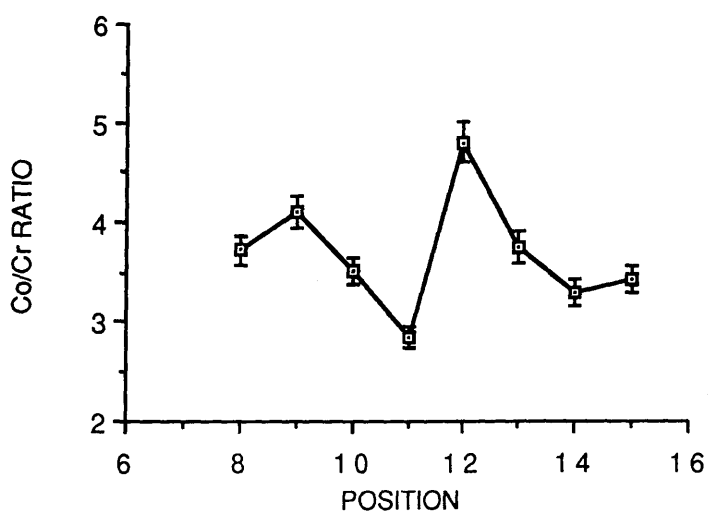
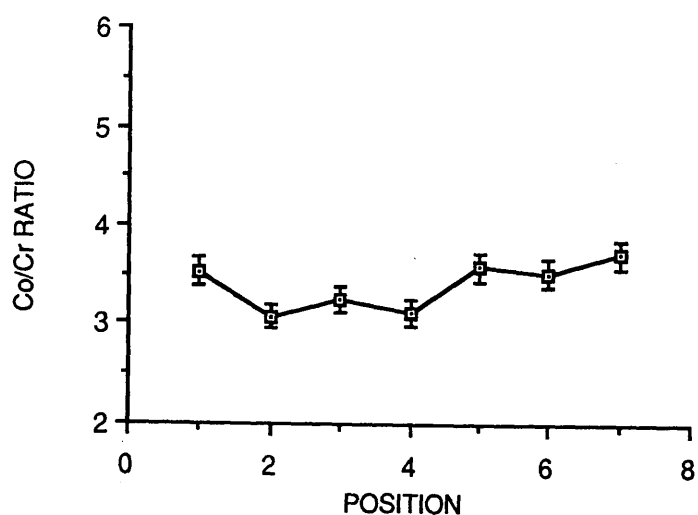


Figure 4.26 Plots of Co/Cr $K\alpha$ count ratios against probe position for orthogonal scans across column in high Ts film on Ge.

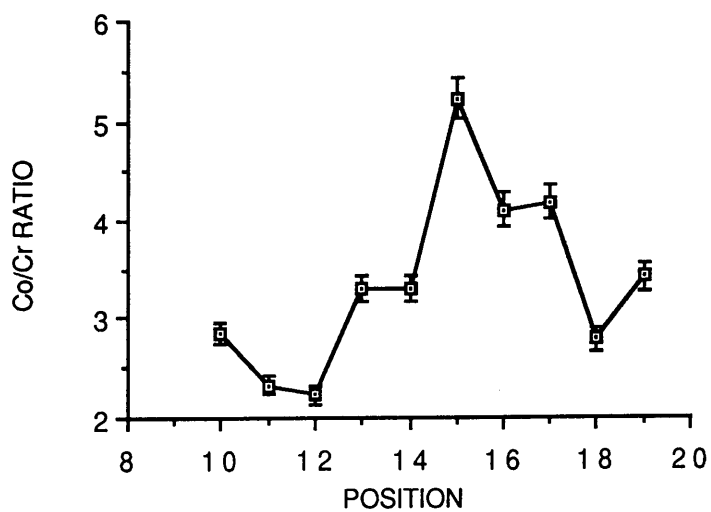
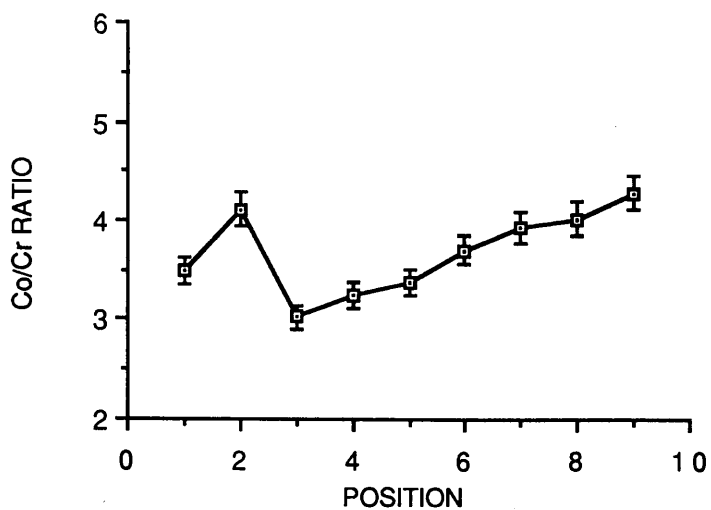


Figure 4.27 Plots of Co/Cr $K\alpha$ count ratios against probe position for orthogonal scans across column in high Ts film on Ge.

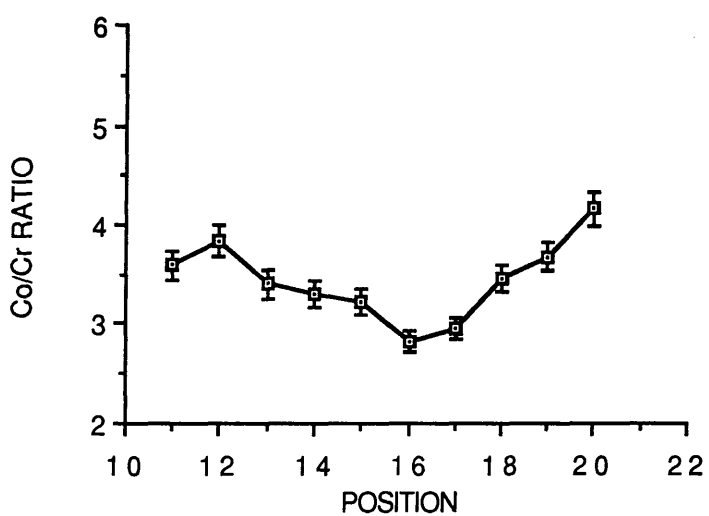
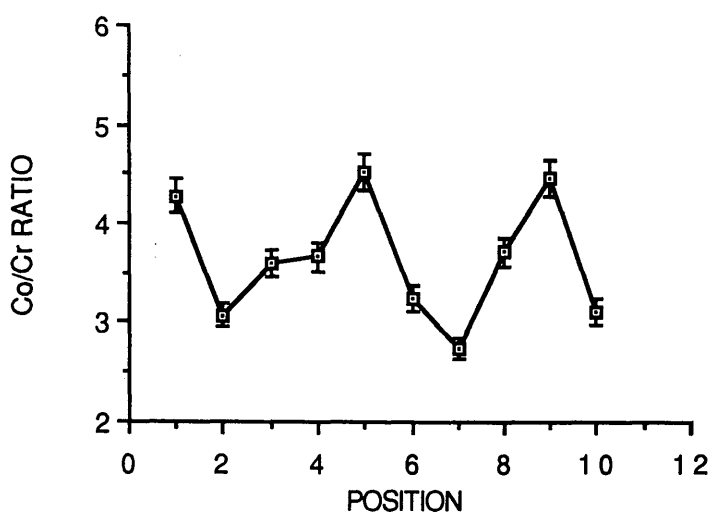


Figure 4.28 Plots of Co/Cr $K\alpha$ count ratios against probe position for orthogonal scans across column in high Ts film on Ge.

For the high T_s film the level of Cr segregation associated with some of the bright spots would be sufficient to affect the local magnetic properties. These bright spots were taken to be microvoids (possibly due to stacking faults parallel to the hcp [001] basal plane) in the surface layer of the CoCr film. In the neighbourhood of these spots the composition was different from that of the surrounding film. Lee et al. (1988) have proposed that such microstructural defects may influence the domain structure and thus the magnetic properties of CoCr films (see section 4.6). It was felt, however, that these spots did not constitute a regular pattern of either Co or Cr enrichment.

Films with little or no boundary segregation of Cr therefore can have a high perpendicularity in magnetic properties. Factors such as underlayers can completely change the pattern of Cr segregation. This section has shown that temperature dependence of the level of boundary Cr enrichment is not an over-riding mechanism.

4.5 CHRYSANTHEMUM PATTERN (CP) Cr SEGREGATION

Standard CTEM imaging techniques can be employed to make qualitative investigations of the pattern of Cr segregation in CoCr films. This method relies on the preparation of samples prior to investigations by immersion in solutions which preferentially chemically etch Co (or Cr). This produces a sample in which areas, which were previously Co (or Cr) rich are thinner. Results of such studies are referenced as evidence for the boundary segregation of Cr (Hoffmann et al. 1985) which was confirmed and quantified in section 4.3 for films deposited directly onto substrates.

Using this technique Maeda and his co-workers at N.T. & T. in Japan found evidence to suggest a complex yet reproducible pattern of segregation in thin films grown under specific conditions (Maeda et al. 1985). The observation of a chemically etched sample of one of these films in a CTEM shows a preferential Co etch to have generated a pattern in each column similar in appearance to a "Chrysanthemum flower", with thin "petals", presumed to be Co rich, extending outwards from a thicker central disc almost to the column boundary.

Films grown under exactly the same conditions as CP films, but to greater thicknesses, on Co etching, have been seen to exhibit a structure similar in appearance to "frog's eggs" (Maeda & Takahashi 1987). Reports of recent EDX studies performed on these films (Maeda & Takahashi 1989) show evidence for a Cr rich core in these films.

4.5.1 Experiment

Unetched as-grown samples of a film ("SP100") previously shown to exhibit the CP structure (Maeda & Asahi 1987) were obtained from Dr. Maeda. This film comprised a 600nm CoCr layer which was prepared by rf sputter deposition from a nominally 18 atomic % Cr target. The layer was deposited directly onto a 50 μ m thick polyimide substrate held at an initial temperature of 150C. A mean perpendicular coercivity of 120kA.m⁻¹ was recorded for the film. Another CoCr film ("V53") which had been seen to exhibit the "frog-egg" structure was also obtained. This film had been rf deposited to a thickness of 4.1 μ m on a polyimide substrate. The target composition was 22 atomic % Cr and the film had a mean perpendicular coercivity of 64kA.m⁻¹.

Planar sections of each film were mounted on specimen grids as

described in chapter 3 and the substrates were chemically removed by immersion in hydrazine hydrate. Sections of both films were Ar ion-beam milled from the substrate side until electron transparent and one section of the SP100 film was subsequently immersed in a preparation of 0.6M HCl/0.067M HNO₃ (as used by Maeda) at a volume ratio of 1:1 to preferentially etch Co. The physical microstructure was investigated in the CTEM and EDX microanalysis was again conducted in the VG HB5 STEM using the same method as in the above sections. For count times of 20s in the purely ion-milled section of film SP100 the number of counts in the Cr K α peaks varied between \simeq 500 and 2000 and the number of counts in the Co K α peaks varied between \simeq 2000 and 7000. From Poisson statistics this led to an inherent error in the Co/Cr count ratio of between 2.5 and 4.5%. For film V53 the number of counts in the Cr K α peak varied between \simeq 200 and 1500 and the number of counts in the Co K α peak varied between \simeq 800 and 7000. This gave a random error in the Co/Cr count ratio of between 2.8 and 7.9%. For both films the numbers of counts corresponded to a range of resolution similar to that estimated in section 4.3.

4.5.2 Results

CTEM studies revealed a reasonably well defined columnar structure in the ion-milled samples of SP100 and V53 but with no CP structure evident since they had not been wet-etched (figures 4.29 and 4.30). In figure 4.30 it can be seen that there was also a small-scale mottling effect on the film which was taken to be due to small topographic variations. Sample SP100 had a mean column diameter between 40 and 50nm and sample V53 had a mean column diameter between 100 and



Figure 4.29 CTEM BF image of typical area in the ion-milled section of "CP" film SP100.



Figure 4.30 CTEM BF image of typical area in the ion-milled section of "frog-egg" film V53.

120nm. Boundary definition was good for film V53 and poor for film SP100 with estimated boundary widths between 1 and 6nm for both films. CTEM bright field images of the wet-etched specimen of SP100 showed a strong CP structure (figure 4.31) with "petals" of dimensions varying between approximately 3 x 10nm and 5 x 40nm.

Figure 4.32 shows the histogram of the Co/Cr K α count ratios obtained from analyses of the spectra recorded from the purely ion-milled section of SP100. An annotated STEM ADF image and corresponding BF image of typical area in the film are shown in figure 4.33. In all 6 areas were examined and over 200 spectra were collected. The mean Co/Cr K α count ratio with associated standard errors for the columns and boundaries were 4.28 ± 0.09 and 3.89 ± 0.06 respectively. The corresponding mean ratio for the overall areas in this film was 4.34 ± 0.04 . From these values it can be seen there is again a moderate degree of Cr boundary segregation and that the column distribution is rather wide (spread $\simeq 4$ as opposed to $\simeq 2.5$ for the boundaries). To investigate the broad column distribution the ratios for the spectra collected from the columns were subdivided to indicate whether they were collected at column centres or at other positions within columns. 8 spectra in the column distribution were judged during acquisition to have been acquired with the probe positioned at column centres. For these a mean Co/Cr K α count ratio with associated standard error of 4.23 ± 0.23 was calculated. This provided no evidence for segregation to the column centre so, to investigate further, orthogonal scans were taken, as in section 4.4.2. BF and annotated ADF images of a typical area analysed are shown in figure 4.34. Plots of Co/Cr K α count ratio against probe position for this and two other areas examined are shown in figures 4.35-4.37. It can be seen from these that although there is evidence of some boundary segregation of Cr there is no evidence of

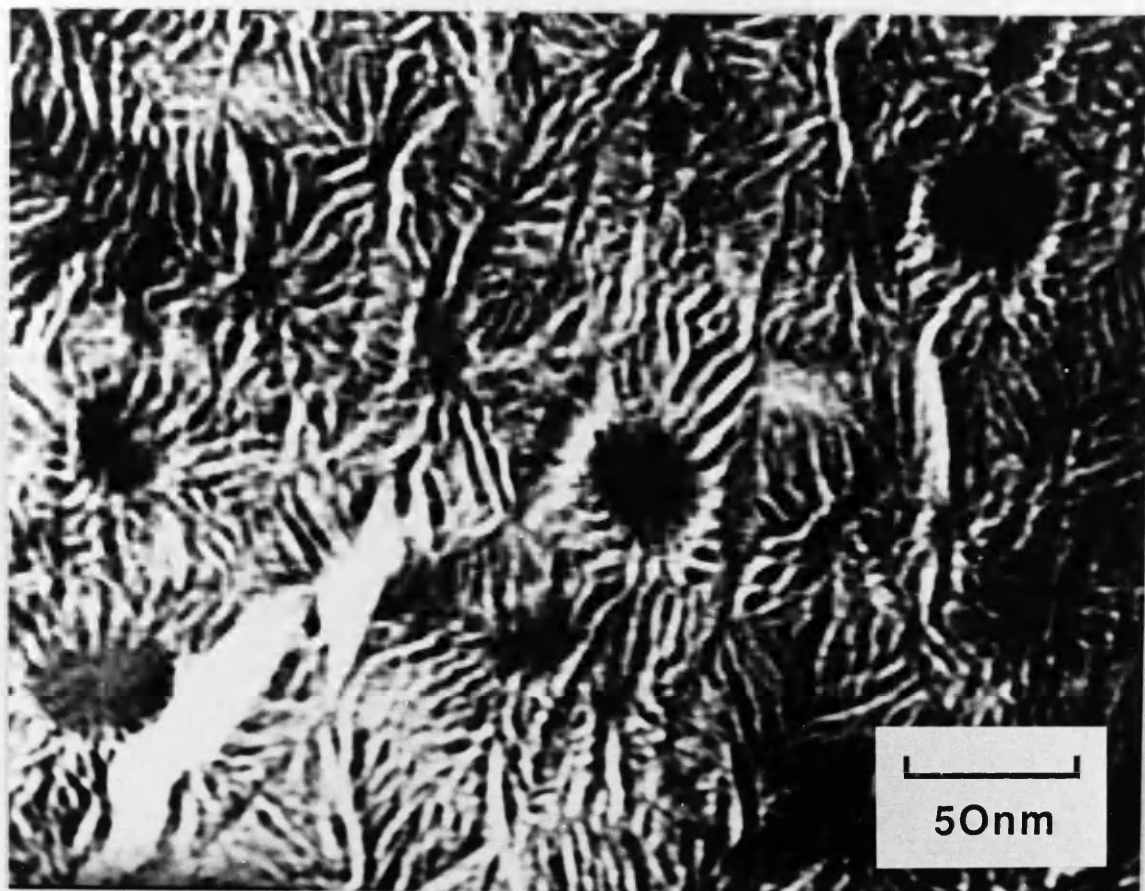


Figure 4.31 CTEM BF image of typical area in the wet-etched section of "CP" film SP100.

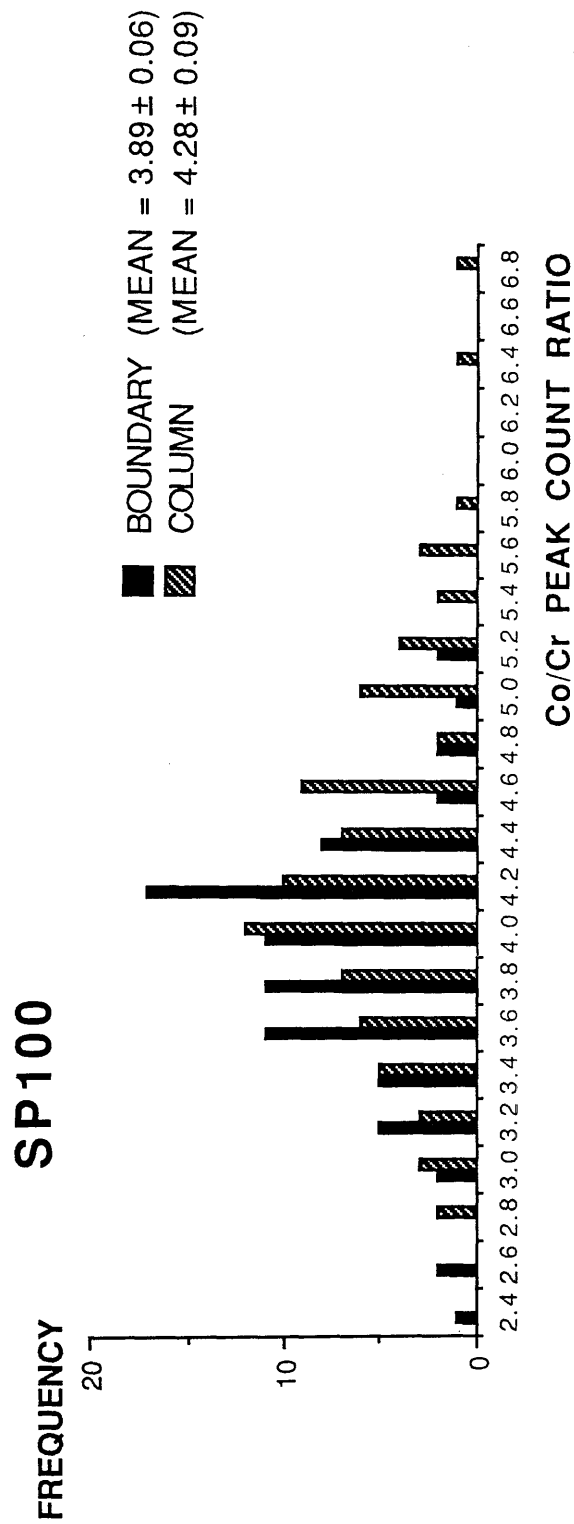


Figure 4.32 Histogram of Co/Cr K α count ratios for boundaries and columns in the ion-milled section of "CP" film SP100.

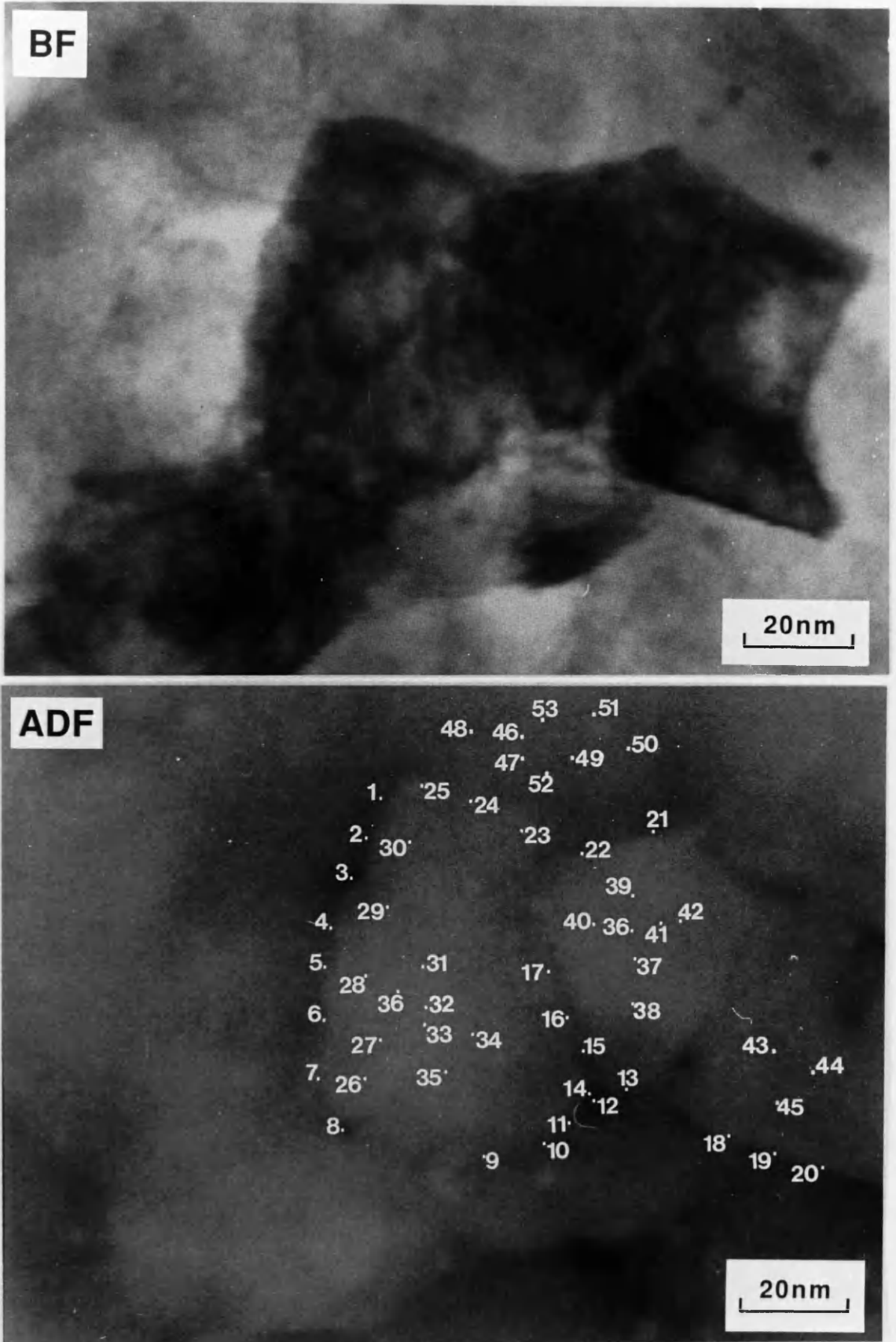


Figure 4.33 STEM BF image and corresponding ADF image of typical area analysed in the ion-milled section of "CP" film SP100.

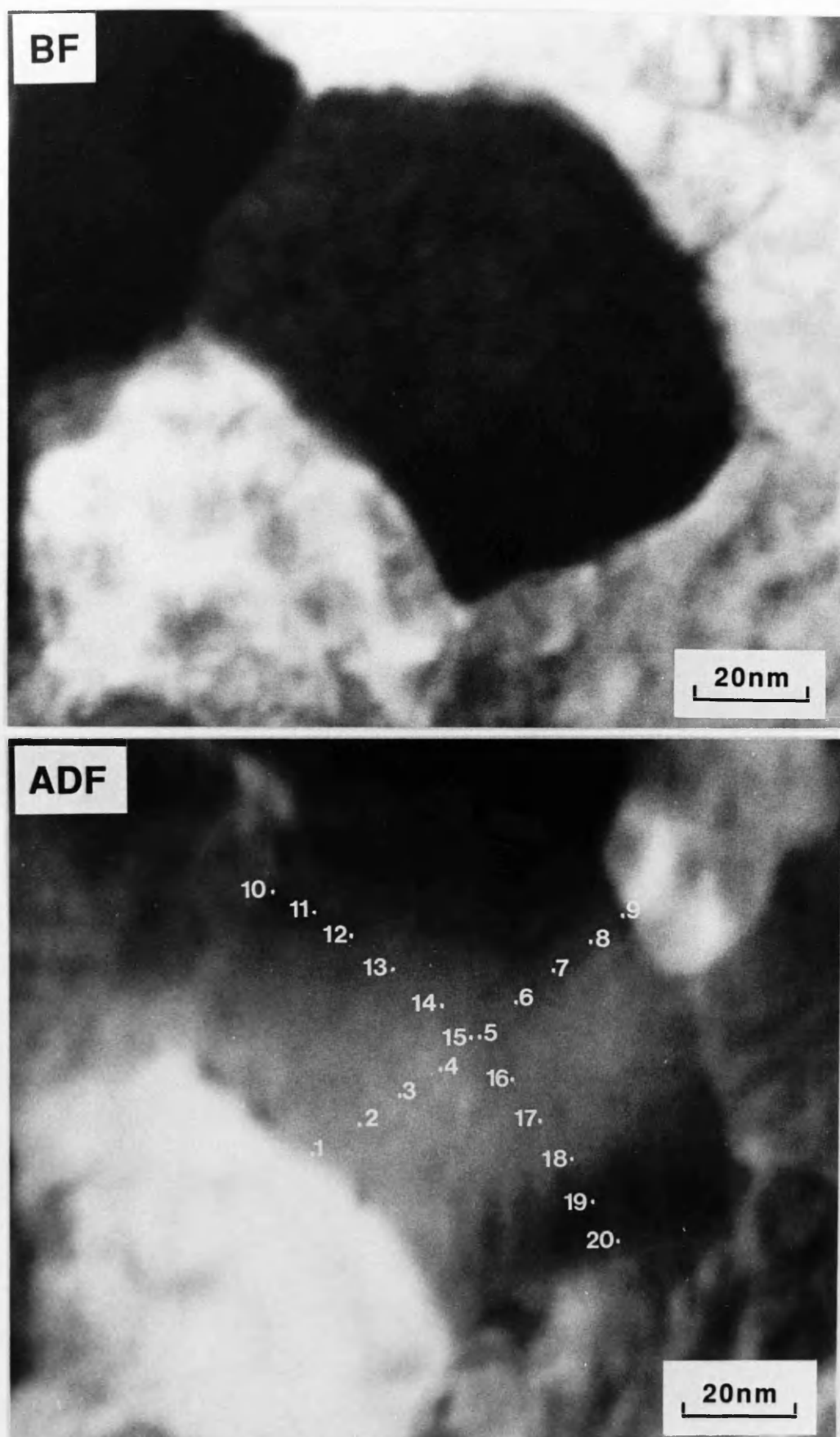


Figure 4.34

STEM BF image and corresponding annotated ADF image of area in the ion-milled section of "CP" film SP100 showing probe position for orthogonal scans across column.

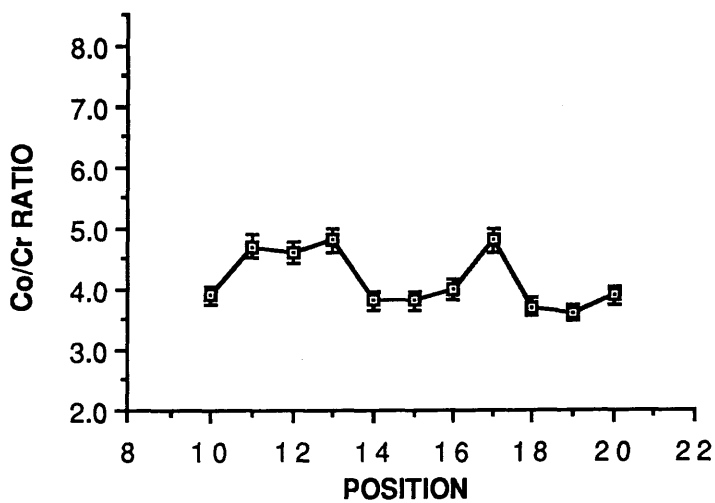
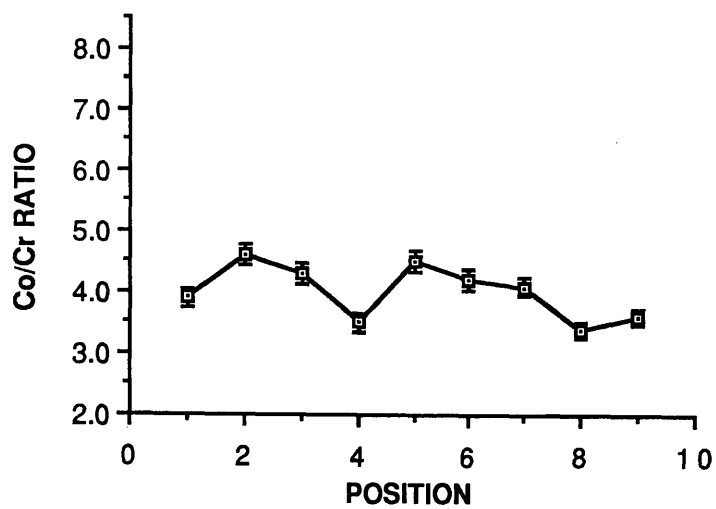


Figure 4.35 Plots of Co/Cr $K\alpha$ count ratios against probe position for orthogonal scans across column in the ion-milled section of "CP" film SP100.

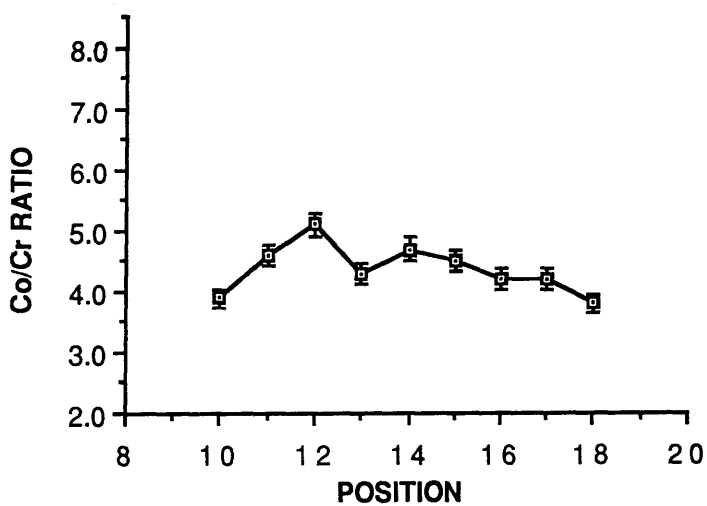
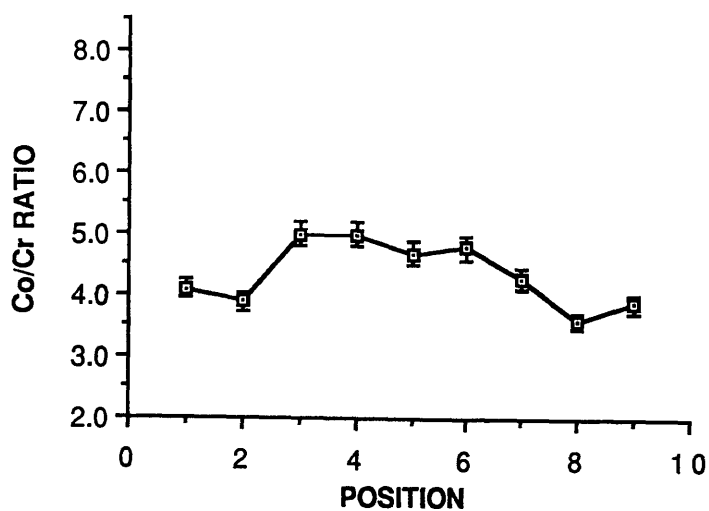


Figure 4.36 Plots of Co/Cr $K\alpha$ count ratios against probe position for orthogonal scans across column in the ion-milled section of "CP" film SP100.

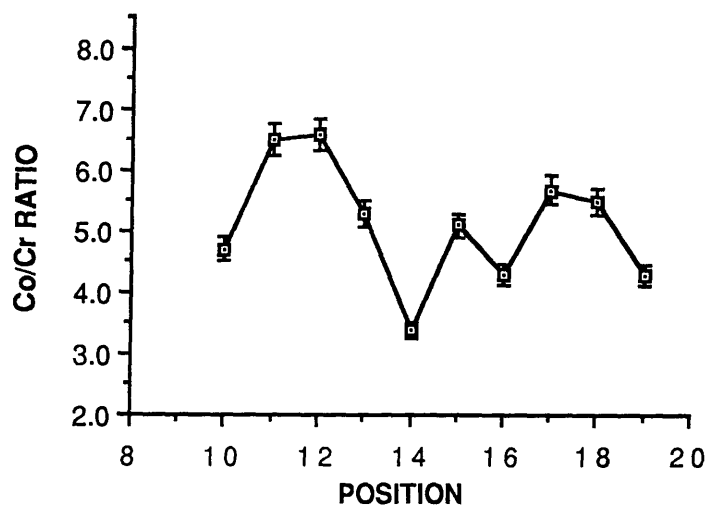
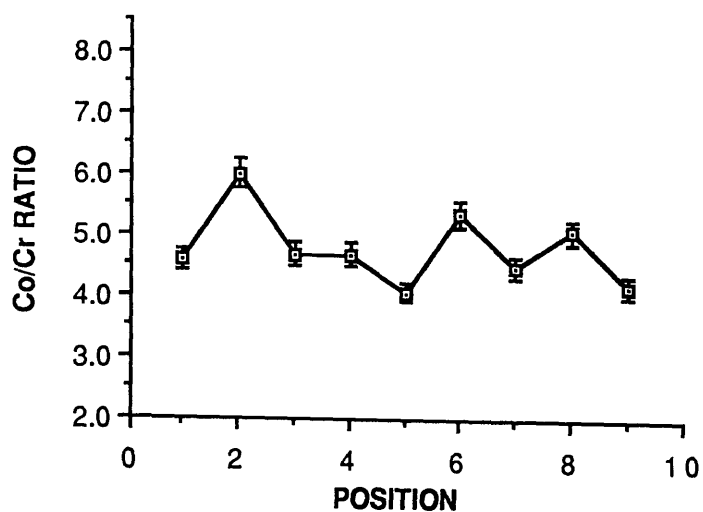


Figure 4.37 Plots of Co/Cr $K\alpha$ count ratios against probe position for orthogonal scans across column in the ion-milled section of "CP" film SP100.

segregation of Cr to the column centre.

An annotated STEM ADF image and corresponding BF image for the preferentially etched sample of SP100 are shown in figure 4.38. In total 6 such areas were examined and over 200 spectra were collected. The EDX microanalysis showed from total peak counts that the thin petals, the thin rings around the cores of the columns and the column boundaries were thinner than the surrounding region of film. The mean Co/Cr K α count ratios and associated standard errors for the petals, the rings around the cores of the columns and the column boundaries were 1.91 ± 0.07 , 1.33 ± 0.07 and 2.21 ± 0.11 respectively. The column centre and other parts of the column had mean Co/Cr K α count ratios with associated standard errors of 2.53 ± 0.05 and 2.60 ± 0.17 respectively.

Annotated ADF and corresponding BF images for the ion-milled "frog-egg" sample, V53, are shown in figure 4.39. For this sample 3 areas were examined and over 100 spectra were acquired. From the histogram shown in figure 4.40 the mean Co/Cr K α count ratios with associated standard errors for the columns and boundaries were 3.22 ± 0.07 and 2.92 ± 0.07 respectively. The corresponding mean for the overall area being 3.18 ± 0.05 . To investigate the possibility of column centre segregation the column distribution was again subdivided. 12 spectra were adjudged to be from the column centres and for these the mean Co/Cr K α count ratio with associated standard error was 2.78 ± 0.29 . Unfortunately the error in this value was too big to make any deductions about a small level of Cr segregation. Orthogonal scans were performed as above. BF and annotated ADF images of a typical area analysed are shown in figure 4.41. Plots of Co/Cr K α count ratio against probe position for this and two other areas examined are shown

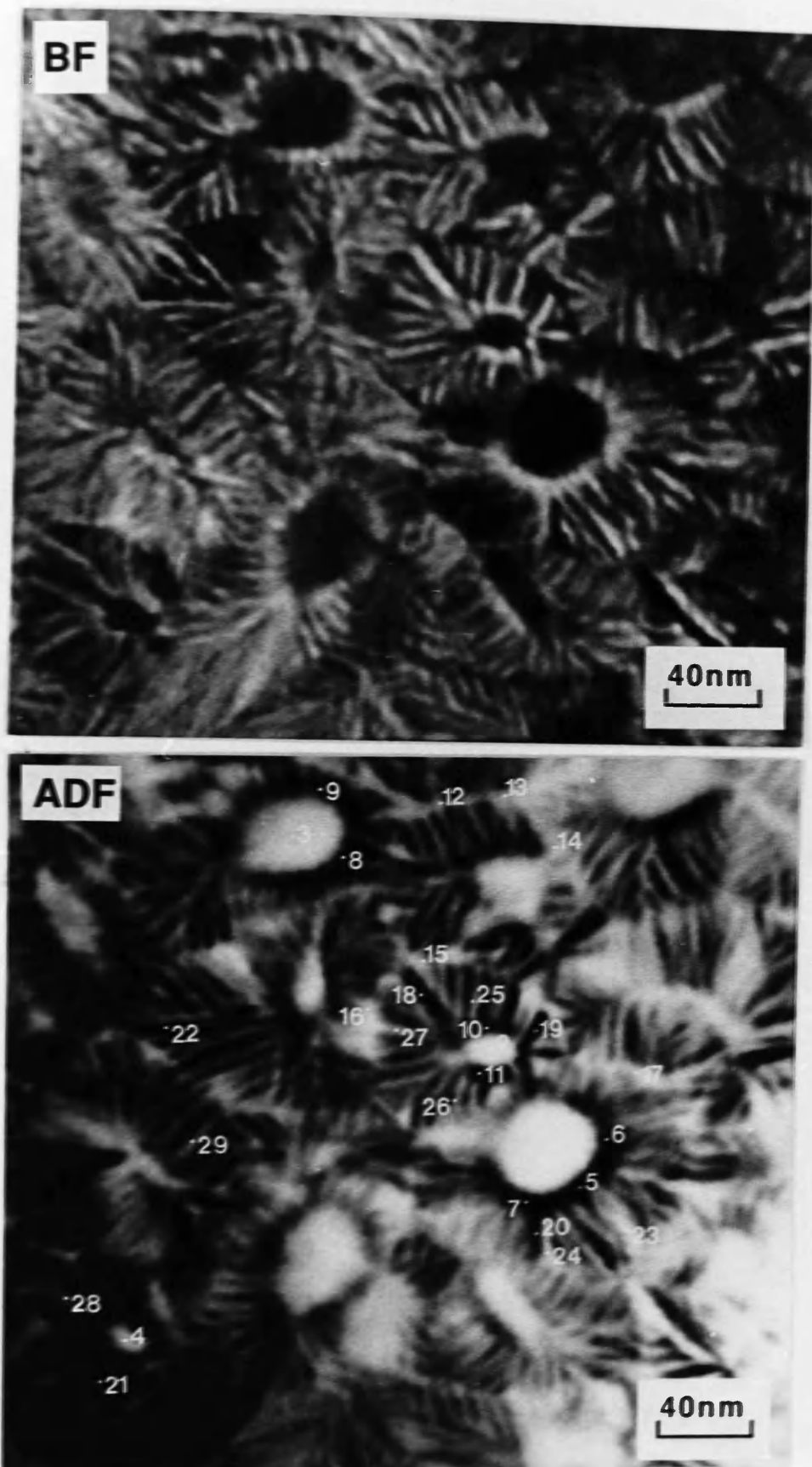


Figure 4.38 STEM BF image and corresponding ADF image of typical area analysed in the wet-etched section of "CP" film SP100.

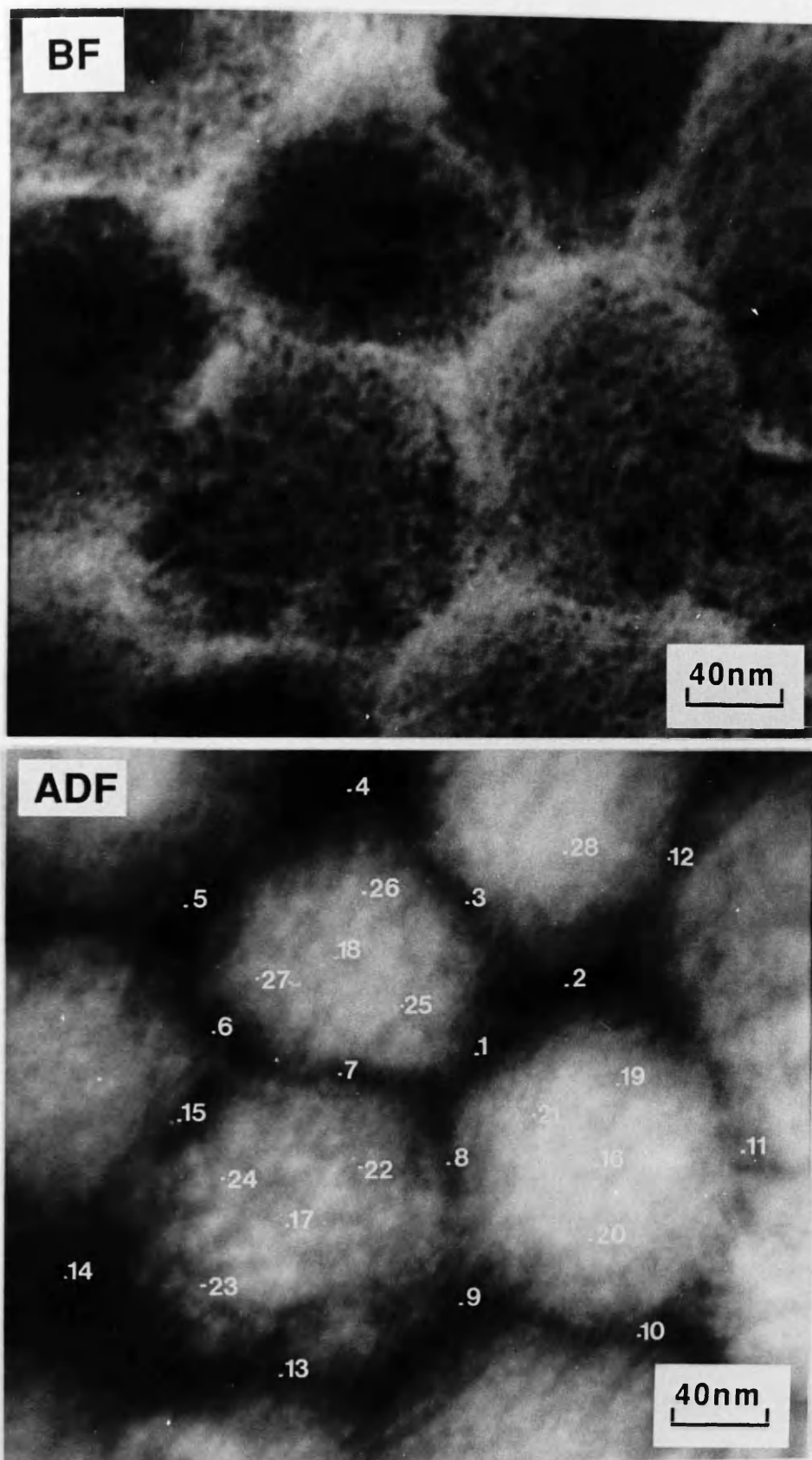


Figure 4.39 STEM BF image and corresponding ADF image of typical area analysed in the ion-milled section of "frog-egg" film V53.

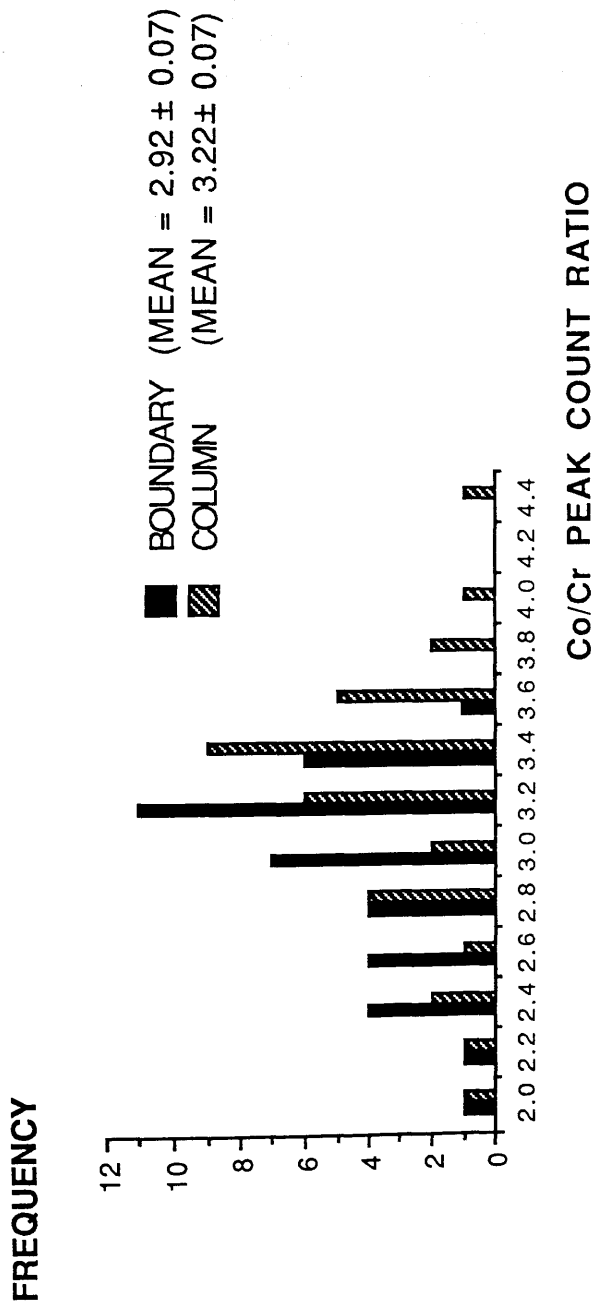


Figure 4.40 Histogram of Co/Cr K α count ratios for boundaries and columns in the ion-milled section of "frog-egg" film V53.

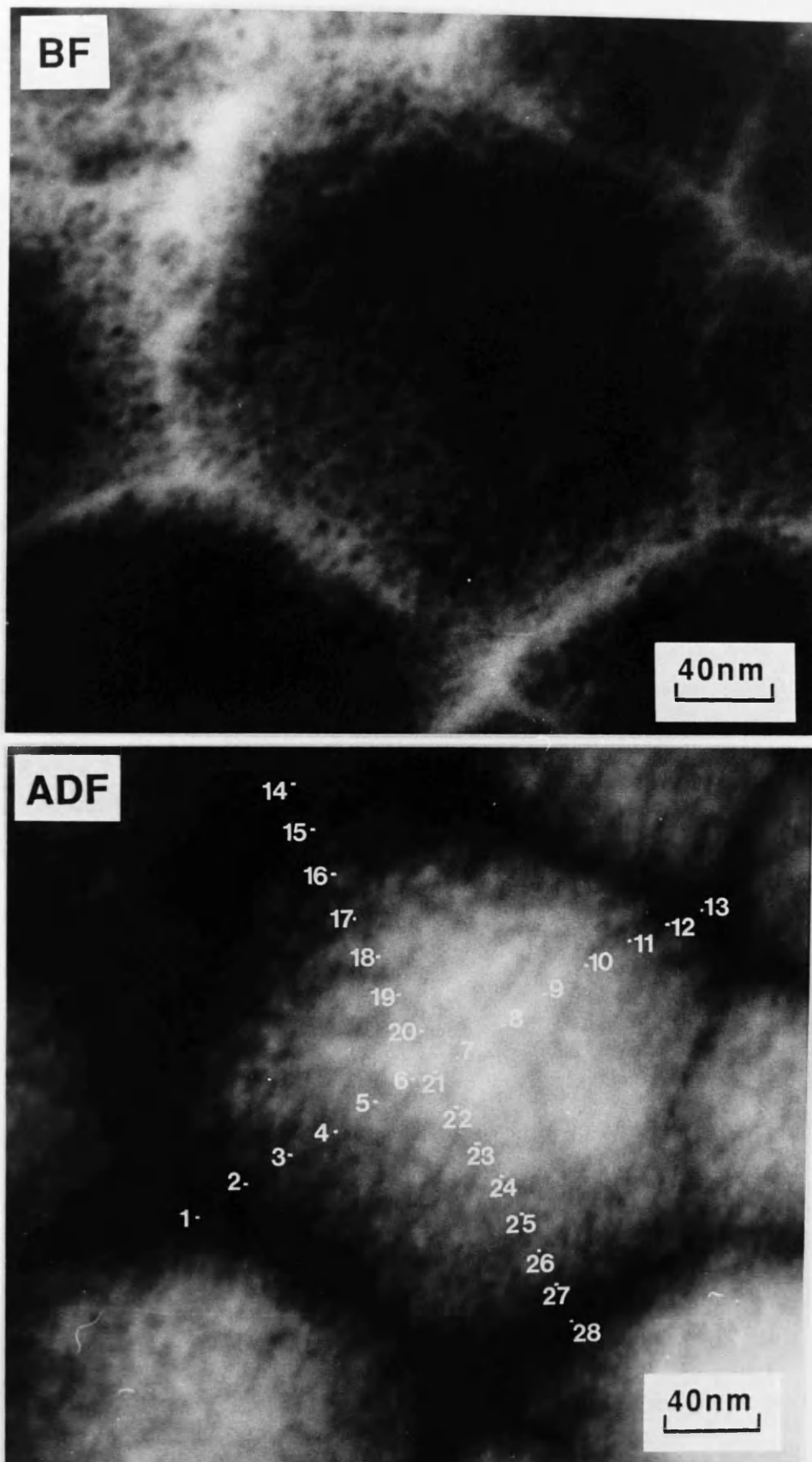


Figure 4.41

STEM BF image and corresponding annotated ADF image of area in the ion-milled section of "frog-egg" film V53 showing probe position for orthogonal scans across column.

in figures 4.42-4.44. These plots confirm a degree of Cr segregation to the column boundaries but reveal no clear pattern within the columns. They therefore do not provide evidence for either Cr segregation to the column centre or a more complicated pattern of segregation in this sample.

Any dependence of Co/Cr $K\alpha$ count ratio on the thickness of specimen was examined (as in sections 4.3 and 4.4) by plotting $\{\text{Co } K\alpha \text{ peak counts}\}/\{\text{VOA current}\}$ against $\{\text{Cr } K\alpha \text{ peak counts}\}/\{\text{VOA current}\}$ for each specimen. Plots of this are shown in figures 4.45 and 4.46 for both purely ion-milled samples. R values were calculated from these plots giving figures for the columns and boundaries of 0.92 and 0.94 respectively for SP100 and 0.93 and 0.99 respectively for V53. The good correlation with a linear fit at all thicknesses again justifies the averaging of the Co/Cr ratio over all specimen thicknesses examined. It should be noted also that the R values again indicate a poorer fit for the columns in both films compatible with there being significant compositional variation within the columns.

Figures 4.45 and 4.46 were also used to estimate the compositional inhomogeneity in the films as in sections 4.3 and 4.4. The range of gradients estimated from the envelope of the distribution for SP100 gave errors in X for the columns and boundaries of ± 0.9 and ± 0.6 respectively, compared with variations from the random error in the number of counts of ± 0.2 in both cases. For V53 the bounds of the gradient envelope for the columns and boundaries were ± 0.8 and ± 0.4 respectively with corresponding variations from the random error in the number of counts of ± 0.2 for both regions. One further observation from the least squares fit lines for SP100 (figure 4.45) was the value of the y (Co) axis intercept for the column distribution. At 9.8 this was

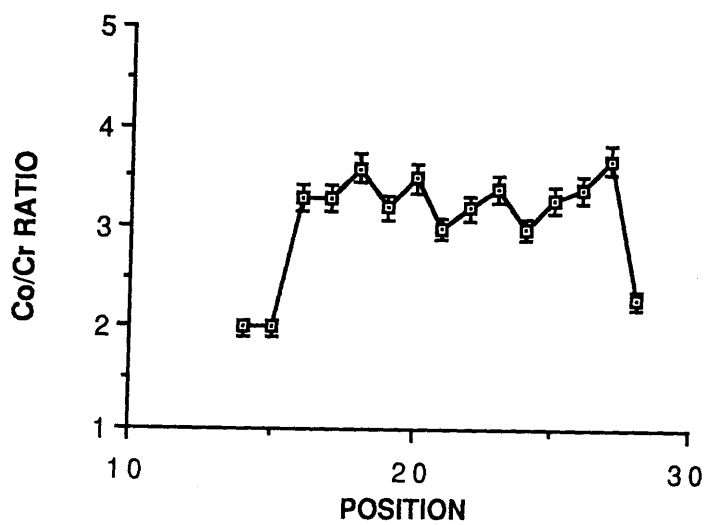
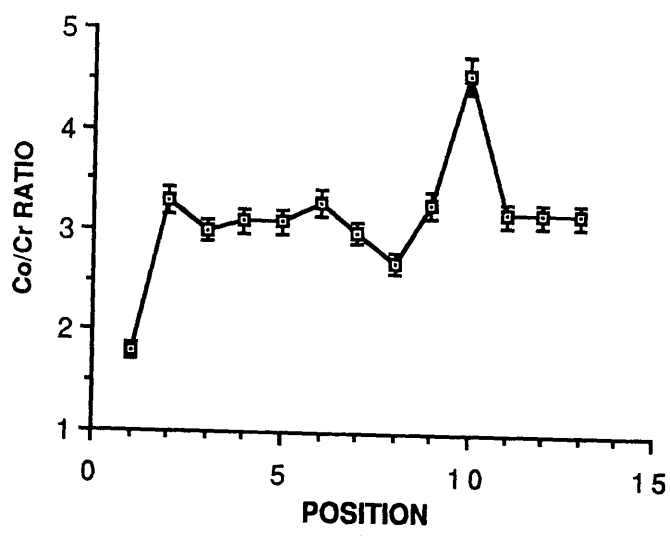


Figure 4.42 Plots of Co/Cr K α count ratios against probe position for orthogonal scans across column in the ion-milled section of "frog-egg" film V53.

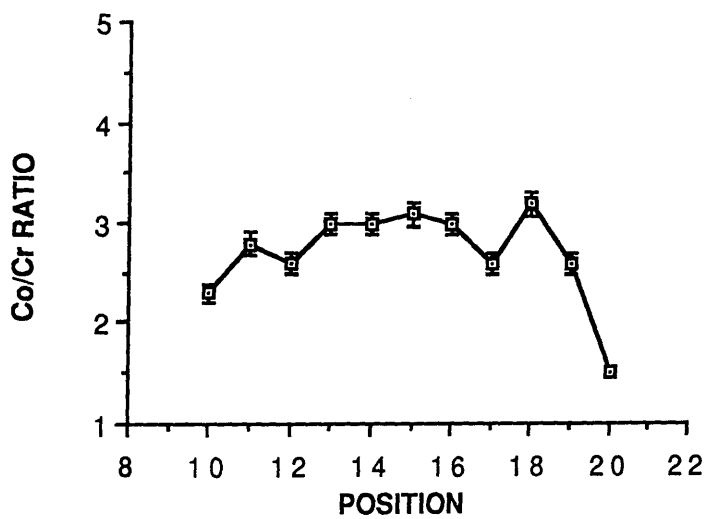
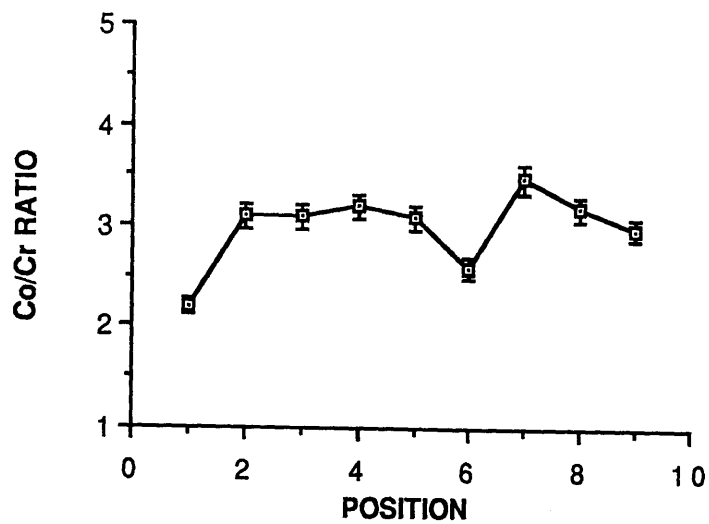


Figure 4.43 Plots of Co/Cr K α count ratios against probe position for orthogonal scans across column in the ion-milled section of "frog-egg" film V53.

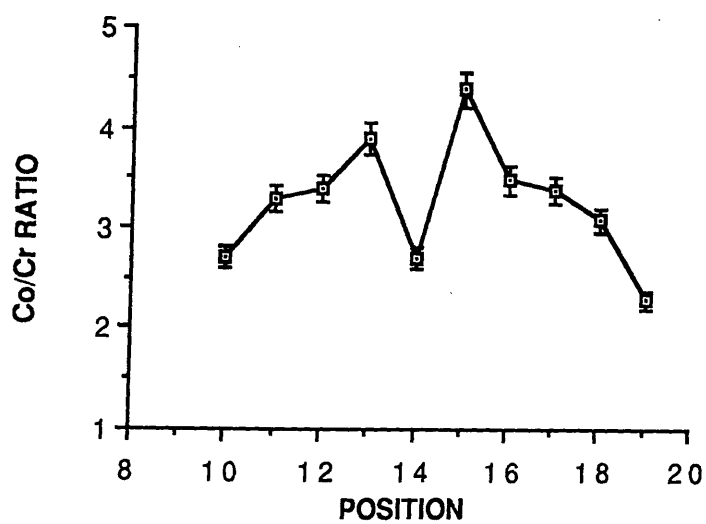
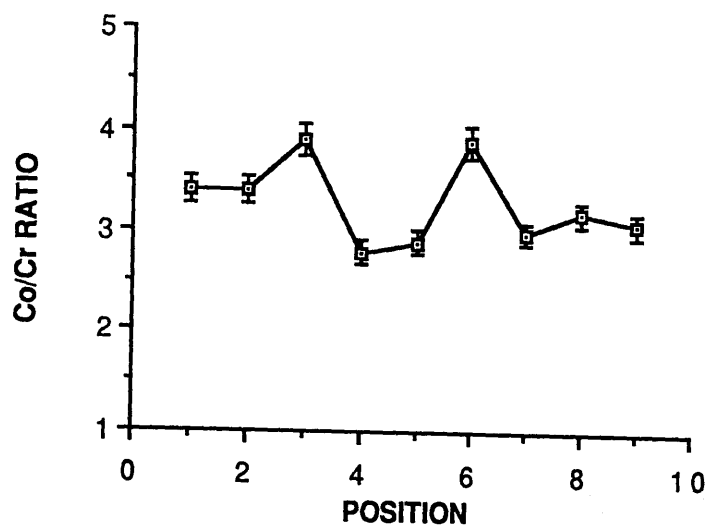


Figure 4.44 Plots of Co/Cr $K\alpha$ count ratios against probe position for orthogonal scans across column in the ion-milled section of "frog-egg" film V53.

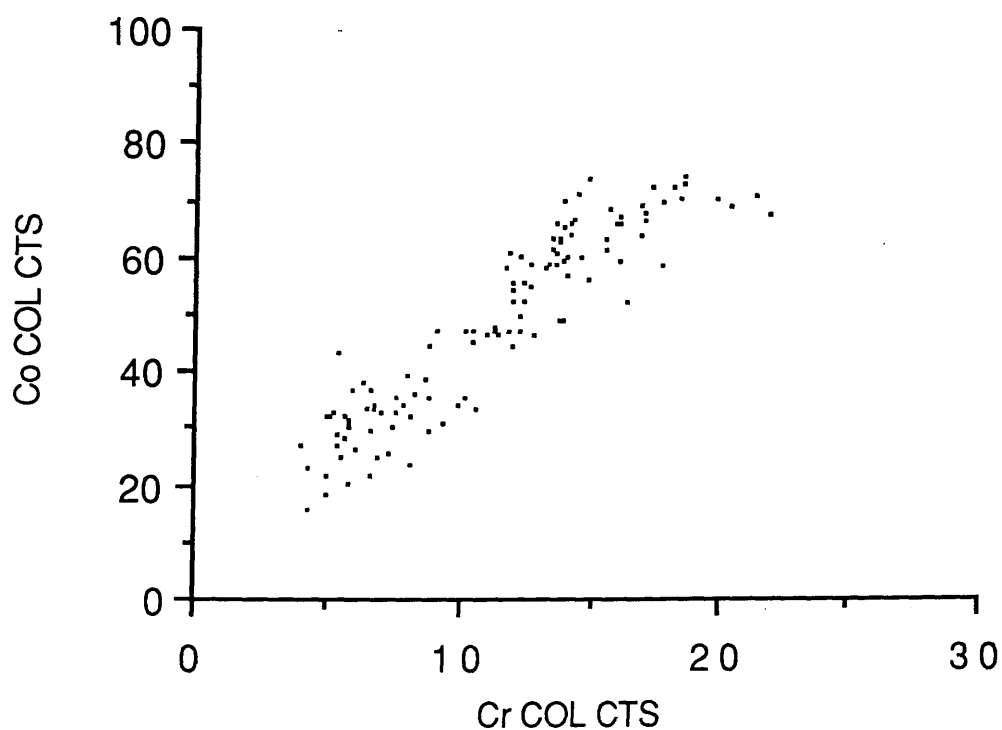
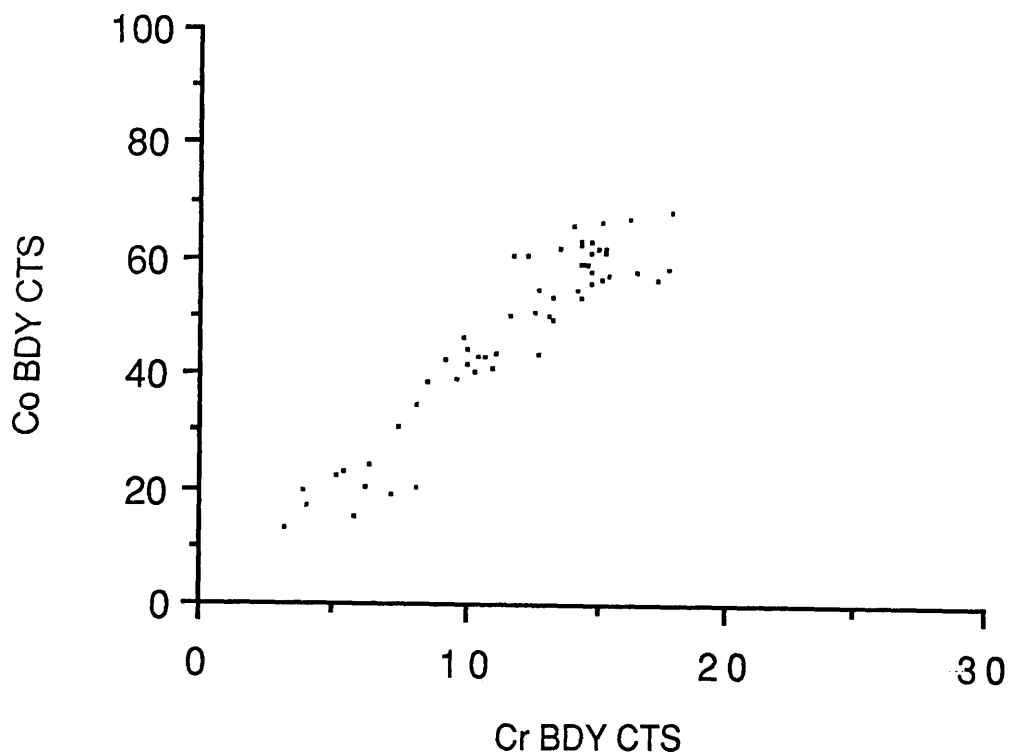


Figure 4.45 $\{Co\ K\alpha\ counts\}/\{VOA\ current\}$ plotted against $\{Cr\ K\alpha\ counts\}/\{VOA\ current\}$ for boundaries and columns in the ion-milled section of "CP" film SP100.

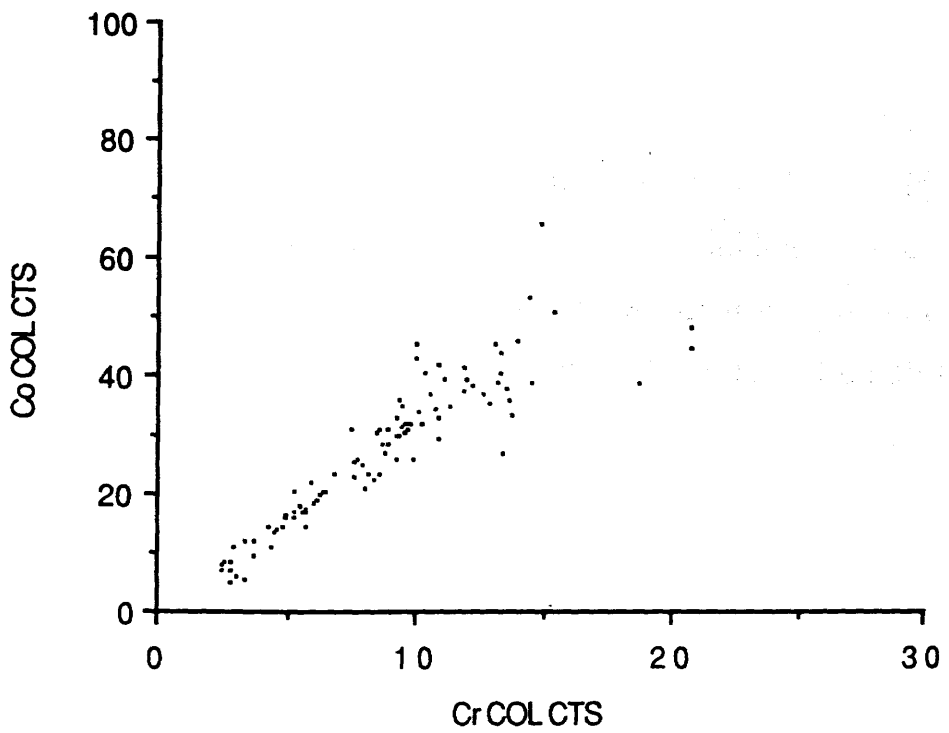
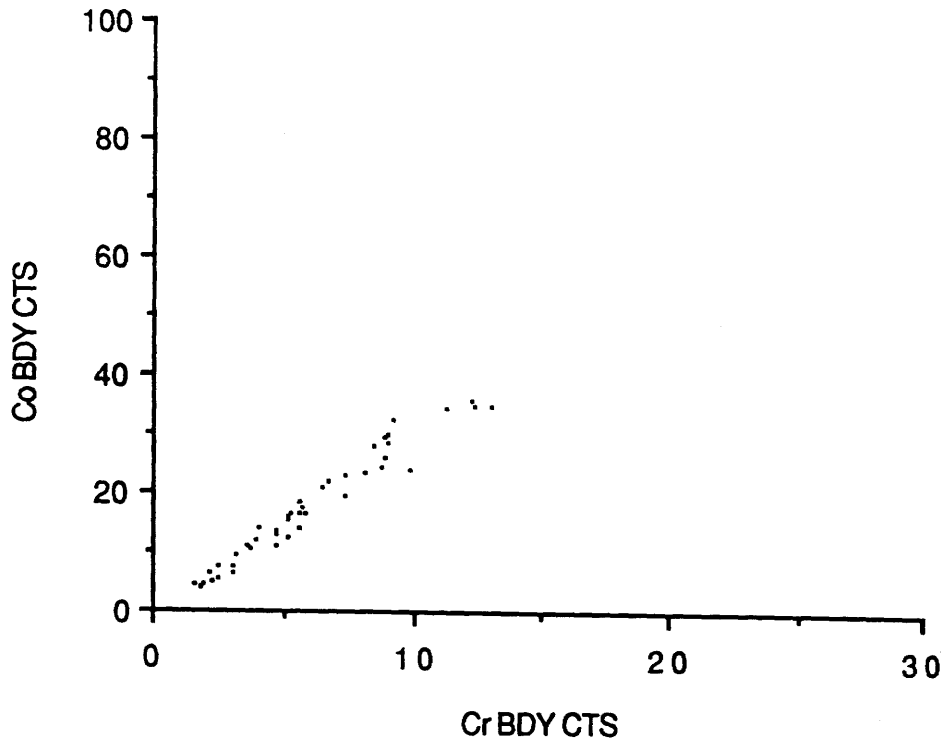


Figure 4.46 $\{\text{Co K}\alpha \text{ counts}\}/\{\text{VOA current}\}$ plotted against $\{\text{Cr K}\alpha \text{ counts}\}/\{\text{VOA current}\}$ for boundaries and columns in the ion-milled section of "frog-egg" film V53.

too big to be a random error and represented the only statistically significant deviation from zero for any of the films examined in this chapter.

Data for the atomic fraction of Cr calculated from the mean Co/Cr $K\alpha$ count ratios in histograms and orthogonal scans for all the CP films is given in table 4.4.

4.5.3 Discussion & Conclusions

In the purely ion-milled section of film SP100 there was evidence for some boundary segregation of Cr with a mean increase in X of 1.7. For the areas of film analysed no dependence of the local composition on the thickness of specimen was observed. Compositional variations were similar for both columns and boundaries with variations of the order of 4 and 3 times the random error respectively. The large value for the intercept in the column distribution in figure 4.45 could be due to Co enrichment at the surface of the specimen adding a fixed number of Co $K\alpha$ counts into the spectra. For the wet-etched section of SP100 the thinned regions in the CP structure were found to be Co rich and the overall level of Co had dropped significantly relative to that in the purely ion milled film.

In the frog-egg film, V53, there was evidence of a low level of Cr segregation to the column boundaries with a mean increase in X for the boundaries of 1.5. This is consistent with the Cr segregation to the column boundaries predicted for this film by Maeda from wet-etching experiments (Maeda & Takahashi 1987). No evidence was found, however, for the Cr rich core, reported by Maeda & Takahashi (1989). Compositional variations for the columns and boundaries were estimated, respectively, at 4 and 2 times the random error calculated

SAMPLE REGION	SP100 ION-MILLED	SP100 WET-ETCHED	V53 ION-MILLED
AREA	17.6 ± 0.2	29.2 ± 0.8	22.6 ± 0.4
COLUMN	17.9 ± 0.4	26.3 ± 1.7	22.4 ± 0.5
BOUNDARY	19.3 ± 0.3	29.6 ± 1.5	24.1 ± 0.6
COLUMN CENTRE	18.0 ± 1.0	26.9 ± 0.5	25.1 ± 2.6
GENERAL COLUMN	17.8 ± 0.4		21.9 ± 0.5
BRIGHT SPOTS		39.1 ± 1.3	

Table 4.4 Mean atomic fraction of Cr measured for regions in the CP and frog-egg films.

†Increased compositional inhomogeneity in the low Ts film on Ge relative to the low Ts film deposited directly onto PET, may be attributable to the increased substrate temperature during deposition.

using Poisson statistics.

4.6 OVERALL CONCLUSIONS

For the films deposited directly onto PET the temperature of the substrate during deposition had a marked effect on the local composition of the films. At higher temperatures very significant elemental redistribution took place leading to well defined columns with Cr rich boundaries. For lower temperatures the films were observed to have less compositional inhomogeneity, less distinct boundaries between columns and, if present, only a small amount of boundary segregation of Cr ($<1\%$).

For the films deposited onto a Ge underlayer the temperature of the substrate during deposition was again shown to have a controlling effect on the local elemental distribution. No significant boundary segregation of Cr, however, was observed in either film. At lower temperatures the column centres were seen to have an enhanced level of Cr with a corresponding Co enrichment in the surrounding parts of the columns. Compositional inhomogeneity was again seen to be greater for the high Ts film.[†] The higher temperature films were not observed to have any regular pattern of segregation with respect to the columnar structure but did have large localised variations in composition across the column. In addition to this, the microstructure had small-scale randomly distributed thinner regions or "pockets" with either Co or Cr enhancement relative to the average level. These "microvoids" in the high Ts film may be significant in that they could provide pinning sites for domain walls and/or act as nucleation sites for domains during the

†It should also be noted that as substrate temperature during deposition rises there is a general trend in the observed distributions of Cr. For the low Ts film deposited directly onto PET (lowest temperature during deposition) there is little evidence of any segregation or compositional inhomogeneity. For the high Ts film on PET and the low Ts film deposited onto Ge (deposited at a similar temperature, higher than that for the low Ts film on PET) there is a clear pattern of segregation and an increased level of compositional inhomogeneity and for the high Ts film on Ge (highest temperature during deposition) there is no clear pattern of segregation but a high level of compositional inhomogeneity.

magnetisation process (Lee et al. 1988). This work shows overall, however, that high perpendicular coercivity and high perpendicular anisotropy in a CoCr film are not necessarily attributable to a large degree of boundary segregation of Cr.[†]

For CP films the thin regions forming the CP structure in wet-etched samples were seen to be Co rich. In purely ion-milled sections of the same film evidence of boundary segregation of Cr was observed with a mean increase in X of 1.7. There was no evidence, however, of Cr segregation to the column centre. Compositional variations in the film were at a moderate level compared with other samples in this chapter. It is possible that the complicated shapes this technique etches in the microstructure of CP films could be indicative of a stress pattern causing these regions to be more susceptible to chemical thinning.

Analysis of ion milled sections of films, which exhibited the frog-egg structure when wet-etched, also showed evidence for boundary segregation of Cr, with a mean increase of X of 1.5. As in the study of the CP film there was no evidence of Cr segregation to the column centre and compositional variations in the film were again at a moderate level compared with other samples in this chapter.

In the above EDX microanalyses it can be seen from the wide range in total number of counts that the total volume of specimen excited by the beam varied considerably. For the boundary regions examined in these studies the plots of {Co K α peak counts}/{VOA current} against {Cr K α peak counts}/{VOA current} showed, however, that a linear fit is appropriate over the full range of specimen thicknesses. This suggests that the resolution of this technique is such that when the probe is centred on a boundary, the majority of x-rays excited come from the boundary phase.

In previous EDX work with CoCr thin films (McFadyen 1986), when analysing boundaries in cross-sections, the volume excited pertained to both the boundary and the adjacent column area. This meant that considerable correction factors had to be applied to deduce the composition of the boundary itself. No such corrections were necessary in this work. This reflects the superior geometry of an ion-thinned planar section over the cross-sections used in the previous EDX microanalysis of CoCr thin films.

For binary solid solutions the two main factors contributing to the driving force for segregation are surface bond breaking and bulk elastic strain energy (Abraham and Brundle 1981). These, in turn, are dependent on the bond strength ratio and the atomic size for the solute atom in the solute matrix. A full understanding of the mechanism for elemental segregation in these films therefore requires a complex theoretical treatment. For the purposes of this study, however, the goal is to understand how such patterns of segregation influence the resultant domain structure. This can best be achieved through simultaneous direct observation of the physical and magnetic microstructure, which is the aim of chapter 5.

CHAPTER 5 - SIMULTANEOUS IMAGING OF PHYSICAL AND MAGNETIC MICROSTRUCTURE

5.1 INTRODUCTION

The linear recording densities projected for CoCr perpendicular recording media in the near future (Iwasaki 1984, Bonnebat 1987) will require domains less than 100nm wide. The resolution achievable using optical techniques is therefore inadequate for detailed investigations of the magnetic structure in current experimental films. Previous studies in Glasgow University have shown that DPC imaging in the modified VG HB5 STEM can reveal magnetic stray fields emanating from the surface of suitably thinned sections of ferromagnetic thin films to a resolution of 10nm (McFadyen 1986). For magnetic recording media the study of the stray field distribution is particularly relevant since it is this rather than the internal magnetisation, from which it arises, which induces the signal in the playback head.

The EDX microanalysis described in chapter 4 showed that for CoCr thin films deposited directly onto PET, elevated temperature during deposition caused sufficient Cr segregation to make the column boundaries predominantly non-ferromagnetic in nature. Such a degree of Cr segregation would be expected to produce marked differences between the magnetic domain configurations of the high and low T_s films. A study was therefore proposed employing the DPC mode of Lorentz microscopy to investigate the effect on the magnetic microstructure of growing films at different substrate temperatures.

5.2 EXPERIMENTAL TECHNIQUE

A further aim of this study was to improve on the experimental technique employed in previous DPC work on CoCr films (McFadyen 1986) and thereby facilitate simultaneous imaging of the external magnetic stray fields and internal microstructure. This section explains the choice of ion-milled cross-sections for the studies, the procedure adopted to set up the DPC imaging mode in the VG HB5 STEM and the operating conditions employed.

5.2.1 Specimens

In chapter 3 it was explained that transverse sections have several advantages over planar sections for magnetic studies. The important points were that the magnetic structure in cross-sections is expected to more closely resemble that of the original film and that the magnetic induction is perpendicular to the beam and therefore causes the maximum deflection.

In the previous DPC work on CoCr thin films (McFadyen 1986) the magnetic microstructure and stray field distributions of microtomed cross-sections of the films were investigated. In these sections there was a considerable degree of deformation of the physical microstructure which made it difficult to distinguish individual columns. In addition, strong crystallographic contrast prevented successful imaging of the internal magnetic microstructure.

To avoid some of the deformation of the physical microstructure, Ar ion-milled cross-sections were used instead of microtomed cross-sections. These were prepared (see chapter 3) from strips of the films

deposited directly onto PET with initial substrate temperatures of 30C (low Ts) and 90C (high Ts) (analysed in chapter 4). No recording experiments had been performed on the films and they had not been subjected to a strong magnetic field.

5.2.2 DPC Imaging

As explained in chapter 2, DPC signals are proportional to the average component of magnetic induction perpendicular to the beam integrated along the electron trajectory. Hence recording orthogonal components of in-plane magnetic induction permits quantitative analysis of the stray field distribution.

In this work all DPC studies were conducted in the modified VG HB5 STEM. The following describes the stages involved in setting up the microscope for DPC imaging.

- 1) A normal bright field image of the specimen was focused and stigmated (as described in chapter 2).
- 2) The PSL's were set at a camera length for which the transmitted beam utilised >50% but <100% of the active area of the quadrant detector (usually a beam diameter of between 6 and 7mm).
- 3) The quadrant detector was wound into the path of the beam. Difference signals from opposite quadrants in the detector were displayed on the two monitors and the position of the detector adjusted until the detector was centred on the optic axis.
- 4) The beam was refocused on the specimen plane and a region of free space was selected. Any systematic movement of the intensity distribution in the detector plane was cancelled out through appropriate manipulation of the descans coils. This was performed down to as low a magnification as necessary for the experiment (in this case down to a

value of 10kX).

5) DPC images of the specimen were formed by amplifying the signals from individual quadrants in the detector and adjusting a mixer unit to feed the difference signals from opposite quadrants to the display.

5.2.3 Operating Conditions

Initial studies were conducted with only C2 excited and a 100 μ m selected area aperture (SAA) used to define the probe angle. This mode was adopted because it is the most straightforward to align and use. In this mode the semi-angle subtended by the probe at the specimen plane, α_o , was 0.5mrad, the resolution was approximately 10nm and the probe current was approximately 0.2nA (McFadyen 1986). PSL's 2 and 3 were excited at coarse/fine settings of 1/5.99 and 9/3.15 respectively giving a camera length of the order of 6m. A 250 μ m VOA was inserted to monitor incident beam current.

As discussed in chapter 2, higher resolution for DPC magnetic imaging can be achieved through operation with C1 on and the objective lens weakly excited (Chapman et al. 1978). With a 100 μ m real objective aperture defining the probe angle and the specimen seated in field-free space, out of the objective lens, α_o was approximately 5mrad. Under these conditions the resolution was approximately 3nm. It should be noted that whilst this is poor by general TEM standards it represents a very high resolution for imaging magnetic structures. For these studies PSLs 2 and 3 were set at coarse/fine settings of 9/0.76 and 0/3.10 respectively giving a camera length of the order of 0.6m.

This DPC mode was set up using a similar routine to that outlined in 5.2.2. The only differences were that a beam cross-over was set at the

SAA plane by focusing and stigmating on the aperture with the condenser lens and that the specimen was focused and stigmated using the weakly excited objective lens.

In both modes, because the Lorentz deflection angle produced by the stray fields from the specimen was very small (assuming $t=50\text{nm}$ and $B_s=0.58\text{T}$, $\beta_L \leq 2 \times 10^{-5} \text{ rad}$), very high amplifier gains were required to image them. The images produced were acquired and stored digitally using the AN10000 system at magnifications between 10 and 50kX. Precision and dwell time were set at 8 bits and $51\mu\text{s}$ per pixel respectively. Each image was integrated, where possible (see 5.4.1), over either 4 or 8 frames to reduce the affect of spurious fluctuations in incident beam current and to improve the signal to noise ratio.

5.2.4 Problems Encountered with DPC Imaging

Two problems were encountered because of the prolonged period required at high magnification for correct configuration of the microscope and acquisition of the images. These were beam-induced contamination and localised electrostatic charging of the specimen. The former (see chapter 4), when severe, caused deposition of a contamination layer on the specimen thick enough to prevent the imaging of stray fields and conceal the columnar structure. To combat this the specimen was flooded with electrons (see chapter 4). Localised electrostatic charging of the specimen was a result of the high incident electron flux on an area of specimen with an inadequate conducting path for charge dissipation. Charging resulted in erratic deflections in the beam and sometimes the associated repulsive forces generated enough stresses in the cross-section to fracture the unsupported area. This

problem was combatted by coating the specimen with a very thin layer of carbon to improve conductivity.

5.3 STUDY OF CoCr DEPOSITED ONTO PET AT 30C

Initial studies were conducted in the mode employing C2 as the probe forming lens (see section 5.2.2). Figure 5.1 shows a relatively low magnification DPC image of a cross-section of the low Ts film, with direction of sensitivity to magnetic induction as indicated by the arrow. In this image the CoCr layer is above the substrate. In the upper half of the image there is a free-space background. Magnetic stray field is revealed as alternating regions of high and low signal extending from the upper surface of the CoCr and modulating the background signal level. The contrast level in these regions tends to zero away from the section as the stray field decreases. Because of the linear relationship between signal level and the phase gradient, local contrast in different parts of the same image provides information on relative magnitudes of the particular component of magnetic induction. The lack of contrast variation within the section indicates negligible electron transmission which meant that no internal information could be obtained.

Figure 5.2 shows a pair of contrast enhanced DPC images of another cross-section of the low Ts film with orthogonal directions of sensitivity to magnetic induction (contrast has been extended more in a) than in b)). In this section the upper half of the CoCr layer ($\simeq 200\text{nm}$) had broken away from the substrate during the thinning process. This meant that the disordered region, at the base of the columns (see chapter 1, section 1.6.1), was left attached to the PET. Magnetic stray fields in this case are seen to extend from both the upper and lower surfaces of the

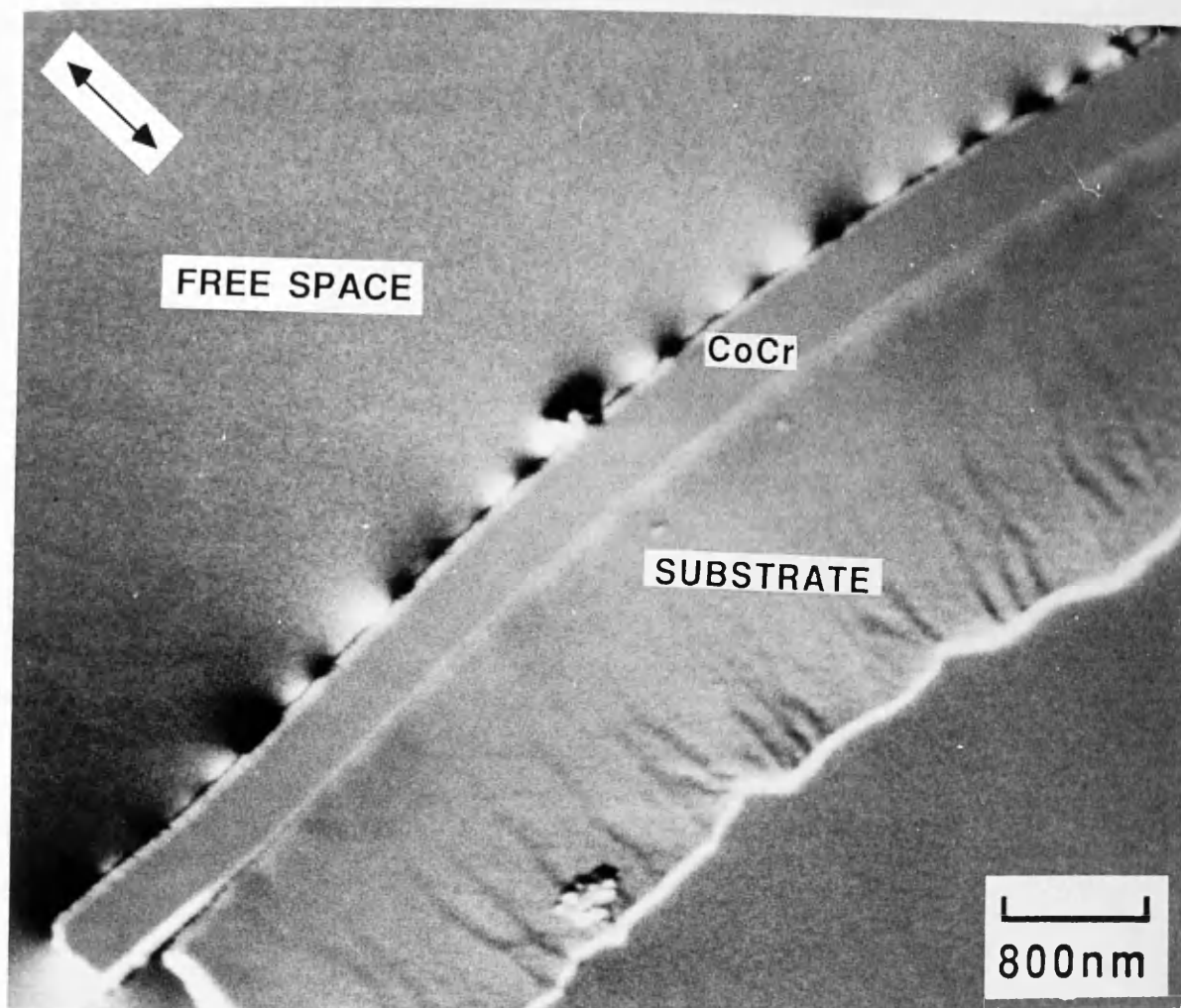


Figure 5.1

DPC image of a cross-section of the low T_s film with direction of sensitivity to magnetic induction as indicated by the arrow.

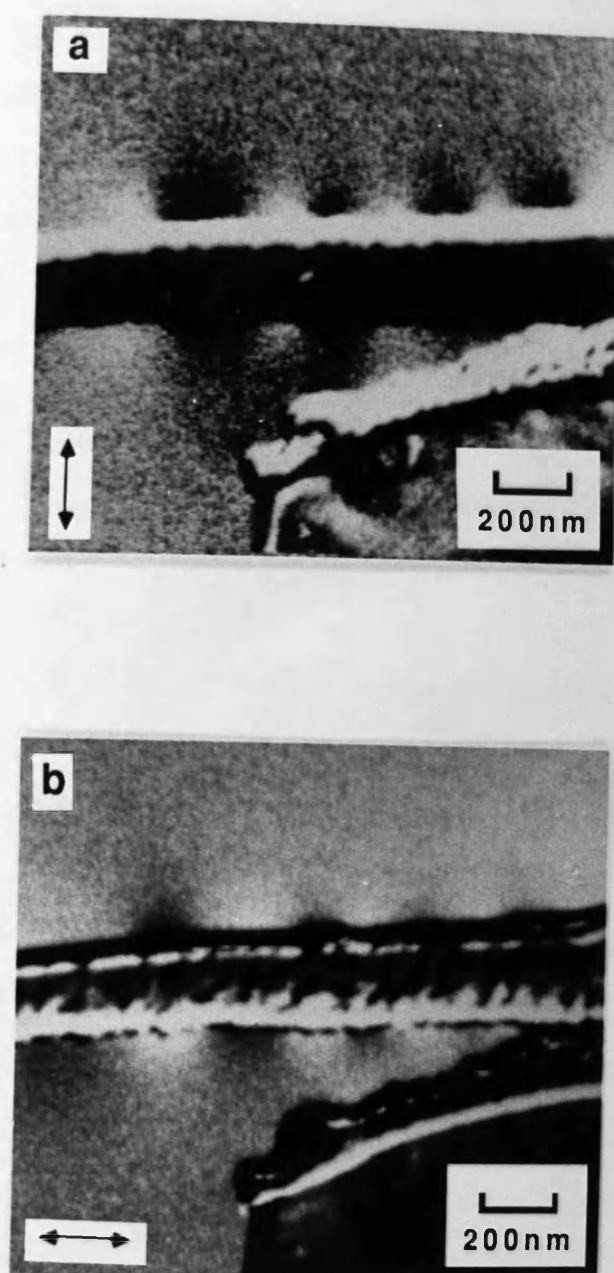


Figure 5.2

Pair of contrast enhanced DPC images of a cross-section of the low T_s film with orthogonal directions of sensitivity to magnetic induction.

CoCr. Directly above and below the film, the horizontal high and low signal bands are caused by the large phase gradient at the edge of the film due to the rapid change in the depth of the section. In figure 5.2a it can be seen the distribution of the stray fields above and below the section is similar. This suggests that vertical domains extend throughout the entire thickness of the film (see section 5.3.2) and is in accordance with results reported elsewhere (Honda et al. 1987). An idealised model of this situation is shown in figure 5.3a. The schematic presented in figure 5.3b shows that such an external stray field distribution gives the position and size of the internal magnetic domain structure.

The affect on the magnetic microstructure of the application of a strong magnetic field was investigated using the same cross-section as in figure 5.2. To do this the objective lens was switched on for a short period. This subjected the specimen to a field of 0.8T directed perpendicular to the plane of the specimen. Figure 5.4 shows a pair of contrast enhanced DPC images of the same part of the specimen as in figure 5.2 after this field was removed. It can be seen from these that although size and position of individual domains with respect to the physical structure has changed, the mean domain size remains approximately the same ($149 \pm 12\text{nm}$ for figure 5.2 as opposed to $142 \pm 19\text{nm}$ for figure 5.4).

A problem encountered in the investigation of these specimens was that the resolution with only C2 as the probe forming lens was insufficient for detailed study of the microstructure. As explained in section 5.2.2 the second magnetic imaging mode (C1 and weakly excited objective as probe forming lenses) allows a higher resolution. It was therefore adopted for further investigations of the low Ts film.

After a number of failed attempts, a thinner cross-section with a

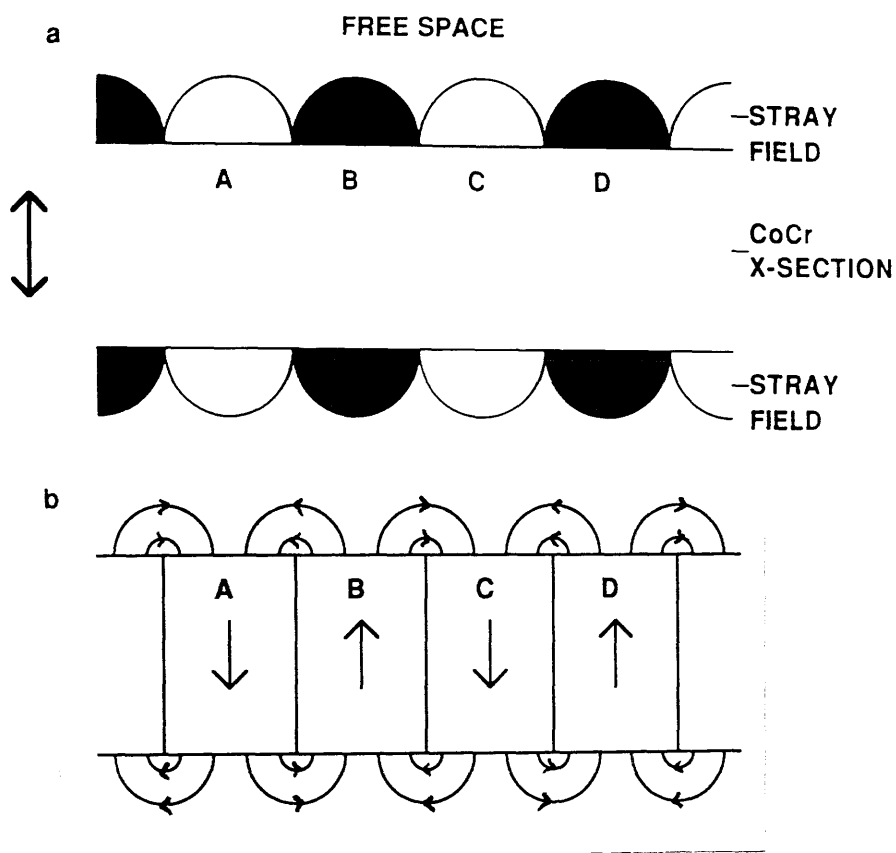


Figure 5.3 Idealised schematic showing a) the stray field distribution and b) the inferred domain structure for a cross-section of CoCr.

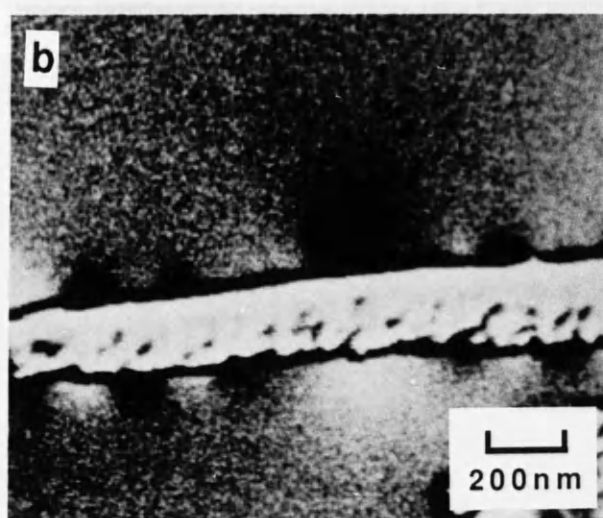
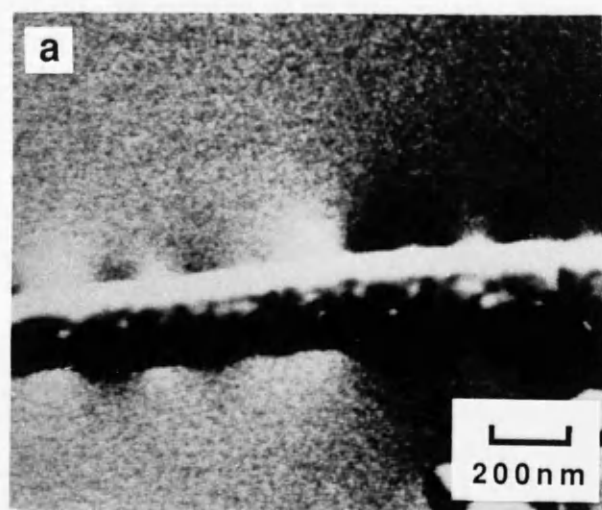


Figure 5.4 Pair of contrast enhanced DPC images of same part of the low T_s cross-section as shown in figure 5.2 after application of a magnetic field perpendicular to the specimen plane.

long, straight region supporting stray fields was obtained (figure 5.5). This again had an area in which the CoCr layer had become separated from the substrate providing a self-supporting region of CoCr approximately 300nm thick. It should be noted that although this did happen on a number of occasions (see above and below), it was by no means typical for a cross-section and could not be performed by design. With the flexibility provided by the PSL's in the HB5 it is possible to choose different directions of sensitivity of magnetic induction for the same camera length. For investigations of this section a suitable PSL configuration was selected and fine adjustment of the PSL settings was made so that the direction of sensitivity to magnetic induction could be either parallel or perpendicular to the major axis along the length of the cross-section.

As in figure 5.2, the similarity between the stray field distributions above and below the section suggests that magnetic domains extend throughout the thickness of the specimen. However, within the section, the DPC images were dominated by strong crystallographic contrast which masked any magnetic signal of interest. Furthermore, the high amplifier gains required to image the stray fields caused internal saturation effects which obscured the physical microstructure itself. To obtain some useful information the sum signal (from all four quadrants in the detector) was collected for the same area of specimen at lower amplifier gains. This gave a structural image in perfect registration with the DPC images (figure 5.6).

5.3.1 Composite Images For The Low Ts Film

With microstructural and micromagnetic images pertaining to the

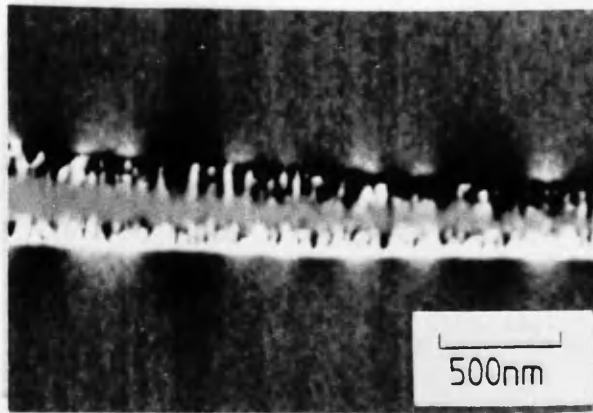


Figure 5.5 Contrast enhanced DPC image of a cross-section of the low Ts film.

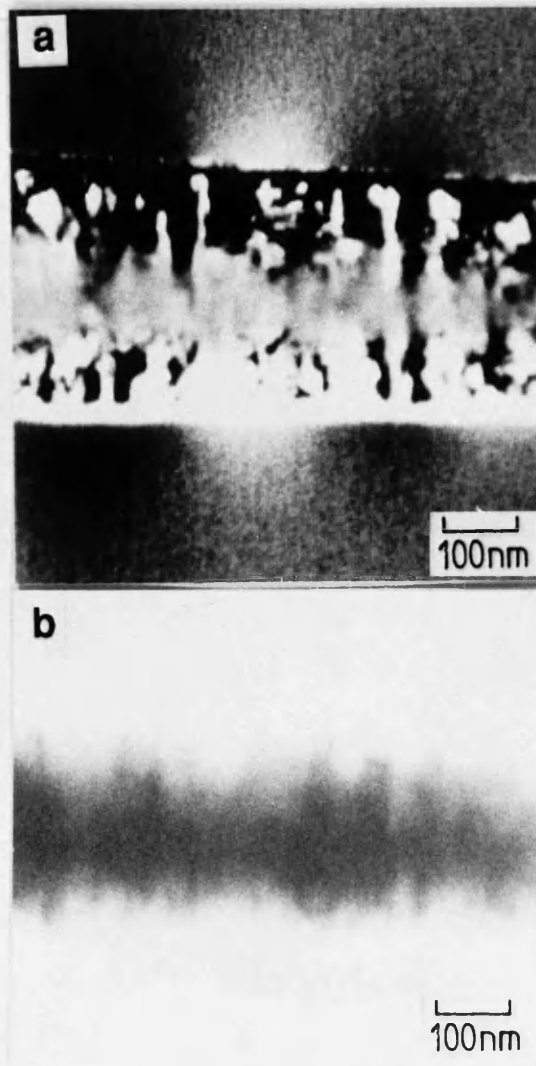


Figure 5.6 a) DPC and b) corresponding sum image of the area of low Ts cross-section shown in figure 5.5 at a higher magnification.

same area of specimen, image processing techniques were employed to produce a "composite" of the DPC and sum images. The aim of this was to investigate any pattern of alignment or non-alignment of the domain boundaries with the column boundaries. All processing was performed on the AN10000 and the procedure adopted to generate composite images was as follows (figure 5.7).

- 1) The saturated free space background in the sum image was designated binary 1 and the film region (anything other than saturation) was designated zero.
- 2) The binary image contrast was scaled up by a factor of 255 to saturate the background, (b), and the image was inverted to give a saturated film region with a null background, (a).
- 3) The saturated binary sum image, (a), was subtracted from the original DPC image to give an image with stray field and a null in the film region. This image was then enhanced using a histogram equalisation transform to emphasise the stray field contrast, (c).
- 4) The background of the sum image was zeroed by subtracting the saturated binary version of the sum image, (b). This image was then enhanced to bring out the columnar structure by performing a 0.7 gamma correction transform and extending the contrast to make use of the full 256 levels, (d).
- 5) Finally the two contrast enhanced images, (c and d), were combined to produce an optimised composite image showing the internal physical structure of the film with stray field background (figure 5.8).

Figure 5.8 shows a contrast enhanced composite image of the same area of section as in figure 5.6. In this image the magnetic stray fields and the columnar structure are both clearly visible. Over a number of such composites it was possible to say that no strong pattern of alignment or non-alignment of the domain boundaries with the column

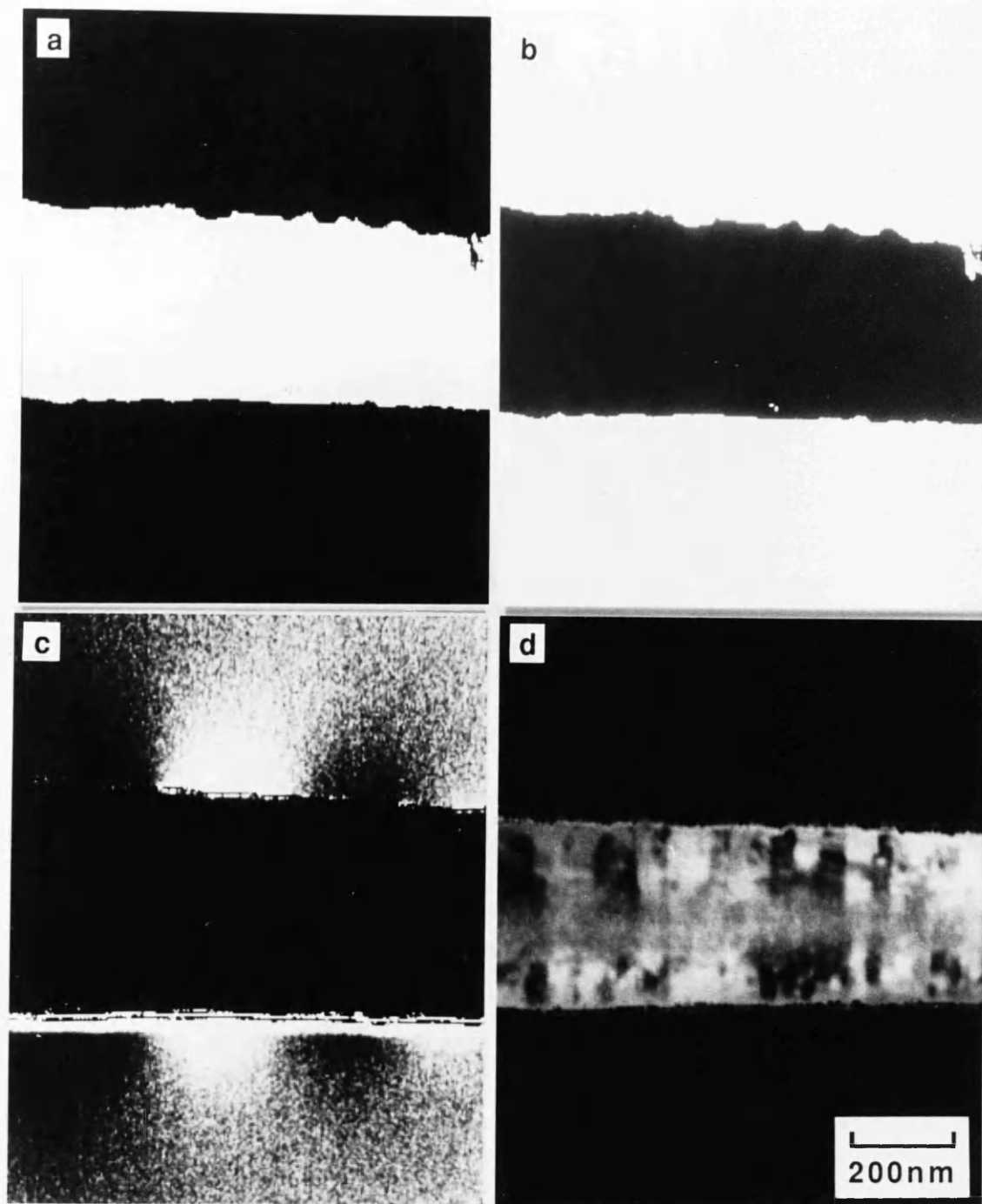


Figure 5.7 a) Binary image with cross-section contrast level at 0 and background at saturation, b) the inverse of a, c) contrast enhanced stray field distribution with cross-section contrast level at zero and d) contrast enhanced image of columnar structure with background at contrast level 0.

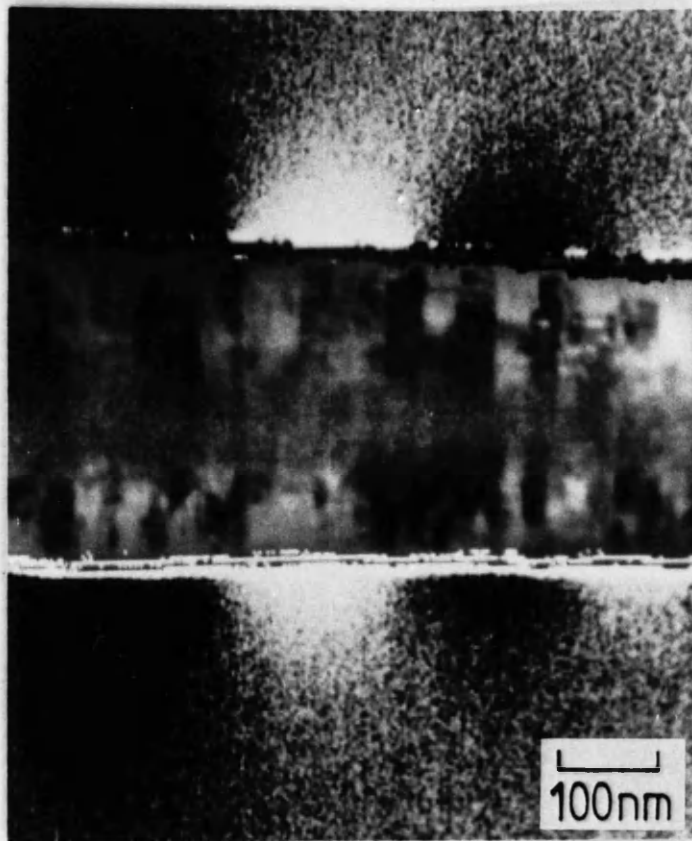


Figure 5.8 Contrast enhanced composite image constructed from DPC and sum images shown in figure 5.6.

boundaries was apparent for this section of the low Ts film.

Even with these images it is still difficult, however, to judge the exact relative positions of the columns and the domain boundaries. This was partly due to the uniform intensity along the centre of the section. The increase in depth towards the centre of the section was the source of this problem since the limited dynamic range of the system was unable to cope with the drop-off in signal level. This meant that along the centre there was no signal variation for the enhancement routines to reveal. To overcome this difficulty it would be necessary to have a uniformly thin cross-section.

5.3.2 Results

DPC images of the kind discussed above revealed variations in stray field spacing and strength (from relative signal levels) along the surface of each cross-section. On average, larger stray field spacings were associated with stronger fields. The lower contrast levels obtained for smaller spacings can be explained with reference to figure 5.9. This illustrates that, for a section of this depth, two oppositely magnetised domains can be present at the same longitudinal position in the film. These produce oppositely directed stray fields whose effects partly cancel producing a low variation in contrast level. This effect is less pronounced for bigger domains because of the increased likelihood of the whole depth of the section being uniformly magnetised. It was decided, however, that the average stray field spacing should best be estimated by calculating the mean, regardless of contrast level.

From the DPC images for the cross-section of the low Ts film shown in figure 5.1 a mean stray field spacing and standard error of

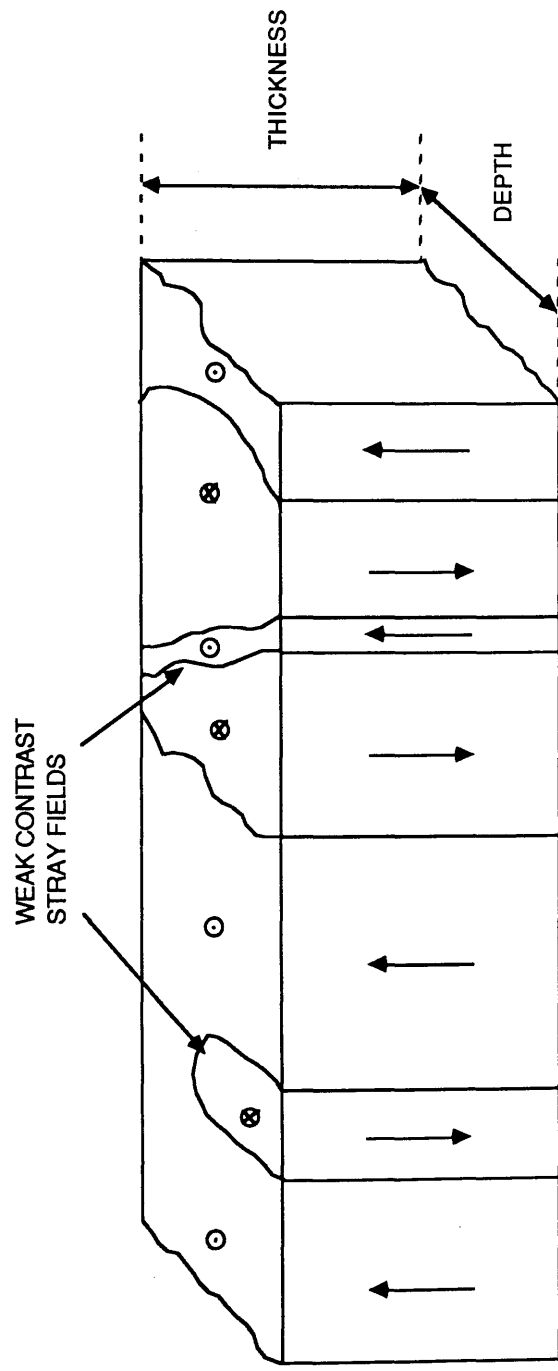


Figure 5.9 Schematic illustrating cancellation of the effects of stray fields due to oppositely magnetised domains at the same longitudinal position in the cross-section.

120 ± 9nm was calculated over a total of 36 flux reversals. Because this film was relatively thick, however, this could not be interpreted directly as the mean domain size. For the cross-section shown in figure 5.2 a mean stray field spacing and standard error of 149 ± 12nm was measured over 9 reversals. For the cross-section shown in figure 5.5 there is a large variation in stray field spacing (35-400nm) with a mean and associated standard error of 160 ± 12nm calculated over 40 reversals. As quoted in chapter 4, the mean column diameter for this film is between 40 and 50nm.

5.3.3 Discussion

The mean domain size being ~4x the mean column diameter and the lack of evidence for correlation of domain boundary position with column boundary position in this film are consistent with a significant degree of exchange coupling at column boundaries. The importance of the information gained from direct imaging of the stray fields and the physical structure is illustrated through the ability to estimate the mean domain wall energy. Following Chikazumi (1964) the mean domain wall energy γ (mJ.m⁻²) is given by:

$$\gamma = \frac{1.08 \times 10^5 d^2 B_s^2}{D} \quad 5.1$$

where d is the mean domain spacing, B_s is the saturation induction and D is the film thickness. With insertion of the values in table 5.1 this equation gives a value of 3.1mJ.m⁻² for the mean domain wall energy. This however does not incorporate the μ^* correction (Shockley 1948).

CROSS SECTION	D (nm)	B _s (T)	d (nm)	K ₁ (kJ.m ⁻¹)
LOW Ts	300	0.578	160	125
HIGH Ts	400	0.628	112	99

Table 5.1 Physical and magnetic properties used to calculate wall energies for films examined in chapter 5.

In magnetic domains the internal field generated by the free poles exerts a torque on the domain magnetisation causing it to rotate away from the easy axis of magnetisation. The resulting change in the magnetostatic energy of the system can be calculated using a "corrected" permeability, μ^* . Following Chikazumi μ^* can be calculated thus:

$$\mu^* = 1 + \frac{B_s^2}{2\mu_0 K_1} \quad 5.2$$

where μ_0 is the permeability of a vacuum ($4\pi \times 10^{-7} \text{H.m}^{-1}$) and K_1 is the perpendicular anisotropy constant (see table 5.1).

This gives a value for μ^* of 2.06. Following Kooy and Enz (1960) the corrected wall energy can then be calculated from:

$$\gamma^* = 2\gamma(1 + \sqrt{\mu^*})^{-1} \quad 5.3$$

This gives a value for the corrected wall energy of 2.6mJ.m^{-2} . Bernards (1990) has estimated a value for γ by comparing the slope of the hysteresis loop at remanence with theoretical predictions (Bernards et al. 1989). This approach yields a value of 1.9mJ.m^{-2} .

5.4 STUDY OF CoCr DEPOSITED ONTO PET AT 90C

Similar difficulties to those reported for the low Ts film were again experienced in attempts to prepare a suitable cross-section. Initial investigations of the high Ts film were also conducted with C2 as the probe forming lens. Figure 5.10 shows part of a cross-section where the

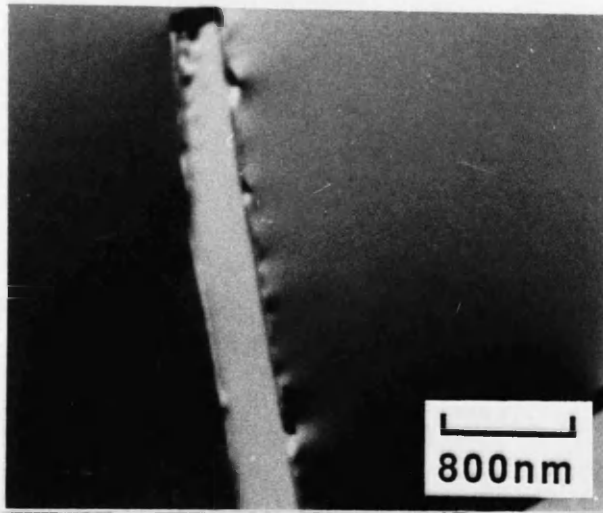


Figure 5.10 DPC image of a cross-section of the high Ts film.

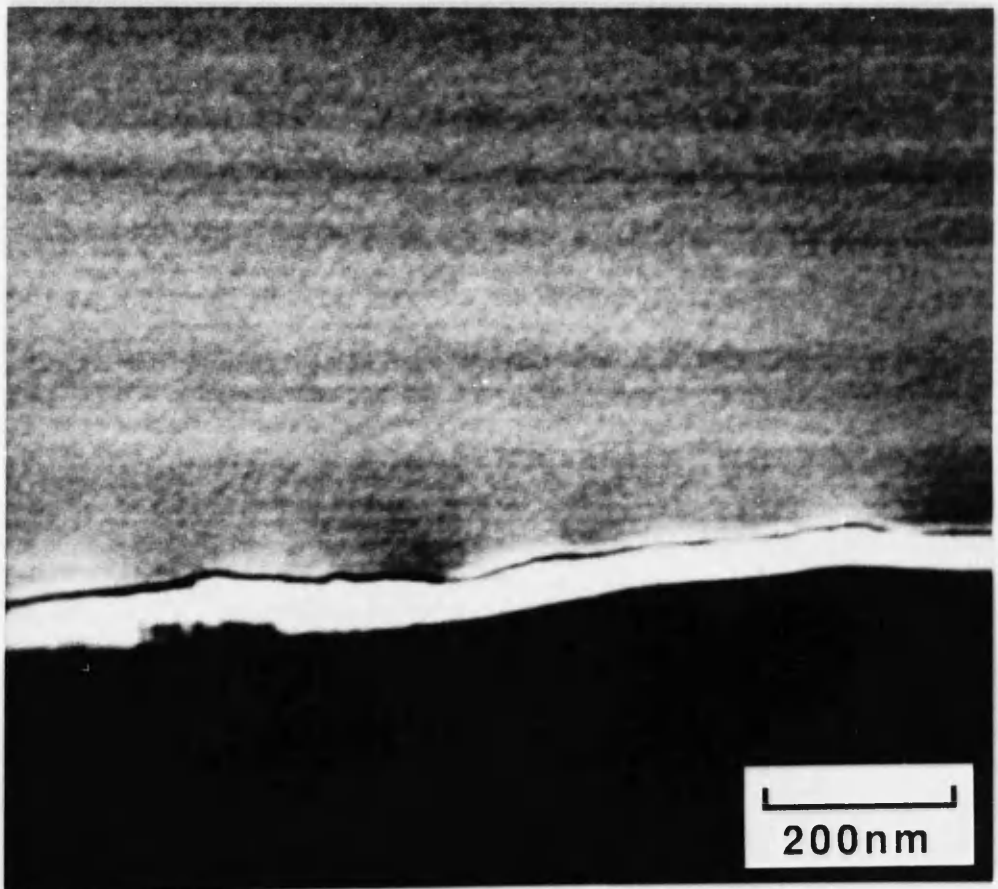


Figure 5.11 DPC image of a cross-section of the high Ts film.

whole CoCr layer had become detached from the substrate. In this image the section is shown with a free space background and stray field on only the right-hand side of the film. The lack of stray fields on the left-hand side is attributable to the disordered layer at the base of the columns. As explained in chapter 1, this layer has a significant in-plane magnetic anisotropy which provides a path for flux closure within the film. It can also be seen from this image that the thickness of the CoCr was again such that there was no signal variation within the film itself.

Figure 5.11 shows a DPC image of a cross-section acquired using the second DPC operating mode (C1 + objective weakly excited). In this section the CoCr has not thinned sufficiently to see the columnar structure.

5.4.1 Composite Images For The High Ts Film

Figure 5.12 shows the sum, DPC and resulting composite images of the best cross-section prepared from the high Ts film. Unfortunately the CoCr layer is still attached to the substrate although the stray fields and physical microstructure are both evident. In this image the contrast generated by the stray fields is much lower than for the low Ts image shown in figure 5.8. This is partly as a result of contamination problems which were severe with this specimen, even after flooding. These restricted both the number of integrations and the period of time which could be spent optimising the acquisition conditions for a given area. This is manifested in the high level of noise modulating the free-space background.

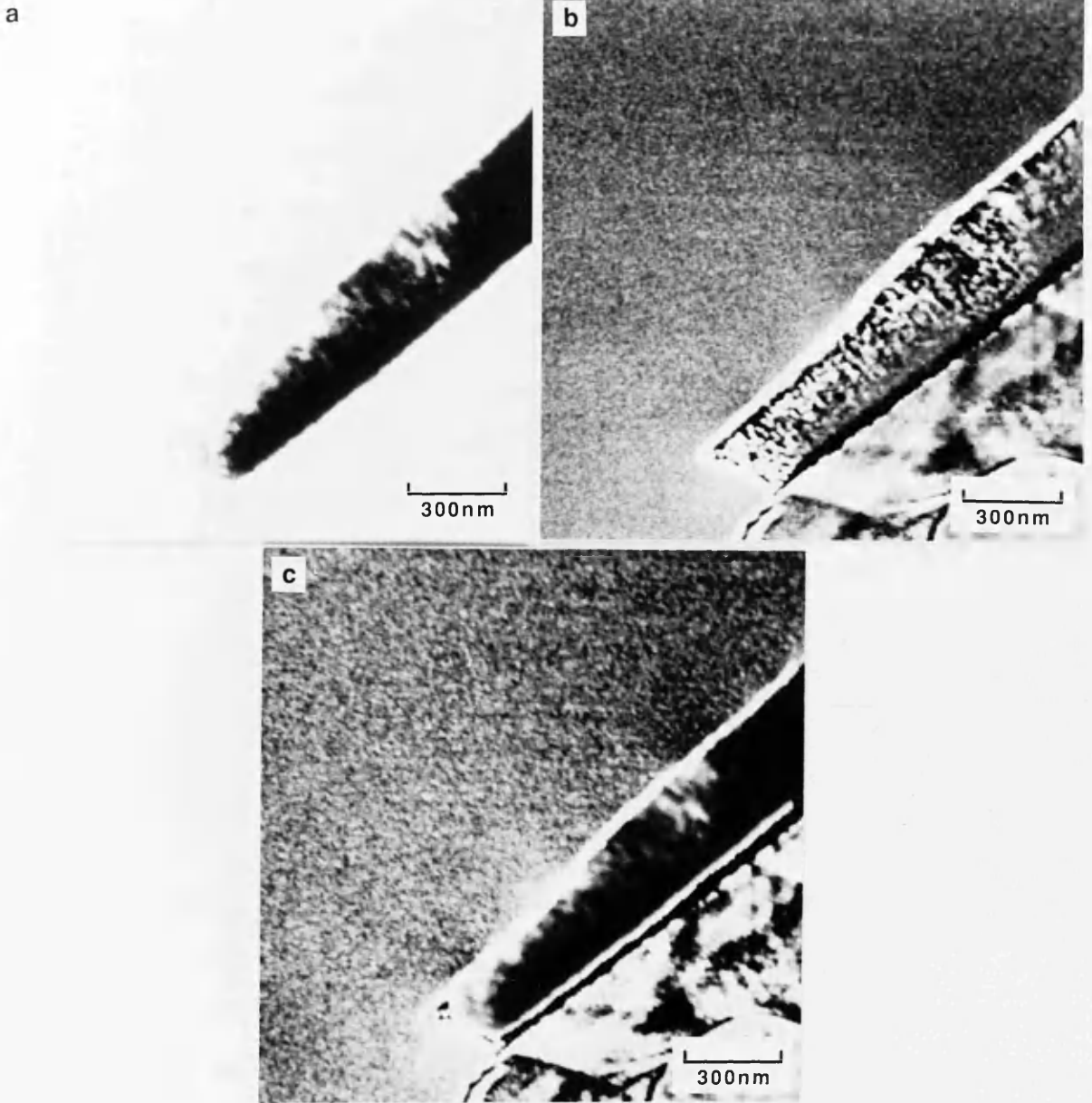


Figure 5.12 This figure shows a) the sum and b) the corresponding DPC image which were used to construct c) the composite image of a high T_s cross-section.

5.4.2 Results

From DPC images of the cross-section of the high Ts film shown in figure 5.10 it can be seen that there is less variation in domain size (70-130nm) than for the low Ts sections. The mean stray field spacing with corresponding standard error, over 27 reversals, was found to be $112 \pm 10\text{nm}$. The mean column diameter in this case again was between 40 and 50nm (see chapter 4). From the thicker cross-section shown in figure 5.11 the mean stray field spacing over 8 reversals was $89 \pm 6\text{nm}$ whilst for the thinner section shown in figure 5.12 a mean of $105 \pm 11\text{nm}$ was calculated over 18 reversals.

5.4.3 Discussion

The mean domain sizes for these cross-sections are smaller than those for the low Ts film. This is compatible with a reduced level of exchange coupling. The mean domain size is $\sim 2\text{-}3\times$ the mean column diameter. These figures are consistent with groups of columns acting as independent magnetic units (ie more particulate in nature - see Zhu & Bertram 1989).

Whilst it is not clear that domain wall energy is a valid concept for particulate media a value was calculated for comparison with the results in section 5.3.3. Making the assumption that vertical domains again extend through the whole thickness of CoCr, γ was calculated using equation 5.1 and the data given in table 5.1. This gave a value of 1.3mJ.m^{-2} for the mean domain wall energy. With a μ^* , from equation 5.2, of 2.59 substituted into equation 5.3, a corrected value of 1.0mJ.m^{-2} was obtained. Bernards (1990) estimates a value for γ of 0.6mJ.m^{-2} from the slope of the hysteresis loop at remanence.

The reduction in γ , relative to the low T_s film, can be explained as a result of the boundary segregation of Cr (chapter 4). This may cause an effective lowering in γ where the domain wall happens to coincide with a column boundary.

5.5 STRAY FIELD SIMULATION

In the above investigation it was assumed that the external stray field distribution revealed the position of the internal magnetic domains. This assumption was based, in part, on there being perfect alignment of the direction of sensitivity to magnetic induction with the domain magnetisation. It was therefore important to see to what extent slight rotational misorientation of the quadrant detector with respect to the specimen would produce a shift in the apparent position of the domain boundaries.

From equations to calculate the x, y and z components of magnetic field from a single uniformly magnetised block (see figure 5.13a) McFadyen (1986) showed that it was possible to produce vector maps of stray field distributions. In these models arrows proportional to the logarithm of the component of magnetic induction integrated with respect to z were plotted at a number of regularly spaced field points.

A program was written by McVitie (1988) to calculate the x, y and z components of magnetic field from a single uniformly magnetised block. To model the stray field distribution produced by a CoCr cross-section this program was adapted to calculate the integrated x and y components of magnetic induction from six uniformly magnetised blocks placed side by side. Adjacent blocks/domains had anti-parallel

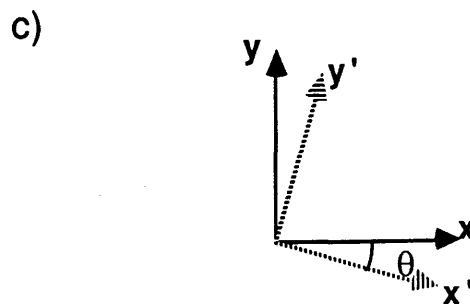
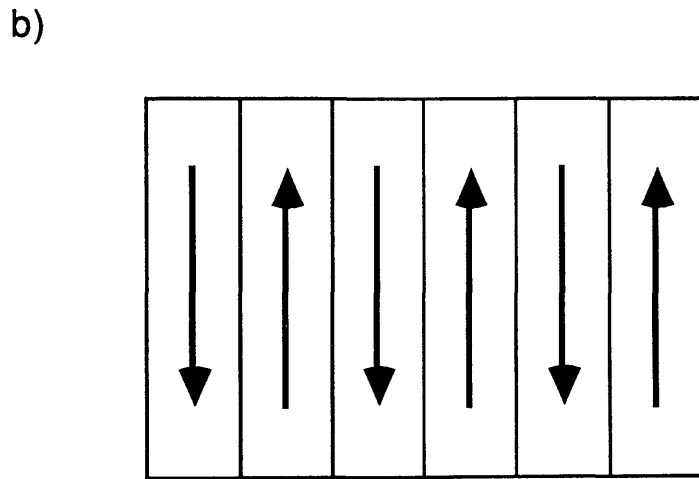
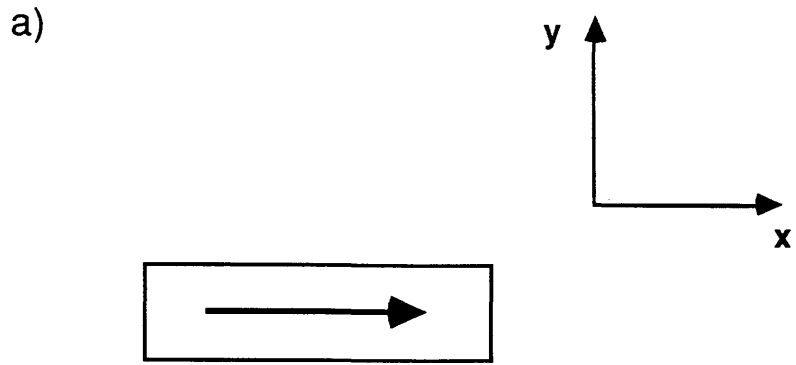


Figure 5.13 Schematics illustrating a) a uniformly magnetised block, b) a cross section consisting of 6 block like domains and c) rotation of the direction of sensitivity to magnetic induction.

magnetisation directed along the y-axis (figure 5.13b). Further adaptations were made to calculate the x' and y' (see figure 5.13c) components of magnetic induction from the blocks for axes rotated through an angle θ in the x-y plane about a common origin. This simulated a rotation of the quadrant detector with respect to a cross-section. The x' and y' components of integrated induction were then scaled to range from 0 to 255. This data constituted contrast levels with which it was possible to generate images with orthogonal directions of sensitivity to magnetic induction (Ferrier 1989). In this way the DPC images for a range of detector orientations could be simulated.

The simulation program was run for 100keV electrons incident on a 304nm thick film comprising 6 vertical domains with saturation induction of 0.58T and a domain size of 160nm (the data for the low Ts cross-section in figure 5.8). The image was divided into 64 x 50 pixels of 16 x 16nm. Figure 5.14a shows the pair of images generated for perfect detector alignment with both the internal magnetic domains and external stray fields visible. Figures 5.14b and c show the pairs of simulation images for rotations of 10° and 20° respectively. It can be seen from these images that for a rotation of 20° in the quadrant alignment the stray fields suggest a difference between the apparent and the actual domain position which is a significant fraction of the domain width. For a rotation of 10° in the quadrant alignment the offset in the domain position, whilst it is only a small fraction of the domain size, is a significant fraction of a column diameter. Thus a quadrant misorientation of 10° is not acceptable when trying to deduce the exact position of the domains.

These models have shown that detector orientation is important if detailed study of the domain position is required. For investigations

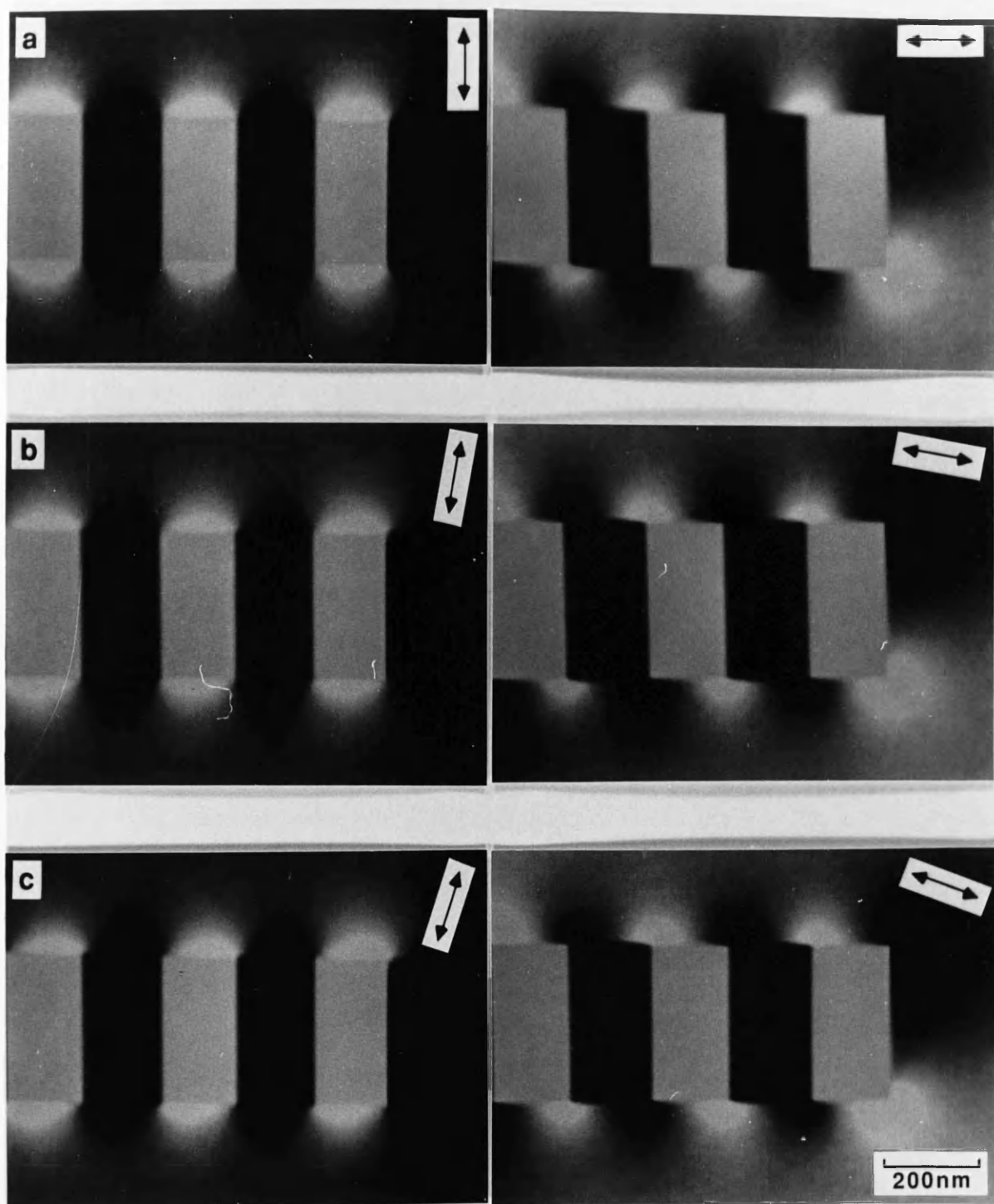


Figure 5.14 Simulation of DPC image of stray field distribution of cross-section for a) perfect detector alignment, b) an offset of 10° and c) an offset of 20° .

such as those in sections 5.3 and 5.4 detector alignment should therefore be as accurate as possible.

5.6 GENERAL DISCUSSION AND CONCLUSIONS

Although each cross-section examined in this study was of slightly different depth and thickness, a histogram was generated showing the distribution of stray field spacings for both films over all the cross-sections (figure 5.15). From this it can be seen that the high Ts film has a narrower distribution with no reversals larger than 220nm and a mean domain size of 106nm. The low Ts film has a wider distribution with a mean of 142nm and spacings up to 400nm (ignoring the values greater than 300nm gives a mean of 134nm). These domain sizes are of the same order of magnitude as found in neutron depolarisation studies of similar films (Kraan et al. 1987).

The smaller domain sizes and the energetic favourability of domain wall formation in the high Ts film suggest less exchange coupling at column boundaries than in the low Ts film. This is consistent with the Cr segregation to the column boundaries reported for the high Ts films in chapter 4 (section 4.3). Therefore a more particulate model seems appropriate for the high Ts film domain structure whilst a stripe-type domain model is probably applicable for the low Ts film. This is in accordance with the lower noise levels found in recording experiments with high coercivity layers (Bernards et al. 1989).

In conclusion we can say that the major problem encountered in performing these investigations was the difficulty in preparing suitable cross-sections. The results presented in this chapter show, however, that with good specimens DPC microscopy is a very powerful technique for

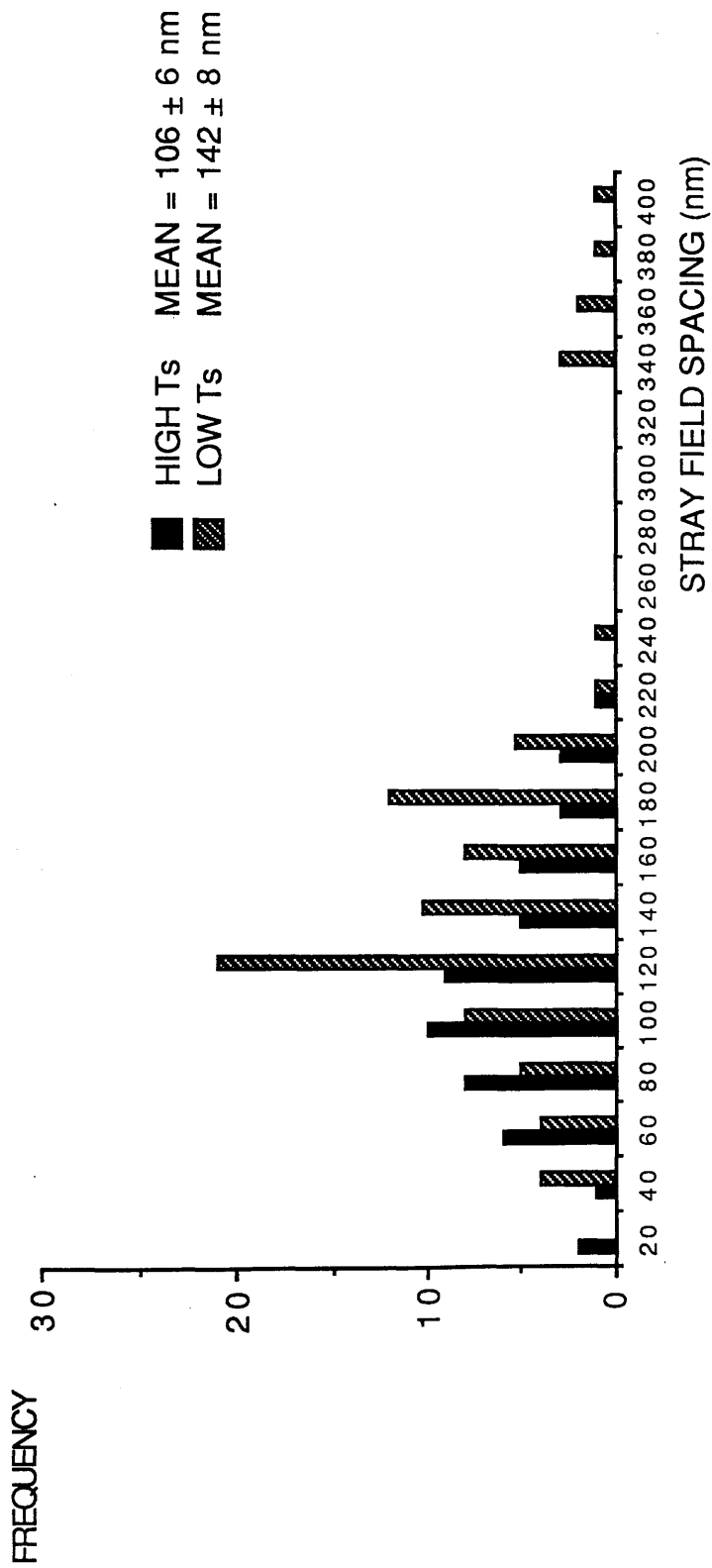


Figure 5.15 Histogram showing the distribution of stray field spacings measured for the high and low Ts films.

micromagnetic studies of CoCr thin films.

CHAPTER 6 - LORENTZ MICROSCOPY OF TRACKS IN PERPENDICULAR CoCr

6.1 INTRODUCTION

Recording experiments and frequency response curves are very difficult to interpret on the scale of individual data units (figure 6.1) (Luitjens 1988). To investigate the behaviour of the magnetic pattern written on a recording medium it is desirable to have direct images of the tracks. There have been many attempts at microscopic imaging of tracks in perpendicular recording media. Amongst the more successful of these have been Bitter decoration (Nishimoto 1984) and electron holography (Yoshida 1987). Such reports indicate, however, that the considerable difficulties associated with imaging perpendicular tracks (see below) have exposed the limitations of these techniques (see chapter 2). A more successful method for imaging perpendicular tracks is still actively being sought.

This chapter is concerned with investigations into the possibility of imaging perpendicular tracks in CoCr thin films using Lorentz microscopy. The first part of the chapter describes the combination of technical improvements which made the experiments feasible in a TEM and the problems that were encountered in conducting the experiments. The concluding sections explain the successful technique and present and discuss images of the tracks.

**TRACK INFLUENCED BY CONFIGURATION
OF COLUMN BOUNDARIES** **TRACK UNINFLUENCED BY COLUMN
BOUNDARIES**



Figure 6.1 Schematic illustrating two possibilities for track configuration in CoCr.

6.2 RECORDING ON FILMS THIN ENOUGH FOR TEM INVESTIGATIONS

In TEM study of recorded tracks there are certain advantages to the use of planar rather than cross-sections of films. Planar sections allow the observation of recorded tracks over a much larger area of specimen and, if the film is thin enough ($\leq 200\text{nm}$ thick for 100keV electrons (Morrison 1981)), it is possible to look at unthinned sections in which there is no alteration of the microstructure or the recorded pattern. This is not possible with cross-sections.

Until recently signal to noise ratios with perpendicular recording systems were such that perpendicular tracks could only be written effectively onto CoCr layers $> 200\text{nm}$ thick. Recent developments in recording-head performance and media properties, however, have enabled the recording of tracks on CoCr layers down to 85nm thick. This is thin enough for examination in a TEM and as a result makes the study of "as-written" perpendicular tracks a possibility.

6.3 SPECIMEN PREPARATION

Two pairs of CoCr films were prepared for analysis by rf sputter deposition from a 21.5 atomic % Cr target onto a $12.5\mu\text{m}$ thick polyimide substrate. The first pair of films had a CoCr layer 85nm thick deposited onto a 15nm thick underlayer of Ge. The second pair had a CoCr layer 100nm thick deposited onto a Au underlayer. This Au underlayer served as a nucleation layer in the same way as Ge but had the added advantage that it could easily be chemically removed.

Substrate temperature during deposition was $\approx 160^\circ\text{C}$ for the first of each pair of films. The resultant mean perpendicular coercivity in both cases was 50kA.m^{-1} . For the second of each pair of films, with substrate temperatures of 50°C , the perpendicular coercivity was 15kA.m^{-1} . Tracks $27\mu\text{m}$ wide were recorded on each medium using a metal-in-gap ring head with a gap of $0.25\mu\text{m}$ (Luitjens et al. 1988, Bernards et al. 1987). Digital recordings were made with alternating bit magnetisation at wavelengths of 10, 2, 1, 0.5, 0.25, 0.2 and $0.125\mu\text{m}$ respectively.

Planar samples were prepared for analysis by mounting a section of each film on a specimen grid, as in chapter 3, and dissolving away the substrates (see chapter 4) and Au underlayers. The Au layer was dissolved using a KI/I_2 solution.

6.4 EXPERIMENT

Initial CTEM investigations at Philips Research Laboratories pinpointed a major problem to be overcome in order to observe the recorded tracks. The crystallographic contrast was so strong that it was likely to swamp any magnetic signal of interest. Since the tracks would generate weak signal at best this increased the difficulty of the search.

6.4.1 Specimen Tilt and Magnetic Deflection Angle

In a TEM, with an untilted specimen, the magnetisation within perpendicular tracks is oriented along the direction of motion of the electron beam. Thus there is no deflection of the transmitted beam. To induce a component of magnetic induction perpendicular to the

direction of motion of the beam a tilt is applied to the specimen. For the maximum magnetic deflection the axis of rotation should be in the plane of the film and oriented along the track direction. A tilt angle was desired for which little Bragg reflection occurred so that a larger proportion of the transmitted electrons remained in the central spot of the diffraction pattern and crystallographic contrast variation in the image was reduced. A tilt angle which fulfilled this requirement was found to be approximately 24° .

For saturation induction, B_s , of 0.53T the component of magnetic induction, perpendicular to the direction of motion of the beam for a specimen tilt angle of 24° , is 0.22T. The maximum magnetic deflection angle for 200kV electrons was estimated from this (using equation 2.4) to be approximately 1.2×10^{-5} rad, taking the film thickness to be 85nm. From equation 2.4 we can see that the magnetic induction in the recorded tracks, B_t , is proportional to β . Therefore we define k as:

$$k = \frac{B_t}{B_s} = \frac{\beta}{\beta_s} \quad 6.1$$

where β is the deflection angle for a magnetic induction of B_t and β_s is the deflection angle (for the same specimen tilt) corresponding to saturation induction.[†] Thus, if we have a measure of the magnetic deflection in the beam, we can estimate the track magnetisation. This can then be compared with the remanent magnetisation measured using a VSM (see table 6.1). For the high coercivity film on Ge the deflection for remanence was estimated to be $\leq 1.9 \times 10^{-6}$ rad for a specimen tilt of 24° (again using equation 2.4).

[†] It should be noted that stray field above and below the medium will contribute to the deflection in the beam.

CoCr LAYER	PERP. H_c (kA.m ⁻¹)	M_r / M_s	M_s (kA.m ⁻¹)
85nm on Ge	15	0.05	420
85nm on Ge	50	0.16	420
100nm on Au	15	0.09	420
100nm on Au	50	0.20	450

Table 6.1 Magnetic data for films examined in chapter 6.

6.4.2 Lorentz Microscopy

DPC imaging in the HB5 STEM was unsuitable for these studies because of the 100kV limit for the accelerating voltage. With this thickness of specimen, a relatively large proportion of the total number of 100keV electrons incident on the specimen undergoes inelastic or thermal diffuse scattering, leaving less electrons in the central spot of diffraction pattern. This produces an ill-defined central diffraction spot surrounded by comparable intensities of diffuse electron scattering. This in turn makes it very difficult to detect a magnetic deflection of the magnitude expected for the tracks and no success was achieved in practice.

The JEOL 2000 FX CTEM was employed for Low Angle Diffraction (LAD), Foucault and Fresnel studies. With a 200kV accelerating voltage a greater proportion of the electrons pass through the specimen unscattered. This gives improved definition in the central diffraction spot and makes it easier to detect a small deflection.

The track direction was deduced in these films from score marks on the medium, which were probably caused by dust particles trapped on the head during recording. Extensive investigations in the Foucault mode failed to reveal any trace of tracks and so it was decided to examine the LAD pattern for evidence of a magnetic deflection in the transmitted beam. At the longest camera length on the 2000FX (80m) no splitting of the central spot was observed. For spot size 7 the diameter of the central spot at this camera length was of the order of 0.1mm, corresponding to a semi-angle at the specimen of 1.3×10^{-6} rad. Scattering in the specimen, however, led to a spot approximately 2mm in diameter. This corresponds to a semi-angle at the specimen of

approximately 2.5×10^{-5} rad. Thus it was not possible to detect a deflection of the order produced by the tracks in this way. It was therefore highly unlikely that it would be possible to image the tracks using Foucault microscopy.

Further efforts to image the tracks employed the Fresnel mode of Lorentz microscopy. In this mode it was known that, because any deflection would be small, a large value of defocus would be necessary. Studies were conducted at magnifications up to 1000X. At these magnifications the objective lens is not excited and the objective-mini (OM) is the image forming lens. With the objective lens switched off the resolution is considerably reduced. Detail on the scale of the columnar structure is therefore not as distinct as detail on the scale of the track wavelength. Initial attempts at selecting an appropriate defocus, made using binocular observation of the fluorescent viewing screen, were unsuccessful. A video camera installed under the camera chamber was employed to determine the correct conditions for imaging the tracks. The signals from the camera were used to generate images which passed through an Arlunya image processor. With this, static or dynamic noise reduction through frame averaging was possible during the experiment. Images viewed with this system were stored on 8mm video tape.

Perpendicular tracks were eventually imaged, but only for the high coercivity film with the Ge underlayer. It is not clear why tracks were seen only in the high coercivity film on Ge and not in the high coercivity film on Au, although it could have been partly attributable to the increased crystallographic contrast because the CoCr layer was 15nm thicker in the latter case. The operating conditions employed were a condenser aperture of either 70 or 120 μ m and spot size 2. A large SAA aperture (300 μ m) was inserted to remove Bragg scattered

electrons from the transmitted beam. Tracks of $2\mu\text{m}$ wavelength were the first seen and initially only in static, integrated images with noise filtration. When conditions were optimised using this technique, tracks could be observed on the fluorescent viewing screen with the naked eye. For each detectable track wavelength long exposure micrographs were acquired both in-focus and at a range of defoci. Images were obtained for the tracks recorded at 10, 2, 1 and $0.5\mu\text{m}$ wavelengths. Figures 6.2-6.5 show micrographs of typical tracks for each wavelength together with the corresponding in-focus images.

To estimate the magnetic deflection in the beam from these images it was necessary to know the defocus, δu , of the OM lens. In order to estimate this, however, the focal length of the OM lens in low magnification mode was required.

6.4.4 Focal Length of Objective-Mini Lens in the JEOL 2000FX

The image plane of the OM lens was set at the SAA plane by simultaneously forming a focused image of both the specimen and the SAA aperture on the viewing screen. For this lens setting the distance from specimen plane to the OM lens plane was the object distance (83mm) and the distance from the lens plane to the SAA plane was the image distance (71mm). From these values a focal length, f_1 , of 38.3mm was obtained using the standard lens equation.

Using this focal length and the respective OM lens currents for this mode and normal low magnification mode operation, it was possible to calculate the low magnification mode OM focal length, f_2 , using the relation:

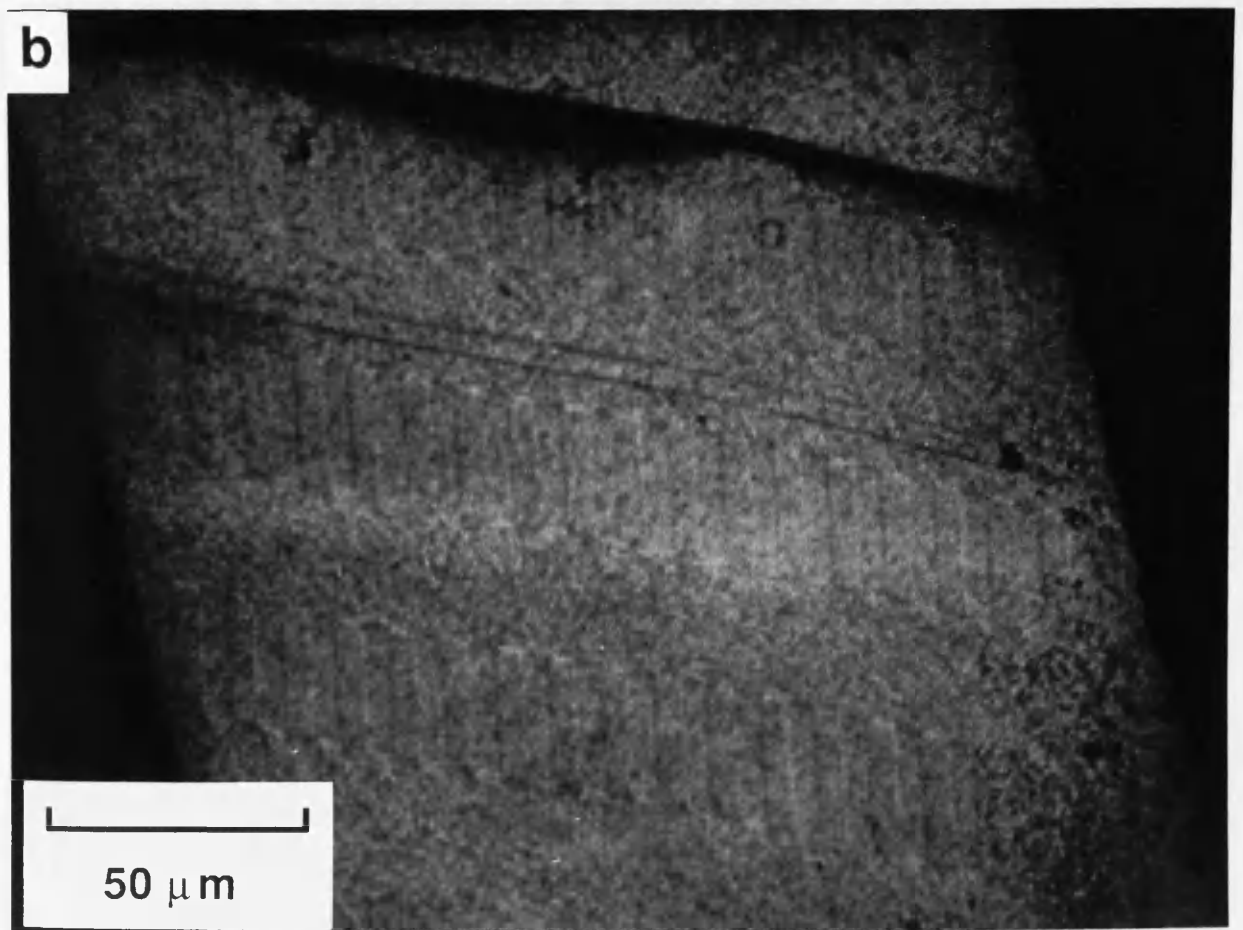
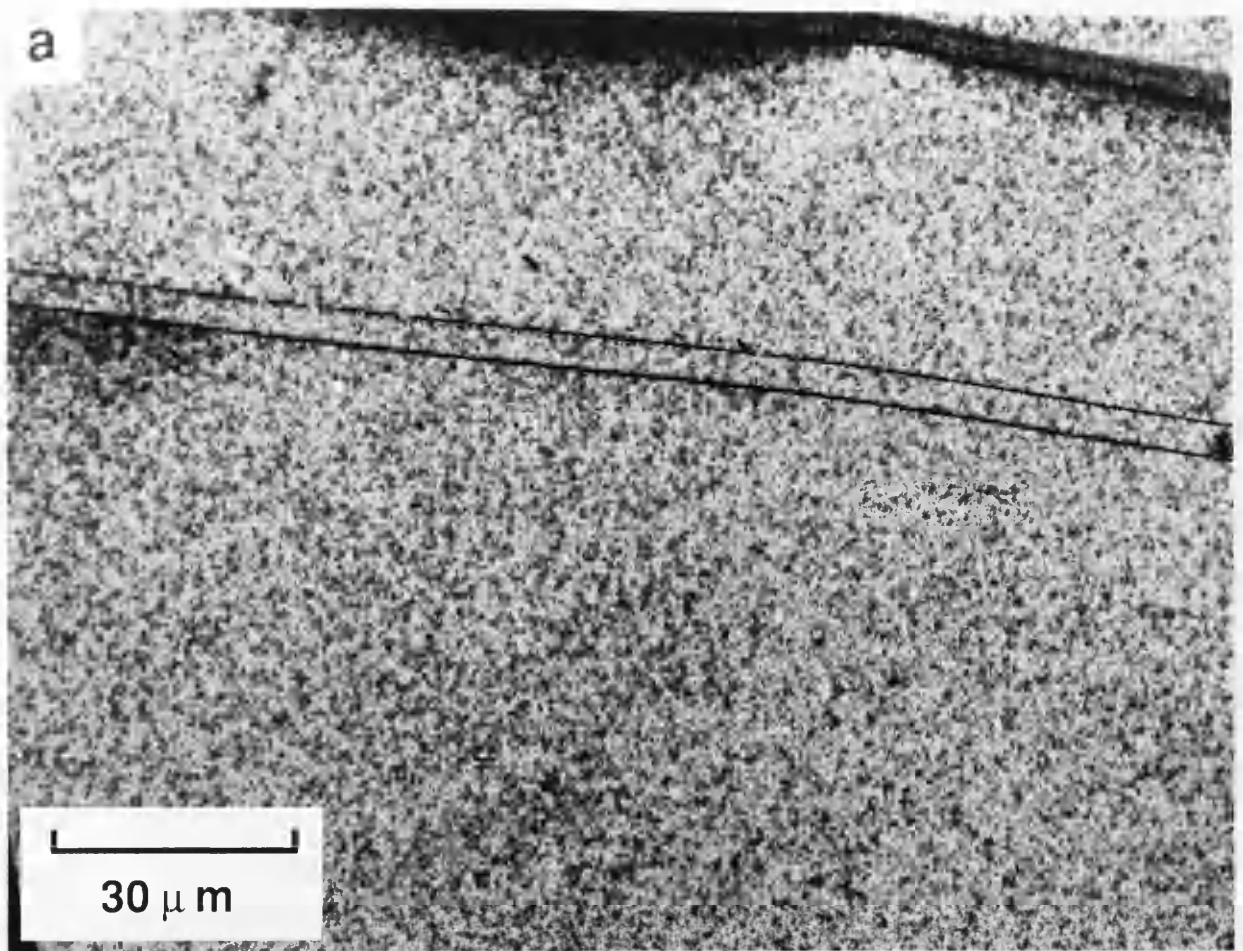


Figure 6.2 a) In-focus image and b) corresponding Fresnel image of 10 μm tracks in CoCr.

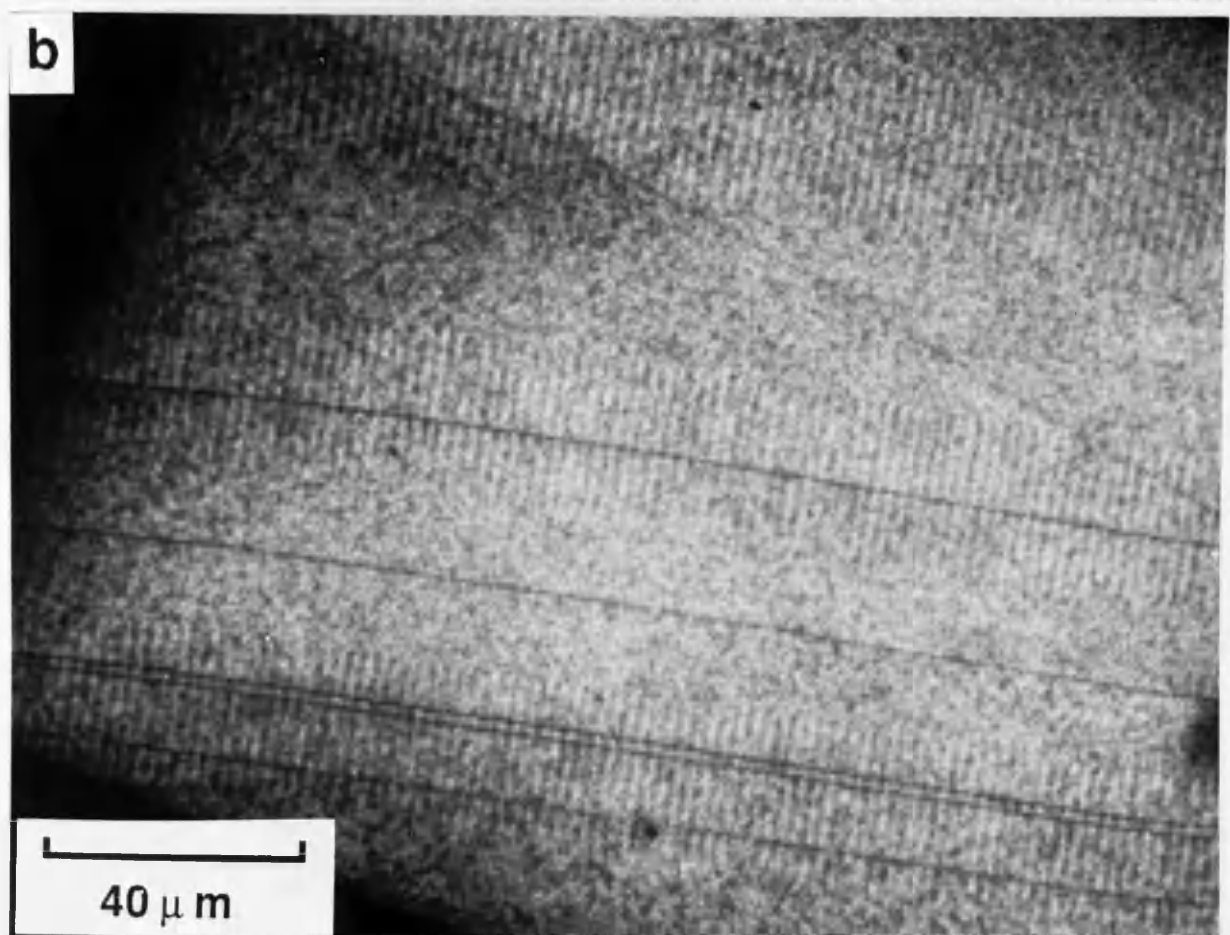
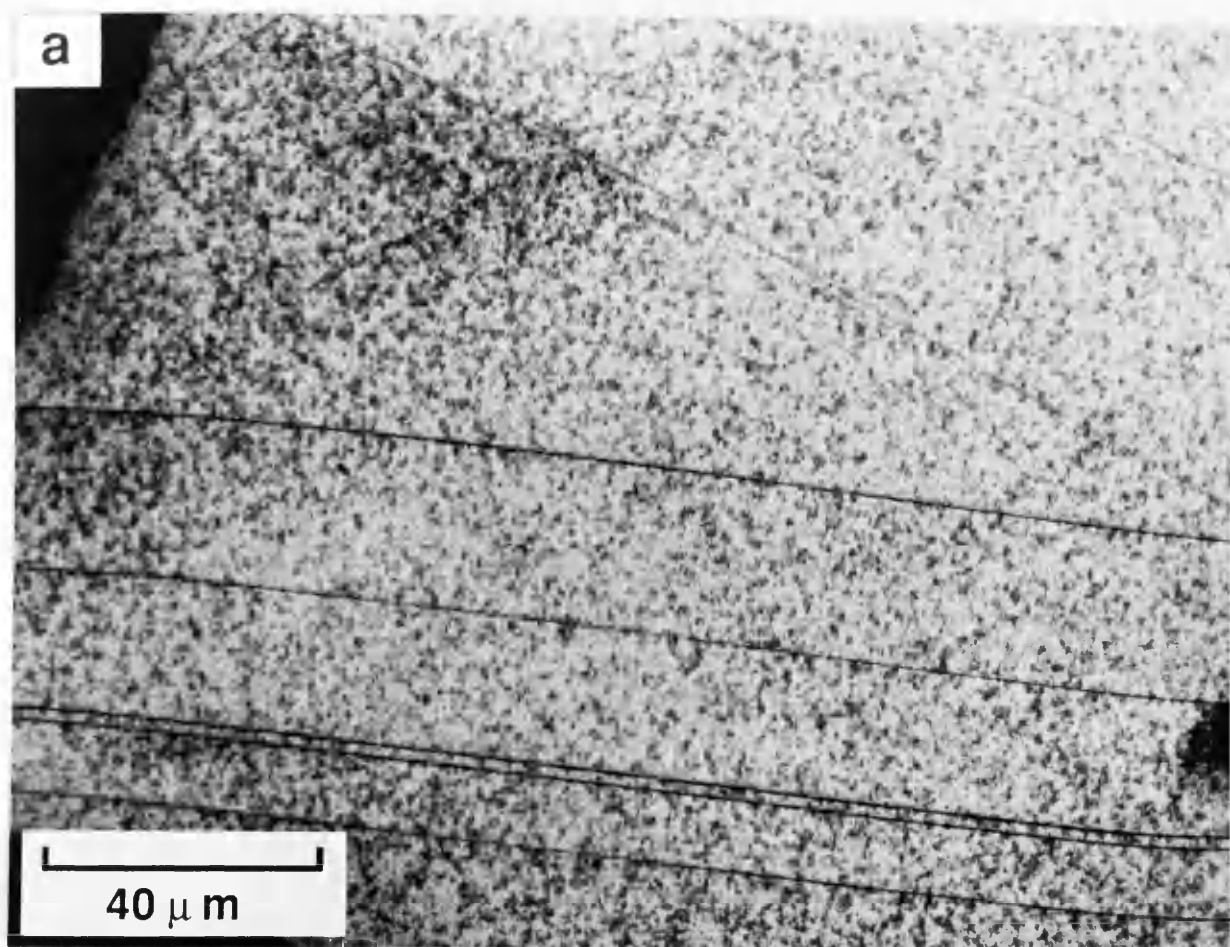


Figure 6.3 a) In-focus image and b) corresponding Fresnel image of 2μm tracks in CoCr.

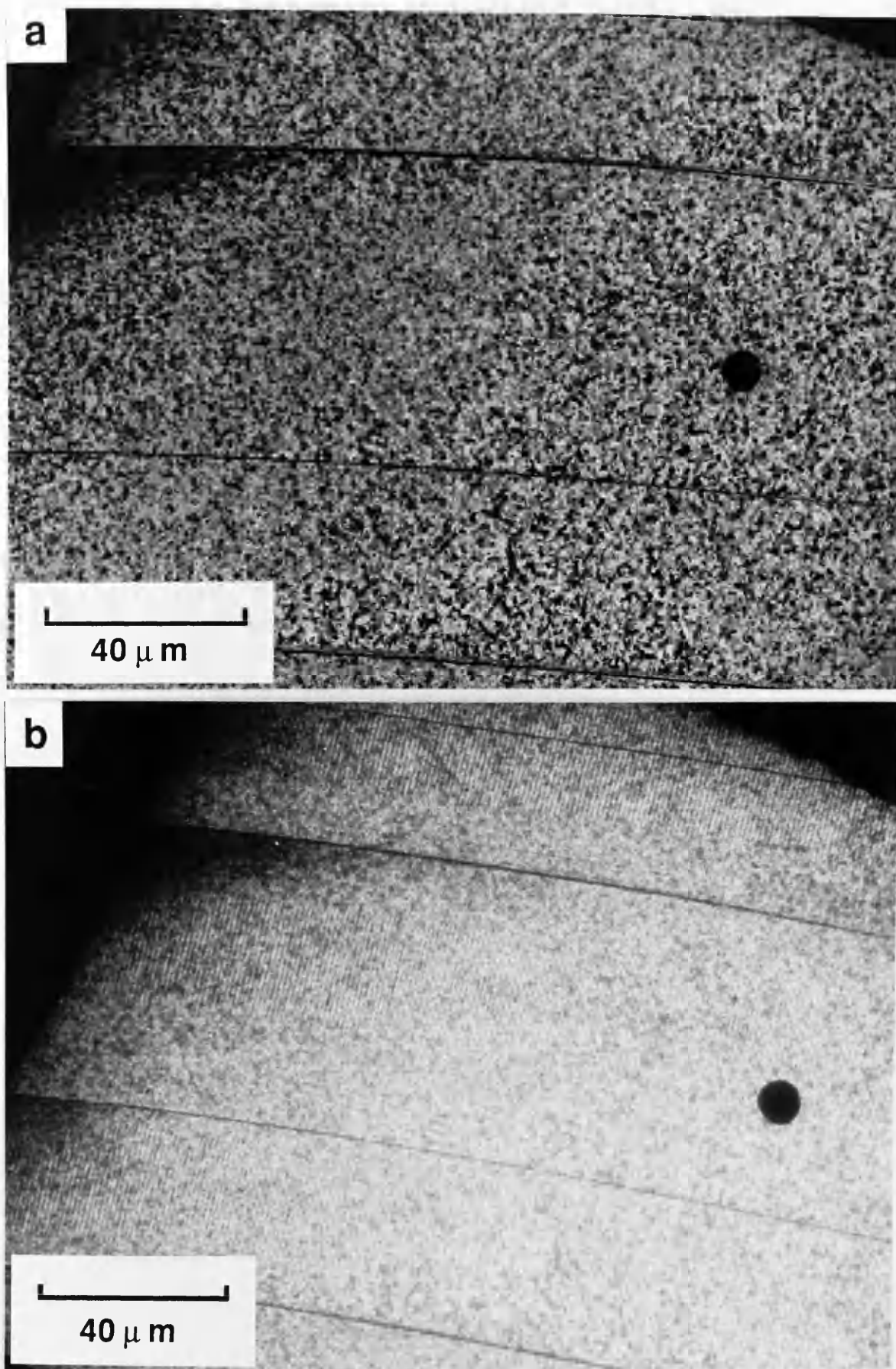


Figure 6.4 a) In-focus image and b) corresponding Fresnel image of 1μm tracks in CoCr.

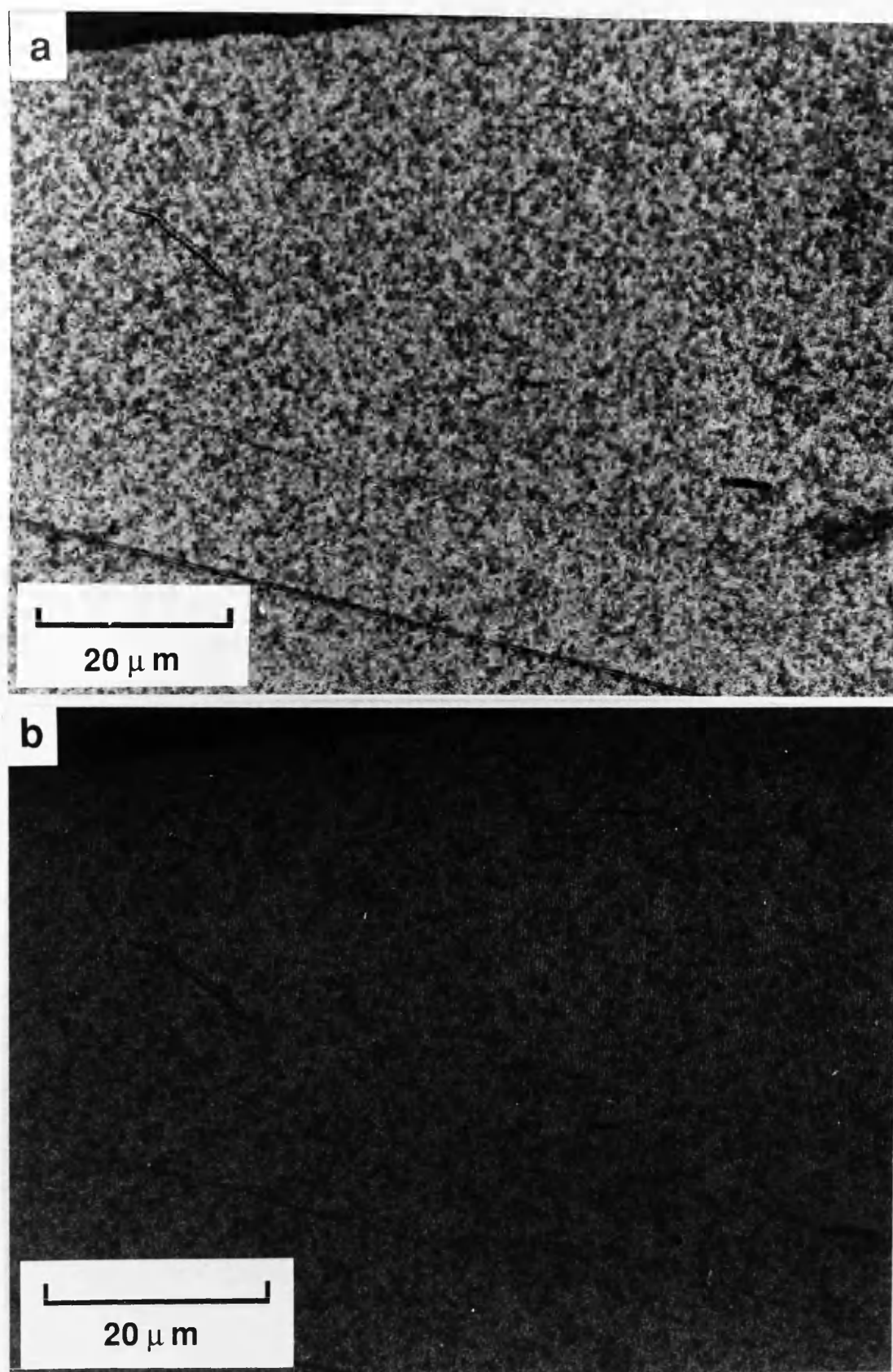


Figure 6.5 a) In-focus image and b) corresponding Fresnel image of 0.5μm tracks in CoCr.

$$\frac{f_1}{f_2} = \frac{I_2^2}{I_1^2} \quad 6.2$$

where I_1 is the lens current with the image plane in the SAA plane and I_2 is the in-focus lens current in low magnification mode. From this equation a low magnification mode OM focal length of 20.5mm was obtained. When combined with the known object distance this gave an OM lens magnification of 0.33X and an image distance, v , of 27.3mm.

6.5 RESULTS AND DISCUSSION

For each image the ratio of the magnification with the OM lens defocused, M' , to that with the lens focused, M , was deduced by measuring the relative sizes of features in the in-focus and defocused images (see table 6.2). From this ratio M' was calculated (see table 6.2). With knowledge of M' and v it was possible to calculate the object distance, u , and therefore the defocus, δu (see table 6.2).

These results show that for optimum images of tracks, less defocus was required for shorter wavelengths. This is because the width of the domain wall image represents a larger fraction of the track wavelength and therefore less defocus can be used before adjacent walls broaden sufficiently for their images to overlap. Crystallographic contrast is stronger in images of tracks with shorter wavelengths because there is less defocus. This explains the inability to image tracks with wavelengths shorter than 0.5 μ m.

In the images of the three shorter wavelength tracks it is impossible

WAVELENGTH (μm)	M'/M	M'	u (mm)	δu (mm)
0.5	0.72	0.24	110 ± 10	30 ± 10
1	0.48	0.16	170 ± 10	90 ± 10
2	0.38	0.13	220 ± 10	140 ± 10
10	0.27	0.09	310 ± 10	220 ± 10

Table 6.2 Magnifications and defoci of OM lens for images of tracks in figures 6.2 - 6.5.

to distinguish the width of the domain wall from half of the track wavelength. For the $10\mu\text{m}$ tracks, however, an estimate of the wall width, distinct from the domain size, can be made. If the width of the domain walls in the Fresnel image in figure 6.2 (375nm) is taken to correspond to an angle at the specimen of $2\beta.\delta u$. It is possible to make an estimate of β using the data from table 6.2. This gives a value for β of approximately 0.9×10^{-6} rad for the $10\mu\text{m}$ tracks. Thus k is approximately 0.07. This is approximately half the value for the ratio of remanent magnetisation to saturation magnetisation for this film (0.16) and corresponds to a magnetisation of 30kA.m^{-1} . The difficulty in measuring the width of the wall in the image, however, is too large for any conclusions to be drawn on the difference between this value and the remanent magnetisation.

6.6 CONCLUSIONS

The images in figures 6.2-6.5 show that perpendicular recordings in CoCr thin films can be imaged "as-written" in the electron microscope. The lack of success in imaging the tracks with the Foucault mode can be attributed to the magnetic deflection in the beam being too small for this mode to detect. Tracks were successfully imaged using the Fresnel mode of Lorentz microscopy, although no direct links with the physical microstructure could be made. For $10\mu\text{m}$ tracks it was possible to estimate the magnitude of the magnetic deflection in the beam and the track magnetisation. At the moment, however, this technique is of limited use for quantitative analysis of recorded tracks in perpendicular recording media.

Tracks in these films have also been imaged using Magnetic Force

Microscopy (Bernards & den Boef 1990). In these investigations an interferometer was used to detect changes in amplitude and phase of the oscillating tip (4kHz) when passed over the tracks. Tracks were imaged down to wavelengths of $0.25\mu\text{m}$. As in the case of the Fresnel images in this chapter, however, it has proved difficult to draw any quantitative conclusions.

CHAPTER 7 - CONCLUSIONS AND FUTURE WORK

The aim of this project was to investigate the relationship between the physical and magnetic microstructure of CoCr thin film recording media. Studies concentrated on improving a combination of TEM techniques adopted by McFadyen (1986) and applying them to investigations of a series of CoCr films with systematically adjusted growth conditions. In this chapter the conclusions from each of the experimental chapters are reviewed and discussed in terms of the study as a whole. Proposals are then put forward for future work.

7.1 CONCLUSIONS

7.1.1 Basic Characterisation

The experiments in chapter 3 showed that it was not possible to deduce the exact effect on the physical microstructure of changing a particular growth parameter without direct microscopic observation of cross-sections and planar sections of the film. The characterisation techniques themselves were shown to be useful for deciding which films to study in subsequent chapters and for obtaining information necessary to interpret the magnetic microstructure. Since the same planar and cross-section preparation techniques were adopted for the EDX and DPC studies, the knowledge gained regarding the limitations and possibilities with specimen preparation was also very useful.

7.1.2 Microcompositional and Micromagnetic Studies

Both microcompositional and micromagnetic studies were conducted in the extended VG HB5 STEM.

For the EDX microanalysis described in chapter 4 the use of ion-milled planar sections allowed the probe to be accurately located on a particular feature of the microstructure. This reduced the correction factors employed in previous studies (McFadyen 1986, Chapman et al. 1986). In addition, high angle ADF imaging was shown to be a useful imaging mode with which to locate the column boundary phase. The technique is now such that, with suitable specimens, the spatial resolution can be up to 2nm and for a given region of specimen we can detect variations of less than 1 in the mean atomic fraction of Cr, X.

Results from these experiments showed that increased substrate temperature during deposition had a different effect on the elemental distribution if a Ge underlayer was present or absent. The highest level of segregation was observed at the column boundaries in the film deposited directly onto PET at high Ts (90C). These showed a composition of $\text{Co}_{73}\text{Cr}_{27}$ whilst no evidence of elemental segregation was observed for the film deposited at low Ts (30C). With a Ge underlayer present, no significant boundary segregation of Cr was observed for films deposited at high or low Ts. For the low Ts film on Ge, however, Cr segregation towards the column centres was observed. The difference between the findings with and without a Ge layer showed that the pattern and extent of any Cr segregation was dependent on more than one growth parameter.

Analysis of specimens from a different source in which preferential

chemical etching of Co had suggested there would be a strong pattern of Cr segregation showed some evidence of boundary segregation of Cr, with a mean increase in X of 1.5 for the "frog-egg" sample and 1.7 for the "chrysanthemum pattern" sample.

The DPC mode of Lorentz microscopy was used to study the magnetic microstructure of some of the same films investigated using EDX microanalysis. The use of ion-milled cross-sections and the adoption of an imaging mode reported by Chapman et al. (1978) were the improvements on the technique employed by McFadyen (1986). DPC images of thin cross-sections revealed magnetic domains extending throughout the entire thickness of the CoCr layer. With the modified technique it was possible to obtain simultaneous images of the physical microstructure and the stray field distribution to a resolution of the order of 3nm. Using these images composite images revealing both the internal columnar structure and the external stray fields were formed.

Such composite images could be used to infer the positions of the domains with respect to the columnar structure provided the orientation of the detector was such that the direction of sensitivity to magnetic induction was aligned with the direction of magnetisation in the domains. Although it would have been ideal to investigate all the samples on which compositional studies had been conducted, difficulties with specimen preparation were such that DPC images were obtained only for the pair of samples deposited directly onto PET. The domain size was on average bigger for the low Ts film (142nm). The smaller domain size (106nm) observed for the high Ts film suggested that the extent of exchange coupling at column boundaries was lower than for the low Ts film. This was in accordance with the higher level of Cr at the column boundary found in the EDX work. With direct images of smaller domain spacings for high Ts films and compositional analyses

showing that the boundaries become predominantly non-ferromagnetic in nature at high T_s , each technique is independently consistent with the high T_s film being more particulate in nature.

The results show that by changing only one growth parameter at a time it was possible to isolate and study the effect of two of the most important parameters affecting the physical and magnetic microstructure and the local elemental distribution. EDX microanalysis and DPC imaging were therefore seen to be complementary techniques, a combination of which provided an integrated method for direct quantitative study of some of the fundamental mechanisms controlling the domain configuration in CoCr thin films.

7.1.3 Lorentz Microscopy of Perpendicular Tracks

Chapter 6 describes investigations into the possibility of imaging perpendicular tracks using Lorentz microscopy. Unthinned CoCr layers were examined. Strong crystallographic contrast proved to be the major obstacle to obtaining images of the tracks. Tracks were, however, successfully imaged, but only using the Fresnel mode with a large defocus in the JEOL 2000FX. Tracks were visible down to wavelengths of $0.5\mu\text{m}$. The magnitude of the magnetic deflection angle for the $10\mu\text{m}$ wavelength tracks was estimated from the width of the wall images to be of the order of $0.9 \times 10^{-6}\text{rad}$. This is approximately 0.07X the deflection that would be expected for saturation induction with the same specimen tilt and approximately half the deflection that would be expected for remanence with the same specimen tilt. With knowledge of the deflection angle it was possible to estimate the magnetisation for a recorded wavelength of $10\mu\text{m}$ (of the order of 30kA.m^{-1}).

It is difficult to draw any firm conclusions from this study other than to confirm the considerable difficulty reported by other groups who have attempted similar work (Ouchi & Iwasaki 1982). The 200kV accelerating voltage of the JEOL 2000FX was advantageous for the imaging of the perpendicular tracks.

7.1.4 General

One of the most important unanswered questions about CoCr perpendicular recording media is that of the minimum realisable bit size. As a conclusion to this study it is informative to consider how the experimental results contribute to answering this question.

It has been proposed that individual columns (Ouchi & Iwasaki 1984) may act as independent, particle-like, magnetic units. The results in chapters 4 and 5 show that for films deposited directly onto PET, increased boundary segregation of Cr is associated with a decrease in size of the domains. Whilst the smallest stray field spacings observed in DPC studies of the more particulate medium (20-30nm) were compatible with the diameter of small columns, the mean stray field spacing (106nm) was between 2 and 3 times the mean column diameter (40-50nm). If boundary segregation of Cr is the mechanism controlling the domain pattern then the minimum practical bit size, for a particulate medium, will be limited by variations in the microstructure. The column diameter was seen to be variable in all the films examined, and for the films investigated using DPC was occasionally in excess of 100nm.

The EDX and DPC studies have revealed another possible restriction on the achievable bit size with a particulate domain model: the atomic

fraction of Cr for the column boundary regions in the film with predominantly non-ferromagnetic column boundaries (high T_s film on PET) is seen to vary about the mean, so that some parts of the boundary phase remain ferromagnetic in nature. With elemental segregation on such a small scale controlling the extent of exchange coupling it will be very difficult to ensure that all columns are independent magnetic units.

The suggestion that Cr segregation on a scale smaller than the column diameter may allow parts of columns (Maeda et al. 1986) to act as independent magnetic particles has not been tested by these studies. If such segregation exists, however, these films could have the potential for higher recording densities than those with only boundary segregation.

It is possible that the microvoids observed in the high T_s film on Ge may act to pin domain walls or provide nucleation sites for domains during magnetisation (Lee et al. 1988). If this is the case, they could hold the key to higher recording densities since they are distributed on a scale smaller than the column diameter.

These conclusions illustrate that the results of this project give an improved understanding of some of the fundamental mechanisms controlling the relationship between the physical and magnetic microstructure. Additionally, we have demonstrated that with Fresnel microscopy it is possible to image perpendicular tracks. This represents valuable groundwork for any future studies on perpendicular recordings.

The combination of CTEM and STEM techniques available using the equipment at Glasgow University has therefore proven very well suited to the study of CoCr thin film perpendicular recording media.

7.2 FUTURE WORK

7.2.1 Specific

The EDX work described in chapter 4 was very fruitful, providing a wealth of compositional data on a range of specimens. Because of the large volume of data, however, it is hard to assimilate all the information. It is felt that these results would yield even more information if they were incorporated into a full theoretical treatment of the patterns of segregation.

An obvious omission in the DPC studies was investigation of CoCr layers deposited on Ge. This was because the difficulty in producing suitable cross-sections of films deposited directly onto PET left no time to attempt the preparation of any other cross-sections. If suitable specimens could be produced the studies reported in chapter 5 suggest that DPC imaging would give a measure of the mean domain sizes for these films and perhaps be able to shed some light on the question of whether or not the microvoids in the high T_s film act by pinning domain walls. Another interesting experiment which could be performed with the DPC technique would be the study of layers deposited directly onto PET at a temperature of 60C and at a temperature in excess of 90C. The mean stray field spacings from such films could indicate whether or not the trend to a particulate medium progresses gradually as T_s goes up (as proposed by Bernardis et al. 1989).

As stated in chapter 5 one of the main problems with the DPC imaging work was the availability of suitable specimens. The success rate in the preparation of ion-milled cross-sections is always low

because of the delicate nature of the specimens. This problem was compounded in these investigations by the exacting demands on specimen thickness of the DPC imaging mode. Development of a more reliable preparation technique is therefore a straightforward way to improve the technique. This could perhaps be achieved by adopting part of the specimen preparation technique employed by McGibbon (1989) in which supporting Si extends over the whole area of the specimen grid and hence gives rise to a more robust specimen. Additionally the advent of the use of Au as an alternative nucleation layer to Ge may allow study of the CoCr layer alone since the Au can be removed chemically.

7.2.2 Apparatus

Chapter 4 has shown that simple patterns of elemental segregation such as to the column boundaries, or to the core of the columns, can be detected by manual probe positioning. This technique, however, cannot reveal more complicated patterns of segregation such as the CP structure suggested by Maeda. The EDX studies would benefit, therefore, from an automated system to sequentially select positions for the acquisition of spectra. This would allow both point analysis (PA) and line analysis (LA). With such a system Maeda (1989) has been able to plot dot maps showing compositional inhomogeneity in samples which when wet etched exhibit the "frog-egg" pattern (see chapter 4).

In the DPC work the exacting demands on specimen thickness are partly attributable to the 100kV accelerating voltage and partly attributable to the limited dynamic range of the detection system. Improvements in either of these would make the specimen thickness constraints less severe. Additionally, image processing facilities on an

IBM 5080 system, superior to those available with the AN10000, have recently become accessible from the Physics Department. These should make it possible to extract more information from images during future experiments.

The goal with the study of perpendicular tracks was to have high resolution images with both the track and the physical microstructure visible. The disparity observed, in chapter 6, between the magnitude of the small signal produced by the magnetic deflection and the strong signal associated with the crystal structure, however, is very large. This means that, even if the crystallographic contrast can be suppressed sufficiently to detect the magnetic signal, attempts to image both will probably require parallel acquisition of a magnetic and a structural signal at different amplifier gains. Chapter 5 showed that it was possible to do this for thin cross-sections and form a composite image through signal recombination using DPC imaging. At the moment attempts to simultaneously collect signals with magnetic and physical information for tracks have been prevented because of specimen thickness constraints with the 100kV limit to the accelerating voltage in the VG HB5 and limited resolution in the JEOL 2000 FX. Therefore, although this technique would seem to have the potential to image tracks it will require either thinner specimens or a higher resolution STEM with an accelerating voltage of $\geq 200\text{kV}$.

7.2.3 General

To attain the maximum recording densities for CoCr it will be necessary to find the optimum domain structure and improve the film properties accordingly. If this turns out to be a particulate model the grains will have to be either more uniform in size or very small on

average so that the diameter of the largest columns is reduced. If Cr segregation controls the domain size it will need to be at a uniform level greater than 25 atomic % Cr, or have a mean level high enough to ensure that fluctuations do not allow any columns to couple magnetically. If microvoids can pin domain walls, or operate in some other manner to increase the recording densities, they will need to be regularly spaced on the smallest scale possible. Additionally, the possibility of a combination of all of these mechanisms and/or other mechanisms acting in a single film must be investigated.

A rough average value of 25 atomic % Cr is required to ensure that the diameter of the largest columns is reduced. If Cr segregation controls the domain size it will need to be at a uniform level greater than 25 atomic % Cr, or have a mean level high enough to ensure that fluctuations do not allow any columns to couple magnetically. If microvoids can pin domain walls, or operate in some other manner to increase the recording densities, they will need to be regularly spaced on the smallest scale possible. Additionally, the possibility of a combination of all of these mechanisms and/or other mechanisms acting in a single film must be investigated.

Cr segregation controls the domain size it will need to be at a uniform level greater than 25 atomic % Cr, or have a mean level high enough to ensure that fluctuations do not allow any columns to couple magnetically. If microvoids can pin domain walls, or operate in some other manner to increase the recording densities, they will need to be regularly spaced on the smallest scale possible. Additionally, the possibility of a combination of all of these mechanisms and/or other mechanisms acting in a single film must be investigated.

Cr segregation controls the domain size it will need to be at a uniform level greater than 25 atomic % Cr, or have a mean level high enough to ensure that fluctuations do not allow any columns to couple magnetically. If microvoids can pin domain walls, or operate in some other manner to increase the recording densities, they will need to be regularly spaced on the smallest scale possible. Additionally, the possibility of a combination of all of these mechanisms and/or other mechanisms acting in a single film must be investigated.

APPENDIX 1

MACROSCOPIC CHARACTERISATION TECHNIQUES

The techniques described in this appendix were employed for macroscopic characterisation of the CoCr films discussed in this thesis. The operating procedures for the techniques were demonstrated during the 3 month placement with Philips Research Laboratories in Eindhoven.

A1.1 MAGNETIC CHARACTERISATION

Vibrating Sample Magnetometer (VSM)

A sample (approximately 1cm in diameter) of foil is held in a fixed orientation (can be in-plane or perpendicular) relative to an applied magnetic field. The sample is vibrated at 80Hz in a vertical plane and the applied field is varied. Sample magnetisation is measured using small coils in the vicinity of the sample.

Using this equipment it is possible to obtain the perpendicular and in-plane volume hysteresis loops. These give macroscopic information on the magnetic properties including \underline{M}_s , \underline{M}_r , and \underline{H}_c .

Torque Magnetometer

A sample (similar in shape to that used above) is placed in an applied magnetic field. The torque required to hold it either in the plane of, or perpendicular to, the applied field is measured as the field is rotated

through 180°. Torque is then plotted against angle of applied field and from this the magnetic anisotropy constants can be deduced.

Kerr Magneto-Optical Surface Hysteresis Loop Measurement

The plane of polarisation of light is rotated on reflection from a magnetic sample. The angle of rotation gives a measure of the surface magnetisation at the point of reflection (see chapter 2, section 2.3).

A magnetic field is applied to the specimen and the angle of rotation is recorded using a polarisation spectrometer. In this way it is possible to obtain a surface hysteresis loop.

A1.2 PHYSICAL CHARACTERISATION

X-ray Crystal Spectroscopy (Rocking Curves)

A collimated beam of monochromatic x-ray photons is incident on a sample of polycrystalline thin film. X-rays are strongly reflected from the crystallites provided the conditions for Bragg scattering are satisfied. The angular dependence of the intensity in the scattered beam can be used to investigate the crystal structure. From such studies the dispersion angle of the hcp c-axis, $\Delta\theta_{50}$, for CoCr thin films can be deduced.

APPENDIX 2

ANALYSIS PROGRAM FOR X-RAY SPECTRA

The program listed in this section, "BEAUTY", was used to calculate the atomic fraction of Cr, X, ($\text{Co}_{100-X}\text{Cr}_X$) from an x-ray spectrum for a CoCr thin film (see chapter 4). BEAUTY was written in FORTRAN for use on the Link Analytical AN10000 system, on which the spectra were acquired. On this system spectra are stored as 5 blocks of information (blocks 0-4), the first of which (block 0) is a header block. The comments on the program listing explain the essentials of the program. In addition to these it should be noted that the background windows, straddling the energy region of interest, were selected for channels as close as possible to the Co and Cr peaks for which there were no significant peaks above the background. To facilitate analysis of all the spectra in a given rootfile (see chapter 2) a sequence was written to call each spectrum individually, rename it "DOG.SP" and run the program. This version of BEAUTY includes the correction for overlap of the $\text{FeK}\beta$ peak with the $\text{Co K}\alpha$ peak.

```

CC PROGRAM TO STRIP BREMSSTRAHLUNG FROM CoCr EDX SPECTRUM &
CC OUTPUT Co/Cr Ka COUNT RATIO & THE ATOMIC FRACTION OF Cr
CC
CC DEFINE THE VARIABLES & CONFIGURE SYSTEM
CC
      REAL Y1,Y2,GRAD,CR,SUM1,CO,RATIO,PERC,Z,FE,FEA
      INTEGER IA,IB,SUM
      DIMENSION ISPEC(1280)
      CALL ALPH16
      CALL FRTON
10    CALL OPEN(1,"DOG.SF",1,NERR,$70)
CC
CC READ SPECTRUM INTO ARRAY "ISPEC"
CC
      CALL RDBLK(1,0,ISPEC,5,NERR)
      CALL CLOSE(1,NERR,$70)

CC
CC CALCULATE & OUTPUT TOTAL NO. OF COUNTS IN THE BACKGROUND (B/G)
CC WINDOWS ABOVE & BELOW ENERGY REGION OF INTEREST & CALCULATE
CC THE MEAN NO. OF COUNTS PER CHANNEL IN THE WINDOW
CC
20    SUM=0
      DO 30 IA=496,522
        SUM=SUM+ISPEC(IA)
30    CONTINUE
      CALL MESS("<15><12>LBG=")
      CALL IPUTNO(SUM,5)
      Y1=SUM/27.
      SUM=0
      DO 40 IB=734,760
        SUM=SUM+ISPEC(IB)
40    CONTINUE
      CALL MESS("<15><12>HBG=")
      CALL IPUTNO(SUM,5)
      Y2=SUM/27.

CC
CC CALCULATE & OUTPUT GRADIENT FOR LINEAR B/G FALL-OFF
CC
      GRAD=(Y1-Y2)/238
      CALL MESS("<15><12>BG GRADIENT = -")
      CALL PUTNO(GRAD,8,4)

CC
CC CALCULATE & OUTPUT TOTAL COUNTS IN B/G-DEDUCTED Cr Ka &
CC Fe Kb (FROM Fe Ka USING PARTITION FUNCTION) PEAKS
CC
      SUM1=0
      DO 50 IA=528,547
        SUM1=SUM1+(ISPEC(IA)-Y2)
50    CONTINUE
      CR=SUM1-(20*209.5*GRAD)
      CALL MESS("<15><12>CORRECTED Cr Ka PEAK COUNTS =")
      CALL PUTNO(CR,11,5)
      SUM1=0
      DO 55 IA=580,596
        SUM1=SUM1+(ISPEC(IA)-Y2)
55    CONTINUE
      FEA=SUM1-(17*159.*GRAD)
      FE=(FEA*0.139)
      CALL MESS("<15><12>CORRECTED Fe Kb PEAK COUNTS =")
      CALL PUTNO(FE,11,5)

CC
CC DEDUCT Fe Kb COUNTS FROM Co Ka COUNTS & OUTPUT CORRECTED
CC Co Ka COUNTS
CC
      SUM1=0
      DO 60 IA=601,627
        SUM1=SUM1+(ISPEC(IA)-Y2)
60    CONTINUE
      CO=(SUM1-FE)-(27*133.*GRAD)
      CALL MESS("<15><12>CORRECTED Co Ka PEAK COUNTS =")
      CALL PUTNO(CO,11,5)

CC
CC OUTPUT Co/Cr Ka COUNT RATIO
CC
      RATIO=CO/CR
      CALL MESS("<15><12>Co:Cr Ka PEAK RATIO =")
      CALL PUTNO(RATIO,6,3)

CC
CC CALCULATE & OUTPUT THE ATOMIC FRACTION OF Cr
CC
      Z=(RATIO*1.076)/((RATIO*1.076)+1)
      PERC=100.-(Z*100.)
      CALL MESS("<15><12>ATOMIC FRACTION OF Cr =")
      CALL PUTNO(PERC,5,2)
70    STOP
      END

```

Figure A2.1

Analysis program for EDX spectra.

REFERENCES

CHAPTER 1

- W. Andra, H. Danan: IEEE Trans. Magn., MAG-23 (1987) 62-64
- J.P.C. Bernardts, G.J.P. van Engelen, C.P.G. Schrauwen, H.H. Stel: J. Magn. Magn. Mat., 78 (1989) 119-121
- R.W. de Bie, S.J. Luitjens, V. Zieren, C.P.G. Schrauwen, J.P.C. Bernardts: IEEE Trans. Magn., MAG-23 (1987) 2091
- J.N. Chapman, I.R. McFadyen, J.P.C. Bernardts: J. Magn. Magn. Mat., 62 (1986) 359-366
- D. Dressler, J.H. Judy 1974: IEEE Trans. Magn., MAG-10 (1974) 674
- M. Futamoto, Y. Honda, H. Kakibayashi, K. Yoshida: IEEE Trans. Magn., MAG-21 (1985) 1426-1428
- F. Greidanus, S. Klahn: Angew. Chem. 101 (1989) 243-249
- J. Hecht: in "New Scientist" 1699, ed. M. Kenward (IPC Magazines) 125 (1990) 40
- W. Heisenberg: Z. Physik, 49, 619 (1928)
- H. Hoffmann: IEEE Trans. Magn., MAG-22 (1986) 472-477
- S. Iwasaki, K. Takemura: IEEE Trans. Magn., MAG-11 (1975) 1173-1175
- S. Iwasaki, K. Nakamura: IEEE Trans. Magn., MAG-13 (1977) 1272
- S. Iwasaki, K. Ouchi, N. Honda: IEEE Trans. Magn., MAG-16 (1980) 1111-1113
- F. Jorgensen: "The Complete Handbook of Magnetic Recording" (TAB) (1980)
- E. Koster, T.C. Arnoldussen: in "Magnetic Recording, Vol. 1: Technology", ed's C.D. Mee, E. D. Daniel (McGraw-Hill) (1987)

- J.C. Lodder, T. Wielinga: IEEE Trans. Magn., MAG-20 (1984) 57-59
- J.C. Lodder, D. Wind, G.E.v. Dorssen, Th.J. Popma, A. Hubert: IEEE Trans. Magn., MAG-23 (1987) 214-216
- S.B. Luitjens, R.W. de Bie, V. Zieren, J.P.C. Bernards, C.P.G. Schrauwen, H.A.J. Cramer: IEEE Trans. Magn., MAG-24 (1988) 2897-2899
- I.R.McFadyen: Ph.D. Thesis, University of Glasgow (1986)
- D. Mee, E.D. Daniel: in "Magnetic Recording, Vol. 1: Technology", ed's C.D. Mee, E. D. Daniel (McGraw-Hill) (1987)
- G.R. Morrison: Ph.D. Thesis, University of Glasgow (1981)
- Y. Nakamura, S. Iwasaki: in JARECT 15 "Recent Magnetism for Electronics" ed. Y. Sakurai (North Holland) (1984)
- M. Ohkoshi, T. Kusuda: Jpn. J. Appl. Phys. 22 (1983) 130-132
- K. Ouchi, S. Iwasaki: in JARECT 15 "Recent Magnetism for Electronics" ed. Y. Sakurai (North Holland) (1984) 51-66
- K. Ouchi, S. Iwasaki: IEEE Trans. J. Magn. Jpn. 2 (1987¹) 24-34
- K. Ouchi, S. Iwasaki: IEEE Trans. Magn., MAG-23 (1987²) 2443
- F.T. Parker, H. Oesterreicher, E. Fullerton: submitted to J. Appl. Phys. (1989)
- J. Smits, S.B. Luitjens, F.J.A. den Broeder, A.G. Dirks: J. Magn. Magn. Mat., 31-34 , (1983) 920-922
- T. Suzuki: IEEE Trans. Magn., MAG-20 (1984) 675-680
- R. Sugita, T. Kunieda, F. Kobayashi: IEEE Trans. Magn., MAG-17 (1981) 3172
- P.Weiss: J. Phys., 6, 661 (1907)
- R.M. White: in "Introduction to Magnetic Recording", ed. R.M. White (1985)
- J-G. Zhu, H.N. Bertram: J. Appl. Phys. 66 (1989) 1291-1307

V. Zieren, S.B. Luitjens, M.J. Piena, R.W. de Bie, C.P.G. Schrauwen,
J.P.C. Bernards: IEEE Trans. Magn., MAG-24 (1988) 2597

CHAPTER 2

Y. Aharonov, D. Bohm: Phys. Rev. 115 (1959) 485-491

F. Bitter: Phys. Rev. 38 (1931) 1903

J.N. Chapman, P.E. Batson, E.M. Waddell, R.P. Ferrier:
Ultramicroscopy 3 (1978) 203-214

J.N. Chapman, E.M. Waddell, P.E. Batson, R.P. Ferrier:
Ultramicroscopy 4 (1979) 283

J.N. Chapman: J. Appl. Phys., 17, (1984) 623-647

J.M. Cowley: Ultramicroscopy 2 (1976) 3-16

J.M. Cowley: Appl. Letts. 15 (2) (1969) 58-59

A.V. Crewe: in "Electron Microscopy and Material Science, ed. U.
Valdre (1971) 162

P.R. Crozier: Ph.D. Thesis, University of Glasgow (1985)

N.H. Dekkers, H. de Lang: Optik 41 (1974) 452-456

J.F. Dillon Jr.: J. Appl. Phys., 29, (1958) 1286

P. Grutter, E. Meyer, H. Heinzelmann, R. Rosenthaler, H.-J. Hidber,
H.-R. Guntherodt: J. Vac. Sci. Technol. A6 (1988) 279

T.A. Hall, B.L. Gupta: in "An Introduction to Analytical Electron
Microscopy", ed's J.J. Hren, J.C. Goldstein, J.C. Joy (Plenum)
(1979)

C.J. Humphreys: Ultramicroscopy 7 (1981) 7-12

G.W. Lorimer: in "Quantitative Electron Microscopy", ed's J.N.
Chapman, A.J. Craven (SUSSP No. 25) ch. 4 (1983)

I.R. McFadyen: Ph.D. Thesis, University of Glasgow (1986)

A.J. McGibbon: Ph.D. Thesis, University of Glasgow (1989)

- G.R. Morrison: Ph.D. Thesis, University of Glasgow (1981)
- W. Rave, R. Schaffer, A. Hubert: J. Magn. Magn. Mat., 65 (1987) 7-14
- L. Reimer: in "Transmission Electron Microscopy", ed. D.L. MacAdam (Springer-Verlag) (1982)
- A. Tonomura: J. Appl. Phys., 61, (1987) 4297-4302

CHAPTER 3

- J.P.C. Bernard, C.P.G. Schrauwen, S.B. Luitjens, V. Zieren, R.W. de Bie: IEEE Trans. Magn., MAG-23 (1987) 125-127
- N.G. Chew, A.G. Cullis: Ultramicroscopy 23 (1987) 175
- M. Futamoto, Y. Honda, H Kakibayashi, K. Yoshida: IEEE Trans. Magn., MAG-21 (1985) 1426-1428
- M. Futamoto, Y. Honda, T. Shimotsu, H Kakibayashi, K. Yoshida: Jap. J. Appl. Phys. 25 (1986) 1128-1129
- P.G. Grundy, M. Ali: J. Magn. Magn. Mat., 40 (1983) 154-162
- C. Kittel, in "Introduction to Solid State Physics", (J. Wiley & Sons) (1953)
- F.T. Parker, H. Oesterreicher, E. Fullerton: submitted to J. Appl. Phys. (1989)
- C.P.G. Schrauwen, J.P.C. Bernard, R.W. de Bie, G.J.P. van Engelen, H.H. Stel, V. Zieren, S.B. Luitjens: IEEE Trans. Magn., MAG-24(2) (1988) 1901

CHAPTER 4

- F.F. Abraham, C.R. Brundle: J. Vac. Sci. Technol., 18 (1981) 506-

- W. Andra, H. Danan: IEEE Trans. Magn., MAG-23 (1987) 62-64
- J.P.C. Bernards, C.P.G. Schrauwen, S.B. Luitjens: J. Appl. Phys. 49 (1989) 491
- R.W. de Bie, S.J. Luitjens, V. Zieren, C.P.G. Schrauwen, J.P.C. Bernards: IEEE Trans. Magn., MAG-23 (1987) 2091
- F. Bolzoni, F. Leccabue, R. Pannizzieri, L. Pareti: J. Magn. Magn. Mat. (1983) 845
- J.N. Chapman, I.R. McFadyen, J.P.C. Bernards: J. Magn. Magn. Mat., 62 (1986) 359-366
- G. Cliff and G.W. Lorimer: Proc. 5th European Congress on Electron Microscopy, Bristol (1972)
- J.I. Goldstein, J.L. Costley, G.W. Lorimer, S.J.B. Reed: SEM 1977, ed. O. Johari, IIRTI, Chicago (1977) 315
- C. Gray: Ph.D. Thesis, University of Glasgow (1983)
- P.G. Grundy, M. Ali: J. Magn. Magn. Mat., 40 (1983) 154-162
- H. Hoffmann, H. Mandl, Th. Schurmann: Proc. of ICM 85, San Francisco (1985)
- J.-W. Lee, B.G. Demczyk, K.R. Mountfield, D.E. Laughlin: J. Appl. Phys. 63 (1988) 2905-2907
- S.B. Luitjens, R.W. de Bie, V. Zieren, J.P.C. Bernards, C.P.G. Schrauwen, H.A.J. Cramer: IEEE Trans. Magn., MAG-24 (1988) 2897-2899
- Y. Maeda, S. Hirono, M. Asahi: Jpn. J. Appl. Phys. 24 (1985) 951-955
- Y. Maeda, M. Asahi: J. Appl. Phys. 61 (1987) 1972-1978
- Y. Maeda, M. Takahashi: IEEE Trans. Magn., MAG-24 (1988) 3012-3014
- Y. Maeda, M. Takahashi: Jpn. J. Appl. Phys. 28 (1989) 248-251

- I.R.McFadyen: Ph.D. Thesis, University of Glasgow (1986)
- A.J. McGibbon: Ph.D. Thesis, University of Glasgow (1989)
- K. Ouchi, S. Iwasaki: IEEE Trans. Magn., MAG-23 (1987) 2443
- L. Reimer: in "Transmission Electron Microscopy", ed. D.L. MacAdam (Springer-Verlag) (1982)
- J. Smits, S.B. Luitjens, F.J.A. den Broeder: J. Appl. Phys. 55 (1983) 2260-2262
- R. Sugita, T. Kunieda, F. Kobayashi: IEEE Trans. Magn., MAG-17 (1981) 3172

CHAPTER 5

- J.P.C. Bernards, C.P.G. Schrauwen, S.B. Luitjens: J.Appl. Phys. 49 (1989) 491
- J.P.C. Bernards: Private communication (1990)
- C. Bonnebat: IEEE Trans. Magn., MAG-23 (1987) 9-13
- J.N. Chapman, P.E. Batson, E.M. Waddell, R.P. Ferrier: Ultramicroscopy 3 (1978) 203-214
- S. Chikazumi: in "Physics of Magnetism" ed. S.H. Charap (J. Wiley & Sons) (1964)
- R.P. Ferrier: Private communication (1989)
- Y. Honda, M. Futamoto, T. Kawasaki, K. Yoshida, M. Koizumi, F. Kugiya, A. Tonomura: Jpn. J. Appl. Phys. 26 (1987) 923-925
- S. Iwasaki: IEEE Trans. Magn., MAG-20 (1984) 657-662
- C. Kooy, U. Enz: Philips Research Reports 15 (1960)
- W.H. Kraan, M.T. Rekveldt, K. Hemmes, J.C. Lodder: IEEE Trans. Magn., MAG-23 (1987) 65-67
- I.R.McFadyen: Ph.D. Thesis, University of Glasgow (1986)
- S. McVitie: Ph.D. Thesis, University of Glasgow (1988)

W. Shockley: Phys. Rev. 73 (1948) 1246

J-G. Zhu, H.N. Bertram: J. Appl. Phys. 66 (1989) 1291-1307

CHAPTER 6

J.P.C. Bernards, C.P.G. Schrauwen, S.B. Luitjens, V. Zieren, R.W. de Bie: IEEE Trans. Magn., MAG-23 (1987) 125-127

J. P. C. Bernards, A.G. den Boef: to be presented at Intermag (1990)

S.B. Luitjens, R.W. de Bie, V. Zieren, J.P.C. Bernards, C.P.G.

Schrauwen, H.A.J. Cramer: IEEE Trans. Magn., MAG-24 (1988) 2897-2899

G.R. Morrison: Ph.D. Thesis, University of Glasgow (1981)

K. Nishimoto: in JARECT 15 "Recent Magnetism for Electronics" ed. Y. Sakurai (North Holland) (1984) 29

K. Yoshida, Y. Honda, T. Kawasaki, M. Koizumi, F. Kugiyama, M.

Futamoto, A. Tonomura: IEEE Trans. Magn., MAG-23 (1987) 2073-2075

CHAPTER 7

J.P.C. Bernards, G.J.P. van Engelen, C.P.G. Schrauwen, H.H. Stel: J. Magn. Magn. Mat., 78 (1989) 119-121

J.N. Chapman, P.E. Batson, E.M. Waddell, R.P. Ferrier:

Ultramicroscopy 3 (1978) 203-214

J.N. Chapman, I.R. McFadyen, J.P.C. Bernards: J. Magn. Magn. Mat., 62 (1986) 359-366

A.J. McGibbon: Ph.D. Thesis, University of Glasgow (1989)

J.-W. Lee, B.G. Demczyk, K.R. Mountfield, D.E. Laughlin: J. Appl.

Phys. 63 (1988) 2905-2907

Y. Maeda, M. Asahi, M. Seki: Jpn. J. Appl. Phys. 25 (1986) 668-670

Y. Maeda, M Takahashi: Jpn. J. Appl. Phys. 28 (1989) 248-251

I.R.McFadyen: Ph.D. Thesis, University of Glasgow (1986)

K. Ouchi, S. Iwasaki: IEEE Trans. Magn., MAG-18 (1982) 1110

K. Ouchi, S. Iwasaki: in JARECT 15 "Recent Magnetism for
Electronics" ed. Y. Sakurai (North Holland) (1984) 51-66

